



HAL
open science

A Novel Anisotropic Elasticity-Palpography IVUS Imaging Tool and Characterization of the Viscoelasto-Plastic Properties of Angioplasty Balloon: Towards a Better Assessment and Treatment of Coronary Artery Diseases

Armida Gomez Lara

► To cite this version:

Armida Gomez Lara. A Novel Anisotropic Elasticity-Palpography IVUS Imaging Tool and Characterization of the Viscoelasto-Plastic Properties of Angioplasty Balloon: Towards a Better Assessment and Treatment of Coronary Artery Diseases. Human health and pathology. Université Grenoble Alpes, 2019. English. NNT : 2019GREAS012 . tel-02419090

HAL Id: tel-02419090

<https://theses.hal.science/tel-02419090>

Submitted on 19 Dec 2019

HAL is a multi-disciplinary open access archive for the deposit and dissemination of scientific research documents, whether they are published or not. The documents may come from teaching and research institutions in France or abroad, or from public or private research centers.

L'archive ouverte pluridisciplinaire **HAL**, est destinée au dépôt et à la diffusion de documents scientifiques de niveau recherche, publiés ou non, émanant des établissements d'enseignement et de recherche français ou étrangers, des laboratoires publics ou privés.

THÈSE

Pour obtenir le grade de

DOCTEUR DE LA COMMUNAUTÉ UNIVERSITÉ GRENOBLE ALPES

Spécialité : **Modèles, méthodes et algorithmes pour la
Biologie, la Santé et l'environnement**

Arrêté ministériel : 25 mai 2016

Présentée par

Armida Leticia GÓMEZ LARA

Thèse dirigée par **Jacques OHAYON, Professeur Université
Savoie Mont-Blanc, Polytech Annecy-Chambéry, Le Bourget
du Lac et Laboratoire TIMC-IMAG, UGA, CNRS UMR 5525,
Grenoble, France** et

codirigée par **Gérard FINET, Professeur des Universités -
Praticien Hospitalier, HCL, Université Claude Bernard, Lyon
1, INSERM Unit 886, Lyon, France**

préparée au sein du **Laboratoire Techniques de l'Ingénierie
Médicale et de la Complexité - Informatique, Mathématiques,
Applications**
dans **l'École Doctorale Ingénierie pour la Santé, la Cognition et
l'Environnement (EDISCE)**

Nouvel Outil d'Imagerie IVUS de Palpographie Anisotrope et Caractérisation des Propriétés Viscoélasto-Plastiques du ballon d'Angioplastie: Pour un Meilleur Traitement de la Plaque d'Athérome Coronarienne en Clinique

Thèse soutenue publiquement le **11 juin 2019**,
devant le jury composé de :

Monsieur Patrick CLARYSSE

Directeur de Recherche CNRS, Lyon, France, Rapporteur

Monsieur David MITTON

Directeur de Recherche, LBMC, Université de Lyon - IFSTTAR, Lyon,
France, Rapporteur

Monsieur Gilles RIOUFOL

Professeur des Universités - Praticien Hospitalier, HCL, Université
Claude Bernard, Lyon 1, INSERM Unit 886, Lyon, France, Président

Monsieur Alex ELÍAS-ZUÑIGA

Professeur des Universités, Tecnológico de Monterrey – ITESM,
Monterrey, Mexique, Examinateur

Monsieur Gérard FINET

Professeur des Universités - Praticien Hospitalier, HCL, Université
Claude Bernard, Lyon 1, INSERM Unit 886, Lyon, France

Monsieur Jacques OHAYON

Professeur Université Savoie Mont-Blanc, Polytech Annecy-Chambéry,
Le Bourget du Lac et Laboratoire TIMC-IMAG, UGA, CNRS UMR 5525,
Grenoble, France



THESIS

Submitted for the grade of

DOCTOR OF THE COMMUNAUTÉ UNIVERSITÉ GRENOBLE ALPES

Specialty : **Models, methods and algorithms for Biology,
Health and the Environment**

Arrêté ministériel: May 25th, 2016

Presented by

Armida Leticia GÓMEZ LARA

Thesis directe by **Jacques OHAYON, Professeur Université
Savoie Mont-Blanc, Polytech Annecy-Chambéry, Le Bourget
du Lac et Laboratoire TIMC-IMAG, UGA, CNRS UMR 5525,
Grenoble, France** et

co-directed by **Gérard FINET, Professeur des Universités -
Praticien Hospitalier, HCL, Université Claude Bernard, Lyon
1, INSERM Unit 886, Lyon, France**

prepared at **Laboratoire Techniques de l'Ingénierie Médicale et
de la Complexité - Informatique, Mathématiques, Applications**
in the **Doctoral School of Engineering for Health, Cognition
and the Environment (EDISCE)**

A Novel Anisotropic Elasticity-Palpography IVUS Imaging Tool and Characterization of the Viscoelasto-Plastic Properties of Angioplasty Balloon: Towards a Better Assessment and Treatment of Coronary Artery Diseases (PRE- SOUTENANCE Version)

Thesis defended publicly on **June 11th, 2019**,
before the jury composed of:

Patrick CLARYSSE, PhD

Directeur de Recherche CNRS, Lyon, France, Rapporteur

David MITTON, PhD

Directeur de Recherche, LBMC, Université de Lyon - IFSTTAR, Lyon,
France, Rapporteur

Gilles RIOUFOL, MD, PhD

Professeur des Universités - Praticien Hospitalier, HCL, Université
Claude Bernard, Lyon 1, INSERM Unit 886, Lyon, France.

Alex ELÍAS-ZUÑIGA , PhD

Professeur des Universités, Tecnológico de Monterrey – ITESM,
Monterrey, Mexique, Examinateur

Gérard FINET, MD, PhD

Professeur des Universités - Praticien Hospitalier, HCL, Université
Claude Bernard, Lyon 1, INSERM Unit 886, Lyon, France

Jacques OHAYON, PhD

Professeur Université Savoie Mont-Blanc, Polytech Annecy-Chambéry,
Le Bourget du Lac et Laboratoire TIMC-IMAG, UGA, CNRS UMR 5525,
Grenoble, France



Contents

Acknowledgements	7
Abstract	9
Résumé	10
Introduction	15
I Imaging the Atherosclerotic Plaque in Clinics	17
1 Cardiovascular disease: clinical and biomechanical overview	19
1.1 The burden of cardiovascular disease	19
1.2 Atherosclerosis	20
1.3 Coronary imaging by IVUS	26
1.3.1 Clinical applications of IVUS	27
1.4 Derived techniques for plaque assessment	27
1.4.1 IVUS strain-elastography	28
1.4.2 Modulography	34
1.4.3 Validation of the morpho-elastic reconstruction imaging tool	36
1.4.4 From model to patient	39
1.5 My next steps and works performed	40
2 Are b-mode images a viable alternative to RF for the computation of modulograms of atherosclerotic plaques?	43
2.1 Introduction	43

2.2	Zhang’s b-mode elastography method	44
2.3	Materials and methods	45
2.3.1	IVUS acquisition and image analysis	47
2.3.2	Spatial displacement and strain field distributions	47
2.3.3	B-mode based algorithm	49
2.4	Results and Discussion on the performance of Zhang’s algorithm	49
2.4.1	Displacement estimations	49
2.4.2	Area strain calculations	54
2.5	Conclusions	54
3	A novel elasticity-palpography technique to characterize the anisotropic mechanical properties of healthy and pathological coronary vessels: theory and numerical feasibility	55
3.1	Introduction	56
3.2	Materials and methods	57
3.2.1	IVUS study and plaque geometries	57
3.2.2	Forward problem: Spatial displacement and strain field distributions	60
3.2.3	Inverse Problem: The Anisotropic Elasticity-Palpography Technique	62
3.3	Results	64
3.3.1	IVUS Study	64
3.3.2	Performance of the Anisotropic Elasticity-Palpography Technique	64
3.4	Discussion	79
4	On the potential of our new elasticity-palpography technique: in vitro validation	83
4.1	Introduction	83
4.2	Materials and methods	84
4.2.1	Experimental in vitro study with PVA-C vessel phantoms	84
4.2.2	Anisotropic elasticity-palpography technique	89
4.3	Results	90
4.3.1	Phantom characterization results	90

4.3.2	In vitro palpography results	93
4.4	Discussion	96
4.5	Conclusions and Perspectives	99
II	Balloon Angioplasty	101
5	Background: Balloon angioplasty technique	103
5.1	Interventional cardiology procedures	103
5.2	The angioplasty procedure	104
5.2.1	The balloon catheter	105
5.2.2	Computational studies of balloon catheters	108
5.3	My next steps and works performed	110
6	Experimental characterization of the viscoelasto-plastic behavior of balloon catheters: Application to Boston Scientific's Maverick² model	113
6.1	Introduction	113
6.2	Materials and methods	114
6.2.1	Balloon catheter measurements	114
6.2.2	Balloon catheter inflation experiments	116
6.2.3	Balloon polymer film tensile tests	123
6.2.4	Internal and external catheters tensile tests	128
6.2.5	Recording of balloon deployment and burst with high speed camera	128
6.3	Discussion	128
6.4	Conclusions and perspectives	131
7	Modeling the viscoelasto-plastic response of balloon catheters for coronary angioplasty: Application to Boston Scientific's Maverick² model	133
7.1	Introduction	133
7.2	Elementary viscoelastic-plastic one-dimensional model: generalized Bingham model.	133
7.3	Results	137
7.4	Conclusions and clinical implications	140

Conclusions and Perspectives	142
7.4.1 Part I. Imaging the atherosclerotic plaque in clinics	143
7.4.2 Part II. Balloon angioplasty	145
Appendices	145
A Constitutive law in linear elasticity for incompressible orthotropic vascular tissues	147
B The elastic anisotropy index AI	149
C Novel anisotropic elasticity-palpography technique applied to RF sequences of rabbit aortas	151
C.1 Experimental <i>ex vivo</i> study of rabbit aortas	151
C.2 Rabbit aorta study results	152
D Balloon mechanical test results	155
D.1 Balloon polymer film tensile tests	155
D.2 Catheter tensile tests	156
List of publications	158
E List of Publications and short CV	159
Bibliography	163
List of Figures	181
List of Tables	195

Acknowledgements

Abstract

Cardiac catheterization has evolved from being initially received with great skepticism to becoming a standard for the diagnosis and treatment of cardiovascular disease. A myriad of derived techniques like balloon angioplasty, intravascular imaging, as well as valve and stent implantation are now routine procedures for interventional cardiologists. Despite these and other great advances in cardiovascular medicine, cardiovascular disease (CVD) still represents the main cause of mortality, accounting for as much as one out of three deaths worldwide. Due to the complexity of CVD, it has become the field of study of researchers among various disciplines in hopes to reduce the burden of the disease. One of such disciplines is mechanics, that applies its principles and approaches to create innovative tools to diagnose, prevent and treat CVD.

The present thesis belongs to the field of cardiovascular biomechanics and aims to develop tools that can be of assistance to physicians in the diagnosis and treatment of coronary artery disease. This dissertation is divided into two parts:

Part I: Imaging the atherosclerotic plaque in clinics, is related to the identification and assessment of coronary atherosclerotic plaque with the presentation of a novel palpography algorithm based on continuum mechanics theory.

First, it was investigated whether gray-scale IVUS images are enough for obtaining an accurate elasticity map to assess plaque composition and evolution. Indeed, it was concluded that radiofrequency (RF) data provides more detailed data than b-mode IVUS images. Then a novel anisotropic elasticity-palpography algorithm is described. It computes an apparent elasticity of the plaque from radiofrequency signals obtained through IVUS images. The derivation of an anisotropic index (AI) that can be related to the mechanical properties of the arterial wall, along with a first validation using simulated IVUS images based on real patient geometries of atherosclerotic and healthy plaques is presented. Using this new palpography algorithm, a study was that aimed to validate this technique in vitro was performed. Polyvinyl-alcohol (PVA) cryogel vascular phantoms were fabricated, two of them with increased anisotropy. The phantoms were imaged with IVUS and their mechanical properties were obtained using different characterization techniques. Then, the anisotropy indices modeled with the experimental results and the ones computed with the algorithm were compared.

Part II: Balloon angioplasty is focused on the treatment of coronary plaque and analyzes the mechanical properties of the balloons used for coronary angioplasty.

First, the visco-elasto-plastic mechanical characterization of a specific balloon catheter model, the Maverick2 from Boston Scientific, is presented. Geometrical measurements using different microscopy techniques, balloon inflation tests, tensile tests and high-speed images are used to describe the mechanical behavior of the balloon components. The previous results are used in to define a model that can accurately predict the viscoelasto-plastic behavior of the angioplasty balloon film. These results could be used as the basis for a model to predict the inflation behavior of the angioplasty balloon during consecutive inflations in clinics.

Résumé

En dépit des grandes avancées dans le domaine de la recherche médicale, les maladies cardiovasculaires (MCV) représentent toujours l'une des causes principales de mortalité dans le monde, et sont globalement responsables d'un tiers des décès dus à des maladies. En raison de la diversité et de la complexité de ces MCV, les recherches dans des domaines variés tels que la biomécanique, médecine, biologie, anatomopathologie, pharmacologie et imagerie se sont accrues. Ces recherches multidisciplinaires se développent dans l'espoir de mieux comprendre ces pathologies afin de mieux les traiter, ainsi que de réduire les coûts hospitaliers liés aux traitements des patients. Mes travaux de thèse rentrent dans ce cadre-là et s'inscrivent dans le champ de la Biomécanique Cardiovasculaire lié aux maladies coronariennes. Ils visent à développer de nouveaux outils d'aide au diagnostic médical pour la cardiologie interventionnelle.

Mon rapport doctoral comporte deux parties :

Dans la 1ère partie, je m'intéresse à l'imagerie de la plaque coronarienne obtenue à partir de l'exploration endovasculaire par ultrason (IVUS) pratiquée en clinique et plus particulièrement en utilisant le signal radio-fréquence (RF) IVUS. Le risque de rupture d'une plaque d'athérome coronarienne vulnérable (PV) est lié à la composition composite de sa lésion athéromateuse. Les proximités de tissus biologiques très différents engendrent des gradients d'élasticité importants responsables de concentrations de contraintes de fortes amplitudes, pouvant potentiellement rompre la PV. La mécanique des milieux continus va nous aider à identifier les propriétés mécaniques de tous les constituants de la PV à partir des séquences IVUS obtenues sur patients. Plusieurs études développées au sein de notre laboratoire TIMC (telles que la Palpographie isotrope, la Modulographie isotrope) permettent une quantification préliminaire des propriétés mécaniques de tous les constituants de la lésion. Au sein de cette 1ère partie, je décris dans un premier temps ces techniques existantes, puis dans un 2ème temps je détaille et explique mes travaux de recherche développés lors de ma thèse dans ce domaine d'imagerie. J'ai essayé de répondre aux deux questions essentielles suivantes : 1) Peut-on travailler directement avec le signal IVUS b-mode disponible en routine clinique pour visualiser l'élasticité de la lésion athéromateuse? , et 2) Est-il possible d'améliorer la technique existante de palpographie isotrope afin de tenir compte des propriétés anisotropes de la lésion et de la paroi vasculaire? . Afin d'y répondre, j'ai mené des études à la fois théoriques et expérimentales pour tester les performances des nouveaux outils d'imagerie IVUS proposés.

Dans la 2ème partie de ma thèse, je me suis intéressée à l'angioplastie par ballonnet et plus précisément aux propriétés viscoélasto-plastiques du ballon. En effet, il est essentiel pour le cardiologue de prendre en compte l'évolution des propriétés mécaniques du ballon lors de son utilisation répétée, et cela afin de permettre un acte chirurgical plus précis lors du gonflement du ballonnet au sein des artères coronariennes pathologiques. Cette dernière étude peut servir de base au développement d'un modèle biomécanique plus complet permettant de prédire l'évolution de la courbe pression-diamètre du ballon lors de son utilisation et plus particulièrement lors de ses gonflements consécutifs en utilisation clinique.

**A Novel Anisotropic
Elasticity-Palpography IVUS
Imaging Tool and Characterization
of the Viscoelasto-Plastic Properties
of Angioplasty Balloon: Towards a
Better Assessment and Treatment of
Coronary Artery Diseases**

Introduction

Cardiac catheterization has evolved from being initially received with great skepticism to becoming a standard for the diagnosis and treatment of cardiovascular disease. A myriad of derived techniques like balloon angioplasty, intravascular imaging, as well as valve and stent implantation are now routine procedures for interventional cardiologists. Despite these and other great advances in cardiovascular medicine, cardiovascular disease (CVD) still represents the main cause of mortality, accounting for as much as one out of three deaths worldwide ([World Health Organisation, 2017](#)). Due to the complexity of CVD, it has become the field of study of researchers among various disciplines in hopes to reduce the burden of the disease. One of such disciplines is mechanics, that applies its principles and approaches to create innovative tools to diagnose, prevent and treat CVD.

The present thesis belongs to the field of cardiovascular biomechanics and aims to develop tools that can be of assistance to physicians in the diagnosis and treatment of coronary artery disease.

This dissertation is divided into two parts:

Part I: Imaging the atherosclerotic plaque in clinics (Chapters 2 through 5), is related to the identification and assessment of coronary atherosclerotic plaque with the presentation of a novel palpography algorithm based on continuum mechanics theory.

Chapter 1 presents a non-exhaustive review of the disease from the medical and biomechanical fronts, which includes the basics of the disease, diagnostic imaging modalities, intravascular ultrasound (IVUS)-derived plaque assessment algorithms and biomarkers for plaque assessment.

Chapter 2 describes a study carried out using b-mode IVUS images that investigated whether gray-scale IVUS images are enough for obtaining an accurate elasticity map to assess plaque composition and evolution.

Chapter 3 describes a novel anisotropic elasticity-palpography algorithm that computes an apparent elasticity of the plaque from radiofrequency signals obtained through IVUS images. This chapter provides the derivation of an anisotropic index (AI) that can be related to the mechanical properties of the arterial wall, along with a first validation using simulated IVUS images based on real patient geometries of atherosclerotic and healthy plaques.

Using this new palpography algorithm, **Chapter 4** presents a study that aimed to validate this technique *in vitro*. Three polyvinyl-alcohol (PVA) cryogel vascular phantoms were fabricated, two of them with increased anisotropy. The phantoms were imaged with IVUS and their mechanical properties were obtained using different characterization techniques. Then, the experimental and computed anisotropy indices were compared.

Part II: Balloon angioplasty (Chapters 5 to 7) is focused on the treatment of coronary plaque and analyzes the mechanical properties of the balloons used for coronary angioplasty.

Chapter 5 is dedicated to a brief review of balloon angioplasty procedures that includes a basic medical introduction and is mainly focused on the mechanics behind these vascular devices.

In **Chapter 6**, the visco-elasto-plastic mechanical characterization of a specific balloon catheter model, the Maverick² from Boston Scientific, is presented. Geometrical measurements using different microscopy techniques, balloon inflation tests, tensile tests and high-speed images are used to describe the mechanical behavior of the balloon components.

The previous results are used in **Chapter 7** to define a viscoelasto-plastic one-dimensional model that could describe the uniaxial strain behavior of the balloon film and identify the elastic and visco-plastic responses.

Finally, the concluding remarks of this dissertation and its perspectives are described.

Part I

**Imaging the Atherosclerotic Plaque
in Clinics**

Chapter 1

Cardiovascular disease: clinical and biomechanical overview

1.1 The burden of cardiovascular disease

Cardiovascular diseases (CVDs) are responsible for the majority of deaths worldwide, accounting for nearly a third of all fatalities ([World Health Organisation, 2017](#)). It refers to a group of disorders related to the heart and blood vessels, commonly related to atherosclerosis, a pathology in which the artery is clogged and the bloodflow is restricted or completely blocked.

According to the World Health Organisation ([World Health Organisation, 2017](#)), it is estimated that 17.7 million people died from CVDs in 2015, representing 31 % of all global deaths. Of these deaths, an estimated 7.4 million were due to coronary heart disease and 6.7 million were attributed to stroke. Due to the increase in elderly population, with an increased risk of diabetes, hypertension and obesity, CVD deaths are expected to rise up to 23.6 million by 2030 ([GlobalData, 2014](#); [World Health Organisation, 2017](#)).

CVDs are associated with high healthcare costs, frequent recurrences and hospitalizations. Treatments range from drug prescriptions to more invasive strategies such as cardiac catheterization and bypass surgery. Drugs like statins, warfarin and beta-blockers are prescribed not only to treat patients after acute coronary syndrome (ACS), but also as a preventive measure for individuals at risk (i.e. patients with hypertension, high cholesterol and diabetes). According to a report ([GlobalData, 2014](#)) focusing on the seven major markets (7MM)(US, France, Germany, Italy, Spain, UK, and Japan), the market size for both branded and generic drugs to treat ACS was of 12.3 billion USD in 2013. And the forecast announces a market value of 43.5 billion USD by 2023.

Interventional cardiology procedures used to treat CVDs include angiography, balloon angioplasty, coronary stenting, PTCA with drug eluting balloons and percutaneous coronary intervention. The number of these procedures performed in the EU5 region (that includes France, Germany, Italy, Spain and the UK), the US, and the Asia-Pacific region (comprised of Australia, China, India, Japan, and South Korea) increased from 2007 to 2014, specially in the Asia-Pacific region (see Fig. [1.1](#)). And the tendency is to increase from the 12,319,970 procedures across all these regions in 2014 to 16,936,740 procedures in 2021.

Finally, coronary artery bypass grafting (CABG), a surgery used to treat severe cases of CHD, was performed 424,276 times in 2007 in the 7MM, decreasing to 364,903 by 2014. This is

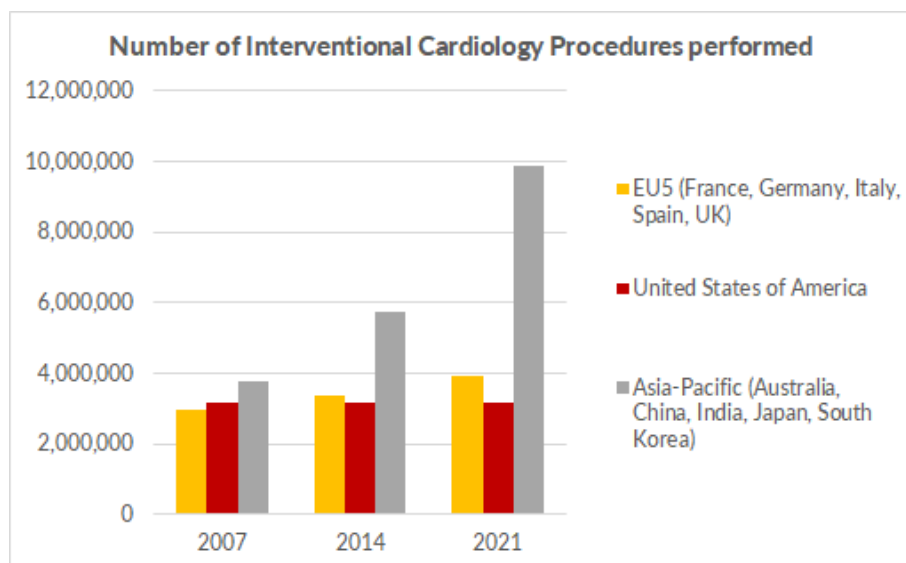


Figure 1.1: In the EU5, US and Asia-Pacific regions the number of Interventional Cardiology Procedures performed grew from 2,967,778, 3,181,248, and 3,748,122 respectively in 2007 to 3,390,703, 3,181,117, and 5,748,150 each in 2014. The number of Interventional Cardiology Procedures performed is forecasted to reach 3,904,138, 3,153,411, and 9,879,191 for each of the aforementioned regions in 2021. Source: ([GlobalData, 2016a,b,c](#))

expected to further decrease to only 338,218 CABGs performed in 2021 ([GlobalData, 2016d,e](#)).

The overall outlook seems to favor drugs to control and prevent CVDs, as well minimally invasive treatments like catheterization ([Yazdani, 2019](#)).

1.2 Atherosclerosis

Atherosclerosis is a disease in which an inflammatory process generates a plaque that grows inside the arterial wall and, as it accumulates with time, obstructs the bloodflow. This plaque has different constituents including lipid, calcifications, necrotic tissue pools, among others. If the plaque undergoes rupture it causes a thrombus that can lead to life-threatening cardiovascular incidents. Atherosclerosis can occur in several arteries in the body. Depending on which arteries are affected by it, different diseases may develop ([NHLBI, 2018](#)).

Coronary heart disease (CHD), also known as coronary artery disease (CAD) or ischemic heart disease (IHD) is the most common type of CVD. It occurs when plaque builds up in the coronary arteries, the arteries that provide blood to the heart, and reduces blood flow to the heart muscles. Depending on the degree of the obstruction, the tissue normally irrigated by the affected artery could be at risk of ischemia (lack of oxygen), injury, or infarction (tissue death). CAD can lead to acute coronary syndrome (ACS), which is an umbrella term for signs and symptoms consequence of myocardial ischemia - the sudden reduction of blood flow to the heart. It includes stable and unstable angina (chest pain), myocardial infarction (MI), and sudden cardiac death ([Overbaugh, 2009](#)).

Structure of the arterial wall

To understand how atherosclerosis develops, we must first observe the structure of the artery. Coronary arteries are classified as muscular arteries because they have a great amount of muscle cells which allow the artery to contract and dilate to adjust the blood flow as needed ([Paxton et al., 2003](#)). These arteries are built with three concentric layers of tissue: the intima, media and

adventitia. Each of these layers has a different mechanical behavior depending on its composition and thickness (Fig. 1.2).

The intima is the thinnest of all three and is in direct contact with the blood that flows through the arterial lumen. It is a single layer of endothelial cells with a supporting layer of elastin-rich collagen. It has vital metabolic and endocrine functions and plays an important role in the regeneration and growth of the artery (Waller et al., 1992). Given its relatively smaller thickness and low stiffness, its contribution to the overall mechanical properties of the vessel is often disregarded.

The media is a layer comprised of smooth muscle cells and connective tissue (collagen and elastin fibers) arranged in up to 40 concentric layers (Waller et al., 1992). From the mechanical point of view this is the most important layer, it is the thickest and it has great strength and elasticity.

Finally, the adventitia is the outermost layer of the artery and is made of fibrous tissue (elastin and collagen fibers) mainly in the longitudinal direction. It connects the vessel to the surrounding tissue and has vasa vasorum - a network of small vessels that supply larger arteries like the coronaries.

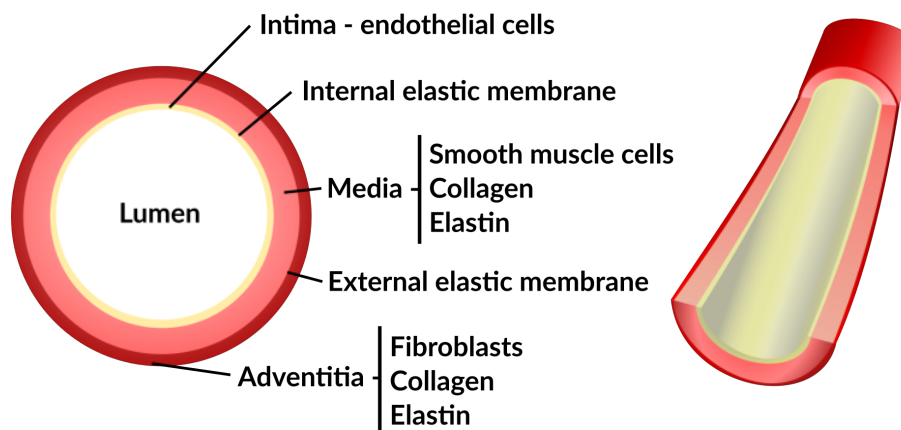


Figure 1.2: Schematic of the three layers of the coronary artery wall.

Development of atherosclerosis

Atherosclerosis is an inflammatory disease that can start early in a person's lifetime. The generally accepted hypothesis for the origin of atherosclerosis points to endothelial dysfunction as the crucial trigger (Rigla, 2017). This dysfunction leads to a higher lipid permeability of the intima, causing lipid infiltration and a consequent inflammatory response that prompts the migration and proliferation of smooth muscle cells. If the offending agents are not neutralized, the continued inflammation leads to the presence of macrophages and lymphocytes, which in turn can worsen the injury and result in focal necrosis (Ross, 1999). If this cycle continues, the lesion evolves to a core of lipid and necrotic tissue separated from the lumen by a fibrous cap.

Given the progressive nature of atherosclerosis, a classification system based on their histological composition and structure was adopted by the American Heart Association (Stary et al., 1994, 1995) in 1995, and has since then been adapted (Virmani et al., 2000; Yahagi et al., 2016). The final version of this classification is illustrated in Table 1.1 and Figure 1.3.

1.2 Atherosclerosis

Table 1.1: An updated version of the modified AHA classification published in [Virmani et al. \(2000\)](#), which was based on the original AHA classification published in the mid 1990s ([Stary et al., 1994, 1995](#)). Reprinted from *Nature Reviews Cardiology*, 13(2), K. Yagahi et al., Pathophysiology of native coronary, vein graft and in-stent atherosclerosis, 79-98, Copyright (2016), with permission from Elsevier.

Type of lesion	Subtype of lesion	Morphological description
Nonatherosclerotic intimal lesions	Intimal thickening	Natural accumulation of smooth muscle cells in the absence of lipid, macrophage foam cells, and thrombosis.
	Intimal xanthoma	Superficial accumulation of foam cells without a necrotic core, fibrous cap, or thrombosis.
Progressive atherosclerotic lesions	Pathological intimal thickening	Plaque rich in smooth muscle cells, with hyaluronan and proteoglycan matrix and focal accumulation of extracellular lipid. Absence of thrombosis.
	Fibroatheroma	During early necrosis: focal macrophage infiltration into areas of lipid pools with an overlying fibrous cap. During late necrosis: loss of matrix and extensive cellular debris with an overlying fibrous cap. With or without calcification. Absence of thrombosis.
	Intraplaque haemorrhage or plaque fissure	Large necrotic core (size >10% of plaque area) with haemorrhage, and plaque area shows presence of angiogenesis. Necrotic core communicates with the lumen through a fissure. Minimal tear without obvious thrombus.
	Thin-cap fibroatheroma	A thin, fibrous cap (<65 μm) infiltrated by macrophages and lymphocytes, with rare or no smooth muscle cells and relatively large underlying necrotic core (>10% of plaque area). Intraplaque haemorrhage and/or fibrin might be present. Absence of thrombosis.
Lesions with acute thrombi	Plaque rupture	Thin-cap fibroatheroma with cap disruption. Thrombosis is present and might or might not be occlusive. The luminal thrombus communicates with the underlying necrotic core.
	Plaque erosion	Can occur on pathological intimal thickening or on a fibroatheroma. Thrombosis is present and might or might not be occlusive. No communication of the thrombus with the necrotic core.
	Calcified nodule	Eruptive (shedding) of calcified nodule with an underlying fibrocalcific plaque with minimal or no necrosis. Thrombosis is usually not occlusive.
Healed lesions	Healed plaque rupture, erosion, or calcified nodule	Healed lesion composed of smooth muscle cells, proteoglycans, and collagen type III with or without underlying disrupted fibrous cap, necrotic core, or nodular calcification. Lesions can contain large areas of calcification with few inflammatory cells and have a small or no necrotic core. The fibrotic or fibrocalcific collagen-rich plaque is associated with significant luminal stenosis. Absence of thrombosis.

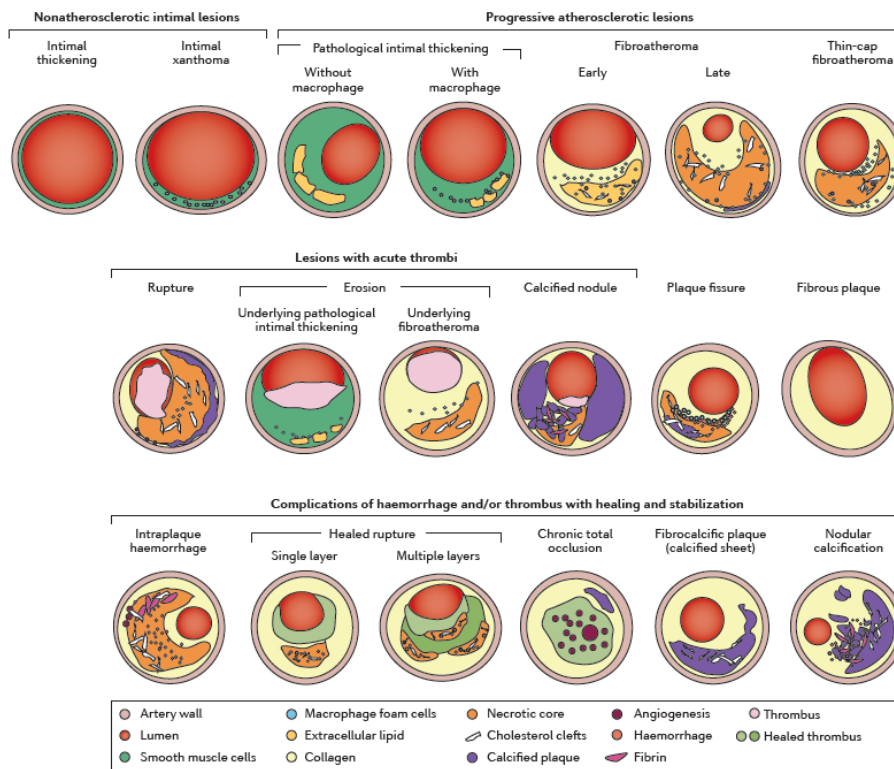


Figure 1.3: Human coronary lesion morphologies categorized as nonatherosclerotic intimal lesions, progressive atherosclerotic lesions, lesions with acute thrombi, and complications of haemorrhage and/or thrombus with healing and stabilization. Reprinted from *Nature Reviews Cardiology*, 13(2), K. Yagahi et al., Pathophysiology of native coronary, vein graft and in-stent atherosclerosis, 79-98, Copyright (2016), with permission from Elsevier.

Vulnerable plaques

The formation of an occlusive thrombus is the main cause of infarction (Hansson, 2005). Therefore, there is great interest in the identification of thrombosis-prone plaques before they rupture. These lesions at high-risk of causing an acute event are referred as vulnerable plaques (Schaar et al., 2004). According to clinical, pathological and biomechanical studies, the criteria that define a vulnerable coronary atherosclerotic plaque (VP) are strongly linked to its morphology and composition (Virmani et al., 2000; Naghavi et al., 2003; Fleg et al., 2012). Macrophage accumulation, a large necrotic core with a thin fibrous cap ($< 65 \mu\text{m}$) and positive remodeling are common morphological characteristics of inflammatory atherosclerotic lesions susceptible to rupture.

Fibrous cap thickness (Capthick) is often regarded as a good predictor of plaque stability (Virmani et al., 2000; Virmani, 2011). However, even a significant criterion for rupture as cap thickness is not enough to give a definite assessment by itself. A study conducted by Virmani et al. (2000) involving 200 cases of sudden death evidenced that, while most culprit lesions (60%) were ruptured thin-cap fibro-atheromas, 70% of these patients also presented unruptured lesions with similar morphologies. This suggests that cap thickness by itself cannot predict the likelihood of rupture, and that other morphological and biomechanical characteristics must come into play.

Although atherosclerosis is normally associated with decreased luminal area and a consequent reduction of blood flow, the lumen of the artery can go unaffected until advanced stages of the disease. This is thanks to a process called remodelling, in which the artery enlarges in relation to

the plaque area and delays functionally important lumen stenosis (see Fig.) (Glagov et al., 1987; Bentzon et al., 2014). Related to this phenomenon, it was thought that the progressive luminal narrowing was the main cause of acute myocardial infarction (Hansson, 2005). But angiographic studies have identified culprit lesions without severe stenosis (Hackett et al., 1988), suggesting that assessing stenosis is not enough to characterize a lesion.

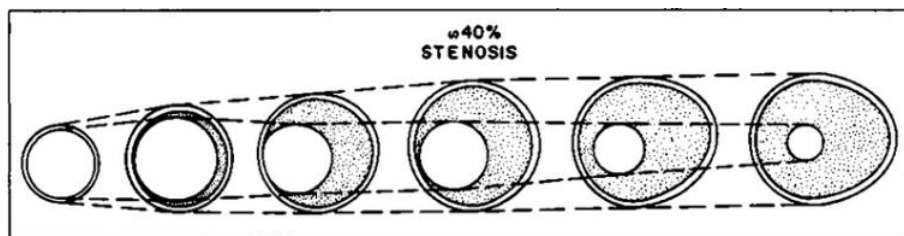


Figure 1.4: Schematic description of the positive coronary remodeling described by Glagov et al. (1987). Reproduced from Glagov et al. (1987).

Glagov et al. (1987) analyzed the left main coronary artery in 136 hearts and found that arteries enlarge as a response to lesion growth. However, when comparing lumen area to stenosis they observed that remodeling occurs in two stages depending on the degree of stenosis. In first instance, when stenosis is below 40%, luminal area is minimally affected by plaque progression. But in a second stage, once plaque burden exceeds 40%, this behavior changes and lumen area decreases rapidly with respect to stenosis fraction, disrupting the blood flow.

Although the previously mentioned characteristics of vulnerable plaques have been extensively studied, most of them are related to the morphology and inflammation activity. Some studies (Ohayon et al., 2008; Motoyama et al., 2015; Ahmadi et al., 2015) have highlighted the importance of monitoring the rate of progression of the plaque. These works identified that plaques with vulnerable morphologies that have a rapid progression are at higher risk of rupture, which implies that - additional to the aforementioned factors - a dynamic monitoring approach could improve rupture prediction.

Techniques for the assessment of atherosclerotic plaques

As discussed in previous sections, the identification of vulnerable plaques is an ongoing clinical and biomechanical issue. Several techniques enable the imaging of atherosclerotic plaques, including intravascular ultrasound (IVUS) (Rioufol et al., 2002; Cheng et al., 2014), optical coherence tomography (Sinclair et al., 2015; Gessert et al., 2018), computed tomography (Fayad et al., 2002) and magnetic resonance imaging (Larose et al., 2005; Cavalcante and Larose, 2016), as well as hybrid techniques resulting from the combination of two or more imaging modalities (Abran et al., 2014; Bourantas et al., 2017).

A brief and non-exhaustive review of diagnostic imaging modalities is presented with special detail to intravascular ultrasound, given its importance - the most widely used invasive modality - and relevance to this dissertation.

Noninvasive imaging techniques

The advantages of noninvasive imaging include shorter hospitalization times, less to no trauma, as well as avoiding complications caused by incisions (i.e. infection, bleeding). There are three main noninvasive techniques used for coronaries:

Computed Tomography (CT) uses the principle of X-ray images and takes several slices in different angles by using a CT scanner. Electron Beam CT or ultrafast CT can quantify

calcifications in the coronary arteries, but its limited spatial resolution and inability to detect non-calcified plaques restrict its clinical use (Taki et al., 2017). CT angiography consists in injecting a contrast agent into the bloodstream to enhance visibility of stenosis. The main challenge of using CT for imaging the heart is cardiac motion. This is achieved by synchronizing CT acquisitions with the heart rate with the aid of simultaneous ECG, producing images from the same phase over multiple cardiac cycles (Rybicki, 2005). It has the potential to assess both the plaque morphology and the lumen (Stefanadis et al., 2017).

Clinical Magnetic Resonance Imaging (MRI) (1.5 T and 3 T) is one of the most promising techniques for noninvasive imaging of the coronary arteries (Gerretsen et al., 2007). It has the potential to assess cardiac anatomy, perfusion, function, metabolism and coronary angiography (van der Wall et al., 1995). It has the advantage of no radiation exposure, although acquisitions are more time-consuming, expensive and its spatial resolution does not allow precise wall characterization of small vessels such as coronaries (Nikolaou et al., 2011; Taki et al., 2017).

Nuclear Imaging uses a gamma camera to detect the radiation emitted by radioactive tracers that are injected into the patient. For coronary arteries, the most used modalities are Single Photon Emission Computed Tomography or SPECT and Positron Emission Tomography or PET scans. They provide valuable functional information that is harder to obtain with other modalities and can help the physician determine the course of action. However, it does not offer anatomical information and is often used in conjunction with CT or MRI to complement its results (Taki et al., 2017).

Invasive imaging techniques

Despite the advantages of noninvasive methods, they have limitations pertaining the availability of the technologies. Minimally invasive catheter-based imaging modalities are the most used in clinical practice, and they include:

Angiography is the gold standard to identify stenotic regions in the arterial tree (Schaar et al., 2007). In this procedure, a catheter is inserted through a peripheral artery and guided through the blood vessels until it reaches the coronary arteries. Then, a contrast medium is injected into the catheter and X-ray images are acquired to observe how the contrast agent travels through the artery (Taki et al., 2017). It provides an evaluation of the lumen boundary, so it is able to detect severe lesions and luminal thrombosis. Although it does not provide any information on the plaque composition and it cannot detect lesions without significant stenosis, it gives information about the whole coronary system and helps guide further imaging techniques and therapies (Schaar et al., 2007).

Angioscopy directly visualizes the arterial lumen by means of an fiber-optic guidewire (Tousoulis et al., 2018). By looking at the plaque surface, features of the wall such as tears, thrombi, and thin fibrous-caps are detectable (Taki et al., 2017). One obvious limitation of the technique is that it can only assess luminal area, and in many cases the vessel must be occluded to enhance visualization, which could lead to ischaemia (Schaar et al., 2007).

Optical Coherence Tomography (OCT), the second major modality for coronary imaging, measures the intensity of back-reflected light and compares it with a reference (Taki et al., 2017). The wavelength of light is much smaller than that of ultrasound, giving OCT a better resolution. These high-resolution images (4-20 μm) (Schaar et al., 2007) provide information about the thin-cap, lipid pools, macrophage infiltration, ruptures and thrombi (Stefanadis et al., 2017). However, its penetration depth is limited, its ability to differentiate a lipid pool from a calcified area is poor, and light absorbance of blood needs to be overcome by means of saline infusion or balloon occlusion (Schaar et al., 2007).

Intravascular Ultrasound (IVUS) introduces a catheter mounted on a guidewire, from a larger artery up to the heart (Fig. 1.5). The IVUS catheter has an ultrasound transducer on its tip that rotates to generate a cross-sectional image of the vessel. It is the predominant invasive imaging technique for coronary arteries (Schaar et al., 2007). Among the advantages of this minimally invasive technique we have high resolution (80-120 μm) (Taki et al., 2017) and the ability to visualize all arterial layers and their composition. A more in-depth description of IVUS is presented in the next section of this chapter.



Figure 1.5: Possible insertion sites for IVUS catheter: the femoral and radial arteries.

1.3 Coronary imaging by IVUS

Intravascular ultrasound imaging of the coronary arteries is a minimally invasive procedure that inserts a guidewire into a large vessel (such as the femoral or radial artery, see Fig. 1.5) and then it travels up to the heart. A catheter with a miniaturized ultrasound transducer is mounted on the guidewire and delivered to the coronary section of interest. The rotating probe emits ultrasound waves that propagate radially through the blood and the arterial wall and are partially reflected (by scatterers present in the tissue), refracted or absorbed. The backscattered radio frequency (RF) echo signals (i.e. A-line signals of amplitude vs time) are received by the transducer at a discrete number of angles (Rosales and Radeva, 2005; Sheet et al., 2014). The positive envelope of each individual A-line is computed to obtain B-mode images, where the local brightness is determined by the amplitude of the signal. These are compressed and stacked in the angular direction to create 2-D gray-scale polar B-mode IVUS images. These polar B-mode images are geometrically transformed into cartesian B-mode frames to provide a more intuitive representation of the data (Fichtinger et al., 2011; Pardalos et al., 2012). A representation of this process is shown in Fig. 1.6.

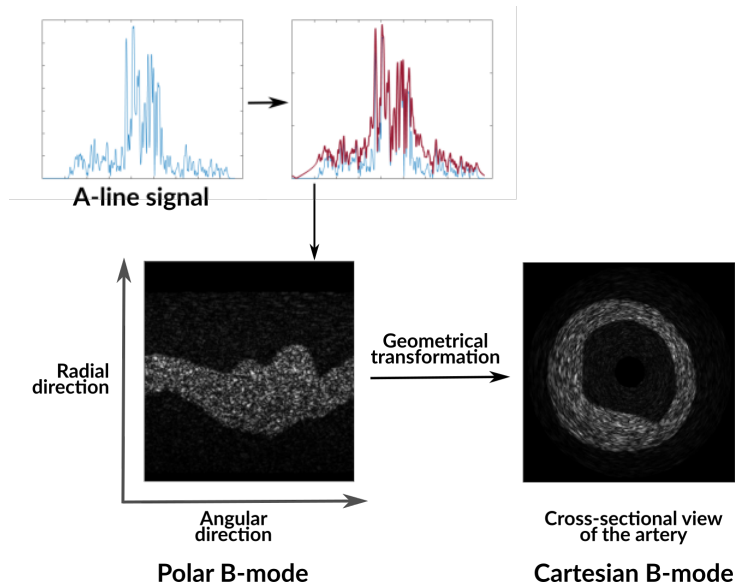


Figure 1.6: Intravascular ultrasound (IVUS) imaging modes. The positive envelope of each of the 1-D A-lines (RF lines) is obtained, stacked in the angular direction and presented in a 2-D gray-scale image to create polar B-mode IVUS images. For a more familiar representation, the polar B-mode IVUS is geometrically transformed to cartesian B-mode IVUS images that depict a cross-section of the artery.

To improve the visualization of the region of interest (ROI) clinicians are able to adjust parameters such as contrast, gain and brightness. B-mode, and consequently digital imaging and communications (DICOM) images, are altered by these changes and they cannot be modified after acquisition. RF raw data remains independent to this parameters and its analysis provides not only unaltered information on the plaque composition, but also images with better contrast compared to their DICOM equivalents (Granero et al., 2015).

The process for image reconstruction is similar to the one for B-mode. First, the IVUS RF signal is filtered with a band-pass filter before applying a time

gain compensation function to compensate for attenuation loss.

Then, the envelope of the signal is computed, log-compressed and normalized to create a gray-scale image in polar coordinates. After this, contrast and edge emphasis are enhanced with a digital development process and the image is later converted into cartesian coordinates. Cartesian B-mode images have a size of 512 x 512 pixels and 256 gray levels. Finally, contrast is improved with an intensity transformation function. A more thorough explanation of this process (depicted in Fig. 1.7) can be found in [Granero et al. \(2015\)](#).

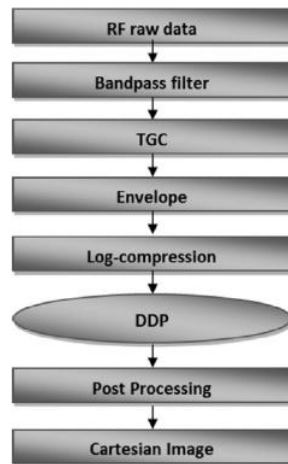


Figure 1.7: Block diagram of reconstruction process of IVUS image from RF raw data. Reprinted from *Emerging Trends in Image Processing, Computer Vision and Pattern Recognition*, Vol /edition number, Granero et al., Chapter 6- Rebuilding IVUS images from raw data of the RF signal exported by IVUS equipment, Pages 87-97, Copyright (2015), with permission from Elsevier.

One parameter of the IVUS probe that can improve image resolution is the vibration frequency of the transducer. Old IVUS probes were available with 20 MHz, and models with 30, 40 and 45 MHz are currently available for clinical practice. New models with 50 and 60 MHz transducers have recently been introduced in the market. While each new generation of catheters has improved in resolution, this comes at a cost of depth of penetration given that the higher the frequency, the lower the signal can penetrate. In spite of this, high-resolution catheters can still provide enough depth to prove useful in the examination of atherosclerotic lesions.

1.3.1 Clinical applications of IVUS

The real-time cross-sectional images generated with the IVUS exploratory technique allow the evaluation of the plaque and the layers of the arterial wall. It has sufficient penetration and resolution to aid clinicians infer the composition of the plaque by highlighting pathologic structures such as calcium deposits and necrotic pools (as high- and low-echogenic regions, respectively). It is helpful in assessing the severity of stenoses and aneurysms. IVUS is also used to guide interventional procedures like angioplasty and stent placement ([Rosales and Radeva, 2005](#); [Sheet et al., 2014](#)).

1.4 Derived techniques for plaque assessment

When encountering a coronary lesion, the interventional cardiologist must analyze if the risk of rupture it poses is significant enough to treat the patient using a surgical or percutaneous revascularization approach. Although helpful, the patient's medical history and paraclinical tests are not enough to give an adequate prognosis due to the unpredictable clinical course of atherosclerotic lesions. Clinical imaging methods have a great potential for improving the crucial *in vivo* detection and evaluation of VPs. Therefore, the development and validation of novel elasticity imaging tools and their implementation on routine clinical examinations could be a

valuable contribution towards proper plaque assessment (Fleg et al., 2012).

Following this premise, several approaches to detect vulnerable plaques based on the determination of their elastic properties have been proposed (Doyley, 2012). In 2004, the virtual histology technique, based on the parametric spectral analysis of the radio-frequency ultrasound backscattered echoes, was developed by Volcano Therapeutics Inc. However, Thim et al. (2010), in their study performed on adult atherosclerosis-prone minipigs, found no correlation between necrotic core size determined by virtual and real histology, questioning the ability of virtual histology to detect rupture-prone plaques. Moreover, this technique does not allow an accurate quantification of the mechanical properties of the plaque constituents, which is essential for the computation of intraplaque stress distribution. The same year, our joint laboratories (TIMC-IMAG, Grenoble, France and LBUM, Montreal, Canada) developed a robust IVUS strain-elastography approach (named EVE for EndoVascular Elastography), based on an optical flow method to estimate the radial strain wall induced by the natural cardiac pulsatile blood pressure (Maurice et al., 2004a). However, this method did not overcome a main limitation related to the complex geometries of atherosclerotic plaques, which alter the intraplaque strain fields and inhibit a direct translation into plaque mechanical properties.

Several computational algorithms have been developed to attempt the reconstruction of elasticity maps within the arterial wall based on the estimation of the strain field obtained with various IVUS-based techniques (De Korte et al., 2002; Maurice et al., 2004b). Either direct (Kanai et al., 2003; Kim et al., 2004) or iterative (Luo et al., 2006; Baldewsing et al., 2008) numerical procedures were used. Iterative methods depend mainly on two crucial elements: the performance of the optimization algorithm that minimizes the error between the calculated and the measured strain or displacement fields and the precision of the contours of the plaque constituents. This has led to the development of several robust optimization algorithms to compute the elastic moduli of the plaque components assuming a known plaque morphology (Soualmi et al., 1997; Khalil et al., 2006). Another interesting solution was developed (Baldewsing et al., 2006a) and extended (Baldewsing et al., 2006b) by Van der Steen's group. It consisted on detecting lipid core contours, analyzing each inclusion separately and superposing these results to obtain the final mechanical solution. Regardless of the robustness of the approach, it inherently neglected the mechanical interactions between inclusions, hindering the accuracy of the results in cases with neighboring inclusions, thus affecting the vulnerability prediction.

Since 2009, significant improvements have been performed and two powerful IVUS biomarkers of coronary plaque instability (namely IE-PT and iMOD for improves elasticity-palpography technique and imaging modulography (or morpho-elasticity), respectively) were developed in our joint laboratories (Le Floc'h et al., 2009, 2010, 2012; Bouvier et al., 2013; Deleaval et al., 2013; Tacheau et al., 2016). This section presents both of these IVUS imaging techniques developed for the in vivo detection and mechanical characterization of vulnerable coronary atherosclerotic plaques.

1.4.1 IVUS strain-elastography

In the two modeling approaches developed within the research group (i.e. IE-PT and iMOD), the strain of the atherosclerotic plaque between two consecutive images (Im^i and Im^{i+1}) was obtained by considering the geometry of the lesion at Im^i as the reference configuration. First, the segmentation of the vessel boundaries (i.e. the lumen and the external adventitia) was performed on the IVUS images using a fast-marching algorithm that combined region and contour information (Roy Cardinal et al., 2006); the resulting contours were then corroborated by a cardiologist before proceeding. These contours delimitating the arterial wall determined the region of interest (ROI). Then, a rigid motion compensation was applied to the IVUS

sequence to dismiss the rotation observed between consecutive images. To do this, the polar representations of each pair of successive frames Im^i and Im^{i+1} was compared using a 2D correlation of the regions of interest, and the shift with the maximal correlation was selected as the correcting angular compensation to avoid the rotation artifact. This step was repeated until the complete sequence was compensated for rotation. Finally, the radial strain was calculated using the Lagrangian speckle model estimator (LSME) (Maurice et al., 2004a). This algorithm consists in dividing the IVUS image within the ROI into a series of overlapping sub-windows (or measurement windows (MWs)) and then calculates the displacement of each MW between Im^i and Im^{i+1} using a 2D cross-correlation analysis, thus computing a displacement field. The LSME algorithm was formulated as a nonlinear minimization problem based on the optical flow equations solved for each MW and allows direct assessment of the spatial IVUS radial strain distribution (ε_{RR}^{LSME}) (Maurice et al., 2004a). The detailed description of the LSME strain elastography algorithm including its governing equations has been published by our joint laboratories (see appendix A in Majdoulina et al. (2014)).

Tangent stiffness matrix obtained from two consecutive IVUS images

As explained previously, the proposed constitutive model takes the plaque configuration at the preceding frame Im^i as the reference, and not the zero-stress configuration \mathbf{R} . Consequently, we used a linear tangent elasticity procedure (Holzapfel, 2000) which remains valid as long as the absolute local incremental strain amplitudes between the two consecutive IVUS images Im^i and Im^{i+1} are $< 2\%$.

The relationship between the 2nd Piola-Kirchhoff stress \mathbf{S} and the right Cauchy-Green tensor \mathbf{C} (or the Lagrangian strain tensor $\mathbf{E} = (\mathbf{C} - \mathbf{I})/2$) is nonlinear:

$$\mathbf{S} = \frac{\partial \psi}{\partial \mathbf{C}} = \frac{\partial \psi}{\partial \mathbf{E}} \quad (1.1)$$

where ψ is the strain energy function per unit of undeformed volume (i.e., at configuration \mathbf{R} associated to coordinates \mathbf{X}). This relationship could be linearized with respect to an incremental displacement \mathbf{u} defining the transformation going from Im^i to Im^{i+1} (Bonet and Wood, 1997):

$$\mathbf{DS}[\mathbf{u}] = \mathcal{C}^{Im^i \rightarrow Im^{i+1}} : \mathbf{DE}[\mathbf{u}] \quad (1.2)$$

with

$$\mathbf{DE}[\mathbf{u}] = \mathbf{F}_{R \rightarrow Im^i}^T \boldsymbol{\varepsilon}(\mathbf{u}) \mathbf{F}_{R \rightarrow Im^i} \quad (1.3)$$

and

$$\boldsymbol{\varepsilon}(\mathbf{u}) = [\nabla \mathbf{u} + (\nabla \mathbf{u})^T] / 2 \quad (1.4)$$

where ∇ indicates the gradient with respect to the coordinates at the current configuration Im^i (i.e. \mathbf{x}), $\boldsymbol{\varepsilon}(\mathbf{u})$ is the small strain tensor, $\mathbf{DS}[\mathbf{u}]$ is the resulting incremental 2nd Piola-Kirchhoff stress and $\mathcal{C}^{Im^i \rightarrow Im^{i+1}}$ is the symmetric fourth-order material elasticity tensor. In particular, if we assume that Im^i is the initial material configuration \mathbf{R} (i.e. when $\mathbf{x} = \mathbf{X}$ and therefore

$\mathbf{F}_{R \rightarrow Im^i} = \mathbf{I}$, where \mathbf{I} is the identity matrix), the linearization of Eqs. (1.2, 1.3, 1.4) yields to the classical linear elastic constitutive law:

$$\mathbf{S}(\mathbf{u}) = \mathcal{C}^{Im^i \rightarrow Im^{i+1}} : \boldsymbol{\varepsilon}(\mathbf{u}) \quad (1.5)$$

Therefore, our computations were performed assuming linear elastic tissue response (i.e. $\mathcal{C}^{Im^i \rightarrow Im^{i+1}}$ remains constant) when the artery was pressurized with a small incremental blood pressure $\Delta P^{Im^i \rightarrow Im^{i+1}}$ and under plane strain condition. Interestingly, this incremental procedure applied to a series of two consecutive IVUS images (Im^i, Im^{i+1} with $i=1$ to n) during the entire cardiac cycle sequence allowed to highlight the nonlinear mechanical response of the plaque media (Le Floc'h et al., 2012).

Almost two decades ago, Van der Steen's group was the first to propose an elasticity palpography technique for estimating the apparent stress-strain modulus of the arterial wall layer (Céspedes et al., 2000). Their model was based on the mechanical behavior of a circular and concentric vascular wall and used IVUS strain measurements as inputs. Later, our group improved this approach by considering realistic anatomical cross-sectional shapes of atherosclerotic lesions (Deleaval et al., 2013). Both of the aforementioned models are presented in this section.

The palpography technique of Céspedes et al. (2000)

Palpography calculates an apparent stiffness of the artery in the radial direction by integrating a certain index inside a selected region called the palpography domain. Céspedes et al. (2000) defined a stress-strain modulus (S-SM), called E_{palpo} , as the ratio of the average radial stress to the average strain along the radial axis.

$$E_{palpo}(\theta) = \frac{\left| \int_{R_i(\theta)}^{R_p(\theta)} \sigma_{rr}(r, \theta) dr \right|}{\varepsilon(\theta)} \quad (1.6)$$

where $\sigma_{rr}(r, \theta)$ is the radial stress component, $R_i(\theta)$ and $R_p(\theta)$ are the inner and outer radii of the considered palpography domain Ω_{palpo} , respectively. $\varepsilon(\theta)$ is the average radial strain, given by:

$$\varepsilon(\theta) = \left| \int_{R_i(\theta)}^{R_p(\theta)} \varepsilon_{rr}(r, \theta) dr \right| \quad (1.7)$$

Céspedes et al. (2000) made the following assumptions: the artery is considered as a thick-walled cylinder (with inner and outer radii $R_i(\theta)$ and $R_o(\theta)$, respectively), isotropic, homogeneous, incompressible, linearly elastic (with Young's modulus E), submitted to uniform pressure (ΔP) on the luminal boundary $r = R_i$ and no pressure in the outer boundary $r = R_o$. Plane strain condition and a concentric circular palpography domain Ω_{palpo} (with $R_i \leq r \leq R_p$) are also assumed. This results in the spatial distribution of local S-SM (Eq. 1.6) being constant through the palpography domain and equal to

$$E_{palpo}^{cylinder}(\theta) = \frac{\Delta P \left| \int_{R_i(\theta)}^{R_p(\theta)} g(r) dr \right|}{\varepsilon} \quad (1.8)$$

$$\text{with} \quad \varepsilon = \frac{3}{2E} \frac{\alpha_o^2}{\alpha_p (\alpha_o^2 - 1)} \Delta P \quad (1.9)$$

$$\text{and} \quad \int_{R_i}^{R_p} g(r) dr = \frac{(\alpha_o^2 - \alpha_p)}{\alpha_p (\alpha_o^2 - 1)} \quad (1.10)$$

where the constant ε is the absolute value of the compressive average radial strain (with amplitude given by Eq. 1.9); and α_o and α_p are the relative thicknesses of the arterial wall and palpography domain Ω_{palpo} , respectively ($\alpha_o = R_o/R_i$ and $\alpha_p = R_p/R_i$). The spatial function $g(r)$ is a correcting shape function that accounts for the geometry of the thick-walled cylindrical artery. For a specific circular palpography domain only (i.e., when $R_p = [2\alpha_o^2 / (\alpha_o^2 + 1)] R_i$), the amplitude of the uniform local S-SM becomes:

$$E_{palpo}^{Céspedes} = E_{palpo}^{cylinder}(\theta) = \frac{\Delta P/2}{\varepsilon} \quad (1.11)$$

Céspedes et al. (2000) were inspired in this simplified S-SM solution for a thick-walled cylindrical vessel (1.11) to propose their S-SM approximation (1.6)

The revisited palpography technique of Deleaval et al. (2013)

Although the palpography of Céspedes et al. (2000) presented a promising technique for the identification of vulnerable lesions. However, it makes the assumption of a concentric, cylindrical arterial wall with homogeneous isotropic mechanical properties and a uniform outer radial stress distribution. This results in a high sensitivity to plaque geometry (i.e. eccentric lesions and non-uniform wall thickness). This is clearly observed when we apply this technique to an eccentric homogenous plaque (see Fig. 1.8)

Therefore, the revisited palpography technique was developed by Deleaval et al. (2013), which accounts for the anatomic shapes of the atherosclerotic plaques and palpography domains. Based on the relationship between the deviatoric radial stress $\sigma_{rr}^{dev}(r, \theta)$ the Young's modulus $E(r, \theta)$ and the radial strain component $\varepsilon_{rr}(r, \theta)$ for a heterogeneous, isotropic, incompressible and linear elastic continuum medium (Timoshenko and Goodier, 1970),

$$\sigma_{rr}^{dev}(r, \theta) = \frac{2}{3} E(r, \theta) \varepsilon_{rr}(r, \theta) \quad (1.12)$$

the S-SM was redefined as the ratio of the average deviatoric radial stress to the average radial strain along the radial axis

$$E_{palpo}^{Deleaval}(\theta) = \frac{3}{2} \frac{\left| \int_{R_i(\theta)}^{R_p(\theta)} \sigma_{rr}^{dev}(r, \theta) dr \right|}{\varepsilon(\theta)} \quad (1.13)$$

where $\varepsilon(\theta)$ is given by 1.7.

Knowing that the radial strain $\varepsilon_{rr}(r, \theta)$ is proportional to the change in pressure ΔP , and inversely proportional to the amplitude of the Young's modulus $E(r, \theta)$,

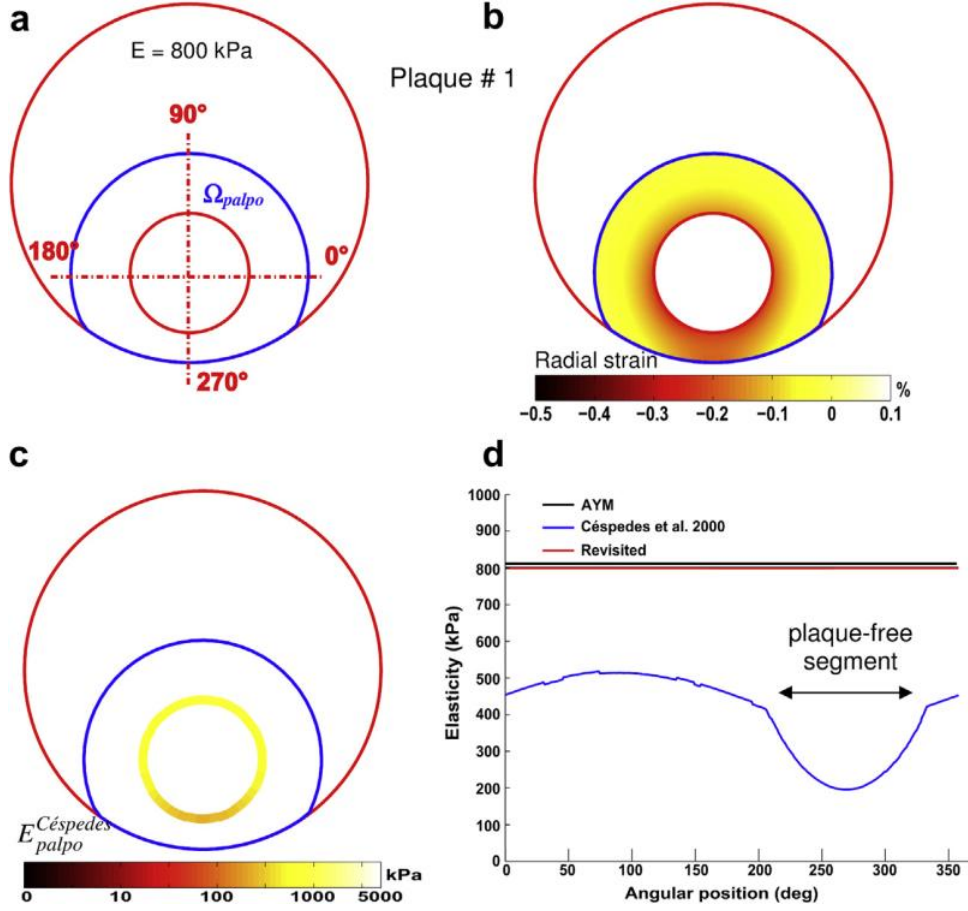


Figure 1.8: Performance of the improved elasticity-palpography technique. (a) Contours (in red) of an idealized eccentric and circular plaque model (called plaque 1) in which the lesion is homogeneous. The palpography domain, Ω_{palpo} , is also given (blue contours). (b) Radial strain elastogram computed in the palpography domain. (c) Computed original (Céspedes et al. 2000) stress-strain modulus (S-SM) palpogram. (d) Comparisons between original S-SM, improved (Revisited) S-SM and averaged Young's modulus (AYM) palpograms. From Deleaval et al. (2013)

$$\varepsilon_{rr}(r, \theta) = \frac{3}{2} \frac{\Delta P}{E(r, \theta)} h(r, \theta) \quad (1.14)$$

(where the constant $3/2$ is introduced for mathematical convenience only), the expression of the deviatoric radial stress given by Eq. 1.12 can be rewritten as

$$\sigma_{rr}^{dev}(r, \theta) = \Delta P h(r, \theta) \quad (1.15)$$

where $h(r, \theta)$ is a correcting shape function that accounts for the entire plaque morphology, including the geometries of all plaque heterogeneities. Taking advantage of such an expression for the deviatoric radial stress, the proposed S-SM (Eq. 1.13) becomes

$$E_{palpo}^{Deleaval}(\theta) = \frac{3}{2} \frac{\Delta P \left| \int_{R_i(\theta)}^{R_p(\theta)} h(r, \theta) dr \right|}{\varepsilon(\theta)} \quad (1.16)$$

The correcting shape function $h(r, \theta)$ is unknown and escapes to direct measurements. Therefore, an approximated correcting shape function was computed, $h^*(r, \theta)$ using an FE

analysis performed in linear elasticity with a loading blood pressure ΔP and by assuming the plaque homogeneous, isotropic and quasi incompressible with a Young's modulus E . This gives the following S-SM formulation

$$E_{\text{palpo}}^{\text{Deleaval}}(\theta) = \frac{3}{2} \frac{\Delta P \left| \int_{R_i(\theta)}^{R_p(\theta)} h^*(r, \theta) dr \right|}{\varepsilon(\theta)} \quad (1.17)$$

Comparison between palpography techniques

Palpography is able to present a simplified and rapid calculation of the apparent stiffness of the plaque by selecting a defined region closer to the lumen. The formulation developed by Céspedes et al. (2000) represents an important step towards the quick assessment of the plaque. However, as mentioned previously, the limitation to concentric vessels renders it incapable of evaluating the majority of lesions, which are eccentric. The improved algorithm of Deleaval et al. (2013) overcomes this morphological limitation by introducing a correcting shape function. Moreover, when a homogeneous vessel is considered, this revisited IE-PT is able to extract the real Young's modulus (Fig. 1.8).

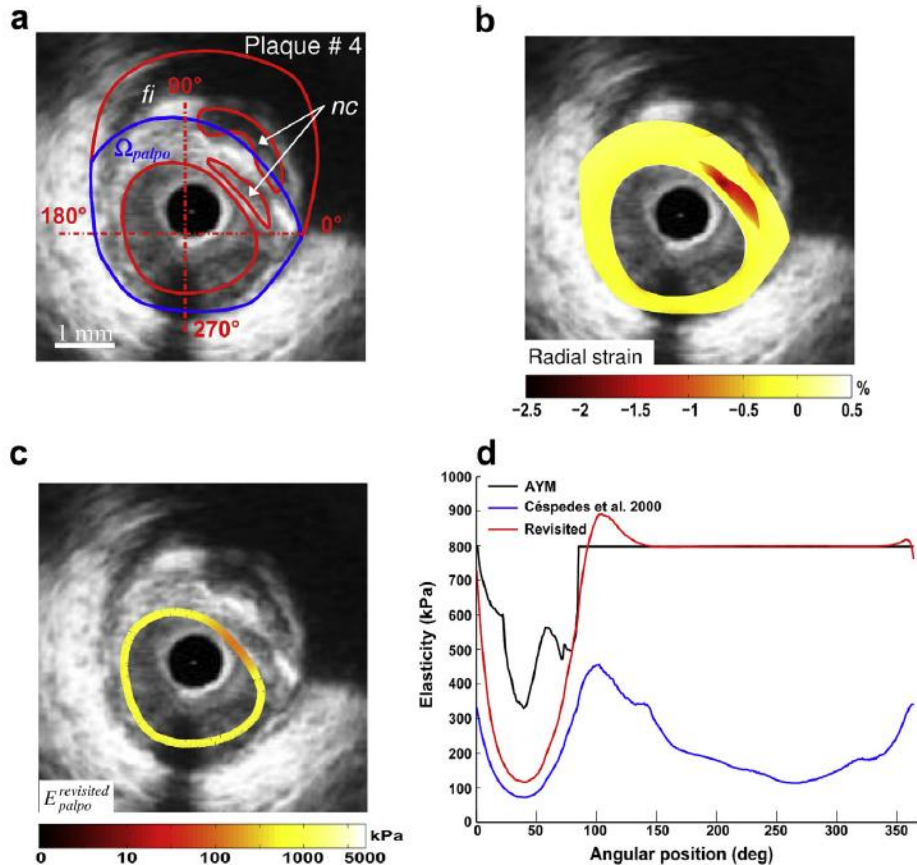


Figure 1.9: Performance of the improved elasticity-palpography technique in detecting a vulnerable plaque with two necrotic cores. (a) Intravascular ultrasound image of plaque 2 with plaque constituents (red contours). The boundaries of the palpography domain, Ω_{palpo} , are also given (blue contours). (b) Radial strain elastogram in the palpography domain. (c) Computed improved (Revisited) stress-strain modulus (S-SM) palpogram. (d) Comparisons between original S-SM (Céspedes et al. 2000), improved (Revisited) S-SM and averaged Young's modulus (AYM) palpograms. nc= necrotic core, fi= fibrous region. From Deleaval et al. (2013)

In the study of Deleaval et al. (2013), the performance of both of these palpography

formulations for the detection of vulnerable plaques is compared using coronary lesions of patients imaged *in vivo* with IVUS. As expected, the revisited IE-PT considerably improved the accuracy of the S-SM palpogram (see Fig. 1.9) and provided a physical meaning to the palpogram amplitude.

1.4.2 Modulography

Morpho-elastic reconstruction of atherosclerotic lesions (i.e. modulogram), based solely on radial strain field measurement, was a challenge addressed by several authors (Baldewising et al., 2005, 2008; Richards and Doyley, 2011; Doyley, 2012). Our group demonstrated that by preconditioning the algorithm based on the best estimate of the boundaries of all plaque components, we could improve the elasticity reconstruction (Le Floc'h et al., 2009, 2010, 2012; Tacheau et al., 2016).

Therefore, an original pre-conditioning step, to first obtain the atherosclerotic lesion morphology, and then an iterative algorithm combining a dynamic watershed segmentation (DWS) method with an optimization procedure were proposed to reconstruct the transmural spatial elasticity distribution. Three main studies were conducted in our collaborative research program to test the performance of the plaque-imaging modulography tool iMOD based on recorded RF-IVUS sequences:

- The first one was to study *in vitro*, using two polyvinyl alcohol (PVA) cryogel vessel phantoms, the potential of iMOD to characterize the vessel wall and to detect soft inclusions (Le Floc'h et al., 2010).
- The second one was to test *ex vivo* the potential of iMOD to characterize healthy rabbit aortic vessels (Deleaval et al., 2013).
- The third one was to test the clinical potential of iMOD to identify VPs based on RF-IVUS sequences obtained in seven patients referred for directional coronary atherectomy intervention (Le Floc'h et al., 2012).

The morpho-elastic biomechanical model

The iMOD algorithm was designed to calculate the elasticity map of the arterial wall from the IVUS radial strain field. An illustration of all successive steps performed in the iMOD morpho-elastic algorithm is given in Fig. 1.10.

Modified Sumi's transform (MST) criterion: The Sumi and Nakayama (1998) method was extended from its original plane stress condition to one of plane strain to define our contour detection algorithm of elastic heterogeneities. Assuming a linear isotropic elastic response between two successive frames Im^i and Im^{i+1} , an incompressible heterogeneous plaque medium and neglecting gravity and inertial forces, the local equation gives the following relationship:

$$\frac{\nabla \mathbf{E}}{E} = \frac{3}{2} \varepsilon^{-1} \frac{\nabla \mathbf{p}}{E} + \mathbf{H} \quad (1.18)$$

and

$$\mathbf{H} = -\varepsilon^{-1} \nabla \cdot \varepsilon \quad (1.19)$$

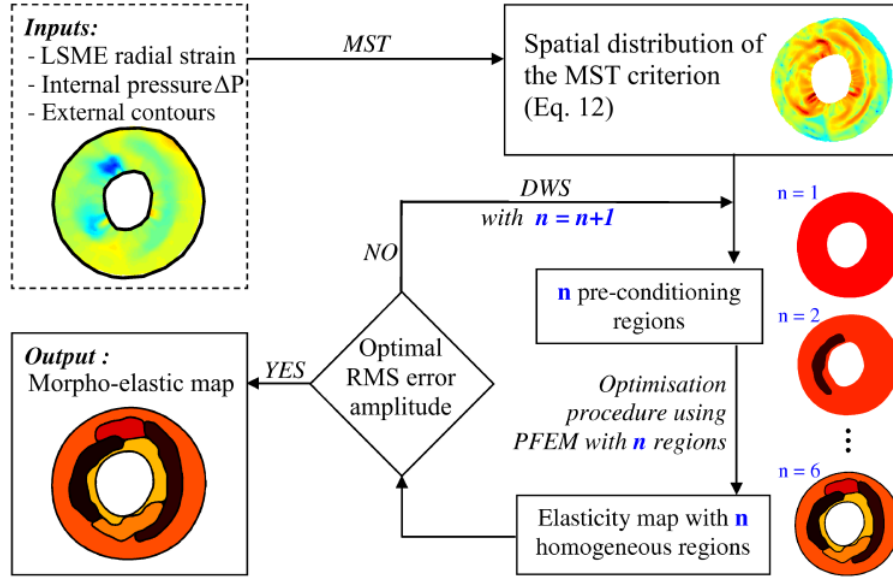


Figure 1.10: Illustration of the successive calculation steps performed in our plaque elasticity reconstruction algorithm iMOD based on a segmentation-driven optimization procedure using LSME strain measurements. LSME= Lagrangian speckle model estimator; MST=Modified Sumi’s transform; DWS= Dynamic watershed segmentation; RMS= Root mean square; PFEM= Parametric finite element model (see section 4.1 for more details). Adapted from Le Floc’h. et al., 2010. On the potential of a new IVUS elasticity modulus imaging approach for detecting vulnerable atherosclerotic coronary plaques: in vitro vessel phantom study. Phys. Med. Biol. 55, 5701-5721. Copyright. Institute of Physics and Engineering in Medicine. Reproduced by permission of IOP Publishing. All rights reserved.

where \mathbf{E} , \mathbf{p} , and $\boldsymbol{\varepsilon}$ are the local Young’s modulus, the Lagrange multiplier and the strain tensor, respectively.

Since the Lagrange multiplier \mathbf{p} cannot be estimated experimentally, we used the second term of Eq. 1.18 right hand side to highlight the Young’s modulus discontinuity boundaries:

$$dW = \mathbf{H} \cdot d\mathbf{X} \quad (1.20)$$

where $d\mathbf{X}$ is the elementary position vector in the undeformed configuration. The amplitude of the morphologic criteria dW was computed to obtain the MST-image. In practical situations, the radial strain component ε_{RR} is the most reliable estimate of the strain tensor $\boldsymbol{\varepsilon}$. Therefore, the criterion was simplified by neglecting the shear strain in the (r, θ) plane (i.e. $\varepsilon_{R\theta} = 0$). Moreover, due to the incompressibility constraint, the circumferential strain $\varepsilon_{\theta\theta}$ was approximated by $\varepsilon_{\theta\theta} = -\varepsilon_{RR}$. The successful morpho-elastic reconstruction maps validated a posteriori the relevance of this choice. Then, a dynamic watershed segmentation (DWS) operation (Watershed function, Imaging Tool Box, MATLAB, version 7.6., the MathWorks, Natick, MA, USA) is applied to the MST-field to obtain the plaque mechanical heterogeneities, treated as “pre-conditioning” regions. We assume a uniform stiffness for each of these regions and compute their Young’s moduli with an optimization process (Optimization Lab Module, COMSOL, version 3.5, COMSOL Inc, Grenoble, France) that minimizes the root mean squared (RMS) error between the radial strain field computed with a parametric finite element model (PFEM) and the IVUS radial strain field estimated by the LSME. The DWS and optimization are repeated increasing the number of regions to account each time for smaller heterogeneities, until the RMS error between two successive iterations is below the designated threshold of 10⁻⁵. A sequential quadratic programming algorithm with a numerical estimation of the gradient by the adjoint method (Gill et al., 2005) was used for the optimization procedure. Summarizing, the iMOD tool comprises

three algorithms: the MST algorithm to extract a pseudo-gradient elasticity map (MST-field), the DWS segmentation procedure to extract the inclusions' contours and the optimization algorithm that provides the Young's moduli for the detected regions. A detailed description of the plaque-imaging algorithm iMOD can be found in [Le Floc'h et al. \(2009\)](#).

1.4.3 Validation of the morpho-elastic reconstruction imaging tool

Two studies were conducted to test and validate the performance of the imaging morpho-elastic reconstruction tool iMOD.

Validation study: In-vitro vessel phantoms. Three vessel phantoms were fabricated from polyvinyl alcohol (PVA) cryogel, a widely used polymer material mimicking passive biological tissues. Phantom manufacturing followed the protocol described by [Fromageau et al. \(2007a\)](#), using a 10% weight solution of PVA in water and adding a 3% weight of Sigmacell particles (Sigmacell cellulose type 50, Sigma Chemical, St Louis, MO, USA) as scatters. Polymerization was achieved by one to six freeze-thaw (F-T) cycles, depending on the mechanical properties desired for each region. Three cylindrical concentric vessel phantoms were made, one homogeneous (one F-T cycle), and the others with one and two soft inclusions (vessel wall with six F-T cycles and inclusions with one F-T cycle), respectively. Cross-sectional IVUS image sequences were acquired while the phantoms were mounted in a bench, with quasi-static pressure provided by a water column. Images at 10 different pressure steps were captured with an IVUS scanner (model In-Vision Gold, Volcano Therapeutics) equipped with a 20 MHz IVUS catheter. Images were digitalized using an external data-acquisition system (model Remora, Volcano Therapeutics). The mechanical properties of all PVA cryogel media used to fabricate our vessel phantoms were investigated by performing compression tests using a dynamic mechanical analyzer (DMA GABO Eplexor, Ahlden, Germany, load cell of 25N, sensor sensitivity of 10^{-4} at full range).

The elasticity reconstruction performed on the homogeneous PVA cryogel phantom (phantom # 1) is presented in Fig. 1.11. A computed quasi-uniform Young's modulus distribution was found with a mean value of 29.6 ± 4.0 kPa. This amplitude agrees with the measured mean amplitude of 17.6 ± 3.4 kPa found when performing DMA mechanical tests on this PVA cryogel medium.

The elasticity reconstruction conducted on the heterogeneous PVA cryogel phantom made of two soft inclusions (phantom # 3) was also successfully estimated (Fig. 1.12). The imaging tool iMOD was able, not only to extract accurately the morphologies and locations of the two soft heterogeneities, but also to reasonably quantify the Young's moduli of the soft inclusions (computed = 19.3 ± 12.9 kPa versus measured = 17.6 ± 3.4 kPa) and surrounding media (computed = 168.6 ± 128.1 kPa versus measured = 145.4 ± 31.8 kPa).

Interestingly, this study showed that the IVUS modulography algorithm iMOD was also able to highlight the nonlinear mechanical properties of the PVA by analyzing a series of successive modulograms during an increase in blood pressure. Because the mechanical property of the PVA cryogel is nonlinear, we investigated the potential of the modulography algorithm to sense the strain hardening of the gel by taking advantage of the series of cross-sectional IVUS images acquired from the phantoms # 2 and # 3 at each pressure step. A series of 10 modulograms were computed by considering 10 sets of two successive IVUS images acquired during the pressure-loading period. By using this protocol, we successfully quantified the increase in Young's moduli with strain from all computed modulograms (see figs. 8 and 9 in [Le Floc'h et al. \(2010\)](#)).

Animal study: Ex-vivo experiment. Experiments were performed on healthy aortas to

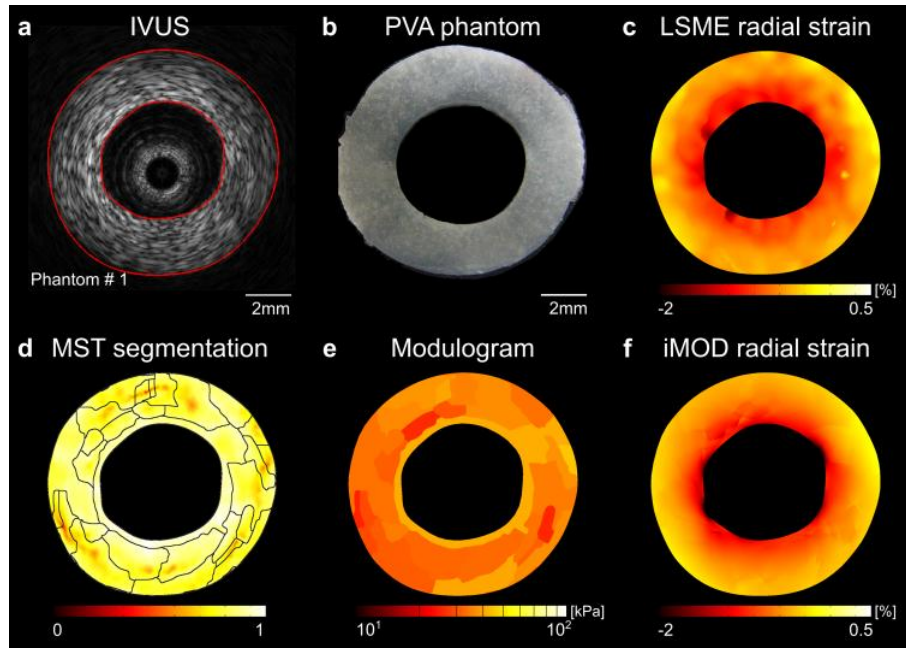


Figure 1.11: Performance of the elasticity reconstruction algorithm iMOD to characterize locally the mechanical properties of the homogeneous vessel phantom wall using experimental RF-IVUS images acquired with a Volcano Therapeutics REMORA IVUS system. a) IVUS image (the red contours delimit the boundaries of the vessel wall); b) cross-section image of the homogeneous cryogel vessel phantom; c) measured LSME radial strain field obtained by using the Lagrangian speckle model estimator (LSME). This strain field results from two consecutive IVUS images recorded at a pressure of 0.25 kPa and 0.5 kPa, respectively; d) spatial pseudo-gradient elasticity field dW (Eq.1.19) resulting from the modified Sumi's transform (MST) procedure. Contours of the elastic heterogeneity domains were obtained thanks to the dynamic watershed segmentation (DWS) method; e) final Young's modulus map (or modulogram); f) resulting computed radial strain map obtained when performing a finite element simulation with the final modulogram presented in (e). Qualitatively, there is a noticeable good agreement between the PFEM-computed (f) and IVUS-measured (c) radial strain distributions. Adapted from Le Floc'h. et al., 2010. On the potential of a new IVUS elasticity modulus imaging approach for detecting vulnerable atherosclerotic coronary plaques: in vitro vessel phantom study. *Phys. Med. Biol.* 55, 5701-5721. Copyright. Institute of Physics and Engineering in Medicine. Reproduced by permission of IOP Publishing. All rights reserved.

acquire RF-IVUS sequences, histologic data and elasticity measurements from the same arterial section. Animal population consisted of two Watanabe rabbits. Rabbit aortas have similar dimensions to those of human coronaries (Abela et al., 2016). The following protocol was conducted. After general anesthesia, rabbits were euthanized, and the thoracic and abdominal aortas were immediately harvested in a 4 °C Krebs-Henseleit (KH) solution. The length of the samples were measured before excision in order to later reproduce the longitudinal in situ stretch of the artery on the experimental bench. The surrounding tissue was removed after dissection and the arteries were submerged on the KH solution bath during all manipulations to avoid tissue deterioration.

Later, the arterial sections were mounted on an experimental bench to acquire IVUS images with pressure recordings. The IVUS platform used to record the RF signal was the GALAXY2 (Boston Scientific, Watertown, MA) equipped with a 30 MHz Atlantis SR Pro 3.6 F catheter. Dynamic pressure profiles of small amplitudes were applied for the image acquisitions; the results presented here were extracted from sequences with cyclic sinusoidal dynamic pressure at 30 beats per minute (peristaltic pump model 1405 PBP, Harvard Apparatus, USA). The maximal and minimal mean cyclic pressure amplitudes were of 2.10 and 2.60 kPa, and a mean incremental pressure amplitude ΔP close to 0.025 kPa was used to extract a series of 300 sets of two consecutive RF-IVUS images (Im^i, Im^{i+1} with $i=1$ to 300). This results in small displacements and allow the use of the small strain hypothesis. Even though these do not represent in vivo

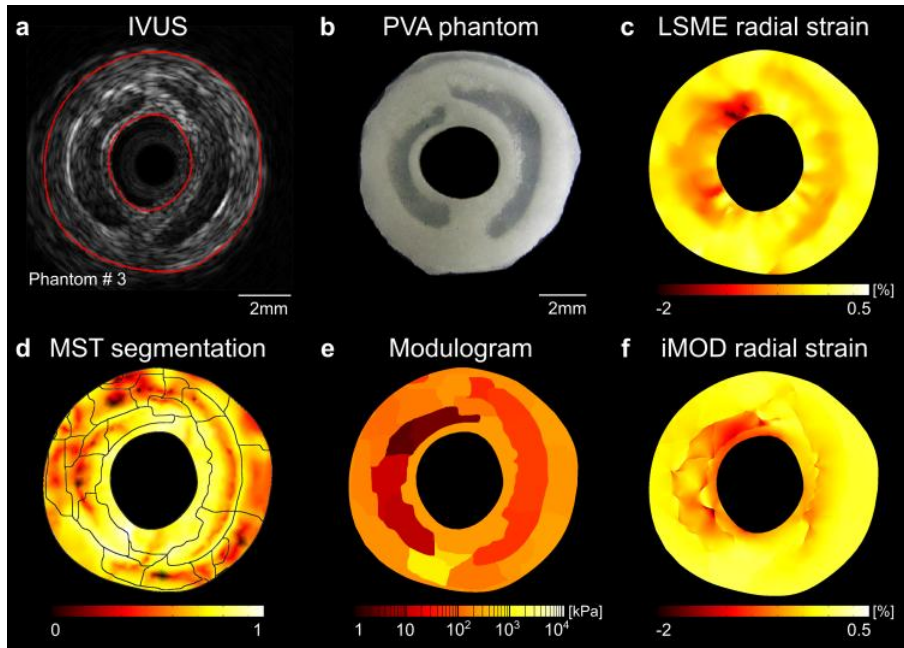


Figure 1.12: Performance of the elasticity reconstruction algorithm iMOD to characterize locally the mechanical properties of the heterogeneous vessel phantom wall with two soft inclusions using experimental RF-IVUS images acquired with a Volcano Therapeutics REMORA IVUS system. a) IVUS image; b) cross-section image of the heterogeneous cryogel vessel phantom; c) measured LSME radial strain field resulting from two consecutive IVUS images recorded pressures of 4 kPa and 4.5 kPa, respectively; d) spatial pseudo-gradient elasticity field with the potential contours of the elastic heterogeneity domains with contours of the elastic heterogeneity domains; e) final Young's modulus map (or modulogram); f) resulting computed radial strain map obtained when performing a finite element simulation with the final modulogram presented in (e). Qualitatively, there is a noticeable good agreement between the PFEM-computed (f) and IVUS-measured (c) radial strain distributions. Adapted from Le Floch, et al., 2010. On the potential of a new IVUS elasticity modulus imaging approach for detecting vulnerable atherosclerotic coronary plaques: in vitro vessel phantom study. *Phys. Med. Biol.* 55, 5701-5721. Copyright. Institute of Physics and Engineering in Medicine. Reproduced by permission of IOP Publishing. All rights reserved.

and pathological conditions, they allow the evaluation of the algorithms' capabilities to extract the elasticity of the arterial tissues.

After the IVUS acquisitions, sections of 10 and 16 microns (selected in the IVUS-imaged zone) were obtained with a microtome to be used in atomic force microscopy (AFM) and immunohistological stainings. Mechanical testing was performed on several sites over the arterial wall cross-sections with a servo-controlled AFM (Nanowizard II, JPK instruments, Berlin, Germany). Serial 16 μm -thick vessel sections were mounted on Poly-L-Lysine slides (Thermo-Scientific, France). The arterial wall, including the intima and media layers, were exposed for probing by AFM. Tissue samples were kept in KH buffer. All AFM measurements were made in liquid at room temperature, including cantilever calibration. For all specimens, mechanical testing was completed within 4 hours of harvesting the sample (a detailed description of the AFM protocol is given in [Tracqui et al. \(2011\)](#)). Biological characterization was achieved by means of two different histologic staining methods: Hematoxylin Eosin Saffron (HES) trichromatic staining and Oil Red O (ORO).

Fig. 1.13 presents a preliminary result showing the capabilities of the elasticity reconstruction algorithm iMOD to characterize locally the Young's modulus of a healthy aortic wall of a Watanabe rabbit using experimental RF images acquired with an IVUS system ([Deleaval et al., 2013](#)). This result shows that the mean modulogram amplitude (57.9 ± 49.2 kPa, Fig. 7e) agrees quite well with the mean Young's modulus of 53.4 ± 60.1 kPa obtained by performing

AFM mechanical tests on $n=24$ random locations of the vessel wall and by assuming the arterial wall as homogeneous, isotropic and quasi-incompressible.

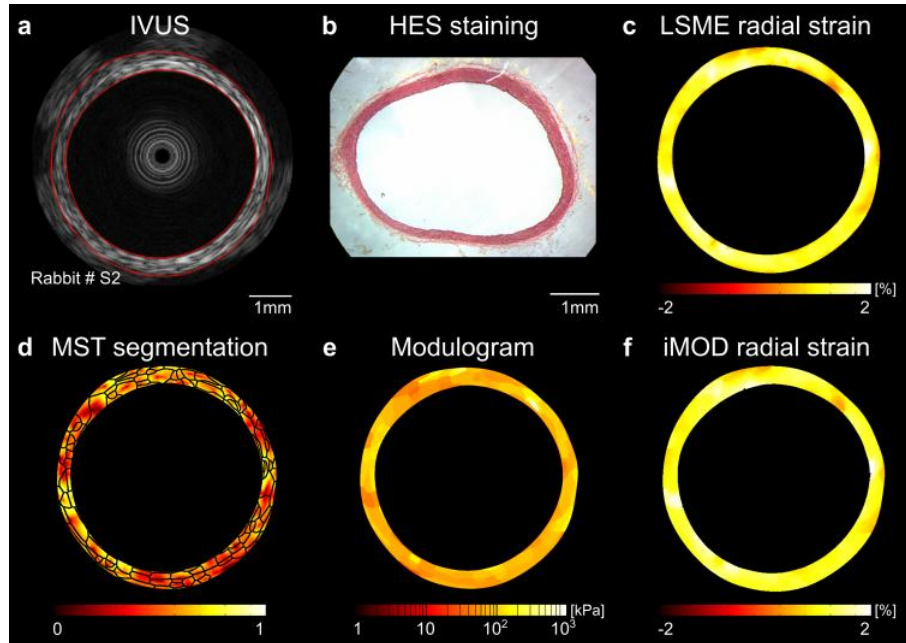


Figure 1.13: Performance of our elasticity reconstruction algorithm iMOD to characterize ex vivo the mechanical properties of a healthy aortic wall of a Watanabe rabbit (Rabbit # S2) using experimental RF-IVUS images acquired with a Boston Scientific GALAXY2 IVUS system. a) IVUS image (the red contours delimit the boundaries of the vessel wall); b) trichrome, haematoxylin, erythosine, safran (HES) staining of the healthy aortic wall where nucleus, cytoplasm and fibrosis are in blue, pink and yellow, respectively (no atherosclerotic lesion was observed); c) measured LSME radial strain field resulting from two consecutive IVUS images recorded at pressures of 2.3 kPa and 2.23 kPa, respectively; d) spatial pseudo-gradient elasticity field dW (Eq.1.20) resulting from the modified Sumi's transform (MST) procedure. Contours of the elastic heterogeneity domains were obtained thanks to the dynamic watershed segmentation (DWS) method; e) final Young's modulus map (or modulogram); f) resulting computed radial strain map obtained when performing a finite element simulation with the final modulogram presented in (e). Adapted from [Deleaval \(2013\)](#).

1.4.4 From model to patient

The performance of the elasticity reconstruction method iMOD was investigated on IVUS sequences obtained from seven patients scheduled for directional coronary atherectomy (DCA) intervention [Le Floc'h et al. \(2012\)](#). The protocol was approved by the Review Ethical Committee of Sendai University Hospital and patients gave their written consent. Imaging sequences consisting of 30 frames were recorded with a 40 MHz IVUS catheter connected to a Galaxy II echograph (Boston Scientific, Natick, MA, USA). Because no pressure measurements were performed during the clinical protocol, the blood pressure differential was calculated by assuming a linear variation between diastolic and systolic pressures.

During the DCA procedure, arterial sections were excised using a specially designed catheter (Flexicut, Guidant Corporation, Santa Clara, CA, USA). Samples were fixed in 10% formalin, embedded in paraffin and cut into $4\mu\text{m}$ slices using a microtome. Then, they were stained with Elastica-Masson's trichrome to quantify the properties of different constituents of the seven excised lesions.

Based on the recorded RF-IVUS-sequences, 29 and 28 modulograms were computed for patients # 9 and # 11, respectively. Figures 1.14 and 1.15 display the representative modulograms, RF-correlation coefficient, MST, and IVUS-estimated and PFEM-computed radial strain maps obtained for these patients. Notice that a low value of the RF-correlation coefficient indicates a poor estimate of displacement due to either high acoustic noise or a

low signal-to-noise ratio. Qualitatively, we found noticeable good agreements between the PFEM-computed and IVUS-measured radial strain distributions (see Figs.1.14c and 1.14f and Figs. 1.15c and 1.15f).

Correlations between the patient's modulogram and the histological analysis of the associated excised lesion were considered relevant (see figure 8 in [Le Floc'h et al. \(2012\)](#)), but not enough to validate these plaque-imaging tools. Consequently, even if the the presented imaging techniques show original and promising results, new in vivo clinical studies in animals and complementary clinical studies are still needed to strongly validate these two techniques.

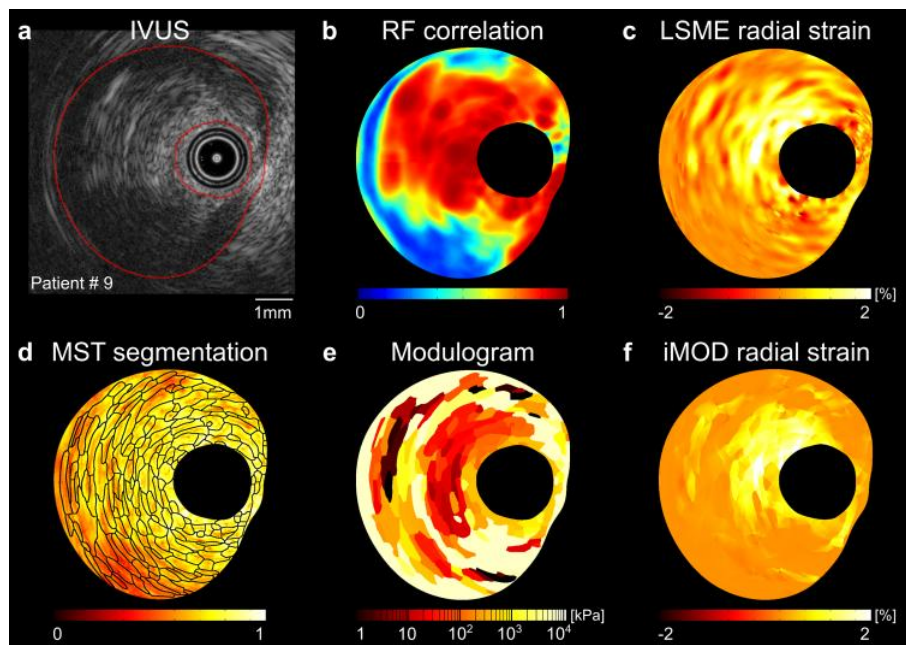


Figure 1.14: Performance of our elasticity reconstruction algorithm iMOD to characterize in vivo the mechanical properties of a human atherosclerotic plaque (patient # 9) using experimental RF-IVUS images acquired with a Boston Scientific GALAXY2 IVUS system. a) IVUS image (the red contours delimit the boundaries of the vessel wall); b) spatial distribution of the RF-correlation coefficient; c) measured LSME radial strain field obtained by using the Lagrangian speckle model estimator (LSME); d) spatial pseudo-gradient elasticity field dW (Eq.1.20) resulting from the modified Sumi's transform (MST) procedure. Contours of the elastic heterogeneity domains were obtained thanks to the dynamic watershed segmentation (DWS) method; e) final Young's modulus map (or modulogram); f) resulting computed radial strain map obtained when performing a finite element simulation with the final modulogram presented in (e). Qualitatively, there is a noticeable good agreement between the PFEM-computed (f) and IVUS-measured (c) radial strain distributions. Adapted from [Le Floc'h et al., 2012](#). A four-criterion selection procedure for atherosclerotic plaque elasticity reconstruction based on in vivo coronary intravascular ultrasound radial strain sequences. *Ultrasound in Med. & Biol.* 38(12), 2084-2097.

1.5 My next steps and works performed

Both the elasticity-palpography and modulography techniques, as well as the majority of IVUS strain elastography and modulography algorithms, are based on radio frequency (RF) IVUS data because it provides a good resolution of the atherosclerotic plaque. Even though b-mode gray-scale IVUS images have a lower resolution, they have some advantages over RF data, such as a wider availability of compatible software and hardware, and a higher portability. This has motivated the development of b-mode based plaque assessment techniques.

Therefore, in a first step (**Chapter 2**), the performance of b-mode based IVUS elastography algorithm developed by [Zhang et al. \(2011b\)](#) is investigated by reproducing this approach in our laboratory. The aim of this study is to determine if b-mode images are enough to get an accurate displacement maps.

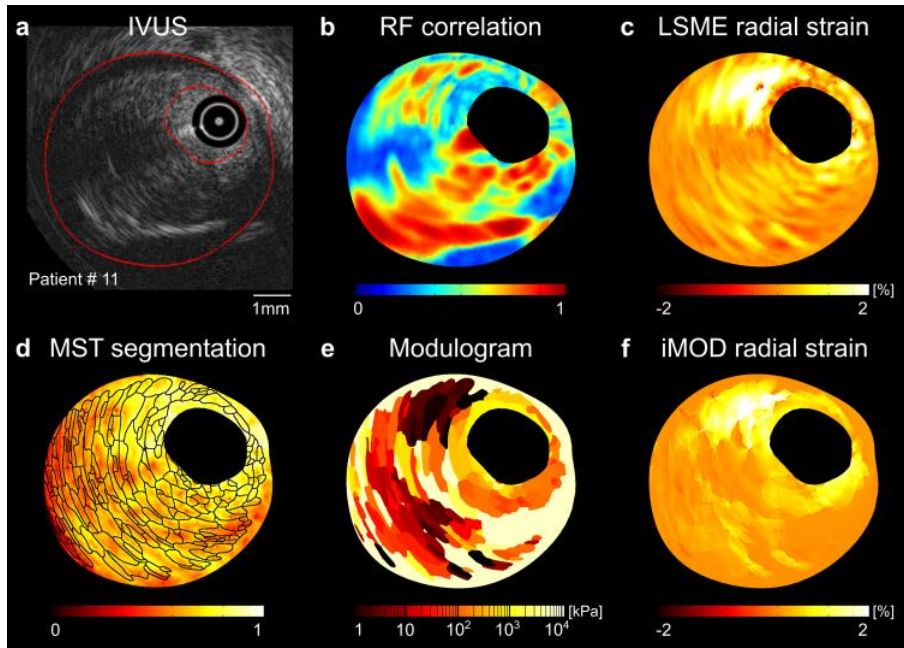


Figure 1.15: Performance of our elasticity reconstruction algorithm iMOD to characterize in vivo the mechanical properties of a human atherosclerotic plaque (patient # 11) using experimental RF-IVUS images acquired with a Boston Scientific GALAXY2 IVUS system. a) IVUS image; b) spatial distribution of the RF-correlation coefficient; c) measured LSME radial strain field; d) spatial pseudo-gradient elasticity MST field with elastic heterogeneity domains; e) final Young's modulus map (or modulogram); f) computed radial strain map. Adapted from Le Floch et al., 2012. A four-criterion selection procedure for atherosclerotic plaque elasticity reconstruction based on in vivo coronary intravascular ultrasound radial strain sequences. *Ultrasound in Med. & Biol.* 38(12), 2084-2097.

In the second step, we revisited the elasticity-palpography technique of [Deleaval et al. \(2013\)](#), which is a promising approach for plaque assessment. However, it does not take into account the anisotropic mechanical behavior of the arterial wall. In **Chapter 3**, a new anisotropic elasticity-palpography algorithm is described, which extends the theoretical framework of the work of [Deleaval et al. \(2013\)](#) by considering the orthotropic mechanical properties of the plaque. A feasibility study using simulated IVUS images is presented.

Later, in **Chapter 4**, this new anisotropic elasticity-palpography technique is tested *in vitro* using polyvinyl-alcohol cryogel phantoms with enhanced anisotropy.

Chapter 2

Are b-mode images a viable alternative to RF for the computation of modulograms of atherosclerotic plaques?

2.1 Introduction

Intravascular ultrasound (IVUS) is the most widely used minimally invasive imaging technique for coronary arteries. Briefly, a rotating ultrasound transducer mounted on the tip of a cardiac catheter generates sound waves that propagate radially through the arterial wall. The way these waves are reflected back to the transducer depend on the acoustic properties of the different tissues (i.e. fibrous, calcified, lipid, etc.) that constitute the vessel wall. Therefore, these raw radio frequency (RF) signals, also called a-line signals, in the form of amplitude vs time, have the potential to characterize the atherosclerotic plaque components ([Garcia-Garcia et al., 2011](#)).

The positive envelope of each of the 1-D RF signals is obtained and presented in a 2-D gray-scale image known as b-mode IVUS. These are the images often analyzed by physicians in order to assess plaque burden and composition. Based on the echogenicity aspect of each tissue, component characterization of the plaque can be performed via visual interpretation by an experienced interventional cardiologist. However, manual segmentation is time-consuming and presents a great inter- and intra-observer variability ([Athanasiou et al., 2013](#)). Therefore, automated computational methods for the segmentation ([Roy Cardinal et al., 2006](#); [Le Floc'h et al., 2009](#); [Katouzian et al., 2012](#)) and characterization ([Zhang et al., 1998](#); [Nair et al., 2002](#); [Athanasiou et al., 2013](#); [Tacheau et al., 2016](#)) of the plaque have been developed to address these limitations.

Some characterization algorithms create a segmentation based on the echogenicity of the pixels and texture features, and classify plaque by types (i.e. soft plaque, hard non-calcified plaque and hard calcified plaque) ([Zhang et al., 1998](#); [Brunenberg et al., 2006](#); [Athanasiou et al., 2013](#)) with some of them focusing only on the detection of calcified areas ([Santos Filho et al., 2008](#); [Zhang et al., 2010](#)). These characterization algorithms use one of two basic approaches ([Garcia-Garcia et al., 2011](#)). The first approach analyzes the raw RF signal ([Granada et al., 2007](#); [Sathyanarayana et al., 2009](#)) while the second one performs a b-mode image-based analysis ([Zhang et al., 1998](#); [Brunenberg et al., 2006](#); [Santos Filho et al., 2008](#); [Zhang et al., 2010](#)).

Most of these methodologies use RF data because it can provide a better description and resolution of the atheromatous plaque and it also remains independent of any brightness, gain or contrast adjustment made during the acquisition (Granero et al., 2015). However, there has been an increased interest in using b-mode images because of their higher portability and wider availability of compatible software and hardware. To test the accuracy of these methods, for both RF and b-mode based, the resulting contours are compared to manual segmentations from experts. Even though these characterizations have good agreement (as high as 89.9 % (Athanasίου et al., 2013)) with manual segmentations, the information they supply to clinicians is still quite limited.

With the objective of providing additional information that cardiologists can use to assess plaque vulnerability, other kind of algorithms that focus on assessing the local mechanical properties of the plaque have been developed. One of such techniques is IVUS elastography (IVUSE) (Le Floch et al., 2010), which calculates elasticity maps (i.e. modulograms) using the intraplaque strain field (i.e. elastograms) obtained from IVUS sequences. It is inspired by palpation, which is a diagnostic examination widely-used by physicians to inspect superficial organs and is based on the premise that pathological tissue is stiffer than healthy tissue. These elastograms can help identify the different plaque components, such as lipid, calcifications and fibrosis, based on the difference in their mechanical properties. Moreover, thanks to finite element simulations performed on these geometries, it can identify high-stress regions within the plaque and assess peak cap stress, which is known to be a good predictor of plaque rupture.

Most strain-elastography and modulography algorithms are based on RF signal analysis (Maurice et al., 2007; Le Floch et al., 2009, 2010; Doyley, 2012; Majdouline et al., 2014). However, the previously mentioned limitations of RF processing are still present. As an alternative, b-mode IVUSE techniques have been developed, reporting good results *in vitro* and with numerical simulations (Talhami et al., 1994; Ryan and Foster, 1997; Mingxi Wan et al., 2001). Furthermore, Zhang’s group developed a b-mode IVUSE system Zhang et al. (2011a) and tested it *in vivo* in a rabbit model (Hu et al., 2011). They used their methodology to investigate the relation between their new index called area strain (AS) (Saijo et al., 2006), which may be viewed as the rate of area deformation, and the features and vulnerability of the atherosclerotic plaques. Subsequently, they used this approach to investigate the effect of statin therapy on diseased rabbit aortas (Li et al., 2016). Their studies found a moderate correlation between the AS index and plaque composition and concluded that this methodology is feasible to assess plaque vulnerability.

The present study aims to determine if IVUS b-mode images are enough to compute accurate strain maps. The first section describes the work of Zhang et al. (2011a), which is used as a basis to define an IVUSE b-mode methodology. Then, the performance of this algorithm to obtain accurate motion estimation is tested using a simulated IVUS sequence and compared to finite element analysis computations.

2.2 Zhang’s b-mode elastography method

This section offers a summary of the b-mode elastography method presented in Zhang et al. (2011a) and Hu et al. (2011). First, IVUS, electrocardiogram and pressure acquisitions are simultaneously recorded. Two frames near end-diastole are chosen as the pre- (Fr^T) and post-deformed $(Fr^{T+\Delta T})$ states. The reason for choosing frames at this phase of the cardiac cycle is because catheter motion is minimal and this reduces speckle de-correlation and catheter oscillation errors (De Korte et al., 2002). Next, the lossless DICOM image corresponding to the pre-deformed state Fr^T (Fig. 2.1 A) was segmented semi-automatically to obtain the intima and adventitia contours (Fig. 2.1 B) using a discrete dynamic contour model (Lobregt and Viergever, 1995).

Once the contours that limit the plaque area were obtained, a block-matching search algorithm was implemented to find the new position of each point within the plaque area in Fr^T to its corresponding best-match in $Fr^{T+\Delta T}$. The algorithm takes each pixel inside the plaque area in Fr^T and selects it to be the center of a block (P) of $M \times M$ pixels (Fig. 2.2 b). In $Fr^{T+\Delta T}$, the same pixel position was selected as the center of a search window of $N \times N$ pixels (Fig. 2.2 c). Values of 10 and 100 were selected for M and N , respectively. The best match for block P inside the search window was labeled as block Q , and its center point was saved as the deformed position of that point. Block Q was selected by maximizing the normalized cross-correlation coefficient as defined in (Zhang et al., 2011a).

Then, points with a correlation coefficient > 0.9 were selected to create a triangular mesh (Fig. 2.1 C) with the Delaunay triangulation technique using the Delaunay process in Matlab (MathWorks, Natick, MA, USA). Finally, for each triangle, the area strain (AS) was calculated as:

$$AS = (S - S_0)/S_0 \quad (2.1)$$

where where S_0 and S are the triangle areas before and after deformation, respectively. AS values were color-coded as red for positive deformation, green for negative deformation, and yellow for no deformation, and superposed on the b-mode IVUS image (Fig. 2.1 D). All these steps are summarized in table 2.1.

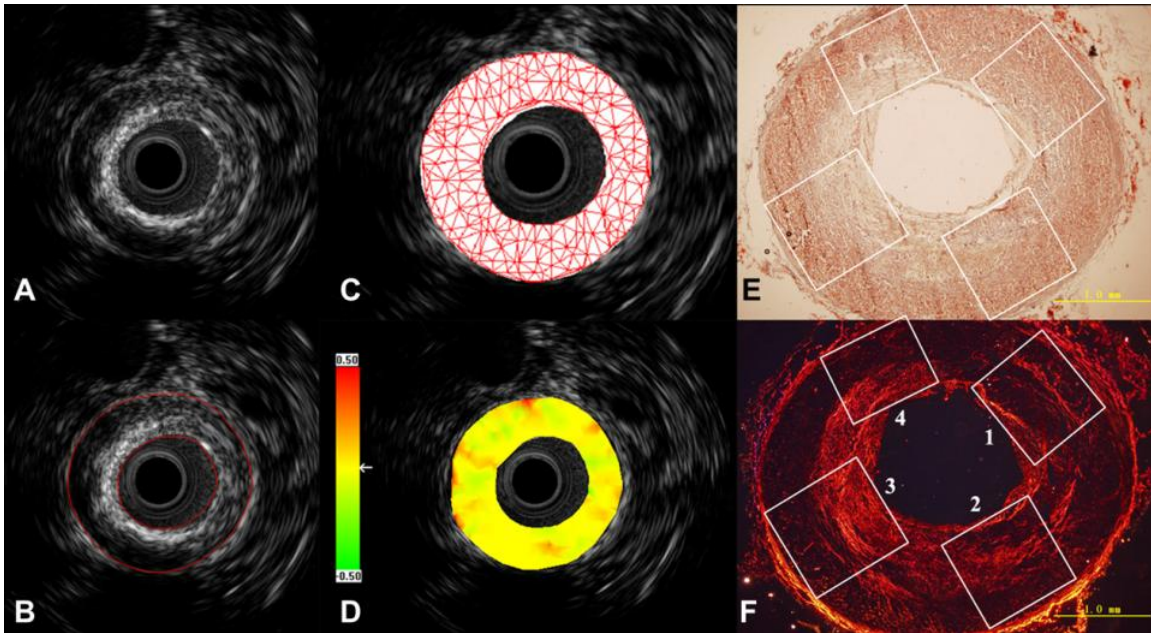


Figure 2.1: (A) Intravascular ultrasound (IVUS) b-mode image of a concentric atherosclerotic plaque, (B) luminal and media-adventitia borders delineated semi-automatically, (C) triangular meshes constructed by Delaunay triangulation, (D) IVUS elastogram for area strain, (E) corresponding histologic slice with Oil-red O staining (4X) showing lipid deposits and (F) corresponding histologic slice with picro-sirius staining by polarized light (4X) showing collagen. ROIs were outlined on histologic slices (E) and (F). Reproduced from Hu et al. (2011).

2.3 Materials and methods

To test the potential of Zhang’s elastography based on b-mode images (as an alternative for the raw RF signal) we reproduced this approach in our laboratory. This study was performed in collaboration with Dr. Antoine Tacheau from TIMC-IMAG Laboratory in Grenoble.

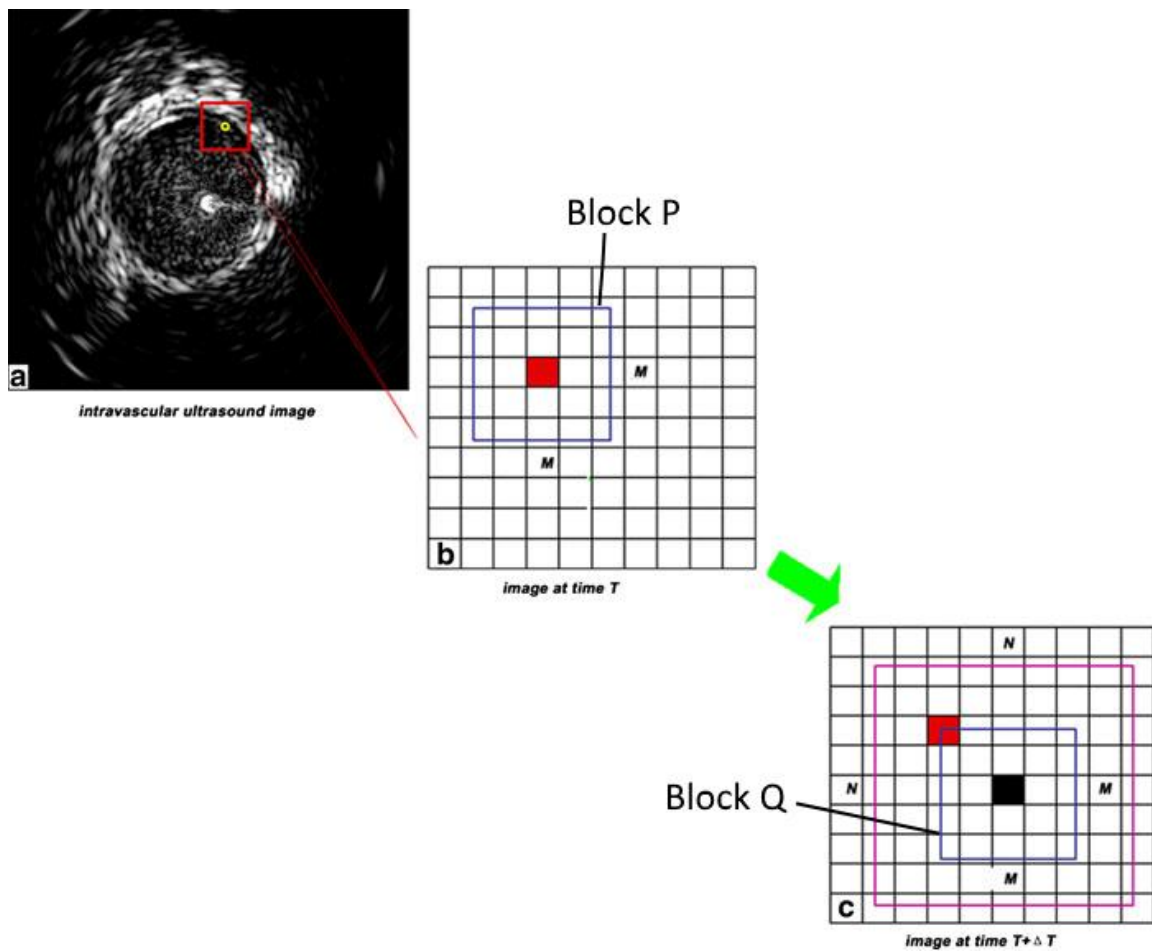


Figure 2.2: Diagram of block-matching algorithm. The red square in image at time T (b) is the yellow tagged point in the original IVUS image (a), and this square will move to the location marked as the black square at time $(T = \Delta T)$ (c). The predefined block size is $M \times M$ pixels, and the search window is $N \times N$ pixels. Reproduced from [Zhang et al. \(2011a\)](#).

Table 2.1: Zhang’s IVUS elastography methodology

IVUS acquisition	Single element rotating IVUS catheter (Atlantis SR Pro 40 MHz). Electrocardiography (ECG) and blood pressure simultaneously recorded. Acquisition of lossless DICOM b-mode images.
Frame selection	Two consecutive frames near end-diastole.
De-noising filter	Fast Fourier Transform (FFT) algorithm (Gonzalez and Woods, 2002) to reduce speckle noise inside the lumen and enhance vessel contours.
Contours’ definition	Borders of the lumen and media-adventitia semi-automatically delineated on the pre-deformed image (frame 1) with a discrete dynamic contour model (Lobregt and Viergever, 1995).
Block-matching (BM) search algorithm	Search block of 10 x 10 pixels and search window of 100 x 100 pixels. Best matching block determined by the normalized cross-correlation coefficient Zhang et al. (2011a). Frame size of 480 x 480 pixels, pixel resolution = 0.025 mm.
Triangle-mesh construction	Points with a correlation coefficient ≥ 0.9 are automatically selected to build triangular meshes using the Delaunay triangulation technique.
Area strain (AS) calculations	For each triangle, AS values are calculated as $AS = (S - S_0)/S_0$, where S_0 and S are the triangle areas before and after deformation, respectively. Strain values are superimposed in the IVUS gray-scale image.

First, the contours of an atherosclerotic plaque with a necrotic core were obtained with manual segmentation of an expert on IVUS sequences acquired *in vivo* on patients. These contours were used to create a 2-D finite element (FE) model. A pressure gradient equivalent to the one between two IVUS frames was applied inside the lumen and the resulting displacement fields were as an input for the ultrasound image simulation software Field II to obtain simulated RF IVUS frames and b-mode images. Later, a b-mode IVUSE algorithm based on Zhang’s methodology was applied to these synthetic b-mode frames. The displacement results were compared between the FE model and the block-matching results.

2.3.1 IVUS acquisition and image analysis

First, a plaque morphology was collected from IVUS scans of the coronary arteries following the protocol described by Rioufol et al. (2002). IVUS exploration was performed after intracoronary administration of 200 μg of nitroglycerine to avoid vasospasms. Cross-sectional IVUS images of the atherosclerotic lesion were recorded with the iLab platform (Boston Scientific, Watertown, MA) equipped with 40 MHz catheters (Atlantis SR Pro 3.6F, Boston Scientific). This IVUS system has a radial spatial resolution in b-mode of approximately 90 μm (Chopard et al., 2010).

Based on IVUS echogenicity aspects, a manual segmentation procedure using ImageJ software (ImageJ, NIH, Bethesda, MD, USA) was performed by a cardiologist (G.Finet) to extract the internal (i.e. lumen) and external contours of the coronary cross-section, as well as the contours of each plaque component (i.e. necrotic core and dense fibrosis).

2.3.2 Spatial displacement and strain field distributions

2D finite element simulations

This study was performed on 3 vulnerable plaque geometries from patients who underwent

IVUS. The obtained segmentation contours (see Fig. 2.3) were introduced into the modeling and simulation software Comsol (Structural Mechanics Module, version 4.3b, Comsol, France). To compute the deformed shape, a 2-D static finite element (FE) simulation was conducted. The geometry was meshed with approximately 20,000 triangular elements. The barycenter (i.e the center of mass) of the luminal area was used as the origin of the cylindrical coordinate system (R, θ) .

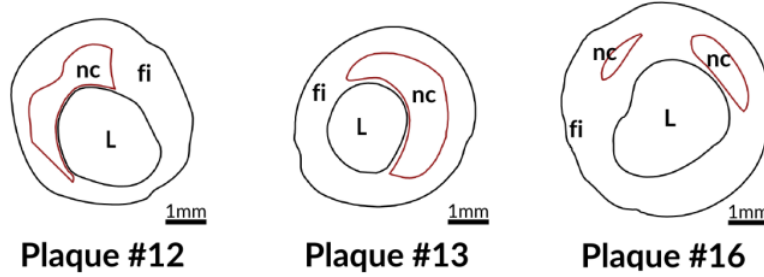


Figure 2.3: Contours of atherosclerotic plaques and constituents obtained from patients' IVUS images. L= lumen, fi= fibrosis, nc= necrotic core.

For our computational approach, the deformation of the atherosclerotic plaque between two successive images (Im^i and Im^{i+1}) of the IVUS sequence was obtained by considering the geometry of the lesion at Im^i as the reference configuration. Therefore, FE simulations were performed in linear elasticity with the small loading blood pressure differential ΔP . Since instantaneous pressures were not recorded during clinical IVUS explorations, a blood pressure differential amplitude $\Delta P = 1$ kPa (i.e 7.5 mmHg) was assumed, corresponding to a realistic pressure gradient occurring between two successive images of the IVUS sequence recorded during the cardiac cycle (Le Floc'h et al., 2009, 2012).

FE simulations were performed under plain strain condition, and free boundary condition was assumed at the external wall of the artery. Additionally, displacement limitations were placed upon nodes located on the four cardinal directions of the external wall of the artery to avoid rigid rotations. The fibrosis and soft necrotic core were modeled as isotropic and quasi-incompressible media (Poisson ratio $\nu = 0.49$) with Young's moduli of $E_{fibrosis} = 800$ kPa and $E_{core} = 5$ kPa, respectively (Fig. 2.3).

Simulation of ultrasound images

The displacement and stress fields resulting from the FE model serve as a reference for our study and are also used to generate the simulated IVUS b-mode images that were later processed with the block-matching (BM) algorithm.

To generate the b-mode images, the open source software FieldII (Jensen and Svendsen, 1992) was modified to simulate the IVUS acoustic field (Fromageau et al., 2003; Nayak et al., 2017; Poree et al., 2017). Briefly, blood, fibrotic plaque, soft necrotic core tissue were characterized by their acoustic scattering amplitude. Acoustic models were built by randomly distributing scatterers over each non-deformed medium. The relative acoustic scatterer amplitudes of blood, necrotic core and fibrotic plaque were set to 10%, 15% and 35%, respectively (Le Floc'h et al., 2010; Maurice et al., 2004b). First, an IVUS image of the non-deformed state (i.e. Im^i) was created. Then the displacement field resulting from the FE simulation was used to track the location of scatterers and to create the post-deformation IVUS image (i.e. Im^{i+1}). A single rotating piezo-electric element was modeled. An incremental circumferential rotation step of 0.7 degrees was set to get 512 lines of RF signal for IVUS image reconstruction. The piezo-electric element had a diameter of $600\mu\text{m}$ and a central emission frequency set to 40MHz. A sampling

frequency of 400MHz was mimicked to represent the RF signal. These values were chosen according to the SVMH HD IVUS system device (ACIST Medical Systems, Eden Prairie, MN, USA). The arterial wall was also adjusted to set the centroid of the lumen coincident with the probe location.

2.3.3 B-mode based algorithm

Based on the methodology of Zhang's group, a three step search (TSS) block-matching (BM) algorithm was defined. First, the synthesized b-mode images and the contours were loaded. Similar to the previously described BM algorithm, the pixels of the plaque area were defined between the lumen and media-adventitia contours. The search parameters were set with M and N being the block, search window and step dimensions. The step corresponded to the number of consecutive pixels to be evaluated in each direction. For each P block in the pre-deformed frame F_r^T , a Q block was selected in $F_r^{T+\Delta T}$ by using the normalized cross-correlation coefficient (CC) (normxcorr2 function in Matlab) as the best matching block criterion. The displacements in the X (U_x) and Y (U_y) directions were calculated for all points using the BM results and the image resolution (pixels/mm) in each direction. The points with $CC > 0.9$ were used to create a mesh with Matlab's the Delaunay function, and the AS was computed for each triangle. A diagram of the BM process is depicted in Fig.

2.4 Results and Discussion on the performance of Zhang's algorithm

2.4.1 Displacement estimations

The cases used for evaluating the block matching (BM) algorithm consisted of fibrotic plaques with one or two necrotic cores. The correlation coefficient (CC)(Figures. 2.5, 2.6 and 2.7) obtained from the block-matching process was good in general, with most values above the 0.9 threshold. The estimated displacements in the X (U_x) and Y (U_y) directions for all cases are shown in Figures 2.5, 2.6 and 2.7, as well as the displacements obtained using the FE model. In general the BM displacement estimations are similar to the FE displacement map, but there are certain areas where the BM estimations fail. For these areas, the pixel resolution is not good enough to capture the real displacement, which causes either over- or underestimations of the displacement.

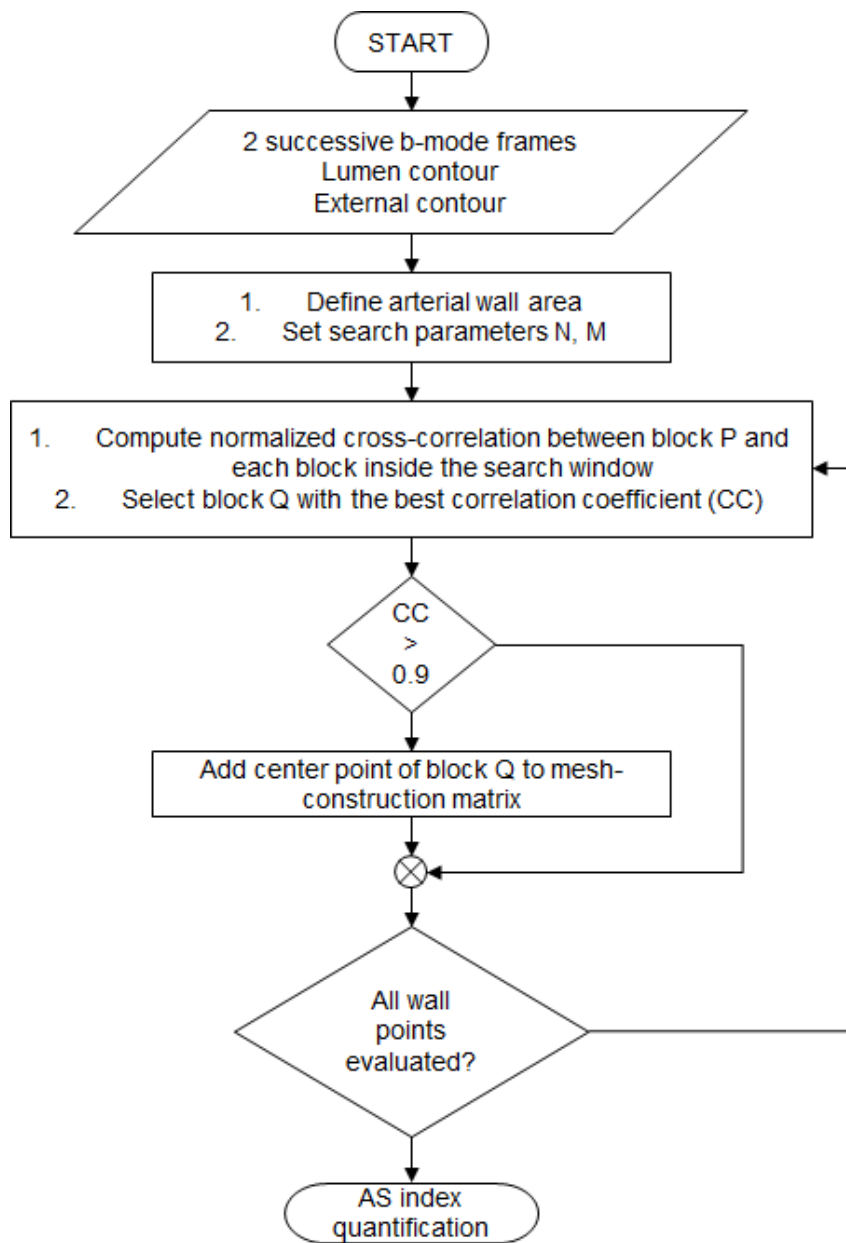


Figure 2.4: Diagram of the block-matching (BM) process for two successive IVUS b-mode images. CC: correlation coefficient; AS index: Area strain index (Eq. 2.1).

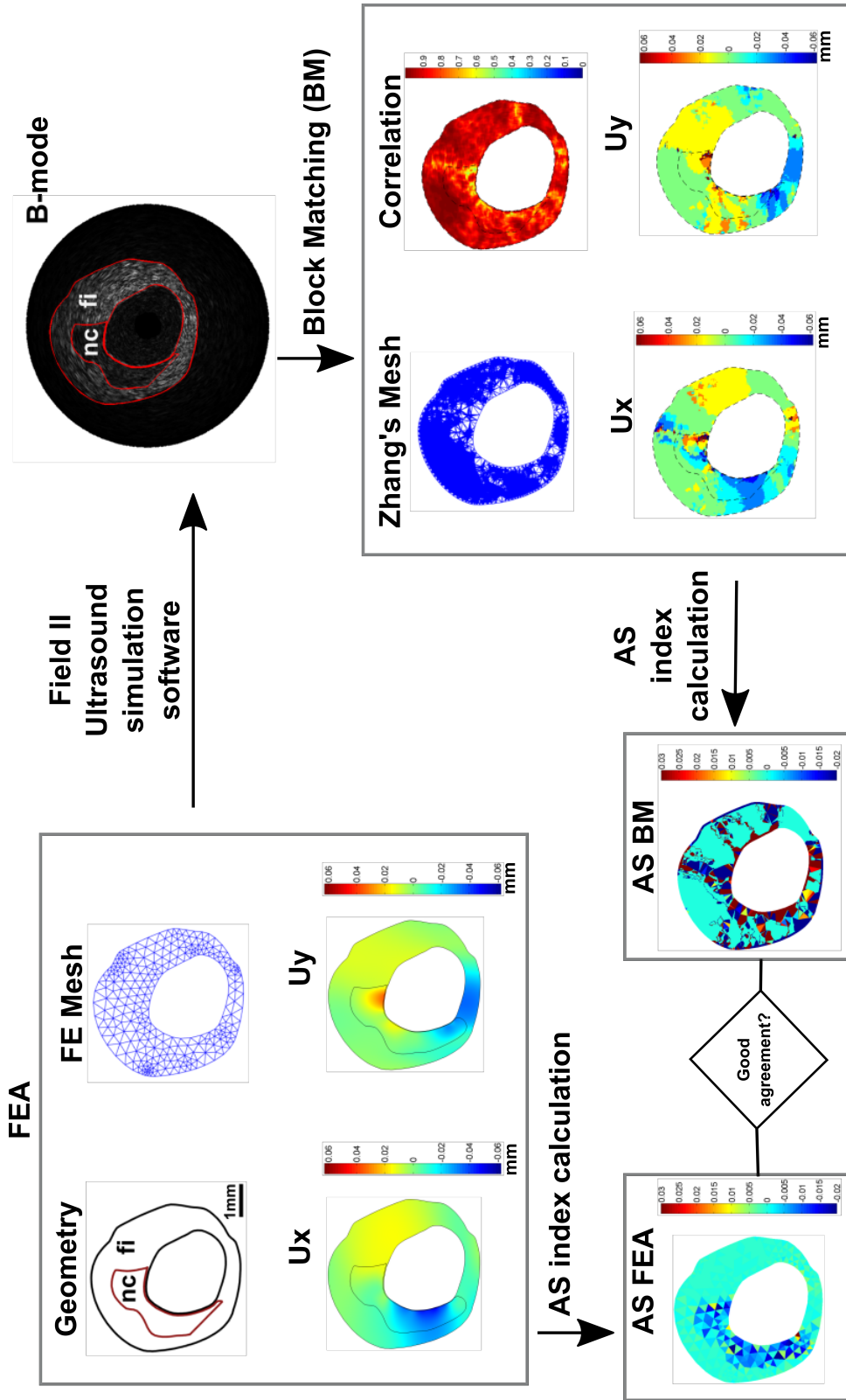


Figure 2.5: Performance of the b-mode based algorithm of Zhang in a plaque with a necrotic core (Plaque# 12). First, a Finite Element Analysis (FEA) is performed using the contours of the arterial geometry and the exact displacement maps U_x and U_y are computed. Then, using the Field II ultrasound simulation software, b-mode images of the plaque are synthesized. These images are used with the Block Matching (BM) algorithm to obtain the estimated displacement maps U_x and U_y . The points with a correlation higher than 0.9 are used to create a triangular element mesh that we call Zhang's mesh. Using Zhang's mesh and the U_x and U_y maps estimated with the BM algorithm, the Area Strain (AS) index is calculated for each element in the mesh. Finally, this estimated BM AS map is compared to the exact AS FEA map obtained using the FE Mesh and the exact FE U_x and U_y maps.

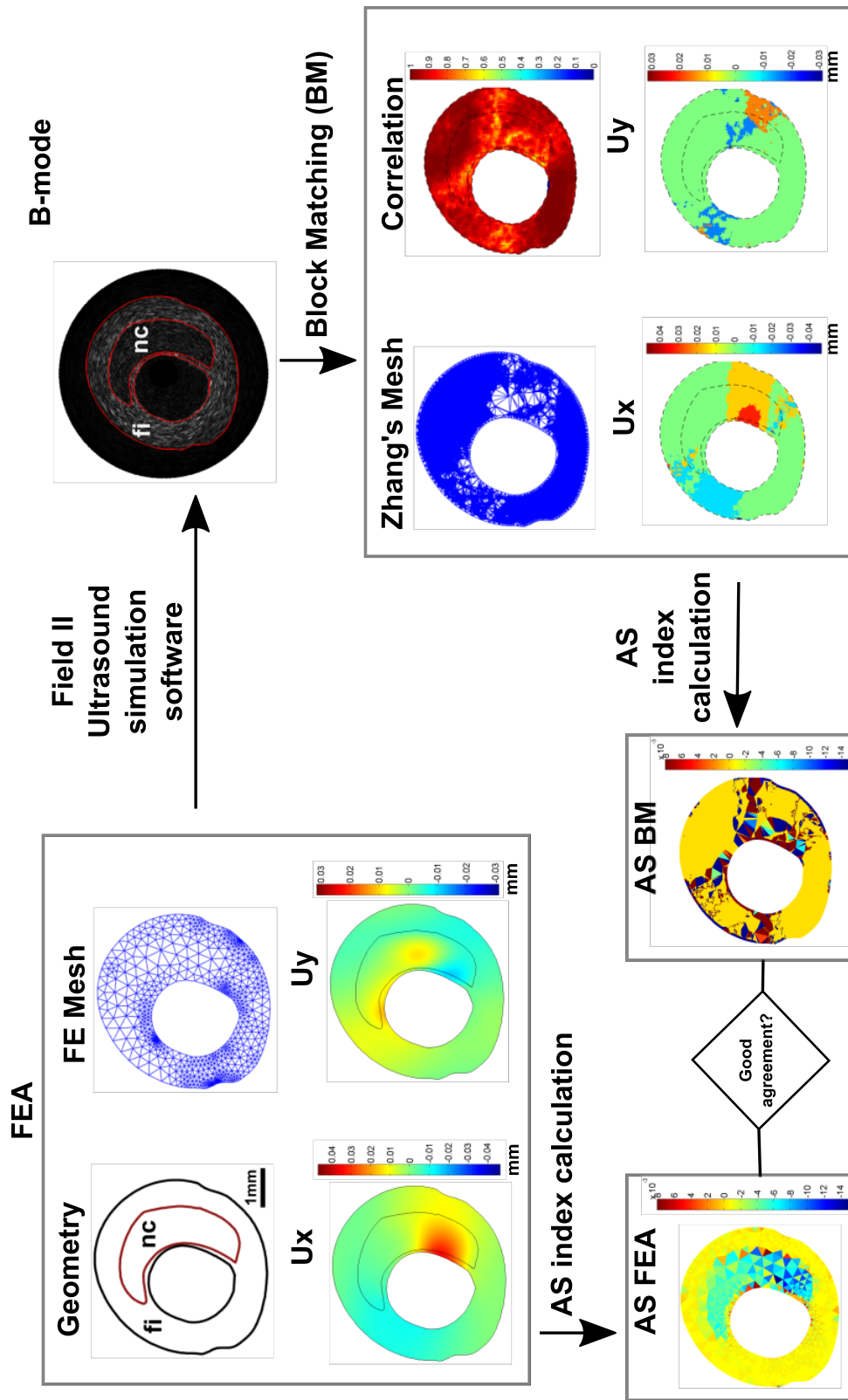


Figure 2.6: Performance of the b-mode based algorithm of Zhang in a plaque with a necrotic core (Plaque# 13). First, a Finite Element Analysis (FEA) is performed using the contours of the arterial geometry and the exact displacement maps U_x and U_y are computed. Then, using the Field II ultrasound simulation software, b-mode images of the plaque are synthesized. These images are used with the Block Matching (BM) algorithm to obtain the estimated displacement maps U_x and U_y . The points with a correlation higher than 0.9 are used to create a triangular element mesh that we call Zhang's mesh. Using Zhang's mesh and the U_x and U_y maps estimated with the BM algorithm, the Area Strain (AS) index is calculated for each element in the mesh. Finally, this estimated BM AS map is compared to the exact AS FEA map obtained using the FE Mesh and the exact FE U_x and U_y maps.

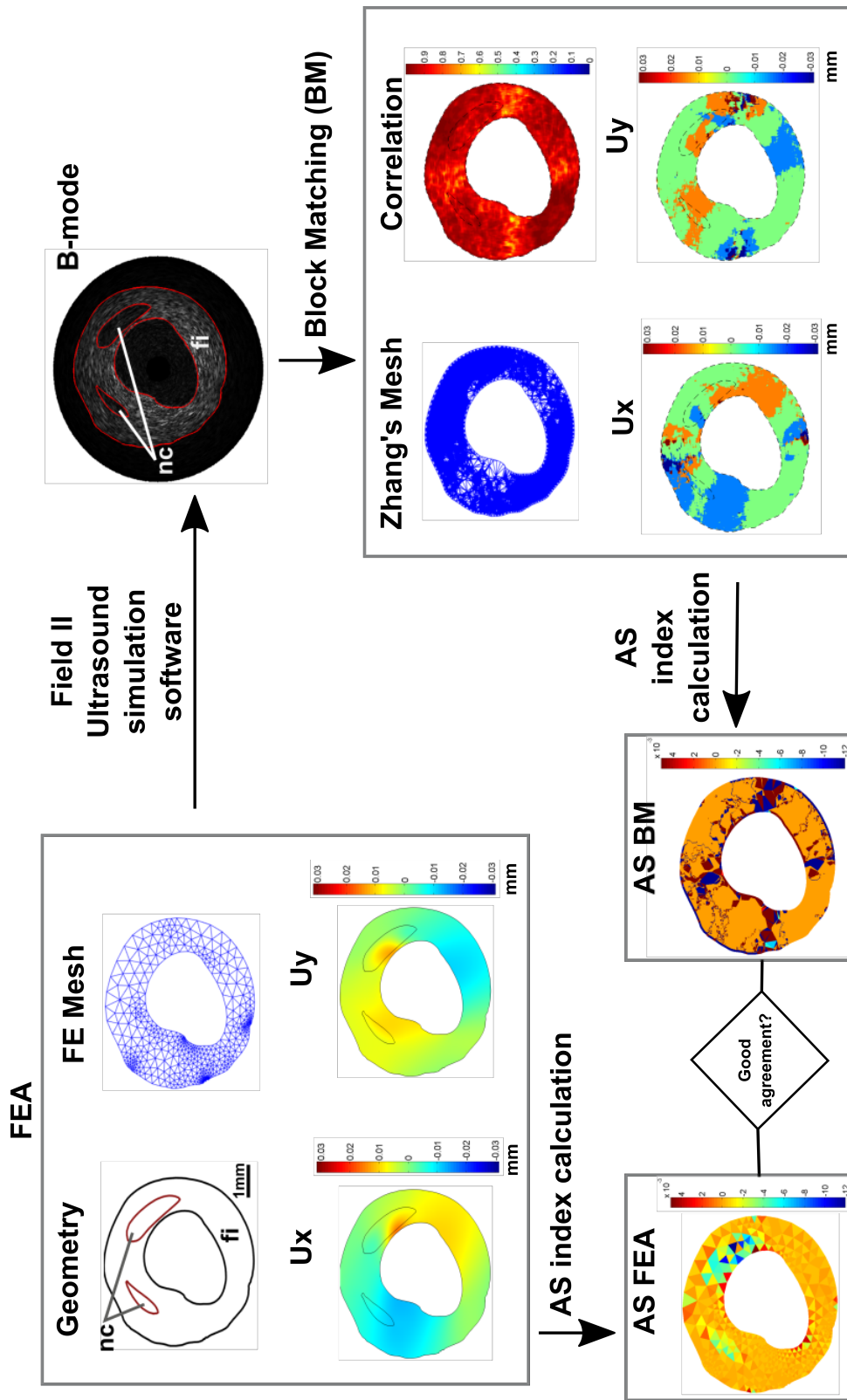


Figure 2.7: Performance of the b-mode based algorithm of Zhang in a plaque with two necrotic cores (Plaque# 16). First, a Finite Element Analysis (FEA) is performed using the contours of the arterial geometry and the exact displacement maps U_x and U_y are computed. Then, using the Field II ultrasound simulation software, b-mode images of the plaque are synthesized. These images are used with the Block Matching (BM) algorithm to obtain the estimated displacement maps U_x and U_y . The points with a correlation higher than 0.9 are used to create a triangular element mesh that we call Zhang's mesh. Using Zhang's mesh and the U_x and U_y maps estimated with the BM algorithm, the Area Strain (AS) index is calculated for each element in the mesh. Finally, this estimated BM AS map is compared to the exact AS FEA map obtained using the FE Mesh and the exact FE U_x and U_y maps.

2.4.2 Area strain calculations

Area strain (AS) values were calculated using the triangular mesh that resulted from applying the Delaunay process to the points where $CC > 0.9$ and the BM results. The triangular mesh used for calculating AS from the FE model results was a coarse mesh of the geometry assuming a homogeneous plaque. Although there were some small sections of the necrotic cores that the BM- AS was able to highlight, no clear features could be differentiated with the AS results from the tested algorithm. However, AS calculations based on the FE model displacements (Figures. 2.5, 2.6 and 2.7) highlight high-strain areas corresponding to the locations of the necrotic cores. These results suggest that AS index could be used to highlight vulnerable plaques and that Zhang's approach needs to be revisited and improved.

2.5 Conclusions

By analyzing simulated IVUS sequences from plaques with one or two soft inclusions, we could observe the performance of an IVUS grayscale-based algorithm to create displacement maps. The block matching algorithm was able to capture the general displacement of the plaque, but the b-mode images lacked the necessary resolution to extract viable displacement estimations.

Although the block-matching algorithm could be improved with pre-processing filtering stages to enhance contrast and reduce noise, or by adapting the block and search area size parameters, the noise and low resolution of gray-scale images would still be a problem. While this could be potentially useful for observing the evolution of the plaque over time, b-mode images do not provide enough detail to assess plaque vulnerability.

Since BM algorithm did not provide good displacement estimations, the area strain (AS) maps were not satisfactory. However, the AS maps calculated using the finite element model results highlight the areas where the soft necrotic cores are located. This clearly indicates the potential of the AS index and the approach proposed by Zhang et al. (2011b) to highlight vulnerable plaques, when using more accurate displacement estimations.

Therefore, despite its more complex implementation, we conclude that, for now, the best alternative is to use IVUS RF-based algorithms that can evaluate plaque displacement and strain maps more precisely, which can in turn improve the calculation of mechanically-based indexes of plaque vulnerability to rupture.

Future works could implement Zhang's approach using RF-based displacement estimations that can improve the resulting AS maps. Due to time restrictions, this improvement is not covered in the present dissertation.

Therefore, we come back to the IVUS RF data in the following chapters (**Chapter 3** and **4**) and used the Lagrangian Speckle Model Estimator (LSME) method to obtain strain maps from IVUS. These maps are used as a base to calculate the apparent stiffness of the artery using a novel palpography technique to evaluate the anisotropic mechanical properties of the plaque (**Chapter 3** and **4**).

Chapter 3

A novel elasticity-palpography technique to characterize the anisotropic mechanical properties of healthy and pathological coronary vessels: theory and numerical feasibility

Based on the published paper:

Gómez, A., Tacheau, A., Finet, G., Lagache, M., Martiel, J.-L., Floc'h, S.L., Yazdani, S.K., Elias-Zuñiga, A., Pettigrew, R.I., Cloutier, G., Ohayon, J. (2019). Intraluminal Ultrasonic Palpation Imaging Technique Revisited for Anisotropic Characterization of Healthy and Atherosclerotic Coronary Arteries: A Feasibility Study. Ultrasound in Medicine & Biology, 45(1), 35-49.

ABSTRACT

Accurate mechanical characterization of coronary atherosclerotic lesions remains essential for the in vivo detection of vulnerable plaques (VPs). Using intravascular ultrasound (IVUS) strain measurements and based on the mechanical response of a circular and concentric vascular model, E.I. Céspedes, C.L. de Korte and A.F. van der Steen ([Céspedes et al., 2000](#)) developed an elasticity-palpography technique (E-PT) to estimate the apparent stress-strain modulus (S-SM) palpogram of the thick subendoluminal arterial wall layer (see **Chapter 1**). More recently, this approach has been improved by our group to consider the real anatomical shape of the VP ([Deleaval et al., 2013](#)) (see **Chapter 1**). Even though these two studies highlighted original promising approaches for improving the detection of VP, they did not overcome a main limitation related to the anisotropic mechanical behavior of the vascular tissue. The present study was therefore designed to extend the theoretical framework of the improved E-PT by considering the orthotropic mechanical properties of the arterial wall and lesion constituents. Based on the continuum mechanics theory prescribing the strain field, an elastic anisotropy index (AI) was defined. This new anisotropic E-PT (named AE-PT) was successfully applied to ten coronary plaques and one healthy vessel geometry of patients imaged in vivo with IVUS. Our results demonstrated that AI-palpograms were estimated with a good: i) accuracy (with a mean relative

error of 26.79 ± 48.84 %) when comparing to the exact ones, and ii) robustness with respect to the IVUS RF noise which induces a mean relative error of 10.24 ± 14.43 %.

3.1 Introduction

Morphologic and mechanical characterization of coronary atherosclerotic lesions remains an essential step for the diagnosis of rupture-prone plaques and subsequent thrombosis which is the leading cause of acute coronary syndrome responsible for the majority of cardiovascular deaths (Arbab-Zadeh et al., 2012; Benjamin et al., 2017; Fleg et al., 2012). Since the progression of the disease is usually silent and symptoms are presented only when the stenosis is severe or the plaque ruptures, many patients are made aware of their condition only after they experience high-risk manifestations (Naghavi et al., 2003; Alsheikh-Ali et al., 2010; Benjamin et al., 2017). The ability to produce an early diagnosis and to accurately identify vulnerable lesions is crucial in reducing the morbidity and mortality rates related to coronary artery disease.

To detect vulnerable plaques (VPs) in a timely manner and prevent adverse coronary events, several endovascular imaging techniques are available to clinicians or in development including intravascular ultrasound (IVUS) (Rioufol et al., 2002; Cheng et al., 2014), optical coherence tomography (OCT) (Sinclair et al., 2015), magnetic resonance imaging (Larose et al., 2005; Cavalcante and Larose, 2016), near infrared spectroscopy (NIRS) (Caplan et al., 2006; Madder et al., 2016), as well as emergent hybrid techniques that combine two or more imaging modalities (IVUS+X-ray, IVUS+OCT, OCT+NIRS, IVUS+fluorescent+photoacoustic among others), either by offline co-registration of the data acquired by the different modalities or through the use of dual-probe catheters that allow simultaneous plaque assessment with two imaging techniques (Abran et al., 2014; Bourantas et al., 2017). Despite these technological advances, identifying which VPs will rupture and induce an acute event has proven difficult and remains a challenging task.

Previous biomechanical studies have identified peak cap stress (PCS) amplitude as a strong indicator of plaque vulnerability to rupture (Finet et al., 2004; Ohayon et al., 2008; Tang et al., 2009; Gijssen and Migliavacca, 2014; Kok et al., 2016). Other research works have established that plaque rupture risk is not only the consequence of a thin-cap fibroatheroma (TCFA) but also of additional factors like the presence of microcalcifications in the TCFA (Kelly-Arnold et al., 2013; Cardoso and Weinbaum, 2014; Thondapu et al., 2016), plaque morphology (Ohayon et al., 2011; Akyildiz et al., 2016), hemodynamics (Gijssen et al., 2008; Ahmadi et al., 2016; Morbiducci et al., 2016), as well as tissue mechanical properties of the atherosclerotic lesion (Ohayon et al., 2014; Guo et al., 2017).

Although plaque morphology and cap thickness can be directly extracted from endovascular images, the stress distribution within the plaque is impossible to obtain using current medical imaging technologies. However, the local deformation (strain) of the arterial wall and plaque caused by the change in intraluminal pressure during the cardiac cycle can be calculated from a series of ultrasound images (Maurice et al., 2004a; Doyley, 2012; Golemati et al., 2016). Based on the postulate that local variations in the elastic properties of tissue are generally correlated to pathological regions, the strain-elastography, a strain-field based technique was developed. This approach was first introduced by Ophir and colleagues (Ophir et al., 1991; Cespedes et al., 1993) as a means to identify pathological tissue by its difference in mechanical strain response to an applied force. Nevertheless, complex non-linear geometric effects do not allow a direct correlation between the measured spatial strain field to the mechanical properties of the tissue. By using the IVUS strain field inside the atherosclerotic lesion (De Korte et al., 2002; Maurice et al., 2004b, 2007; Doyley, 2012), several plaque-elasticity reconstruction approaches have been developed to characterize the entire lesion (Baldewsing et al., 2006b; Le Floc'h et al., 2009, 2010; Richards and Doyley, 2011; Doyley, 2012; Le Floc'h et al., 2012; Deleaval et al., 2013; Richards

et al., 2015; Tacheau et al., 2016; Nayak et al., 2017; Poree et al., 2017) and to delineate a thick subendoluminal layer of the arterial wall called the palpography domain (Céspedes et al., 2000; Doyley et al., 2001; Schaar et al., 2005; Deleaval et al., 2013; Widynski et al., 2014). Both techniques aim to characterize the mechanical properties of atherosclerotic lesions and ultimately differentiate vulnerable from stable plaques.

In the latter approach, namely the elasticity-palpography technique (E-PT) developed by Céspedes et al. (2000) and Doyley et al. (2001) and improved by our group to account for the anatomic shape of the VP (Deleaval et al., 2013), the apparent local stiffness (also called the stress-strain modulus (S-SM) palpogram) of the thick subendoluminal arterial wall layer, the palpography domain, is computed assuming that all plaque constituents are elastically isotropic. of the subendoluminal arterial wall layer was computed assuming that all plaque constituents are elastically isotropic. Even though these studies highlighted promising results, they failed to address the anisotropic mechanical behavior of the arterial wall and atherosclerotic lesion (Holzapfel et al., 2005).

Therefore, the purpose of this study is to extend the theoretical framework of the elasticity-palpography technique implemented by Deleaval et al. (2013) to account for the anisotropic mechanical behavior of the arterial wall. Based on continuum mechanics theory prescribing the radial strain field, a new anisotropic elasticity-palpography technique (AE-PT) was successfully applied to five modeled plaque geometries, 10 coronary lesions and one healthy vessel of patients imaged in vivo with IVUS. An elastic anisotropy index (AI) was extracted. The robustness and performance of the new AE-PT were also investigated with respect to IVUS radio frequency (RF) noise, which may affect the assessment of plaque anisotropy and thus the identification of vulnerable plaques.

3.2 Materials and methods

3.2.1 IVUS study and plaque geometries

Patient population

Vulnerable plaque geometries were extracted from IVUS images acquired on patients referred for percutaneous coronary intervention at the Louis Pradel Cardiology Hospital of Lyon after a first acute coronary syndrome with troponin I elevation. Patients' consent was obtained and the study was approved by the ethical institutional review board of the Cardiology Hospital.

Intravascular ultrasound imaging

A set of one healthy and 10 non-ruptured plaque morphologies were collected from IVUS scans of the coronary arteries following the protocol described by Rioufol et al. (2002). All IVUS explorations were performed after intracoronary administration of 200 μg of nitroglycerine to avoid vasospasms. Cross-sectional IVUS images of the atherosclerotic lesions were recorded at sites exhibiting the thinner fibroatheroma cap or at sites with the largest degree of stenosis. IVUS scans were performed with the iLab platform (Boston Scientific, Watertown, MA) equipped with 40 MHz catheters (Atlantis SR Pro 3.6F, Boston Scientific). This IVUS system has a radial spatial resolution in B-mode of approximately 90 μm (Chopard et al., 2010).

3.2 Materials and methods

Table 3.1: Characteristics of the IVUS-detected and modelled atherosclerotic plaques and healthy artery used to test the performance of the proposed anisotropic elasticity-palpography technique. Cap_{thick} was randomly assigned (value in parentheses) when found to be under the limit of the B-mode spatial resolution obtained with the 40-MHz IVUS catheter (i.e., $< 90\mu\text{m}$).

Plaque no.	Origin of geometry	Cap thickness (μm)	Area (mm^2)		Plaque	Lumen	Stenosis (%)
			Necrotic core	Dense Fibrosis			
0	Model	-	-	-	14.14	1.77	89
1	Model	-	-	-	25.13	3.14	89
2	IVUS	93	1.36	-	8.74	2.79	76
2A	Model	200	1.36	-	8.74	2.79	76
2B	Model	400	1.36	-	8.74	2.79	76
2C	Model	600	1.36	-	8.74	2.79	76
Healthy 1	IVUS	-	-	-	8.45	11.87	42
11	IVUS	-	-	-	9.88	7.59	57
12	IVUS	<90 (55)	3.48	-	14.24	6.06	70
13	IVUS	<90 (63)	4.41	-	15.48	4.28	78
14	IVUS	<90 (49)	1.97	-	19.38	6.8	74
15	IVUS	<90 (48)	1.89	-	17.29	8.44	67
16	IVUS	100	1.41/0.46	-	19.5	7.67	72
17	IVUS	<90 (65)	2.20/0.53	-	29.53	4.34	87
18	IVUS	<90 (60)	-	1.36	6.34	5.99	51
19	IVUS	<90 (88)	-	0.9	5.31	5.35	50

IVUS image analysis and plaque morphological measurements

IVUS echogenicity aspects were used to characterize VP components according to the following observations: (i) highly hypo-echogenic components (or anechogenic zones), suggestive of quasi-cellular tissues (lipid or cellular deposition); or (ii) homogeneous reflective components, suggestive of organized or disorganized fibrosis (Di Mario et al., 1998). A manual segmentation procedure using ImageJ software (ImageJ, NIH, Bethesda, MD, USA) was performed by a cardiologist (G.Finet) to extract the internal (i.e. lumen) and external contours of the coronary cross-section, as well as the contours of each plaque component (i.e. necrotic core and dense fibrosis). The morphology of each cross-sectional IVUS lesion image was quantified for plaque area (Pla_{area} , mm^2), lumen area (Lu_{area} , mm^2), soft necrotic core area, dense fibrosis area, degree of stenosis ($Stenos_{deg}$, %) as $100 \times Pla_{area} / (Pla_{area} + Lu_{area})$ and cap thickness (Cap_{thick} , μm), which was defined as the shortest distance between the lumen and the necrotic core. These measurements are resumed in Table 3.1.

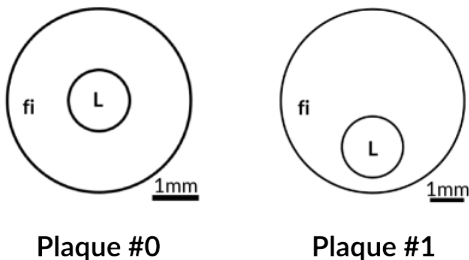


Figure 3.1: Contours of idealized concentric and eccentric plaques used to validate the theoretical background. L= lumen, fi= fibrosis.

Idealized geometries for validation of the AE-PT

First, one concentric and one eccentric idealized circular plaque geometries (plaques # 0 and # 1, respectively) with homogeneous anisotropic and quasi-incompressible atherosclerotic lesions were simulated to validate the theoretical background of the AE-PT (Fig. 3.1).

Patients' geometries

Once the theory was successfully validated with the idealized plaques, vulnerable plaque geometries from patients were used. These were acquired on patients referred for percutaneous coronary intervention at the Louis Pradel Cardiology Hospital of Lyon after a first acute coronary syndrome with troponin I elevation. Patients' consent was obtained and the study was approved by the institutional board of the Cardiology Hospital. From the 10 plaque geometries studied, 7 had necrotic inclusions, two had dense fibrosis inclusions and one lesion was homogeneous. Also, a healthy artery geometry was used to observe how the AE-PT performed on a normal artery. The contours of these real geometries are shown in Figure 3.2 and in Figure 3.3 for plaque # 2 and 2A to 2C.

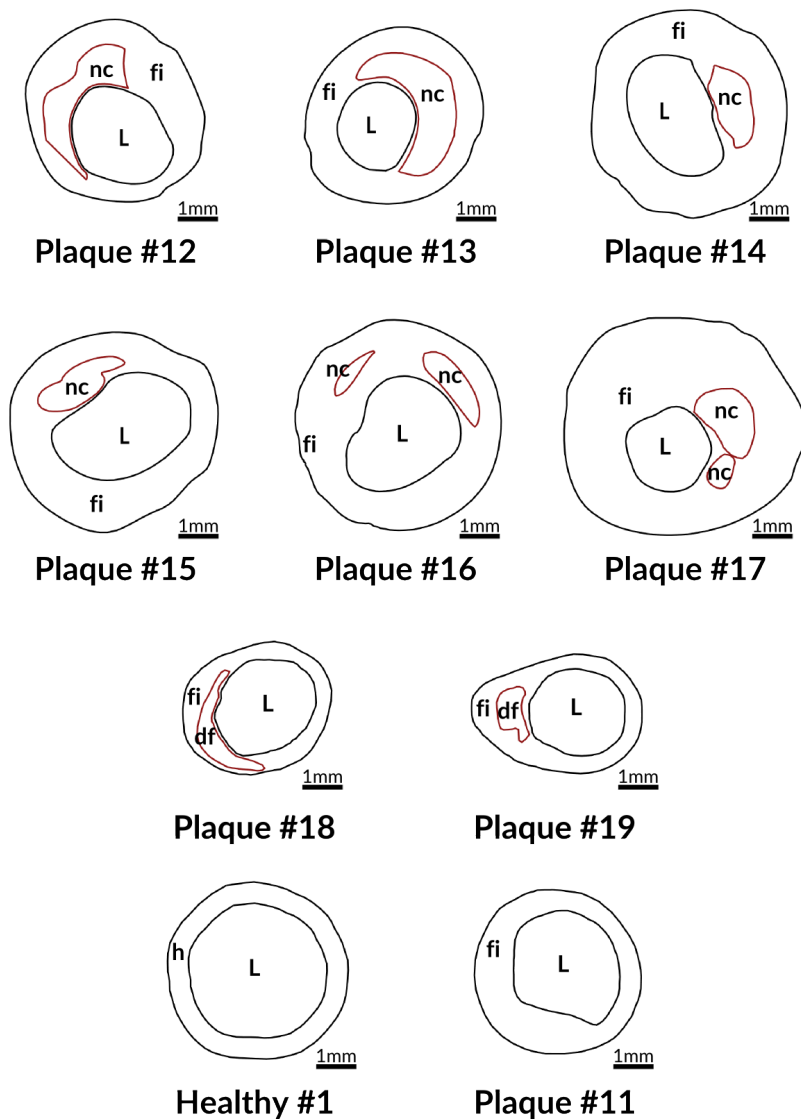


Figure 3.2: Contours of atherosclerotic plaques and constituents obtained from patients' IVUS images. L= lumen, fi= fibrosis, nc= necrotic core, df= dense fibrosis, h= healthy arterial tissue.

Idealized geometries to study the effect of Capthick

To study the effects of cap thickness (Cap_{thick}) on the resulting anisotropic elasticity palpogram, three idealized models were designed (plaques 2A, 2B and 2C), from one non-ruptured VP morphology acquired on a patient using IVUS (plaque 2). To mimic different degrees of vulnerability, the Cap_{thick} was increased from $93 \mu\text{m}$ (plaque 2) to 200, 400 and $600 \mu\text{m}$ in the idealized models (Fig. 3.3).

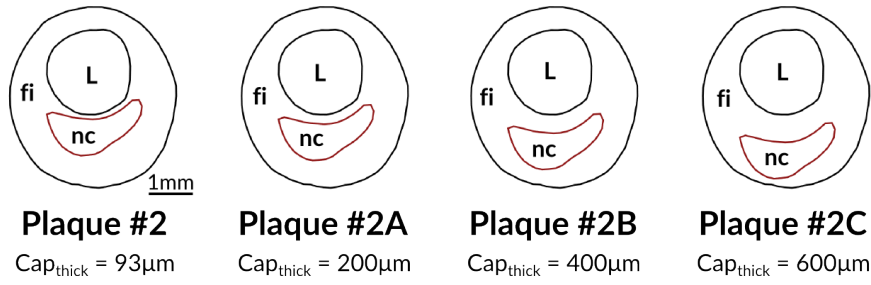


Figure 3.3: Real contour (plaque 2) of an atherosclerotic plaque with a necrotic core obtained from a patient's IVUS image. From this plaque, three modeled contours were built (plaques 2A-C) where the cap thickness (Cap_{thick}) increases from $93\mu m$ to $600\mu m$. L= lumen, fi= fibrosis, nc= necrotic core.

3.2.2 Forward problem: Spatial displacement and strain field distributions

3D finite element simulations

The 2D digitized contours obtained from the manual segmentation procedure of the lesions were transferred into the modeling and simulation software Comsol (Structural Mechanics Module, version 4.3b, Comsol, France). To compute the deformed shape, a 3-D static finite element (FE) simulation was conducted on each thin-sliced (slice thickness = 0.1mm) volumetric plaque obtained by extrusion of the cross-sectional plaque profile in the longitudinal direction of the artery. The obtained 3-D geometry of each plaque was meshed with approximately 5,000 six-Node Prism elements. The barycenter (i.e the center of mass) of the luminal area was used as the origin of the cylindrical coordinate system (R, θ, Z).

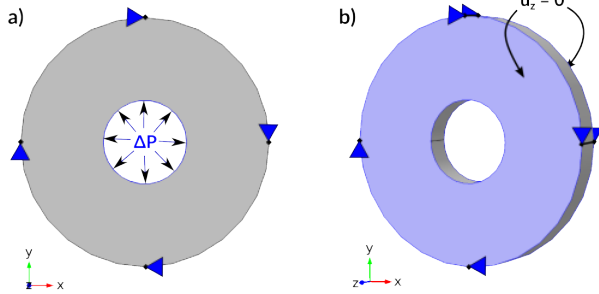


Figure 3.4: Boundary conditions applied for the FE simulations. a) Pressure was applied to the lumen boundary and the external boundary was left free. b) The edges corresponding to the four cardinal points were constrained in the circumferential direction and sliding conditions were imposed on the two cross-sections of the vessel segment.

cardiac cycle (Le Floc'h et al., 2009, 2012). The pressure difference was adjusted between the above values to achieve a radial strain close to 2%. The exact pressure applied for each case can be found in Table 3.2.

For these FE simulations, a free boundary condition was assumed at the external wall of the artery and sliding conditions were imposed on the two cross-sections of the vessel segment ($R-\theta$ planes, $Z=0$ and 0.1 mm). Such boundary conditions constrain the deformation to take place in the planes where $Z = a$ constant (see Fig. 3.4). Additionally, displacement limitations were placed upon nodes located on the four cardinal directions of the external wall of the artery to avoid rigid rotations. These latter boundary conditions allow free-radial expansion of the vessel

during pressure loading resulting in more realistic vessel inflation kinematics.

Table 3.2: Pressure applied inside the lumen for the FE simulations. Pressure values equivalent to the pressure change between two IVUS frames and are adjusted to achieve a radial strain close to 2%

Plaque no.	0	1	2-2C	Healthy	1	11	12	13	14	15	16	17	18	19
ΔP (kPa)	1	1	1	0.3	0.3	3	1	1	0.3	0.5	0.3	0.8	0.3	

The orthotropic initial mechanical properties measured by [Holzapfel et al. \(2005\)](#) for the quasi-incompressible pathologic coronary thick intima layer were considered in our FE simulations to model the fibrotic plaque medium: Young's moduli $E_R = 360$ kPa, $E_\theta = 230$ kPa, $E_Z = 330$ kPa, shear's moduli $G_{R\theta} = G_{RZ} = G_{\theta Z} = 30$ kPa and Poisson's ratios $\nu_{\theta R} = 0.471$, $\nu_{ZR} = 0.241$ and $\nu_{Z\theta} = 0.759$ ([Chagnon et al., 2017](#)). The healthy coronary arterial wall was assumed to be quasi-incompressible orthotropic (Appendix A) and the following initial material constants measured by [Holzapfel et al. \(2005\)](#) for the coronary adventitia layer were used for our simulations: $E_R = 120$ kPa, $E_\theta = 80$ kPa, $E_Z = 170$ kPa, $G_{R\theta} = G_{RZ} = G_{\theta Z} = 12$ kPa, $\nu_{\theta R} = 0.897$, $\nu_{ZR} = 0.402$ and $\nu_{Z\theta} = 0.103$. The mechanical properties of the dense fibrosis and soft necrotic cores were considered as isotropic and quasi-incompressible (Poisson ratio $\nu = 0.49$) with Young's moduli $E_{dense-fib} = 1500$ kPa and $E_{core} = 5$ kPa, respectively ([Lee et al., 1991](#); [Loree et al., 1994](#)). These mechanical properties are summarized in Table 3.3.

Table 3.3: Orthotropic and isotropic mechanical properties and anisotropy index values assigned for the healthy wall, fibrous plaque, dense fibrosis and soft necrotic core inclusions.

Medium	Young's Moduli (kPa)			Anisotropic Index AI (kPa)	Reference (Medium)
	E_R	E_θ	E_Z		
Healthy wall	120	80	170	121.8	Holzapfel et al. (2005) (Adventitia)
Pathological wall					
Fibrous plaque	360	230	330	384.3	Holzapfel et al. (2005) (Thick intima)
Dense fibrosis*		1500		2000	Loree et al. (1991)
Necrotic core*		5		6.7	Lee et al. (1999)

*Isotropic ($E_R = E_\theta = E_Z$)

Simulation of ultrasound images

The results of the previously described FE simulation — displacement and stress fields, and exact radial strain field $\varepsilon_{RR}^*(R, \theta)$ — not only serve as a reference for our study but are also used to generate the simulated IVUS images that were later processed to obtain the estimated displacement fields and the estimated radial strain field $\varepsilon_{RR}(R, \theta)$.

To generate these images, the open source software FieldII ([Jensen and Svendsen, 1992](#)) was modified to simulate the IVUS acoustic field ([Fromageau et al., 2003](#); [Nayak et al., 2017](#); [Poree et al., 2017](#)). Briefly, blood, fibrotic plaque, soft necrotic core and non-arterial surrounding tissue were characterized by their acoustic scattering amplitude. Acoustic models were built by randomly distributing scatterers over each non-deformed medium. The relative acoustic scatterer amplitudes of blood, necrotic core, fibrotic plaque and dense fibrosis were set to 10%, 15%, 35% and 60 %, respectively ([Maurice et al., 2004b](#); [Le Floc'h et al., 2010](#); [Cardoso and](#)

Weinbaum, 2014). First, an IVUS image of the non-deformed state (i.e. Im^i) was created. Then the displacement field resulting from the FE simulation was used to track the location of scatterers and to create the post-deformation IVUS image (i.e. Im^{i+1}). A single rotating piezo-electric element was modeled. An incremental circumferential rotation step of 0.7 degrees was set to get 512 lines of RF signal for IVUS image reconstruction. The piezo-electric element had a diameter of $600\mu\text{m}$ and a central emission frequency set to 40MHz. A sampling frequency of 400MHz was mimicked to represent the RF signal. These values were chosen according to the SVMH HD IVUS system device (ACIST Medical Systems, Eden Prairie, MN, USA). The arterial wall was also adjusted to set the centroid of the lumen coincident with the probe location.

Intravascular strain elastography

Sequences of simulated RF images were processed using the Lagrangian speckle model estimator (LSME). Radial strain fields were computed using a two-step strain imaging algorithm (Maurice et al. 2004a; Maurice et al. 2005; Maurice and Bertrand 1999; Poree et al. 2017). First, a block matching method provides local registration on overlapping sub-windows (measurement windows - MWs). It allows compensating for rigid translation movements using a 2-D cross correlation coefficient. Once MW locations have been registered, the 2-D-deformation matrix is estimated. Estimation is based on the resolution of a first-order optical flow equation for each MW (Majdoulina et al., 2014). Sizes of MWs in radial and circumferential directions were set to 101 pixels (about $192.5\mu\text{m}$) and 21 pixels (about 14.7°). Overlapping between MWs was set with a spacing parameter of 1 pixel in the radial direction and 1 pixel in the circumferential direction. Such values optimized the performance of the LSME algorithm for our ultrasound data acquired at 40 MHz (Maurice et al., 2004a). As a result, we obtained the IVUS estimated radial strain distribution $\varepsilon_{RR}(R, \theta)$. A diagram summarizing the calculation of the spatial displacement and strain field distributions is shown in Figure 3.5.

3.2.3 Inverse Problem: The Anisotropic Elasticity-Palpography Technique

To account for the orthotropic mechanical properties of the vascular tissues, we extended the isotropic E-PT formulations of Deléaval et al. (Deleaval et al., 2013) by defining an elastic anisotropy index (AI) as the ratio of the averaged difference between the radial and circumferential stresses (σ_{RR} and $\sigma_{\theta\theta}$) over the averaged radial strain (ε_{RR}) along the radial axis:

$$AI(\theta) = \frac{\int_{R_i(\theta)}^{R_p(\theta)} \{\sigma_{RR}(R, \theta) - \sigma_{\theta\theta}(R, \theta)\} dR}{\varepsilon(R, \theta)} \quad (3.1)$$

with

$$\varepsilon(\theta) = \int_{R_i(\theta)}^{R_p(\theta)} \varepsilon_{RR}(r, \theta) dR \quad (3.2)$$

where $R_i(\theta)$ and $R_p(\theta)$ are the inner and outer radii of the considered palpography domain, respectively. Appendix B provides the details of the computation of this index.

Note that the amplitude of $AI(\theta)$ remains constant and equal to:

$$AI(\theta) = E_R^0 \left[1 - \frac{1}{4} \left(1 - \frac{E_R^0}{E_\theta^0} + \frac{E_R^0}{E_Z^0} \right) \left(1 + \frac{E_Z^0}{E_R^0} - \frac{E_Z^0}{E_\theta^0} \right) \right]^{-1} \quad (3.3)$$

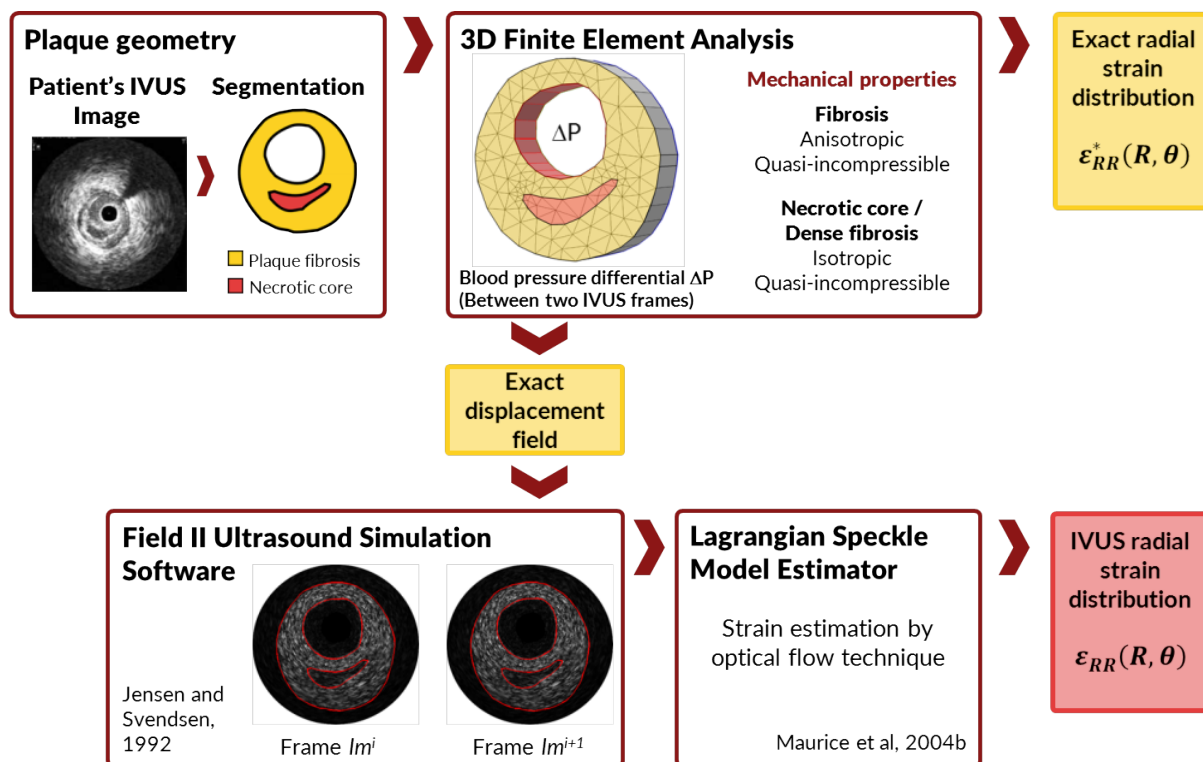


Figure 3.5: Diagram for the process to obtain the spatial displacement and strain field distributions. First, the contours of the plaque constituents were extracted from IVUS images and used to create a 3-D model. A pressure gradient equivalent to the one between two IVUS frames was applied inside the lumen and the resulting radial strain distribution within the plaque was extracted ($\varepsilon_{RR}^*(R, \theta)$). This exact radial strain distribution was used as an input for the ultrasound simulation software Field II to obtain simulated RF IVUS frames. Later, the Modified lagrangian speckle estimator (MLSME) technique was used to estimate the radial strain distribution $\varepsilon_{RR}(R, \theta)$, as it would do when applied directly to patient's RF data.

when considering a homogeneous pathologic lesion made of the same incompressible orthotropic medium (i.e. when $E_R(R, \theta) = E_R^0$, $E_\theta(R, \theta) = E_\theta^0$ and $E_Z(R, \theta) = E_Z^0$), whatever the plaque geometry and the palpography domain Ω_{palpo} considered (with $R_i(\theta) \leq R \leq R_p(\theta)$).

For a homogeneous incompressible transversely isotropic lesion (i.e. when $E_R(R, \theta) = E_R^0$ and $E_Z(R, \theta) = E_\theta(R, \theta) = E_\theta^0$), the AI amplitude is reduced to the constant:

$$AI = \frac{4E_R^0}{E_R^0 - E_\theta^0} \quad (3.4)$$

and to $AI = 4E/3$ for a homogeneous incompressible isotropic plaque (i.e. when $E_R(R, \theta) = E_\theta(R, \theta) = E_Z(R, \theta) = E$).

Table 3.3 gives the amplitudes of the AI for the considered mechanical properties of the adventitia (healthy arterial wall), thick intima (fibrotic plaque), dense fibrosis and soft necrotic media.

Method used to verify the accuracy of the anisotropic elasticity-palpography technique

Two anisotropy index palpograms were computed; the first, $AI(\theta)$, with the estimated radial strain elastogram $\varepsilon_{RR}(R, \theta)$ and the second, $AI^*(\theta)$ considering the exact radial strain map

$\varepsilon_{RR}^*(R, \theta)$. To investigate the accuracy of each palpogram (i.e. $AI(\theta)$ and $AI^*(\theta)$), we compared them with the exact circumferential distribution of the averaged anisotropic material constant $C(R, \theta)$ along the radial axis :

$$AI = \frac{1}{R_p(\theta) - R_i(\theta)} \int_{R_i(\theta)}^{R_p(\theta)} C(R, \theta) dR \quad (3.5)$$

and we computed the two following mean relative anisotropy index errors (MR_{error}^{AI} and $MR_{error}^{AI^*}$):

$$MR_{error}^{palpo}(\%) = \frac{100}{2\pi} \int_{\theta=0}^{2\pi} \left| \frac{palpo(\theta) - AI^{exact}(\theta)}{AI^{exact}(\theta)} \right| d\theta, \text{ with } palpo = AI, AI^* \quad (3.6)$$

$MR_{error}^{AI^*}$ indicates the best accuracy that could be reached when using the new anisotropic palpography technique, while MR_{error}^{AI} quantifies the cumulative error induced by both the proposed palpography technique and the estimated radial strain-elastogram. Therefore, to quantify the error only induced by the radial strain estimation on the AI-palpogram, we defined the following mean relative error (MR_{error}^{AI/AI^*}):

$$MR_{error}^{AI/AI^*}(\%) = \frac{100}{2\pi} \int_{\theta=0}^{2\pi} \left| \frac{AI(\theta) - AI^*(\theta)}{AI^*(\theta)} \right| d\theta \quad (3.7)$$

3.3 Results

3.3.1 IVUS Study

Seven non-ruptured VPs with soft necrotic cores, one homogeneous plaque, two atherosclerotic lesions with dense fibrosis inclusions, and one non-pathologic cross section were identified after extensive IVUS scanning. The geometric characteristics of these 11 cross sections scanned in vivo are summarized in Table 3.1. All computed AI-palpograms presented in the figures were obtained from radial strain elastograms estimated from sequences of simulated RF images.

3.3.2 Performance of the Anisotropic Elasticity-Palpography Technique

Validation cases, AI-palpogram accuracies and RF noise effects

Simulations on the idealized concentric and eccentric plaque geometries with homogeneous orthotropic and quasi-incompressible fibrotic atherosclerotic plaques were performed first (Fig. 3.6). AI-palpograms computed with the AE-PT for the concentric and eccentric plaques remain almost constant with mean values (\pm standard deviation [SD]) of 395.78 ± 8.78 kPa and 393.82 ± 14.31 kPa, respectively - which is also close the expected theoretical value ($AI = 384.34$ kPa, Table 3.3) given by Eq. 3.3 - even in the high-strained free-plaque arc length of the eccentric plaque geometry which is the thinnest region of the palpography domain (i.e. between the angular positions 180 and 360 degrees, Figs. 3.6e and 3.6f). The small amplitudes of the mean relative anisotropy index errors ($MR_{error}^{AI} = 3.08$ % and 3.70 %) together with the small

amplitudes of the standard deviations ($SD = 1.62\%$ and 2.08%) highlight the robustness of the AE-PT algorithm with respect to the IVUS RF sequences when estimating AI-palpograms for concentric and eccentric plaque morphologies, respectively. More generally, our results revealed that all 18 AI-palpograms were estimated with a reasonable accuracy (with a mean relative error of $26.79 \pm 48.84\%$) when compared with the exact ones, and with a good robustness with respect to the estimated strain elastogram which induces a mean relative error of $10.24 \pm 14.43\%$ (Table 3.4).

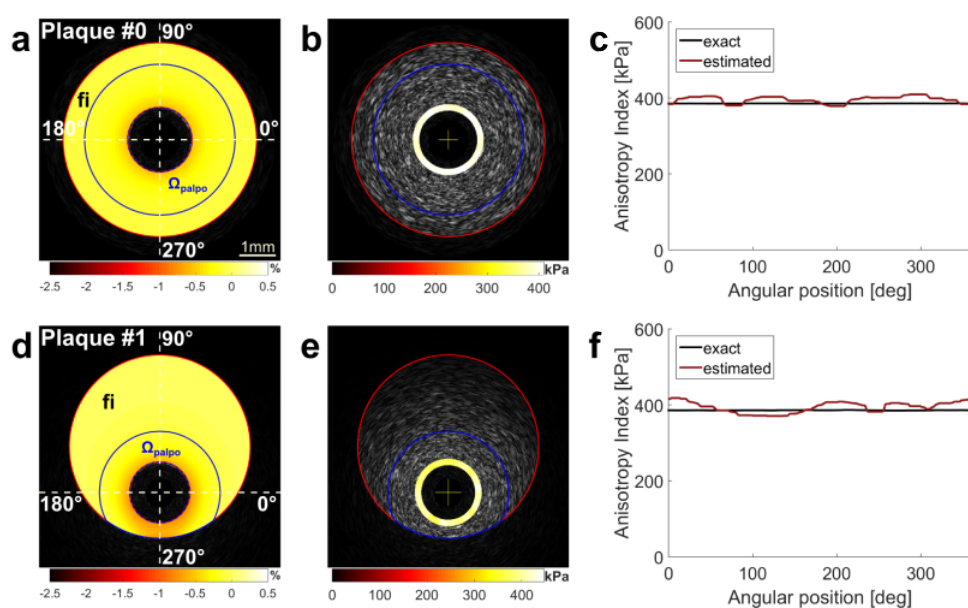


Figure 3.6: Performance of the anisotropic elasticity-palpography technique on idealized homogeneous concentric and eccentric plaque models (plaques 0 and 1, respectively). **a,d**) Plaque geometries (red contours), palpography domains (blue contours) and estimated radial strain maps **b,d**) IVUS images with AI-palpograms. **c,f**) Comparisons between exact and estimated $AI(\theta)$ palpograms. fi = fibrotic plaque region.

Detection and characterization of vulnerable plaques with soft inclusions

AI-palpograms computed for VPs with one (plaques 2, 2A to 2C and 12 to 15, Figs. 3.7 and 3.11) and two distinct (plaques 16 and 17, Fig. 3.8) necrotic cores are also presented. These AI-palpograms were estimated with a mean relative error of $34.36 \pm 57.03\%$ (Table 3.4). Locations of the necrotic core sites were accurately detected using the AE-PT. For these VPs, the AI-palpogram amplitudes were found close to the AI value of the fibrotic plaque (i.e close to 384.3 kPa, Table 3.3) except at soft inclusion locations, for which the AI amplitudes were found significantly lower, as expected. Figures 3.7 and 3.8 illustrate the ability of the proposed AE-PT to accurately detect soft inclusions.

Detection and characterization of stable plaques with dense fibrosis inclusions

For one stable plaque (plaque 19, Fig. 3.9 and plaque 18 Fig. 3.20) with one isolated dense fibrosis inclusion, the proposed palpography technique detected and distinguished the fibrotic plaque from dense fibrosis. Compared to the exact value, the estimated AI amplitude at the dense fibrosis inclusion location was underestimated by almost a factor of 2 (plaque 18 Fig. 3.20).

3.3 Results

Table 3.4: Accuracy of the proposed anisotropic elasticity-palpography technique and effect of estimated radial strain-elastogram (computed with a measurement window size of (101 pixels x 21 pixels)) on the estimated AI-palpograms (see Eqs. 3.6 and 3.7 for definitions of the mean relative errors MR_{error}^{AI} , $MR_{error}^{AI^*}$ and MR_{error}^{AI/AI^*}). Palpography thickness is 1mm unless otherwise indicated in parentheses beside the plaque number. SD= standard deviation.

Plaque no.	NC	DF	H	$MR_{error}^{AI^*}$ (%)	MR_{error}^{AI} (%)	MR_{error}^{AI/AI^*} (%)
0	-	-	✓	0.22 ± 0.14	3.08 ± 1.62	2.9 ± 1.49
1	-	-	✓	3.72 ± 1.72	3.7 ± 2.08	4.24 ± 3.2
2	✓	-	-	4.86 ± 4.53	13.41 ± 9.45	8.76 ± 6.06
2A	✓	-	-	5.97 ± 5.26	11.13 ± 7.9	5.53 ± 4.28
2B	✓	-	-	3.74 ± 2.29	7.84 ± 4.35	4.22 ± 3.06
2C	✓	-	-	1.91 ± 1.55	5.05 ± 3.85	4.03 ± 2.79
Healthy 1	-	-	✓	0.65 ± 0.5	10.03 ± 7.67	10.49 ± 7.66
11	-	-	✓	2.45 ± 2.24	6.66 ± 3.55	5.91 ± 3.43
12	✓	-	-	21.71 ± 27.64	33.16 ± 52.64	16.4 ± 19.1
13 (0.75)	✓	-	-	66.6 ± 52.63	83.23 ± 71.73	16.1 ± 21.47
13	✓	-	-	59.43 ± 57.53	74.14 ± 67.96	15.98 ± 18.61
13 (1.25)	✓	-	-	36.96 ± 41.17	46.45 ± 55.68	15.84 ± 17.44
14	✓	-	-	35.21 ± 62.45	44.87 ± 78.06	9.96 ± 11.05
15	✓	-	-	35.54 ± 73.87	45.19 ± 92.07	8.49 ± 7.47
16	✓	-	-	8.72 ± 9.57	14.46 ± 17.38	8.11 ± 9.05
17	✓	-	-	24.86 ± 22	33.3 ± 33.19	8.36 ± 9.24
18	-	✓	-	11.32 ± 12.96	35.34 ± 31.27	29.5 ± 31.75
19	-	✓	-	3.76 ± 6.38	11.25 ± 8.91	9.43 ± 6.69
Mean \pm SD				18.2 ± 37.99	26.79 ± 48.84	10.24 ± 14.43

NC : necrotic core, DF : dense fibrosis, H : homogeneous

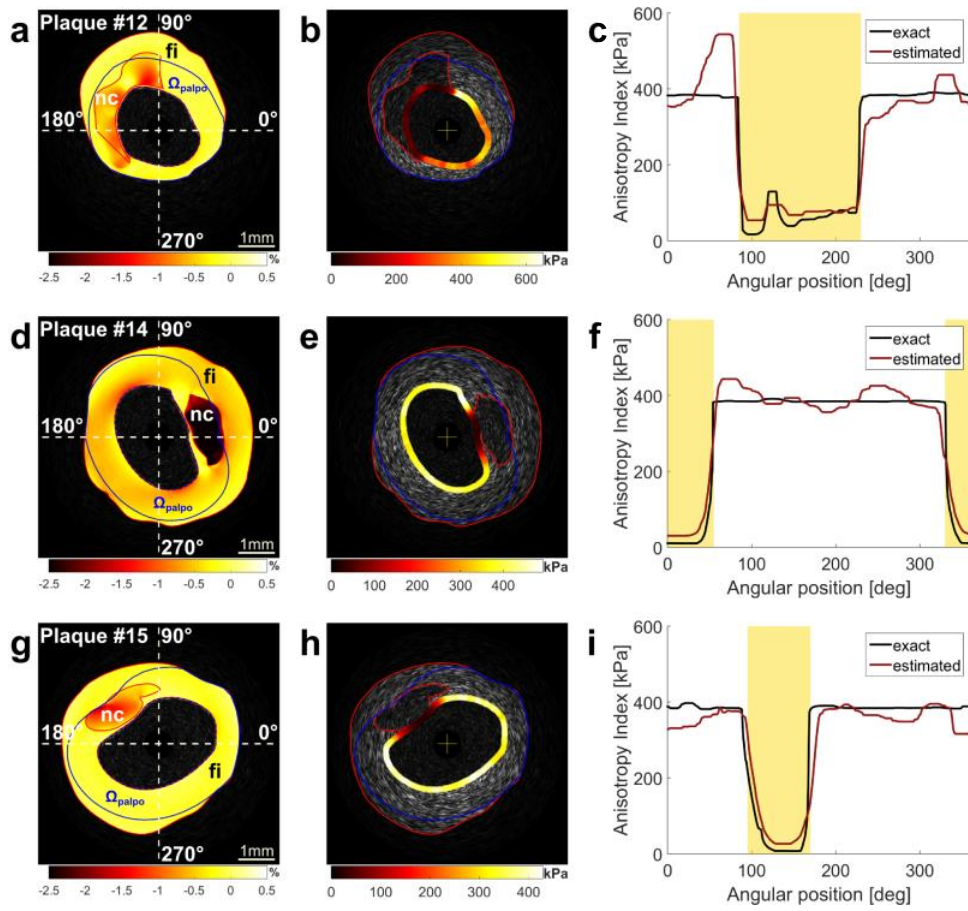


Figure 3.7: Performance of the anisotropic elasticity-palpography technique to detect vulnerable plaques with one necrotic core (plaques 12, 14 and 15). **a, b, c)** Plaque geometries (red contours), palpography domains (blue contours) and estimated radial strain maps. **b, e, h)** IVUS images with AI-palpograms. **c, f, i)** Comparisons between exact and estimated $AI(\theta)$ palpograms. Areas shaded in yellow indicate the location of the necrotic core.

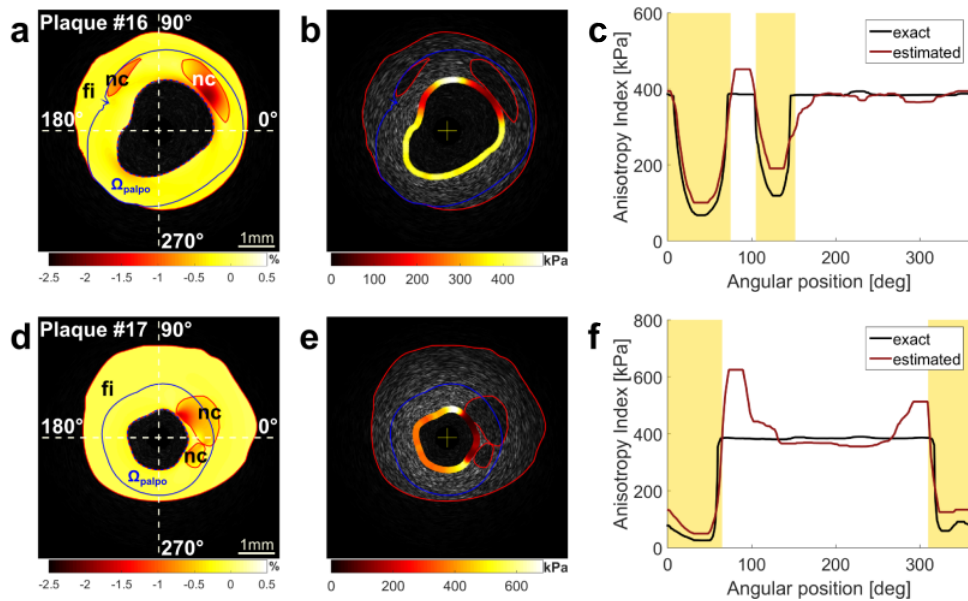


Figure 3.8: Performance of the anisotropic elasticity-palpography technique to detect vulnerable plaques with two necrotic cores (plaques 16 and 17). **a, d)** Plaque geometries (red contours), palpography domains (blue contours) and estimated radial strain maps. **b, e)** IVUS images with AI-palpograms. **c, f)** Comparisons between exact and estimated $AI(\theta)$ palpograms. Areas shaded in yellow indicate the locations of the two necrotic cores.

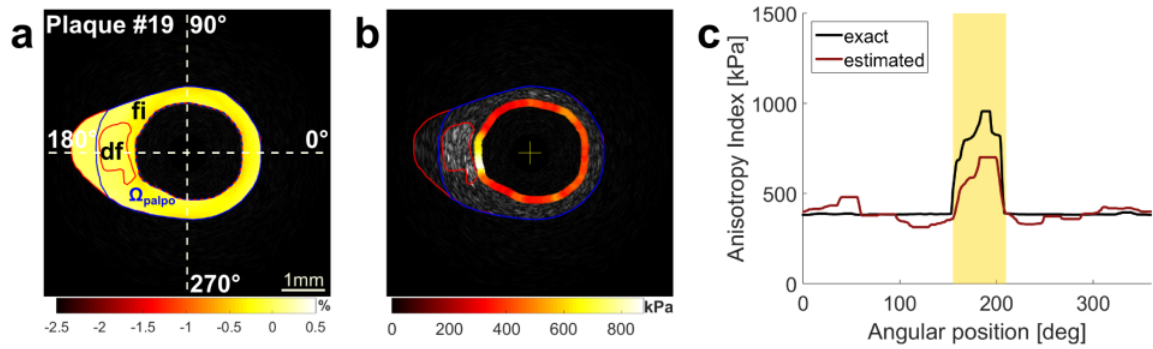


Figure 3.9: Performance of the anisotropic elasticity-palpography technique to detect a stable plaque with one dense fibrosis inclusion (plaque 19). **a)** Plaque geometry (red contour), palpography domain (blue contour) and estimated radial strain map. **b)** IVUS images with AI-palpogram. **c)** Comparison between exact and estimated $AI(\theta)$ palpograms. The area shaded in yellow indicates the location of the dense fibrosis inclusion. df = dense fibrosis.

Detection and characterization of homogeneous stable plaques and healthy vessel wall

AI-palpograms were also computed for one eccentric homogeneous stable plaque (plaque 11, Fig. 3.10a-c) and one healthy coronary wall (healthy 1, Fig. 3.10d-f). The AE-PT successfully characterized the orthotropic mechanical properties of the pathologic lesion (made of fibrotic plaque tissue) and of the non-pathologic coronary artery. The two AI-palpograms were found almost constant with mean values (\pm SD) of 360.33 ± 15.07 kPa and 134.25 ± 9.4 kPa, respectively. Notice that these computed AI values were found close to the expected theoretical values given by Eq. (3): $AI = 384.3$ kPa and 121.8 kPa for the pathologic and healthy arteries, respectively (Table 3.3).

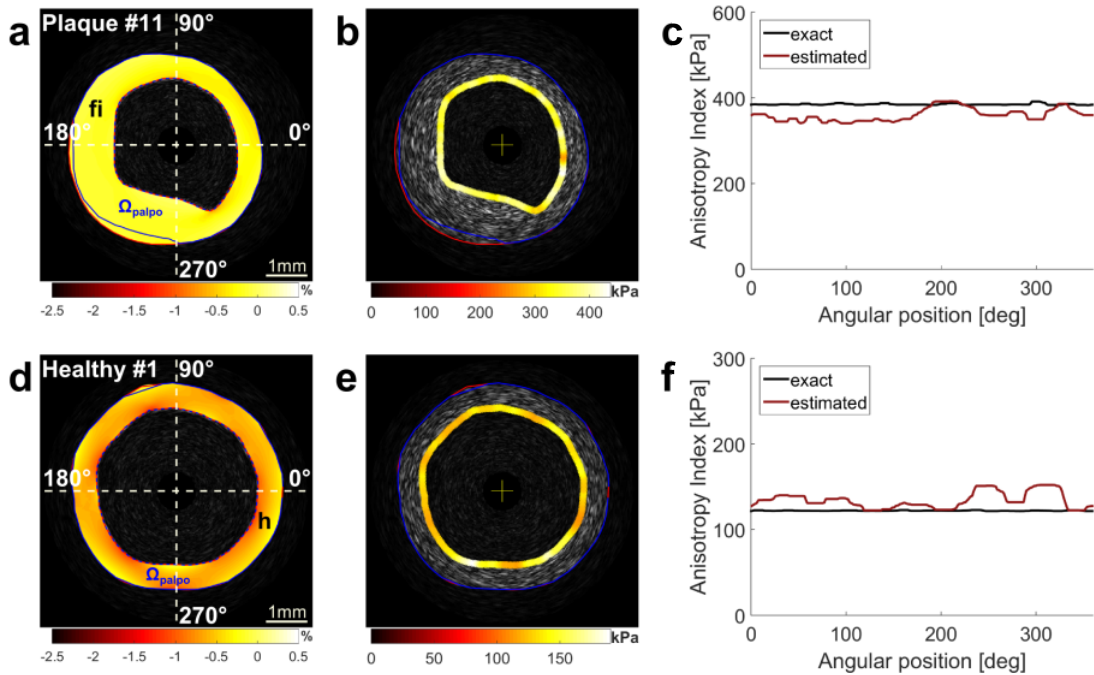


Figure 3.10: Performance of the anisotropic elasticity-palpography technique to detect a stable homogeneous fibrotic plaque (plaque 11) and a healthy coronary cross-section (healthy 1). **a,d)** Plaque/artery geometry (red contours), palpography domain (blue contours) and estimated radial strain map. **b,e)** IVUS image with the AI-palpogram. **c,f)** Comparison between the exact and the estimated $AI(\theta)$ palpograms.

Effects of Cap_{thick} on estimated AI-palpogram

For a given palpography domain, the cap thickness significantly affects the AI-palpogram at the soft inclusion location (plaques 2 and 2A to 2C, Fig.3.11). Simulations performed with the idealized VP models (Fig.3.3) in which the Cap_{thick} increases from 93 to 600 μm revealed that the mean AI amplitude at the location of the necrotic core increased from 138.5 ± 73.8 kPa for a $Cap_{thick} = 93$ μm to 300.12 ± 65.15 kPa for a $Cap_{thick} = 600$ μm (Table 3.5).

Table 3.5: Anisotropic Index values for different cap thicknesses (Cap_{thick}). Values for the exact ($AI^{exact}(\theta)$) and estimated indexes with the exact ($AI^{exact}(\theta)$) and estimated strain-palpograms ($AI^*(\theta)$).

Plaque	Cap_{thick} (μm)	$AI^{exact}(\theta)$ (kPa)	$AI^*(\theta)$ (kPa)	$AI(\theta)$ (kPa)
2	93	111.87 ± 61.43	120.69 ± 58.92	138.54 ± 73.88
2A	200	147.73 ± 74.56	161.56 ± 71.14	175.6 ± 78.94
2B	400	219.47 ± 82.13	228.78 ± 79.17	241.56 ± 81.51
2C	600	286.22 ± 64.44	285.01 ± 62.51	300.12 ± 65.15

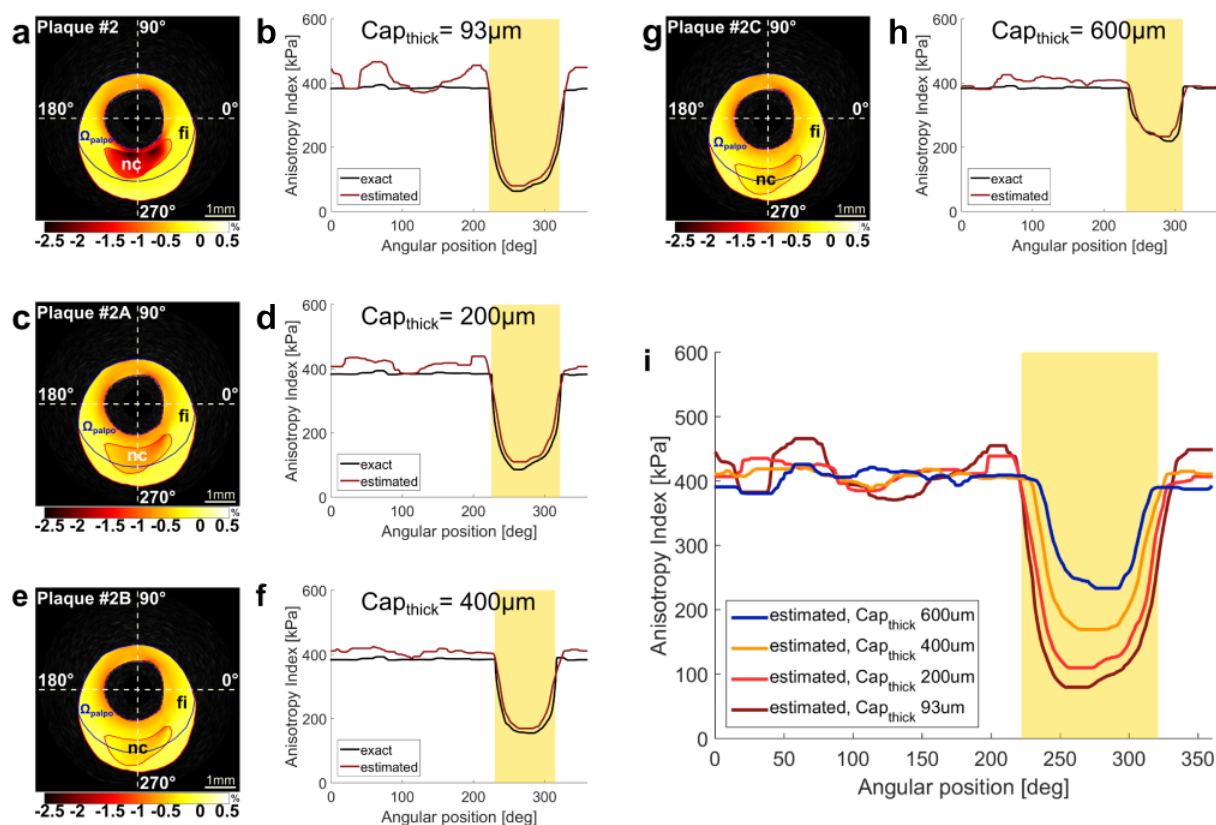


Figure 3.11: Effect of Cap_{thick} on the resulting anisotropic elasticity palpogram. Simulations were performed with plaque 2. **a, c, e, g** Plaque geometries (red contours), palpography domains (blue contours) and estimated radial strain maps. **b, d, f, h** Comparisons between exact and estimated $AI(\theta)$ palpograms. **i**) Comparison between all estimated AI-palpograms. Areas shaded in yellow indicate the location of the necrotic core. fi = fibrotic plaque region. nc = necrotic core.

Effects of the palpography domain size on estimated AI amplitude

We computed the AI-palpograms for the same VP considering three palpography domains with mean thicknesses of 0.75, 1 and 1.25 mm. This analysis was performed using one homogeneous idealized plaque (Fig.3.12) and 5 plaques with necrotic core inclusions (Figures 3.13, 3.14, 3.15, 3.16, 3.17). For all cases, increasing the palpography domain thickness from 0.75 mm to 1.25 mm improved the accuracy of the AI palpogram (see MR_{error}^{AI} on Table 3.6). For the plaques with soft inclusions, the location of the necrotic core sites were accurately detected using all palpography domains.

Table 3.6: Effect of palpography domain thickness ($\Omega_{palpo} = 0.75$ mm, 1 mm and 1.25 mm) on the accuracy of the anisotropic elasticity-palpography technique. All palpograms were computed with a measurement window size of 101 pixels x 21 pixels.

	Ω_{palpo} thickness	MR_{error}^{AI*} (%)	MR_{error}^{AI} (%)	$MR_{error}^{AI/AI*}$ (%)
Plaque 0	0.75	0.28 ± 0.17	3.57 ± 2.07	3.34 ± 1.89
	1	0.22 ± 0.14	3.08 ± 1.62	2.9 ± 1.49
	1.25	0.19 ± 0.13	2.7 ± 1.44	2.55 ± 1.33
Plaque 2	0.75	8.75 ± 9.98	17.75 ± 14.88	8.54 ± 6.38
	1	4.86 ± 4.53	13.41 ± 9.45	8.76 ± 6.06
	1.25	2.58 ± 2.95	10.12 ± 6.88	8.84 ± 6.01
Plaque 12	0.75	33.27 ± 34.76	45.08 ± 53.01	17.12 ± 19.21
	1	21.71 ± 27.64	33.16 ± 52.64	16.4 ± 19.1
	1.25	12.34 ± 18.46	22.96 ± 38.99	16.03 ± 18.05
Plaque 13	0.75	66.6 ± 52.63	83.23 ± 71.73	16.1 ± 21.47
	1	59.43 ± 57.53	74.14 ± 67.96	15.98 ± 18.61
	1.25	36.96 ± 41.17	46.45 ± 55.68	15.84 ± 17.44
Plaque 14	0.75	36.55 ± 59.14	49.84 ± 88.43	11.77 ± 14.29
	1	35.21 ± 62.45	44.87 ± 78.06	9.96 ± 11.05
	1.25	14.17 ± 18.62	19.9 ± 27.02	9.94 ± 9.66
Plaque 17	0.75	21.84 ± 17.94	32.39 ± 31.52	10.63 ± 10.67
	1	24.86 ± 22	33.3 ± 33.19	8.36 ± 9.24
	1.25	22.89 ± 22.77	29.67 ± 33.76	7.9 ± 8.58

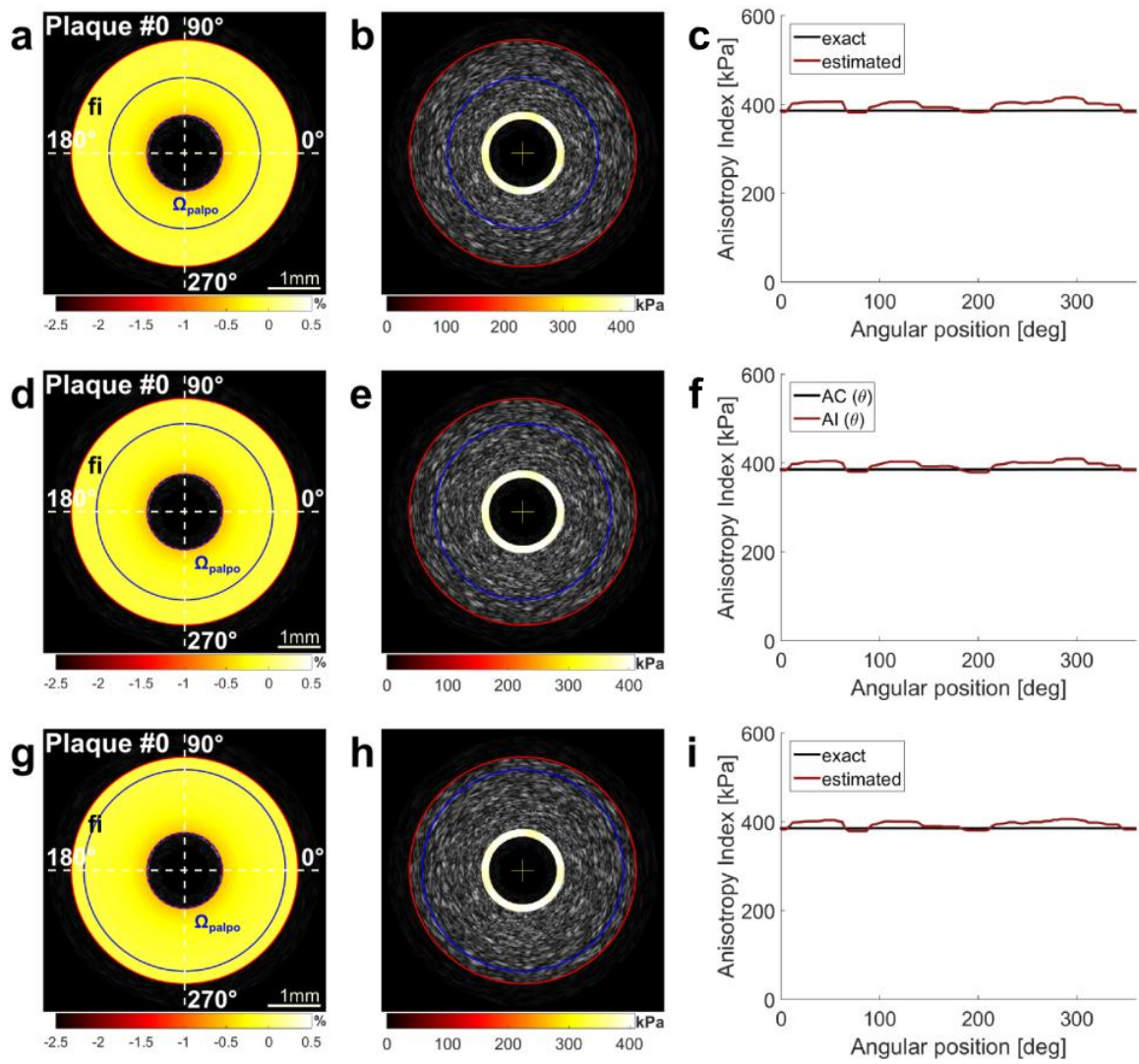


Figure 3.12: Effect of the palpography domain size on the resulting anisotropic elasticity palpogram. Simulations were performed with plaque 0 considering three palpography domain thicknesses. **a, d, g**) Plaque geometries (red contours), palpography domains (blue contours) and estimated radial strain maps. **b, e, h**) IVUS images with AI-palpograms. **c, f, i**) Comparisons between exact and estimated $AI(\theta)$ palpograms.

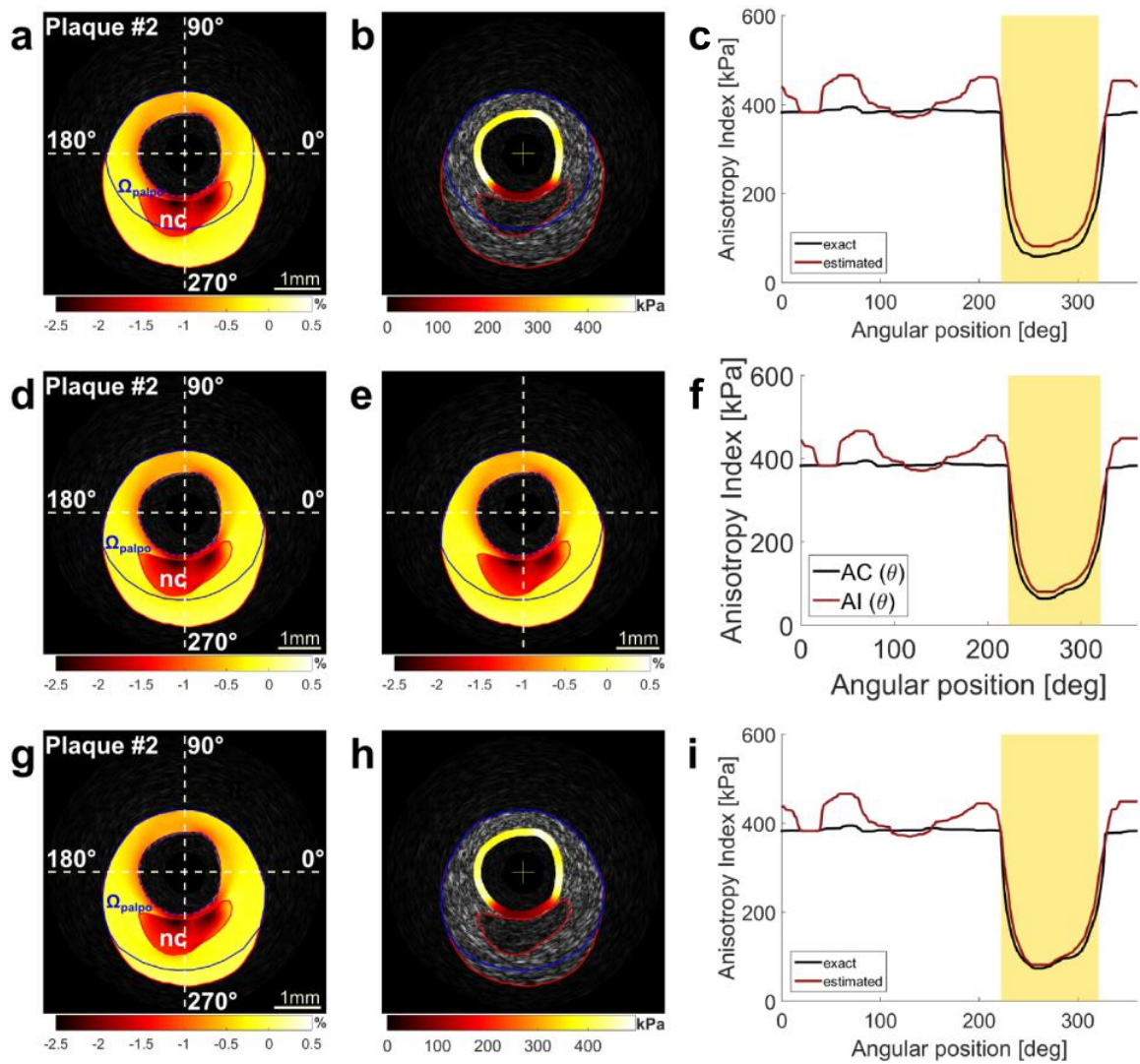


Figure 3.13: Effect of the palpography domain size on the resulting anisotropic elasticity palpogram. Simulations were performed with plaque 2 considering three palpography domain thicknesses. **a, d, g)** Plaque geometries (red contours), palpography domains (blue contours) and estimated radial strain maps. **b, e, h)** IVUS images with AI-palpograms. **c, f, i)** Comparisons between exact and estimated $AI(\theta)$ palpograms. The area shaded in yellow indicates the location of the necrotic core.

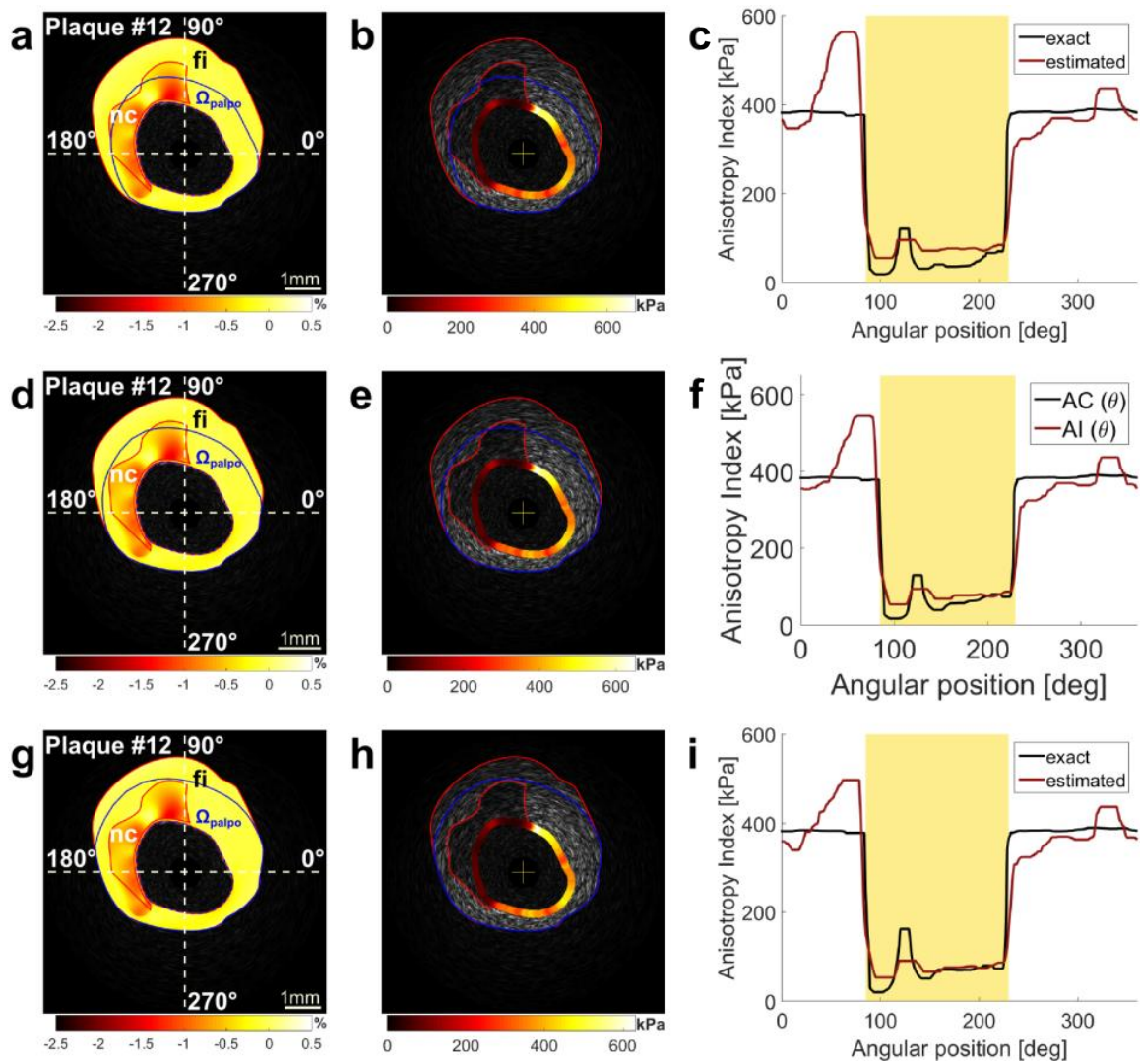


Figure 3.14: Effect of the palpography domain size on the resulting anisotropic elasticity palpogram. Simulations were performed with plaque 12 considering three palpography domain thicknesses. **a, d, g**) Plaque geometries (red contours), palpography domains (blue contours) and estimated radial strain maps. **b, e, h**) IVUS images with AI-palpograms. **c, f, i**) Comparisons between exact and estimated $AI(\theta)$ palpograms. The area shaded in yellow indicates the location of the necrotic core.

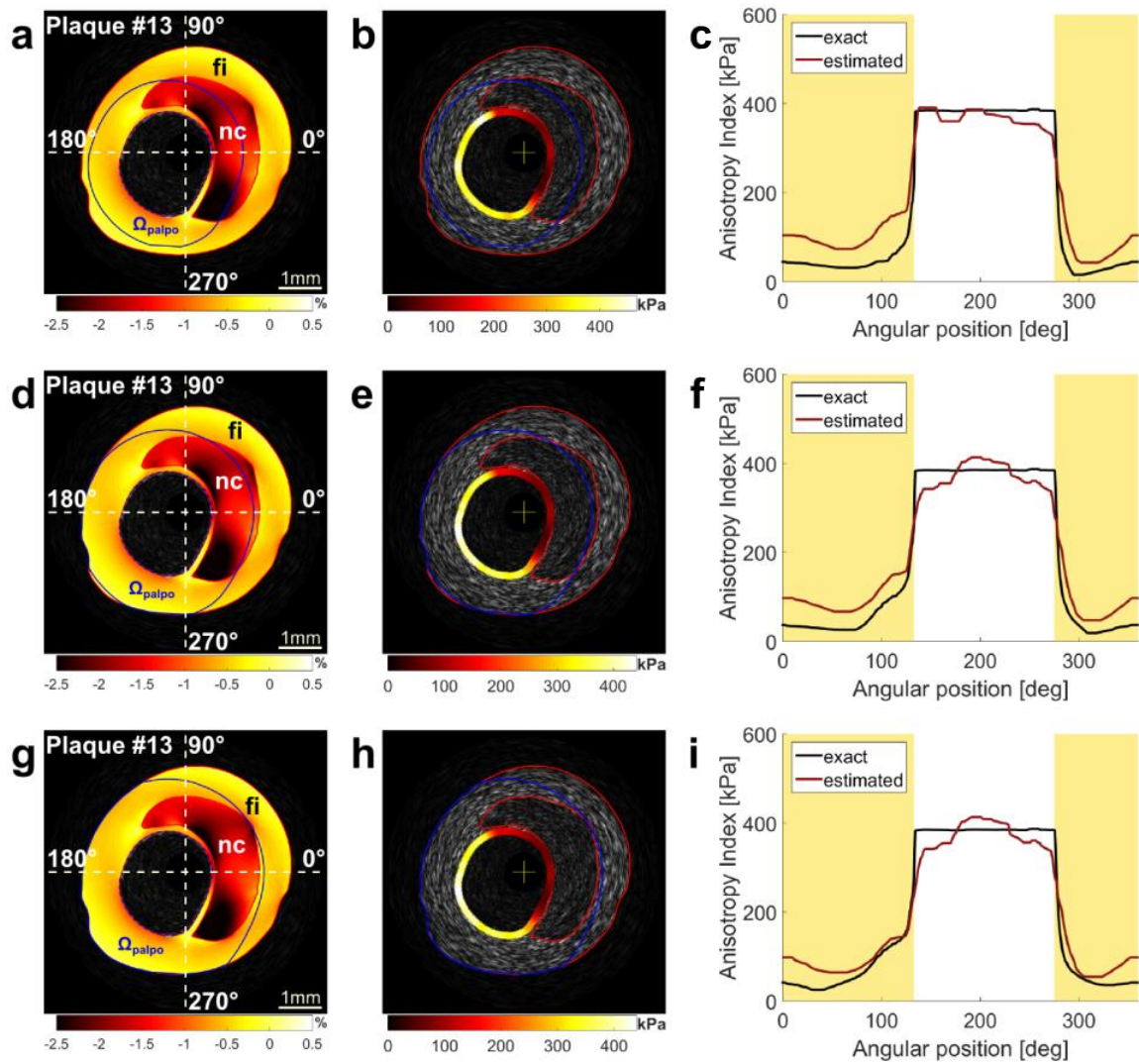


Figure 3.15: Effect of the palpography domain size on the resulting anisotropic elasticity palpogram. Simulations were performed with plaque 13 considering three palpography domain thicknesses. **a, d, g**) Plaque geometries (red contours), palpography domains (blue contours) and estimated radial strain maps. **b, e, h**) IVUS images with AI-palpograms. **c, f, i**) Comparisons between exact and estimated $AI(\theta)$ palpograms. Areas shaded in yellow indicate the location of the necrotic core.

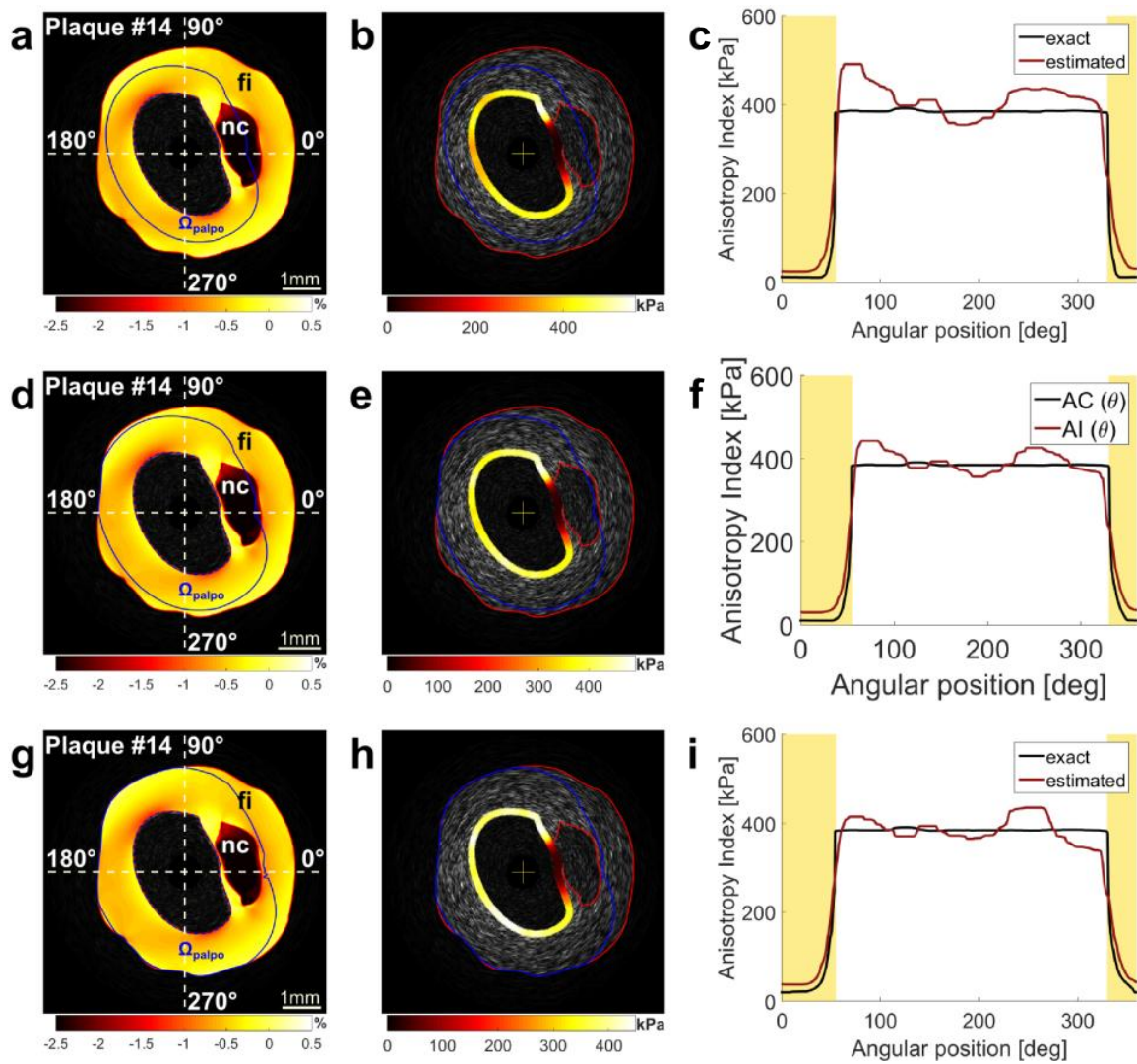


Figure 3.16: Effect of the palpography domain size on the resulting anisotropic elasticity palpogram. Simulations were performed with plaque 14 considering three palpography domain thicknesses. **a, d, g**) Plaque geometries (red contours), palpography domains (blue contours) and estimated radial strain maps. **b, e, h**) IVUS images with AI-palpograms. **c, f, i**) Comparisons between exact and estimated $AI(\theta)$ palpograms. Areas shaded in yellow indicate the location of the necrotic core.

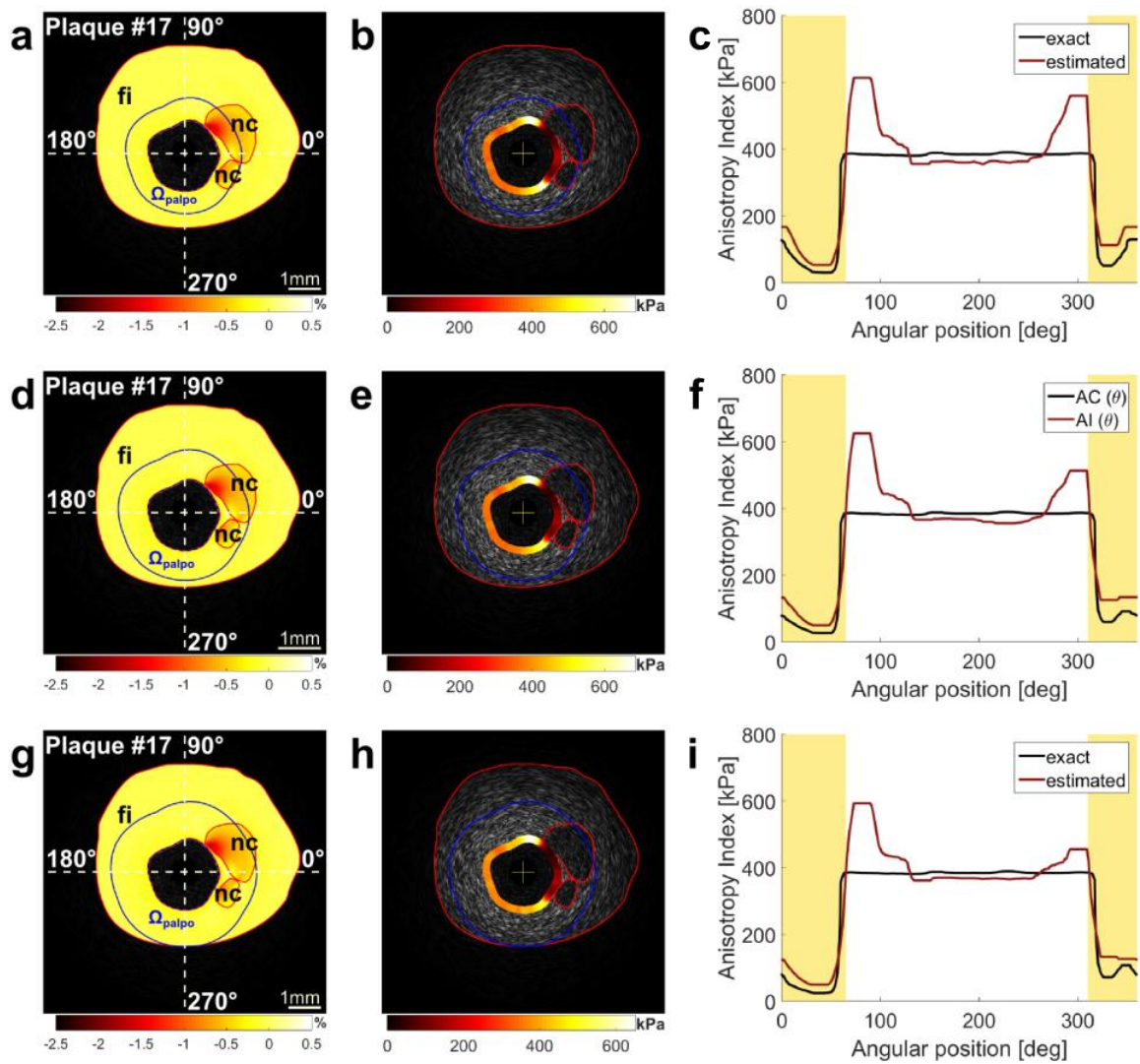


Figure 3.17: Effect of the palpography domain size on the resulting anisotropic elasticity palpogram. Simulations were performed with plaque 17 considering three palpography domain thicknesses. **a, d, g**) Plaque geometries (red contours), palpography domains (blue contours) and estimated radial strain maps. **b, e, h**) IVUS images with AI-palpograms. **c, f, i**) Comparisons between exact and estimated $AI(\theta)$ palpograms. Areas shaded in yellow indicate the locations of the necrotic cores.

Sensitivity of AI-palpograms to the accuracy of the estimated strain elastograms

Since the MW size is one of the main parameters driving the accuracy of the computed strain elastograms, we restricted our sensitivity analysis to this parameter. These computations were performed on idealized plaques (plaques 0 and 1), plaques with soft inclusions (plaques 2, 13) and plaques with dense fibrosis (plaques 18 and 19) by considering four MW sizes: 75 x 15 pixels (i.e. 144.4 μm x 10.6 $^\circ$), 101 x 21 pixels (i.e. 194.5 μm x 14.8 $^\circ$), 121 pixels x 31 pixels (i.e. 232.9 μm x 21.8 $^\circ$) and 151 pixels x 31 pixels (i.e. 290.6 μm x 21.8 $^\circ$). The errors for these computations are summarized in Table 3.7.

Table 3.7: Effect of measuring window (MW) size on the accuracy of the anisotropic elasticity-palpography technique. All palpograms were computed with a palpography domain size Ω_{palpo} = 1mm.

	MW	MR_{error}^{AI*} (%)	MR_{error}^{AI} (%)	$MR_{error}^{AI/AI*}$ (%)
Plaque 0	75 15	0.22 \pm 0.14	3.32 \pm 1.94	3.15 \pm 1.82
	101 21	0.22 \pm 0.14	3.08 \pm 1.62	2.9 \pm 1.49
	121 31	0.22 \pm 0.14	2.82 \pm 1.37	2.61 \pm 1.27
	151 31	0.22 \pm 0.14	2.48 \pm 1.22	2.27 \pm 1.14
Plaque 1	75 15	3.72 \pm 1.72	5.41 \pm 4.27	4.58 \pm 3.59
	101 21	3.72 \pm 1.72	3.7 \pm 2.08	4.24 \pm 3.2
	121 31	3.72 \pm 1.72	4.39 \pm 2.35	4.24 \pm 2.88
	151 31	3.72 \pm 1.72	3.48 \pm 2.18	4.59 \pm 3.14
Plaque 2	75 15	59.43 \pm 57.53	68.65 \pm 65.51	11.17 \pm 13.45
	101 21	59.43 \pm 57.53	74.14 \pm 67.96	15.98 \pm 18.61
	121 31	59.43 \pm 57.53	92.16 \pm 77.88	30.78 \pm 42.81
	151 31	59.43 \pm 57.53	95 \pm 81.79	32.36 \pm 47.33
Plaque 13	75 15	4.86 \pm 4.53	11.89 \pm 9.09	7.42 \pm 5.06
	101 21	4.86 \pm 4.53	13.41 \pm 9.45	8.76 \pm 6.06
	121 31	4.86 \pm 4.53	14.31 \pm 9.63	9.4 \pm 5.79
	151 31	4.86 \pm 4.53	14.17 \pm 10.48	9.29 \pm 5.96
Plaque 18	75 15	11.32 \pm 12.96	21.55 \pm 18.31	17.17 \pm 13.88
	101 21	11.32 \pm 12.96	35.34 \pm 31.27	29.5 \pm 31.75
	121 31	11.32 \pm 12.96	51.1 \pm 36.89	45.68 \pm 39.13
	151 31	11.32 \pm 12.96	56.86 \pm 57.96	52.26 \pm 60.44
Plaque 19	75 15	3.76 \pm 6.38	21.06 \pm 18.44	19.2 \pm 16.43
	101 21	3.76 \pm 6.38	11.25 \pm 8.91	9.43 \pm 6.69
	121 31	3.76 \pm 6.38	16.78 \pm 14.85	16.02 \pm 12.04
	151 31	3.76 \pm 6.38	10.59 \pm 7.34	10.41 \pm 7.25

For the idealized homogeneous cases, there is only a slight variation between the AI palpograms resulting from the different MW sizes (Fig. 3.18), where the largest MW size (151 x 31 pixels) had the least MR_{error}^{AI} . In cases with soft inclusions, the MR_{error}^{AI} suggests a large difference in the performance depending on the MW size, specially in plaque 2, with a better approximation when employing smaller window sizes. However, the AI palpograms (Fig. 3.19) have a very similar shape, and despite the clear difference in the MR_{error}^{AI} , all window sizes were able to detect the drop in the mechanical properties caused by the presence of the necrotic cores.

In contrast, for plaque 19 with a dense fibrosis inclusion, the MW sizes that performed best were the 151 x 31 pixels and 101 x 21 pixels, being these two the only sizes that were able to clearly detect the stiffer inclusion (Fig. 3.20d). For plaque 18, an important palpogram variation was found at the free-plaque arc length. Only for this particular plaque, the AI-palpogram obtained with (101 x 21 pixels) MW size fail to characterize the atherosclerotic lesion; indicating that the accuracy of AI-palpogram depends on the MW size used when estimating the radial strain elastogram (Fig. 3.20b).

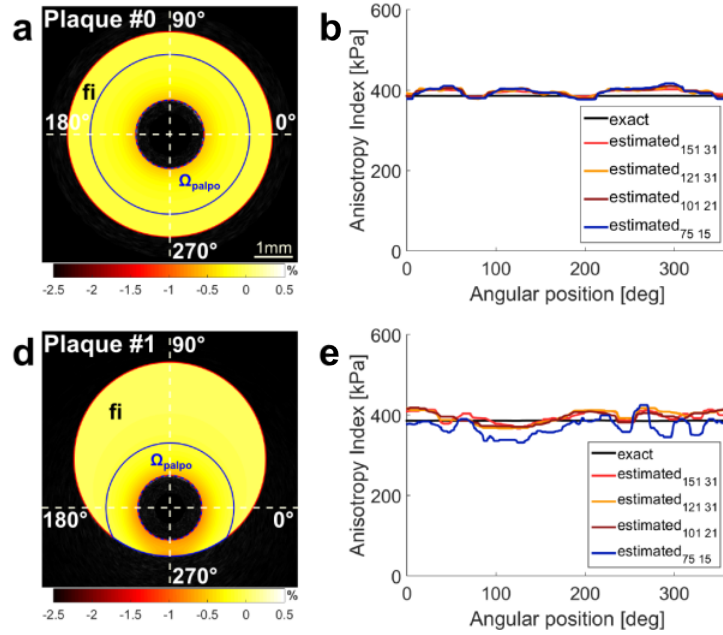


Figure 3.18: Sensitivity analysis revealing the influence of measurement window (MW) size on the computed AI index-palpogram for idealized homogeneous plaques 0 and 1. Four MW sizes were considered for these simulations: 75 x 15 pixels, 101 x 21 pixels, 121 x 31 pixels and 151 x 31 pixels. **a, c**) Plaque geometries (red contours), palpography domains (blue contours) and estimated radial strain maps obtained with the 101 x 21-pixel MW size. **b, d**) Comparisons between exact and estimated $AI(\theta)$ palpograms.

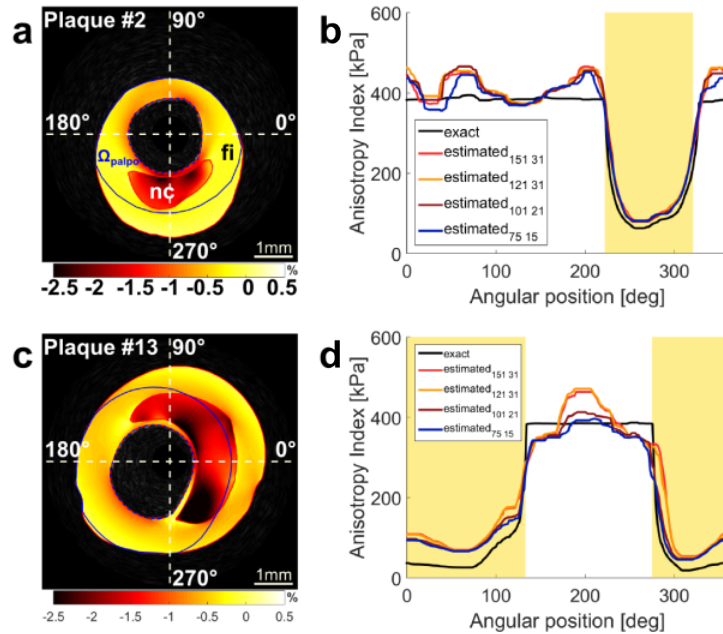


Figure 3.19: Sensitivity analysis revealing the influence of measurement window (MW) size on the computed AI index-palpogram for plaques with soft inclusions (2 and 13). Four MW sizes were considered for these simulations: 75 x 15 pixels, 101 x 21 pixels, 121 x 31 pixels and 151 x 31 pixels. **a, c**) Plaque geometries (red contours), palpography domains (blue contours) and estimated radial strain maps obtained with the 101 x 21-pixel MW size. **b, d**) Comparisons between exact and estimated $AI(\theta)$ palpograms. Areas shaded in yellow indicate the locations of the necrotic cores. nc= necrotic core.

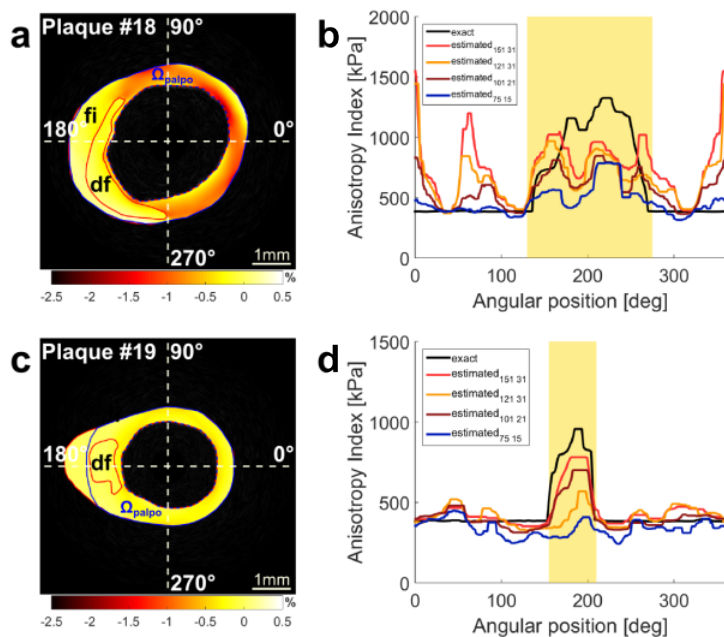


Figure 3.20: Sensitivity analysis revealing the influence of measurement window (MW) size on the computed AI index-palpogram for idealized homogeneous plaques 0 and 1. Four MW sizes were considered for these simulations: 75 x 15 pixels, 101 x 21 pixels, 121 x 31 pixels and 151 x 31 pixels. **a, c**) Plaque geometries (red contours), palpography domains (blue contours) and estimated radial strain maps obtained with the 101 x 21-pixel MW size. **b, d**) Comparisons between exact and estimated $AI(\theta)$ palpograms. Areas shaded in yellow indicate the locations of the dense fibrosis inclusions. df= dense fibrosis.

3.4 Discussion

The new intraluminal ultrasonic palpation imaging technique successfully quantified the apparent wall stiffness of the anisotropic vascular wall based on the arterial radial strain and blood pressure dataset.

Physical meaning of the elastic anisotropy index AI

One of the advantages of AI, which may be viewed as an anisotropic apparent modulus, is to account for the three Young's moduli of the orthotropic atherosclerotic lesion. Even though the AE-PT does not allow identifying individually the 3 orthotropic material constants, this index, which combines the three orthotropic Young's moduli, is proportional to the radial Young's modulus and depends on the two stiffness ratios $k_1 = E_\theta/E_R$ and $k_2 = E_Z/E_R$. Equation 3.3 indicates that the normalized elastic anisotropy index AI/E_R increases with k_2 and decreases with k_1 when ($i=1, 2$). In other words, an increase of AI may be due to either an increase of E_R and E_Z or a decrease in E_θ . Furthermore, the AI amplitude appears to be very sensitive to the presence of mechanical heterogeneities, dropping significantly when predicting soft inclusions in the composite atherosclerotic lesions.

The AE-PT highlights the nonlinear mechanical response of the vascular tissue

Because the proposed constitutive model refers to the configuration of the plaque at Im_i , rather than the initial zero-stress configuration, the linear tangent elasticity procedure used in our approach (Bonet and Wood, 1997) remains acceptable as far as the absolute amplitudes of the incremental strain components estimated between the two successive IVUS images Im_i and Im_{i+1} remain small ($\leq 2\%$, Le Floc'h et al. (2012)). Therefore, the computed AI must be viewed as an anisotropic linearized tangent modulus (Holzapfel 2000) measured for the physiological

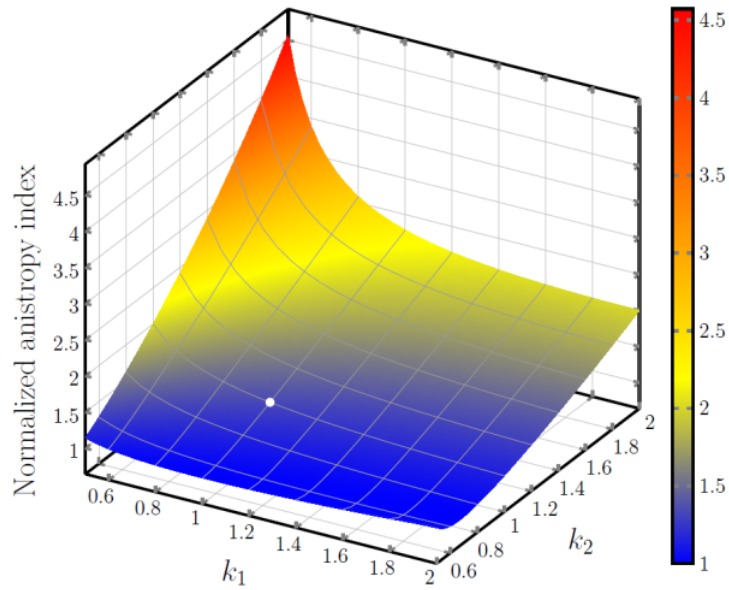


Figure 3.21: A 3-dimensional plot showing the significant influence of two Young's modulus ratios $k_1 = E_\theta/E_R$ and $k_2 = E_Z/E_R$ on the amplitude of the normalized elastic anisotropy index AI/E_R for values of k_1 and k_2 between 0.5 and 2. The white circle represents the value of the normalized AI for an isotropic atherosclerotic lesion when $E_R = E_\theta = E_Z$ (i.e $k_1 = k_2 = 1$).

pressure range considered. The other advantage of such an incremental linearized technique applied on a series of IVUS images is that it allows quantifying the non-linear mechanical response of the fibrotic plaque tissue during the physiologic increase in blood pressure.

How should the cardiologist choose the palpography domain?

With the AE-PT, the interventional cardiologist may define the palpography domain by considering any arbitrary endoluminal thick layer size and shape. The results clearly indicated that an increase in the palpography domain thickness does not necessarily decreases the accuracy of the AI-palpogram (see Table 3.6 and Figures 3.12 to 3.17). This could be explained by the fact that the palpography domain must be thin enough to obtain a reasonable signal-to-noise (SNR) ratio (Céspedes et al., 2000; Doyle et al., 2001) and large enough for a good performance of the strain imaging algorithm (Maurice et al., 2004a).

What is the advantage of using the AI instead of the fractional anisotropy index for characterizing a VP?

The principal strain and fractional strain anisotropy indexes are two strain-based metrics that were defined and applied in non-invasive clinical cardiovascular magnetic resonance imaging and ultrasound studies (Nayak et al., 2017; Soleimanifard et al., 2010). However, extracting the anisotropic mechanical properties of the tissue from these indexes is difficult. Furthermore, while the estimations of these indexes need accurate knowledge of all strain tensor components, estimation of the AI only requires only the radial strain component, which is the only component that can be extracted from the coronary RF-IVUS signal with reasonable accuracy.

Is the AE-PT sufficient to detect VPs and diagnose plaque rupture?

The proposed AE-PT cannot diagnose the degree of plaque vulnerability to rupture since it does not allow measurements of other key geometrical factors (Cilla et al., 2012; Ohayon et al., 2008). However, this technique remains reliable to detecting and highlighting complex VPs with

one or several soft inclusions (see Figs. 3.11 to 3.8, 3.13 to 3.17, and 3.19).

Study limitations

Several limitations deserve to be pointed out. First, the anisotropic palpation technique was tested and validated only on synthesized RF echo frames. Although further animal and clinical studies are needed to extend and strengthen the present findings, our preliminary results appear to be promising and indicate the potential and feasibility of this novel imaging technique. The second limitation of this study is that the palpography model neglected the residual strain, which has a significant effect on the stress amplitude in the thin fibrous cap (Ohayon et al., 2007). However, because the AI is an anisotropic linearized tangent modulus (Holzapfel, 2000) measured during physiologic conditions, it implicitly accounts for all existing internal stresses/strains, including the residual ones. Finally, the sensitivity analysis regarding the MW size highlighted the importance of considering optimal MW sizes to compute accurate AI-palpograms. A more exhaustive study clearly deserves to be investigated as future work to define an MW size that would optimize the performance of the strain-imaging algorithm of Majdoulina et al. (2014).

Relevance for other clinical applications

Modifying the mechanical properties of the vulnerable atherosclerotic lesion could be the key issue for the stabilization of VPs. Finet et al. (2004) reported that a very slight increase in the soft necrotic core stiffness can tilt a VP from instability to stability. Today, therapies based on statins (Libby et al., 2002; Nozue et al., 2012) and other emergent medications (Nicholls et al., 2016) are used by clinicians to enhance plaque stability. However, the effects of all these drugs on the mechanical properties of coronary atherosclerosis lesions still remain unclear. The proposed improved anisotropic elasticity-palpography imaging technique could be used by clinicians to investigate the evolution of the anisotropic mechanical properties of atherosclerotic plaques during drug therapies.

Perspectives

The novel AE-PT has been successfully validated using synthesized IVUS images of plaque geometries of patients. Therefore, the next step would be to further validate this technique *in vitro*. Chapter 4 presents a study where polyvinyl-alcohol cryogel vascular phantoms were fabricated with enhanced anisotropic mechanical properties. These vascular phantoms were imaged using IVUS and the AE-PT was applied to the resulting RF IVUS sequences. The estimated AI palpograms were compared to the expected AI values obtained by characterizing the orthotropic mechanical properties of the phantom.

Chapter 4

On the potential of our new elasticity-palpography technique: in vitro validation

4.1 Introduction

Atherosclerosis is a silent pathology that leads to a collection of diseases depending on the arterial segment it affects. Coronary artery disease, one of the leading causes of death worldwide, often initially manifests in the form of an acute coronary event (Alsheikh-Ali et al., 2010). This is usually the result of a ruptured thin-cap fibroatheroma (TCFA) (Virmani et al., 2006), which can lead to thrombosis and myocardial infarction. The timely and accurate identification and assessment of atherosclerotic plaques are essential in the prevention of these potentially lethal events.

The criteria that define a vulnerable plaque (VP) are strongly linked to its morphology and composition (Virmani et al., 2000; Naghavi et al., 2003; Fleg et al., 2012). Macrophage accumulation, a large necrotic core with a thin fibrous cap ($< 65 \mu\text{m}$) and positive remodeling are common morphological characteristics of inflammatory atherosclerotic lesions susceptible to rupture.

Several endovascular imaging techniques are currently used in clinical practice to detect vulnerable plaques (VPs) and inform clinical decision-making. Among these modalities, the most widely used is intravascular ultrasound (IVUS) (Taki et al., 2017). IVUS delivers a sequence of cross-sectional images of the arterial wall that allow the identification of plaque components based on their echogenicity aspect.

Although plaque morphology and composition have been identified by several clinical and biomechanical studies as a key predictor of plaque vulnerability (Ohayon et al., 2008; Loree et al., 1992), rupture prediction using only these factors is still imprecise. Biomechanical studies have highlighted the effect of the mechanical properties in the rupture mechanisms of atherosclerotic lesions (Ohayon et al., 2014; Guo et al., 2017). Moreover, biomarkers such as peak cap stress amplitude appear as good predictors of plaque rupture site (Lee et al., 1993; Ohayon et al., 2001; Finet et al., 2004). Therefore, there has been great interest in the development of techniques that can assess the mechanical properties of the plaque and its components.

While intraplaque stress quantification using current imaging techniques is not yet feasible,

it is possible to calculate the deformation (strain) caused by pressure changes during the cardiac cycle using a sequence of ultrasound images (Maurice et al., 2004a; Doyley, 2012; Golemati et al., 2016). Strain-field based techniques such as strain elastography, tend to identify plaque constituents, based on the premise that soft tissues deform more than stiffer ones (Ophir et al., 1991). However, due to intricate non-linear geometric effects, a direct correlation between the measured spatial strain field and the mechanical properties of tissue is not possible. Several approaches have been developed to use the IVUS strain field within atherosclerotic lesions with the objective of characterizing the mechanical properties of atheromas and identifying vulnerable plaques. Some of these techniques characterize the whole plaque (Baldewsing et al., 2006b; Le Floch et al., 2009, 2010; Richards and Doyley, 2011; Doyley, 2012; Le Floch et al., 2012; Deleaval et al., 2013; Richards et al., 2015; Tacheau et al., 2016; Nayak et al., 2017; Poree et al., 2017) while others such as the elasticity-palpography technique (E-PT) focus on an endoluminal layer of aspecified thickness known as the palpography domain (Céspedes et al., 2000; Doyley et al., 2001; Schaar et al., 2005; Deleaval et al., 2013; Widynski et al., 2014).

Despite presenting promising approaches, previous elasticity-palpography techniques (Céspedes et al., 2000; Deleaval et al., 2013) ignore the anisotropic mechanical behavior of the arterial wall. To overcome this limitation, our group recently proposed an original anisotropic elasticity palpography technique (AE-PT) (Gómez et al., 2019) by extending the isotropic E-PT formulations of Deleaval et al. (Deleaval et al., 2013) by defining an elastic anisotropy index (AI). This index may be viewed as an anisotropic apparent modulus, and combines the three Young's moduli (E_R , E_θ and E_Z) of the orthotropic atherosclerotic lesion. Although the AE-PT does not allow the individual identification the 3 orthotropic material constants, AI amplitude appears to be very sensitive to the presence of mechanical heterogeneities, dropping significantly when predicting soft inclusions in composite atherosclerotic lesions (Gómez et al., 2019). When tested using simulated IVUS images of coronary plaques, good accuracy was reported between the estimated and exact AI palpograms (mean relative error of 26.79 ± 48.84 %), as well as good robustness regarding RF noise.

Therefore, the present experimental study was designed to investigate the *in vitro* performance of the AE-PT with real IVUS sequences. Three anisotropic polyvinyl alcohol (PVA) cryogel vascular phantoms were fabricated and imaged with IVUS. The orthotropic mechanical properties of these phantoms were characterized and the experimental anisotropic indices (AI) were compared to the estimated AI palpograms.

4.2 Materials and methods

4.2.1 Experimental *in vitro* study with PVA-C vessel phantoms

Three polyvinyl alcohol (PVA) cryogel phantoms were fabricated to test the anisotropic elasticity-palpography technique. PVA is a hydrophilic polymer widely used in biomechanical applications that can be transformed into a solid hydrogel by physical crosslinking using a low-temperature thermal cycling process (Chu and Rutt, 1997). PVA phantoms have been widely used to assess the performance of several imaging modalities such as shear wave elastography (Fromageau et al., 2007b; Chatelin et al., 2014) and modulography (Le Floch et al., 2010).

Anisotropic phantom preparation

The protocol to fabricate the phantoms was based on the methodology described in Fromageau et al. (2007b). A solution with a concentration of 10% by weight of PVA dissolved

in distilled water was prepared. Sigmacell particles (Sigmacell Cellulose, type 50, Sigma Chemical, St Louis, MO, USA) were added to serve as acoustic scatterers, with a weight by weight percentage of 1%. Crosslinking and solidification of the polymer were achieved with freezing-thawing cycles performed with a temperature-controlled chamber. Consequently, the number of cycles sustained by the phantom determine its mechanical properties. Based on previous studies of PVA phantoms (Le Floc'h et al., 2010), we determined that 8 cycles were sufficient to obtain mechanical properties similar to those of coronary arteries. Each low-temperature cycle consisted of 6 stages, which are summarized in Figure 4.1.

Even though the mechanical properties of PVA phantoms are often considered as isotropic, there is some inherent anisotropy present in the material. To induce further anisotropy in our phantoms, we followed a protocol similar to the one described by Millon et al. (2006), where strain is applied during the freeze-thaw cycles. This stretches the physical crosslinks of the polymer chains and results in oriented mechanical properties (Chatelin et al., 2014).

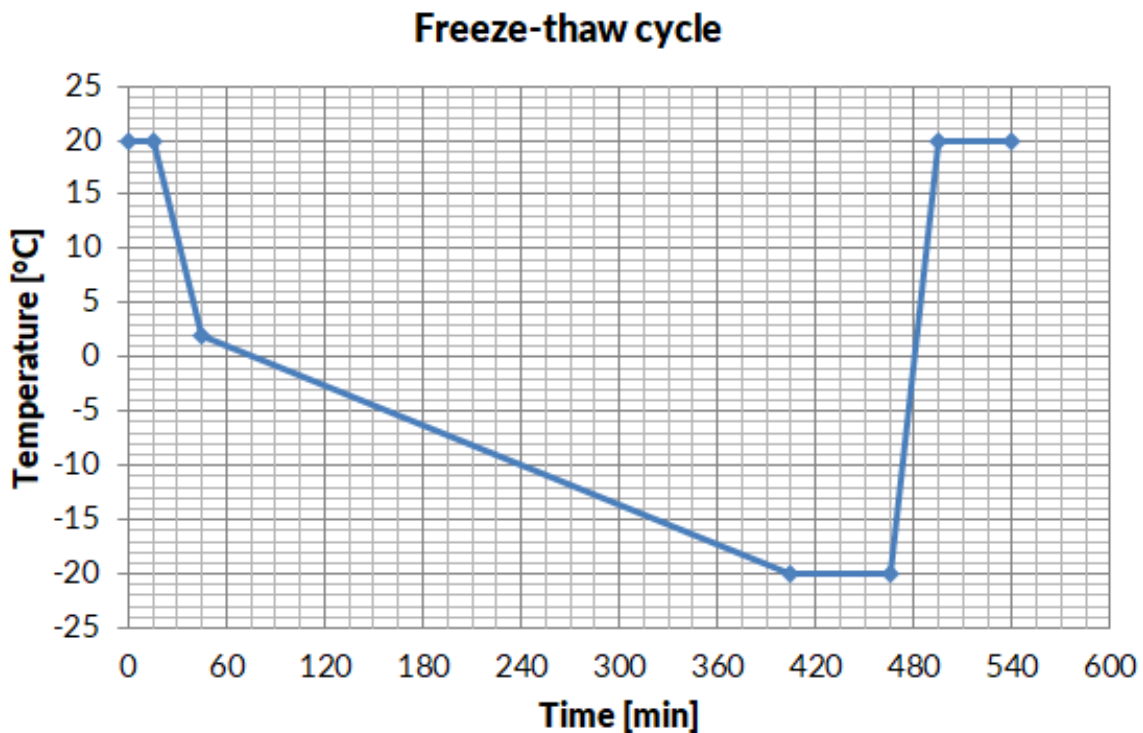


Figure 4.1: Temperature profile for one freeze-thaw cycle for PVA phantom fabrication. A total of 8 cycles were applied to each phantom.

Three phantoms were fabricated by performing the following protocol. The PVA solution was poured into three cylindrical molds with an external diameter of 8 mm and a concentric cylindrical core to achieve a specific internal diameter. Phantoms 1 and 2 were fabricated so that their anisotropic mechanical properties were enhanced. First, a core with a diameter of 1mm was used for the first two freeze-thaw cycles. Then, the phantoms were removed from their molds and strain was applied by increasing the core diameter (i.e. internal diameter of the phantom) from 1 mm to 4 and 4.5 mm, for Phantom 1 and 2, respectively. Since these two phantoms were removed from their molds, a plastic film was wrapped around each phantom to preserve moisture for the remainder of the cycles (cycles 3 to 8). The remaining phantom, Phantom 3, was left on its original mold with a 4.5mm core for the whole duration of the low-temperature cycles to be used as a control semi-isotropic specimen. All three phantoms sustained a total of 8 freeze-thaw cycles before being de-molded and stored in distilled water and away from light. Cross-sections of the three phantoms are shown in Figure 4.2a.

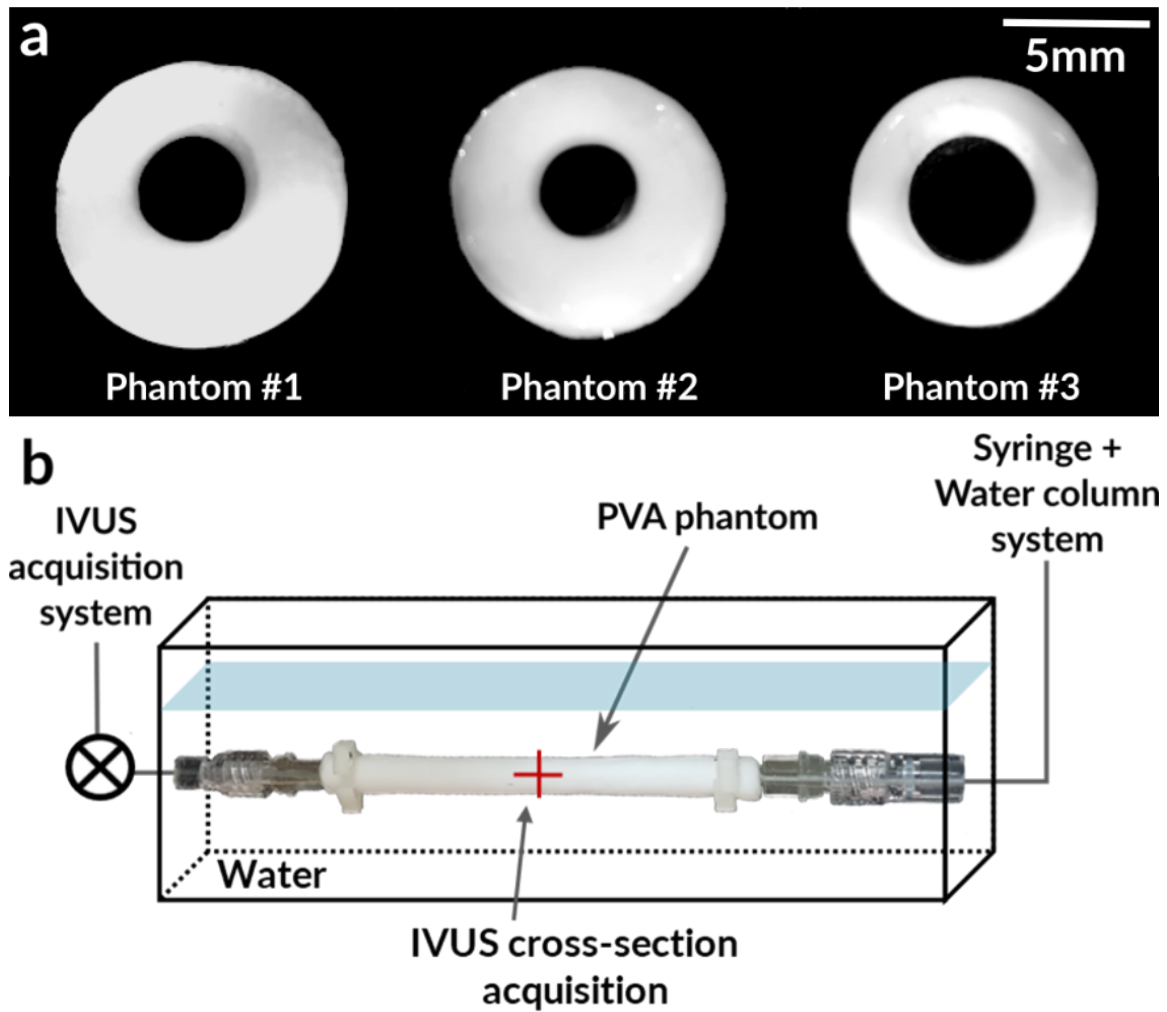


Figure 4.2: a) Cross-sections of the three PVA anisotropic phantoms. b) Schematic drawing of the experimental setup used for IVUS acquisitions. The PVA phantom was placed on a water tank and pressurized using a water column and an automatic syringe pump during the ultrasound acquisitions.

IVUS acquisitions

The SVMi IVUS system (ACIST Medical Systems, Eden Prairie, MN, USA) equipped with a 40 MHz IVUS catheter was used to perform a series of ultrasound acquisitions with constantly increasing pressure. Using an automatic syringe pump (Model) and a water column, a volume of $100 \mu\text{L}$ was injected at a rate of 3.92 mL/min . Pressure was monitored with a pressure sensor (Gems Sensors, 0-40 bar range, resolution of 0.1 bar) connected to an Arduino microprocessor. Given the difference in internal diameter and length of the phantoms, the resulting pressure gradient between each IVUS frame was 2.86, 3.87 and 1.59 mmHg for Phantoms 1, 2 and 3, respectively. A schematic of IVUS acquisition experimental bench is presented in Figure 4.2b. For each test, a phantom was attached to a rigid tube at both ends, allowing the phantom to increase its diameter during inflation but restricting any movement in the longitudinal direction (Z). One end of the phantom was connected to the syringe pump and the other was closed to allow a controlled pressurization.

Mechanical characterization of PVA phantoms

All three phantoms were used for a series of tests to evaluate their orthotropic mechanical properties.

Phantom tensile tests. Uniaxial tensile tests were performed to measure the Young's moduli in the circumferential (E_θ) ($n=5$) and longitudinal (E_Z) ($n=5$) directions. The coordinate system is shown in Fig. ??a. Specimens ($5 \text{ mm} \times 5 \text{ mm} \times \text{wall thickness}$) (Fig. ??b) were tested with the Biotester 5000 test system (Cellscale, CA) with a load cell of 10 N (0.02 N accuracy). The samples were mounted on the machine using a rake system (Figure 4.4). All tests were performed at a constant displacement rate of 3 mm/min until a displacement of 60% of the sample length was achieved. Force was measured at a rate of 1 Hz, and the applied strain was calculated by tracking graphite markers placed on the center of the samples. Using the images obtained during testing (resolution 1280×960 pixels), displacement was calculated with the digital image correlation (DIC) module of the Labjoy software (Cellscale, CA). Search region and source template were set to 15×15 pixels and 31×31 pixels, respectively. The engineering stress was calculated by dividing the force measurements over the initial cross-sectional area of the phantom ($5 \text{ mm} \times \text{sample thickness}$).

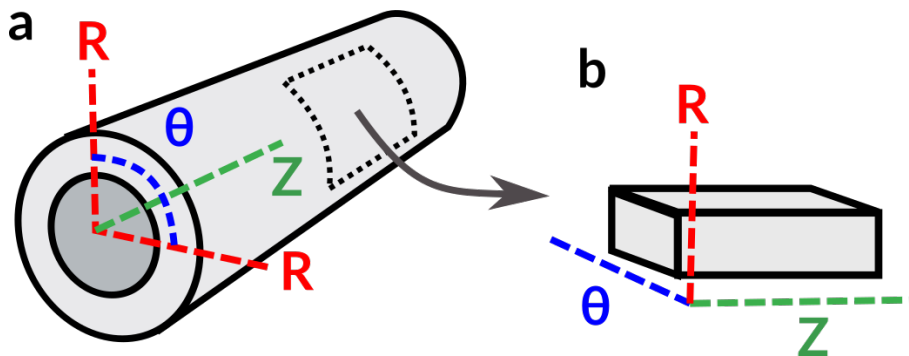


Figure 4.3: a) Phantom diagram showing the coordinate system (R, θ, Z). b) Diagram of a sample cut for the tensile tests.

Atomic force microscopy. The Young's moduli of the three phantoms in the radial direction were explored using atomic force microscopy (AFM) in force-spectroscopy mode. Furthermore, to compare the values obtained with the macroscopic tensile tests with the ones using AFM indentations, samples of Phantom 1 on the circumferential and longitudinal directions were

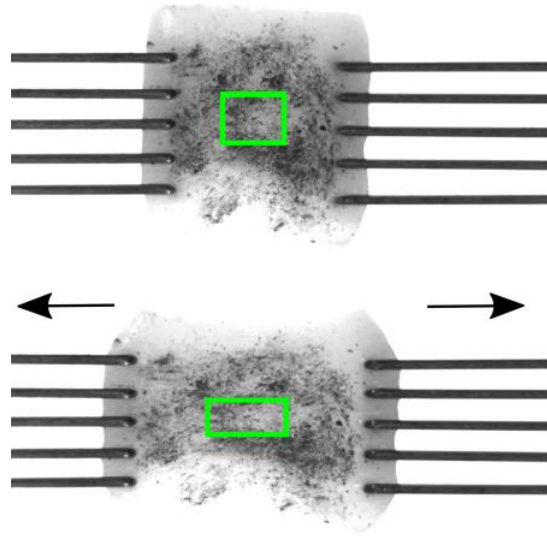


Figure 4.4: Phantom sample mounted on the Biotester 5000 test system (Cellscale, CA) for uniaxial tensile testing using the biorakes system. The green rectangles indicates the tracking box used to calculate the strain using the block matching algorithm.

tested as well. Slices of 100 μm thickness were cut on a vibration microtome (Microm HM 650 V, Thermo Fisher Scientific, Waltham, MA, USA). PVA slices were mounted on glass slides by adhering the edges of the sample using an epoxy resin. Mechanical testing was performed using a servo-controlled AFM (Nanowizard II, JPK instruments, Berlin, Germany). Indentations were made with silicon nitride sphere-tipped cantilevers with a borosilicate glass particle tip of 12 μm and a nominal spring constant of 0.12 N/m (Novascan Technologies, Inc., USA). Data from the tests were processed using the Hertz model for spherical indentation or an elastic medium. Cantilever stiffness was determined via thermal calibration. A minimum of 10 points close to the center of the sample and away from the edges were tested. Each point was indented 5 times for each experiment. Calibration and experiments were performed with the samples submerged in PBS solution.

Opening angle

To assess the residual stresses inside the phantoms, opening angle tests were performed using the procedure detailed in [Ohayon et al. \(2007\)](#). First, a cross sectional cut of 2mm was taken from each phantom; a picture (OA-1) was taken at this point. Then, the phantoms were cut in the circumferential direction at the thinnest (external diameter – internal diameter) point. A picture (OA-2) was taken immediately after the cut. The samples were left submerged in water for two hours before a third picture (OA-3) was taken. Using the second and third pictures, two opening angles (initial and final) were calculated for each phantom.

Microscopic analyses

Quantitative microscopic analyses were performed on our samples. For each of these microscopy tests, one sample from each phantom wall was tested (5 mm x 5 mm x sample thickness). Scanning electron microscopy (SEM, EVO LS10, Carl Zeiss, Germany) was used to inspect the internal, external and border surfaces of each sample. Samples were sputtered with gold-palladium prior to their examination.

4.2.2 Anisotropic elasticity-palpography technique

Intravascular strain elastography

First, using the Lagrangian speckle model estimator (LSME) (Maurice et al., 2004b), the radial strain field was computed from the IVUS RF sequences recorded during the inflation of the samples. Radial strain fields were computed using a two-step strain imaging algorithm (Maurice and Bertrand, 1999; Maurice et al., 2004a, 2005; Poree et al., 2017). First, a block matching method provides local registration on overlapping sub-windows (measurement windows - MWs). It allows compensating for rigid translation movements using a 2-D cross correlation coefficient. Once MW locations have been registered, the 2-D-deformation matrix is estimated. Estimation is based on the resolution of a first-order optical flow equation for each MW (Majdouline et al., 2014). Sizes of MWs in radial and circumferential directions were set to 101 pixels (about 192.5 μm) and 21 pixels (about 14.7°). Overlapping between MWs was set with a spacing parameter of 1 pixel for both the radial and circumferential directions. Such values optimized the performance of the LSME algorithm for our ultrasound data acquired at 40 MHz (Maurice et al., 2004b).

Anisotropic index (AI) palpograms

The anisotropic elasticity palpography technique described in Gómez et al. (2019), was used to compute the anisotropic index (AI) palpograms for each phantom. Briefly, an elastic anisotropy index (AI) was defined as the ratio of the averaged difference between the radial and circumferential stresses (σ_{RR} and $\sigma_{\theta\theta}$) over the averaged radial strain (ε_{RR}) along the radial axis:

$$AI(\theta) = \frac{\int_{R_i(\theta)}^{R_p(\theta)} \{\sigma_{RR}(R, \theta) - \sigma_{\theta\theta}(R, \theta)\} dR}{\varepsilon(R, \theta)} \quad (4.1)$$

with

$$\varepsilon(\theta) = \int_{R_i(\theta)}^{R_p(\theta)} \varepsilon_{RR}(r, \theta) dR \quad (4.2)$$

where $R_i(\theta)$ and $R_p(\theta)$ are the inner and outer radii of the considered palpography domain, respectively. The computation of this index is described on Appendix B.

Notice that the anisotropic index is a combination of the orthotropic Young's moduli. When considering a homogeneous cross-section made of the same incompressible orthotropic medium (i.e. when $E_R(R, \theta) = E_R^0$, $E_\theta(R, \theta) = E_\theta^0$ and $E_Z(R, \theta) = E_Z^0$), whatever the cross-sectional geometry ($R_i(\theta) \leq R \leq R_o(\theta)$, where $R_i(\theta)$ and $R_o(\theta)$ are the internal and external contours of the phantom, respectively) and the palpography domain Ω_{palpo} considered, the amplitude of $AI(\theta)$ remains constant and equal to:

$$ModelAI(\theta) = E_R^0 \left[1 - \frac{1}{4} \left(1 - \frac{E_R^0}{E_\theta^0} + \frac{E_R^0}{E_Z^0} \right) \left(1 + \frac{E_Z^0}{E_R^0} - \frac{E_Z^0}{E_\theta^0} \right) \right]^{-1} \quad (4.3)$$

which is the AI calculated with the incompressible model. All palpograms were computed with a palpography domain thickness of 1mm.

4.3 Results

4.3.1 Phantom characterization results

Experimental mechanical properties results

Uniaxial tensile tests. The resulting engineering stress (σ) -strain(ε) curves for each phantom were fit using an exponential model in the form $\sigma = ae^{(b\varepsilon)} + c$. The coefficients for each of the tested 5 specimens in each direction, circumferential and longitudinal, were averaged to obtain the mean curves $\sigma = a_{mean}e^{(b_{mean}\varepsilon)} + c_{mean}$ (Figure 4.5). From the linearization of the exponential function we obtain:

$$\sigma = ae^{(b\varepsilon)} + c = a\left(1 + b\varepsilon + \frac{(b\varepsilon)^2}{2} = \dots\right) + c = ab\varepsilon + (a + c) \quad (4.4)$$

which gives us:

$$\sigma = E\varepsilon + (a + c) \quad (4.5)$$

where $E = ab$ is the initial Young's modulus. These coefficients and the initial Young's moduli are summarized in Table 4.1. The initial Young's moduli of the three phantoms in the circumferential (E_θ) and longitudinal (E_Z) directions are also given in Table 4.2.

Table 4.1: Coefficients for the exponential curve fit of the uniaxial tension tests in the circumferential (C)(E_θ) and longitudinal (L)(E_Z) directions. The product ab corresponds to the initial Young's modulus.

Coefficients (Mean \pm SD)					
	a	b	c		ab
PH1-C	89.05 \pm 40	2.8 \pm 0.37	88.99 \pm 41.4	$E_\theta^1 =$	238.85 \pm 80.48
PH1-L	36.25 \pm 5.9	2.56 \pm 0.22	36.15 \pm 5.98	$E_Z^1 =$	92.29 \pm 14.37
PH2-C	71.75 \pm 33.09	2.73 \pm 0.6	71.88 \pm 34.32	$E_\theta^2 =$	185.72 \pm 64.35
PH2-L	33.49 \pm 7.5	2.69 \pm 0.2	33.3 \pm 7.9	$E_Z^2 =$	89.07 \pm 18.34
PH3-C	74.08 \pm 29.1	2.59 \pm 0.41	74.53 \pm 29.4	$E_\theta^3 =$	186.63 \pm 61.4
PH3-L	48.8 \pm 16.2	2.32 \pm 0.28	48.03 \pm 15.7	$E_Z^3 =$	109.23 \pm 24.55

Atomic force microscopy The radial moduli E_R for all three phantoms were measured using AFM. To verify if the values obtained with AFM are comparable with the ones obtained with uniaxial tensile tests, Phantom 1 (PH1) samples were tested for all directions (R , θ , and Z). The mean experimental Young's Moduli calculated with the AFM for the circumferential and longitudinal directions of PH1 had a good agreement with the tensile tests results. All results of the AFM indentations along with the tensile tests results are summarized in Table 4.2.

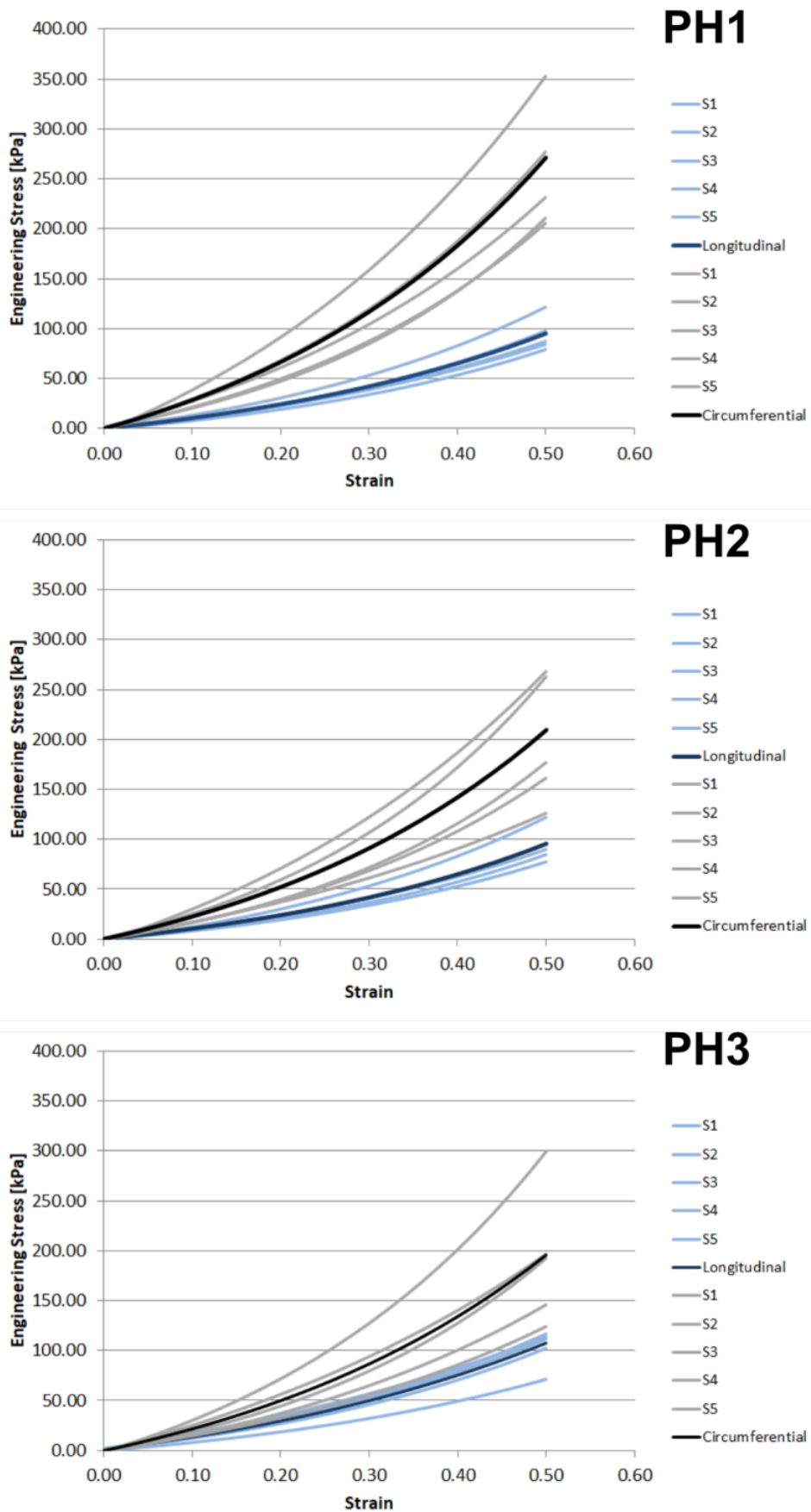


Figure 4.5: Engineering stress vs strain curves obtained from all the uniaxial tests of (a) PH1, (b) PH2 and (c) PH3 for the longitudinal (blue) and circumferential (black) directions. The mean curves for each direction (circumferential and longitudinal) are shown in a darker color.

Table 4.2: Atomic force microscopy (AFM) and tensile tests (TT) results of the anisotropic phantoms PH1, PH2 and PH3. The AFM values of PH1 in the circumferential (θ) and longitudinal (Z) directions shown in parenthesis were obtained to compare them to TT results in the same direction and show a good agreement between them.

Phantom	E_R [kPa]	E_θ [kPa]	E_Z [kPa]
PH1	$^{AFM} 235.93 \pm 120.24$	$^{TT} 238.85 \pm 80.48$ $^{AFM} (236 \pm 93.31)$	$^{TT} 92.29 \pm 14.37$ $^{AFM} (116.25 \pm 93.46)$
PH2	$^{AFM} 216.98 \pm 106.27$	$^{TT} 185.72 \pm 64.35$	$^{TT} 89.07 \pm 18.34$
PH3	$^{AFM} 181.98 \pm 140.93$	$^{TT} 186.63 \pm 61.4$	$^{TT} 109.23 \pm 24.55$

Opening angle results

The opening angle test was performed to assess the presence of circumferential residual stress in the phantoms. For all samples, the opening angle was 0° (Fig. 4.6), indicating the absence of residual circumferential stress. However, our assumption of no residual stress still needs to be proven by investigating the existence of residual stresses in the radial and axial directions too. For technical reasons, these later works have not been performed and the zero stress assumption was postulated in this work.

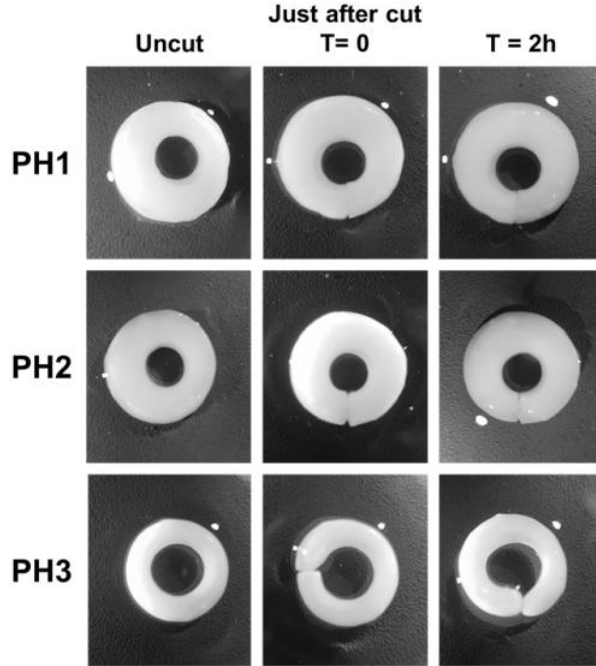


Figure 4.6: Pictures of the opening angle tests. Cross-sections with a thickness of 2mm were cut from all three phantoms (PH1, PH2 and PH3). A cut in the radial direction was made to each of them and images were recorded before, right after and two hours after the radial cut. No change was observed.

Microscopy results

Scanning electron microscopy (SEM) images (Fig. 4.7) were obtained from the internal and external borders of the phantom, as well as from its cross-section (see Fig. 4.7 a-c). From the images of the internal surface (Fig. 4.7d) that corresponds to the θ - Z plane, PH1 and PH2 appear to have an alignment in the circumferential direction (more pronounced for PH1 which may explain its higher circumferential Young's modulus (see Table 4.2)), whereas PH3 does not have this feature. On the external surface (Fig. 4.7e) that corresponds to the θ - Z plane, PH2 and PH3 have a similar appearance, while PH1 presents a slightly different texture. However,

the alignment observed in the internal surface is missing. Finally, the cross-sectional surface (Fig. 4.7f), corresponding to the R - θ plane, has similar features for all three phantoms.

4.3.2 In vitro palpography results

Anisotropic index (AI) palpograms were obtained by applying the anisotropic elasticity-palpography technique (AE-PT) to the first 10 frames of each phantom sequence. The initial RF IVUS AI palpogram, which is the palpogram computed using the first 2 frames of the sequence, is presented for each phantom (Fig. 4.8). In these results, we can observe that the AI estimated for PH1 (121.31 ± 11.67 , Mean \pm SD) is the highest of the three, followed by PH2 (89.52 ± 6.54). The AI estimated for PH3, the phantom without enhanced anisotropy, is the lowest (78.18 ± 5.39).

We used the experimental values of the Young's Moduli (E_R , E_θ and E_Z) to calculate the AI using the previously presented model (Eq. 4.3) that assumes an incompressible medium (Model AI). To provide a range for the Model AI, three different Model AI values were computed by employing the minimum, mean and maximum values for each of the Young's moduli, respectively. The calculations for each of the phantoms, along with the initial RF IVUS AI value, are summarized in Table 4.3.

Comparing the two results, the Model AI and the initial RF IVUS AI, we observe that the RF IVUS AI computed values underestimated the mean Model AI values by a factor close to 5.

Table 4.3: Anisotropic Index (AI) calculation using a model with incompressibility assumption (Eq. 4.3) (Model AI). Model AI is computed with the minimum (Min), average (Mean) and maximum (Max) experimentally obtained values for each of the Young's moduli (E_R , E_θ and E_Z) for phantoms PH1, PH2 and PH3. The initial RF IVUS AI is obtained applying the anisotropic elasticity-palpography technique to the first frame of each phantom sequence.

Initial Young's Moduli					
PH1	E_R [kPa]	E_θ [kPa]	E_Z [kPa]	Model AI [kPa] (from Eq. 4.3)	Initial RF IVUS AI [kPa]
Min	54.51	162.07	74.69	162.79	121.31 ± 11.67
Mean	236.36	238.85	92.28	666.84	121.31 ± 11.67
Max	431.90	367.30	114.56	3012.51	121.31 ± 11.67
Initial Young's Moduli					
PH2	E_R [kPa]	E_θ [kPa]	E_Z [kPa]	Model AI [kPa] (from Eq. 4.3)	Initial RF IVUS AI [kPa]
Min	67.85	140.35	74.26	154.10	89.52 ± 6.54
Mean	216.98	185.71	89.07	459.44	89.52 ± 6.55
Max	471.70	289.21	119.30	1562.70	89.52 ± 6.56
Initial Young's Moduli					
PH3	E_R [kPa]	E_θ [kPa]	E_Z [kPa]	Model AI [kPa] (from Eq. 4.3)	Initial RF IVUS AI [kPa]
Min	41.93	122.06	72.88	123.08	78.18 ± 5.39
Mean	181.98	186.62	109.22	318.74	78.18 ± 5.40
Max	538.00	271.15	139.43	1157.79	78.18 ± 5.41

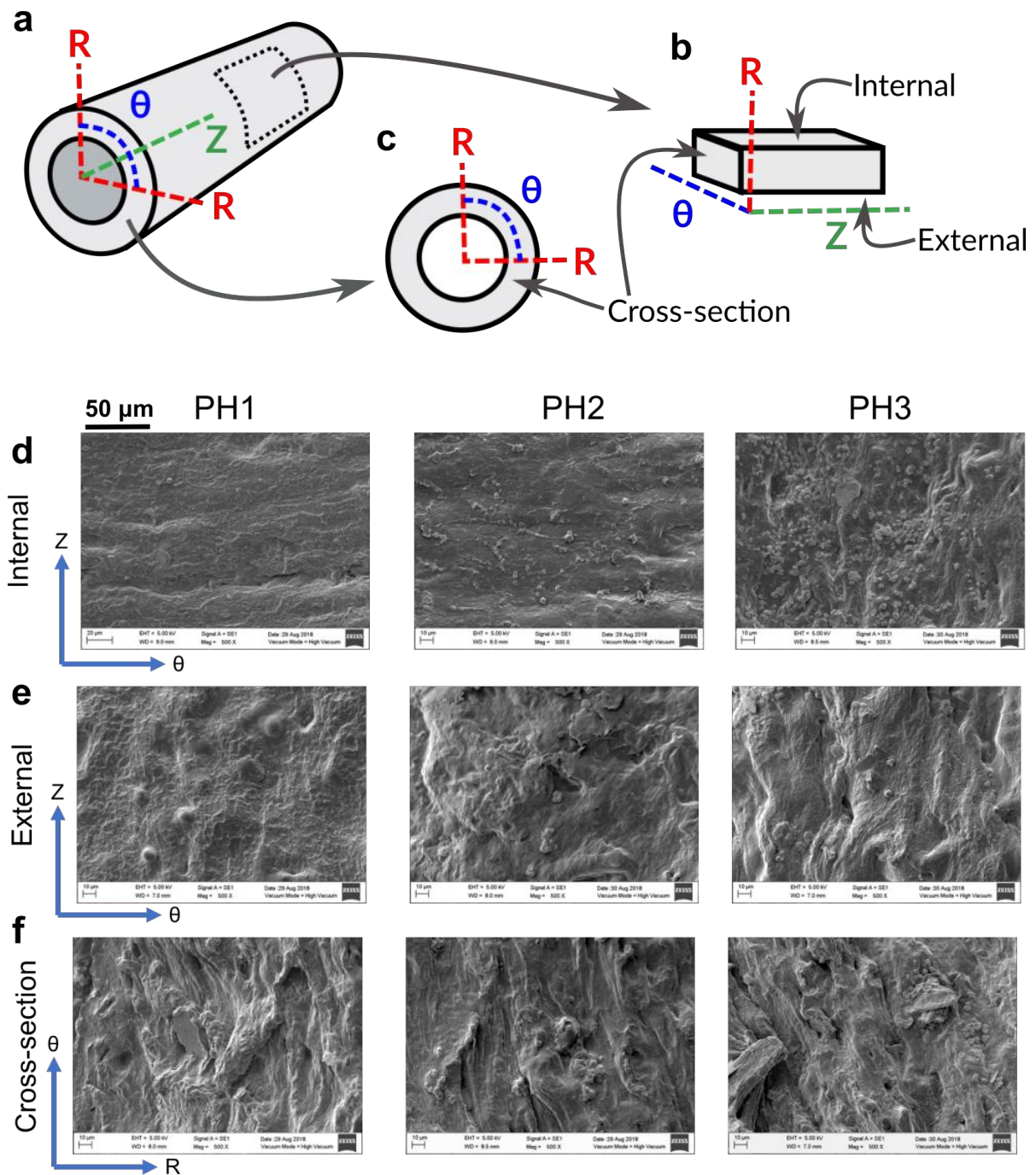


Figure 4.7: Scanning electron microscopy (SEM) results. a) Phantom diagram showing the coordinate system used. b and c) Diagrams for cuts used to obtain samples for SEM that show the internal and external borders (plane θ - Z) and the cross-section (plane R - θ) surfaces imaged with SEM. d-f) SEM images obtained from the d) internal, e) external and f) cross-sectional surfaces for each of the phantoms (PH1, PH2 and PH3) with a magnification of 500x. The planes for each surface are also given.

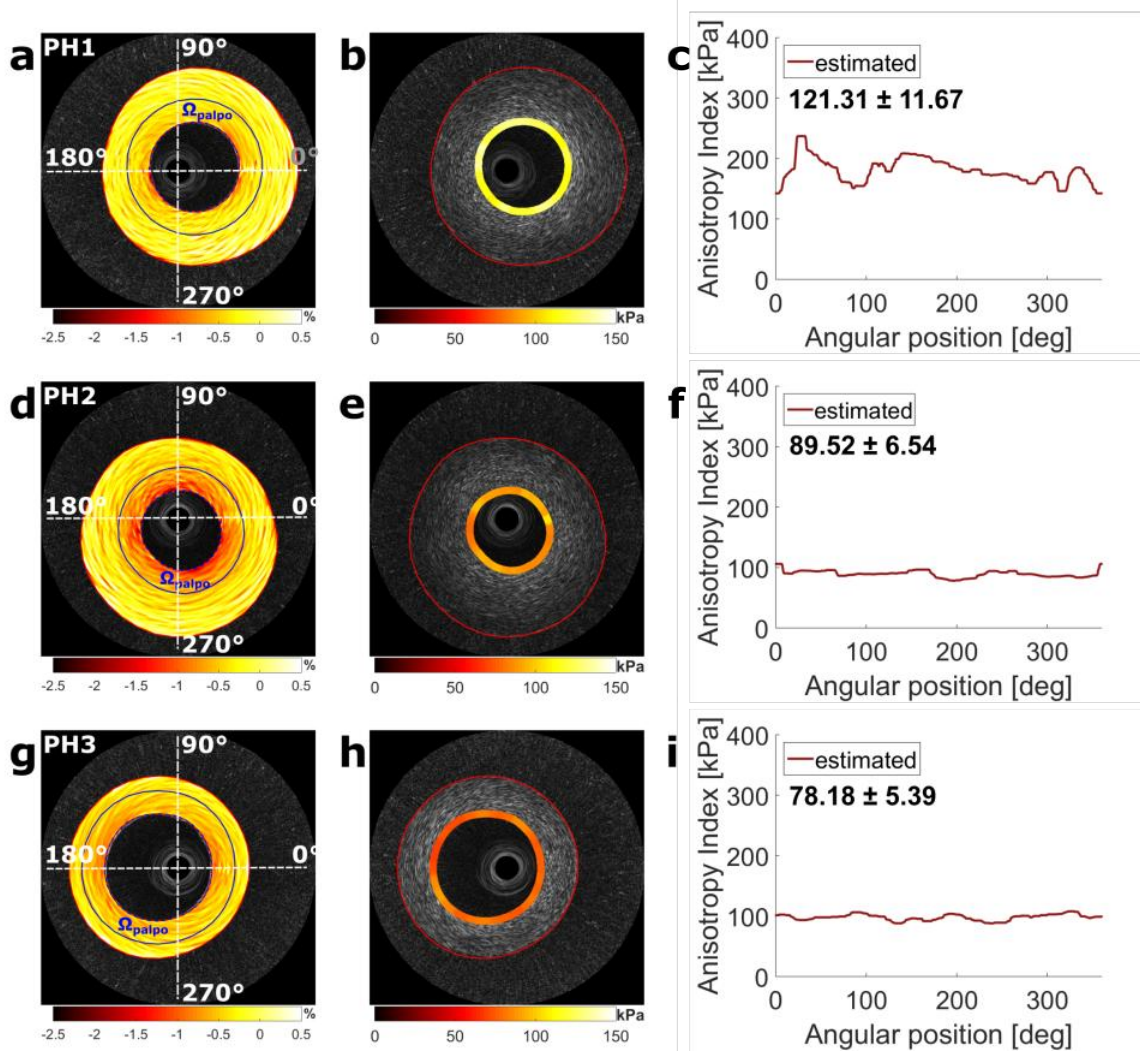


Figure 4.8: Performance of the anisotropic elasticity palpogram using *in vitro* IVUS sequences of polyvinyl-alcohol cryogel vascular phantoms. **a, d, g)** Phantom geometries (red contours), palpography domains (blue contours) and estimated radial strain maps. **b, e, h)** IVUS images with AI-palpograms. **c, f, i)** Estimated $AI(\theta)$ palpograms with mean \pm standard variation values.

Nonlinear response of the computed AI palpograms

Figure 4.9 provides the results of the AE-PT applied to the first 10 frames of the RF IVUS sequences of the PVA phantoms. The initial RF IVUS palpogram for each phantom is highlighted with a red dot on the plot. IVUS sequences were acquired with linearly increasing pressure, which means that there is a constant pressure increase between frames. From this data, we can see that the mean AI values tend to increase with pressure, which highlights the nonlinear mechanical responses of the orthotropic materials.

Anisotropic index (AI) tendency

In order to investigate the effect of the enhanced anisotropy has on the computed AI values, a tendency index was defined. Taking PH3 - the phantom without enhanced anisotropy - as a reference, the mean Model AI and the mean RF IVUS AI values of each phantoms were divided by the corresponding PH3 mean value. The tendency indices for both the Model AI and RF IVUS AI values increase in a similar manner (Table 4.4).

Table 4.4: Tendency indices of the mean Model AI values obtained with the model assuming incompressibility (Eq. 4.3) and mean Initial RF IVUS AI values computed with the anisotropic elasticity-palpography technique (AE-PT). The asterisk symbol indicates that the calculation of the tendency index is referred to PH3.

	Mean Model AI [kPa] (from Eq. 4.3)	Tendency Index	Mean Initial RF IVUS AI [kPa]	Tendency Index
PH1	666.84	2.09	121.31	1.55
PH2	459.44	1.44	89.52	1.14
PH3*	318.74	1	78.18	1

4.4 Discussion

Mechanical characterization of the phantoms

Experimental results of the tensile tests (TT) and atomic force microscopy (AFM) indentations were presented in Table 4.2. Although AFM results present a higher standard deviation, good agreement was found between the mean values of the Young's moduli measured with both testing techniques for E_θ (AFM= 236 ± 93.31 kPa , TT= 238.85 ± 80.48 kPa) and E_Z (AFM= 116.25 ± 93.46 kPa, TT= 92.29 ± 14.37 kPa) for PH1. This suggests that the experimental measurements were successful in characterizing the orthotropic mechanical properties of the three phantoms.

Additionally, our results showed that even without purposely promoting anisotropy during the fabrication process the PVA phantoms already present a certain degree of anisotropy. This finding supports the work of other studies in this area (Millon et al., 2009) where applying a strain during the fabrication process, the anisotropy is enhanced. Furthermore, in the SEM images of the phantom's internal surface, PH1 and PH2 appear to have an alignment in the circumferential direction (more pronounced for PH1) consistent with the desired fiber alignment promoted during the fabrication process, which may partially explain the higher amplitude of E_θ measured for PH1.

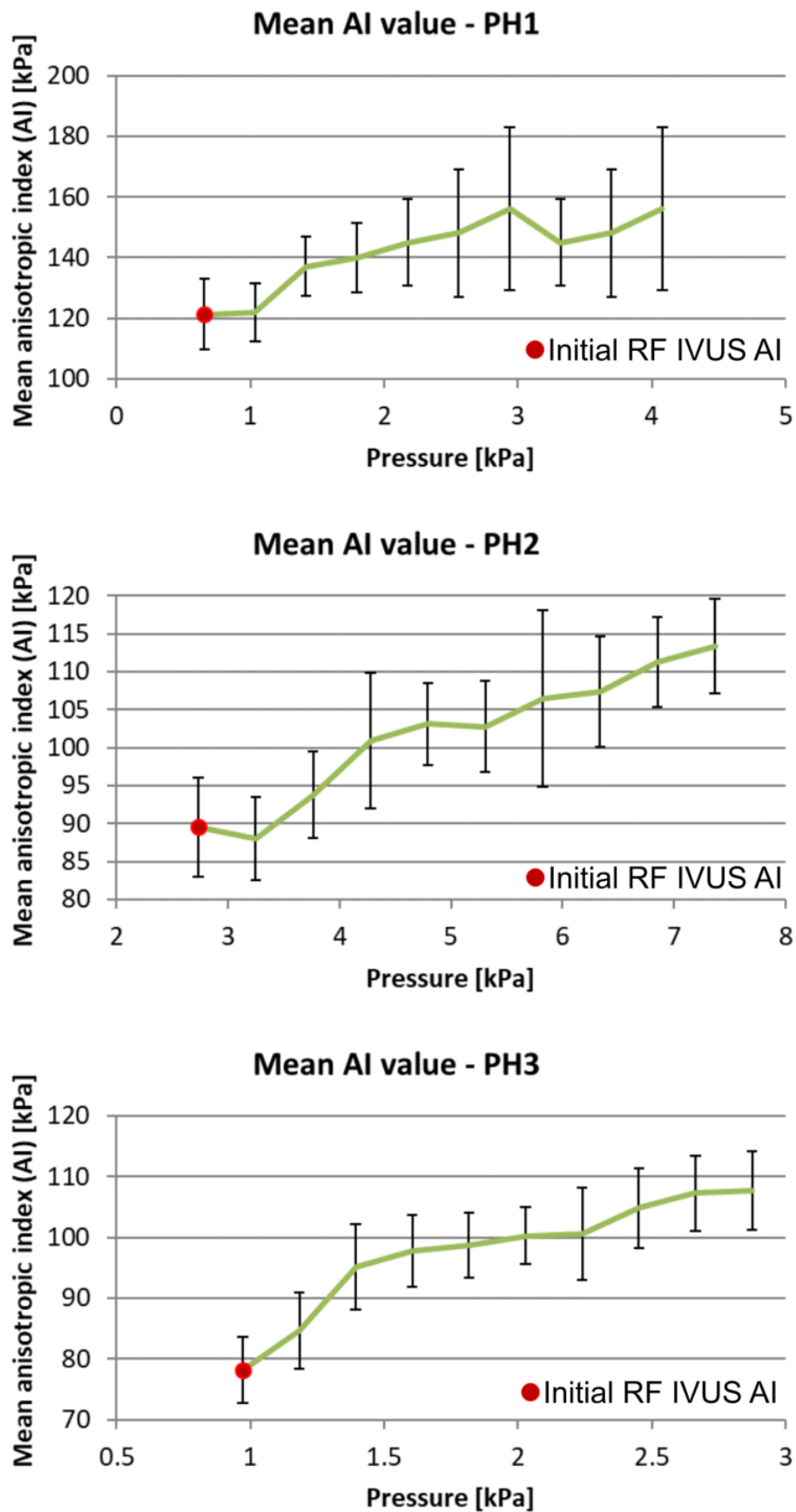


Figure 4.9: Mean anisotropic index (AI) value for each pressure step for phantoms PH1, PH2 and PH3. The bars indicate the standard deviation of AI at each pressure step. The first point, highlighted with a red dot, corresponds to the initial radio-frequency (RF) intravascular ultrasound (IVUS) AI.

Performance of the AE-PT on PVA phantom IVUS sequences

The initial RF IVUS AI palpograms were estimated from IVUS data by employing the anisotropic elasticity-palpography technique (AE-PT). The highest estimated AI value corresponded to PH1 (121.31 ± 11.67 kPa), which is the phantom that presented the highest anisotropy degree (Table 4.2). PH2 presented the second highest estimated AI value (89.52 ± 6.54 kPa) and the second highest anisotropy. Finally, the lowest estimated AI value belonged to PH3 (78.18 ± 5.39 kPa), which also had the lowest anisotropy. These results suggest that the estimated AI palpogram is able to capture the change in the anisotropic mechanical properties of the phantoms. Moreover, the variation of the index was small throughout the palpogram, accurately identifying the homogeneity of the phantom material.

Comparison between the Model AI and initial RF IVUS AI values

When comparing the estimated initial RF IVUS AI values to the ones computed using the mean experimental Young's moduli along with the incompressible anisotropic medium model (Eq. 4.3) (Table 4.3) there was not a good agreement between these two values. Although the RF IVUS AI values underestimated the mean Model AI values by a factor close to 5, they were in the order of magnitude of the computed Model AI values obtained when using the minimum experimentally obtained Young's moduli. This discrepancy between the model and palpogram AI values could be due to the incompressibility assumption used to generate the model presented in equation 4.3. By making this assumption, the resulting Model AI values may no longer be comparable to the AI values estimated by the AE-PT.

AI value tendency

By analyzing the tendency index of the AI among the mean Model AI values and the estimated RF IVUS AI values, a similar trend was found. Both indices had similar proportions between the phantoms, with the highest value corresponding to PH1 and the lowest to PH3. This indicates that even though the AE-PT underestimated the Model AI values and is not able to quantify the individual Young's moduli, it is able to assess the proportional change in the anisotropic mechanical properties between the phantoms.

Study limitations

Some limitations of this study must be pointed out at this stage of our work.

First, we did not find a good agreement between the predicted RF IVUS AI computed by using the AE-PT, and the AI estimated by using the experimentally measured Young's moduli along with the incompressible homogeneous model (Eq. 4.3). Although the AE-PT underestimated the Model AI, this is not necessarily invalidates the technique. Indeed, our previous study validating the AE-PT on simulated IVUS RF sequences (Gómez et al., 2019) indicated a good agreement between the estimated AI palpograms and the AI computed using the results of finite element model under incompressibility and plain strain conditions. This could indicate that the incompressibility assumption made to calculate the Model AI values (Eq. 4.3) is not valid for the PVA phantoms, and therefore not comparable with the estimated palpograms.

Second, the influence of residual stress/strain (RS/S) have been completely ignored in these studies. Indeed, neglecting RS/S in the structural analysis would bias the determination of the physiological spatial distribution of stresses but not the characterization of the estimated mechanical properties using palpography and modulography techniques.

Thirdly, in order to take into account the dynamics of the 2-D IVUS sequence, our computational finite element simulations were conducted in two dimensions by assuming the plane strain constraint. This assumption remains reasonable since the plaque length is large with regard to radial dimension, which is often the case for mature VPs with high degree of stenosis (Ohayon et al., 2005).

Another possible limitation of this study is that the pressure is linearly increasing and not pulsatile. Although this differs from realistic physiological conditions for IVUS sequence acquisitions, a linear pressure increase has a similar effect between to IVUS frames and allows to assess the performance of the AE-PT.

Finally, the three phantoms tested for this study were homogeneous. According to biomechanical and clinical studies, the morphology of vulnerable plaques is described as having a large necrotic core and a thin fibrous cap (Virmani et al., 2000). Since the AE-PT aims to characterize vulnerable plaques, it would be ideal to test it with phantoms with soft inclusions that could mimic a necrotic core. Nonetheless, this study was designed with homogeneous phantoms to provide an easier characterization of the orthotropic material properties and assess the *in vitro* performance of the AE-PT to detect changes in the anisotropic mechanical properties using IVUS sequences.

4.5 Conclusions and Perspectives

In this chapter, the *in vitro* performance of the anisotropic elasticity-palpography technique was investigated. The experimental mechanical characterization of the three Young's moduli of the anisotropic PVA phantoms was consistent between the results obtained with AFM and the ones from tensile tests, suggesting a successful characterization of the moduli. Anisotropic index values were computed using the AE-PT with IVUS sequences of the three phantoms. It was found that a higher estimated AI value was related to a higher anisotropy of the phantom material. The experimental values were used with an incompressible anisotropic medium model to calculate the Model AI. Although Model AI values differed from estimated RF IVUS AI values by a factor close to 5, previous positive results of the AE-PT (Gómez et al., 2019) suggest that the incompressibility assumption of the model might render it incomparable to the estimated AI. Therefore, additional analyses must be performed to characterize precisely the amplitudes of the 3 Poisson's ratios of our orthotropic phantoms based on the sequences of images acquired during our uniaxial test protocols (see Fig. 4.4).

Future works to improve this method should include the definition of an AI based on a homogeneous compressible orthotropic medium. This would mean that Equation 4.3 might need to be revisited to find a model that describes an AI equivalent to the RF IVUS AI computations. Further studies should also include phantoms with soft inclusions that could mimic vulnerable plaques.

From the results of this *in vitro* study and those of **Chapter 3** investigating the feasibility of the AE-PT, we can conclude that the AE-PT was able to capture changes in mechanical properties present between the three phantoms, estimating a higher value for higher anisotropic properties. This further demonstrates the potential of this technique to assess the evolution of the mechanical properties of plaques.

Part II

Balloon Angioplasty

Chapter 5

Background: Balloon angioplasty technique

Nomenclature:

All the following values are given by the manufacturer:

$D_{Nominal}$: Diameter of the balloon at the nominal pressure.

$P_{Nominal}$: The amount of pressure required to inflate the balloon to its labeled nominal diameter.

P_{Burst} : The pressure level a balloon is designed to accept without rupture.

D_{Burst} : Diameter of the angioplasty balloon at the burst pressure.

5.1 Interventional cardiology procedures

Among the interventional cardiology procedures available to treat coronary artery disease, angioplasty is one of the most widely used. It is a minimally invasive procedure that increases the lumen size with controlled barotrauma using a balloon-tipped catheter.

Before the advent of angioplasty, the only treatment option to restore coronary blood flow in clogged arteries was bypass surgery. The first human cardiac catheterization was conducted by Forssmann in 1929. Performing the procedure on himself, he inserted a catheter into a vein in his arm, slid it into his heart and verified the catheter position with an x-ray tube. Later, in 1941, the cardiac catheter was used by doctors Cournand and Richards for cardiac output measurement and drug delivery (Cournand et al., 1945). Forssmann, Cournand and Richards shared the Nobel prize in 1956 for their groundbreaking work (King, 1996). The first catheter-based revascularizations were achieved on peripheral arteries by Dotter and Judkins in 1964 using coaxial dilators to progressively enlarge blocked sites on femoral arteries (Dotter et al., 1968; Mauro et al., 2014). In 1975, Andreas Gruentzig developed the first angioplasty balloon, and the first human percutaneous transluminal coronary angioplasty (PTCA) was performed in 1977. Despite representing a major innovation in the treatment of cardiovascular disease, first-generation angioplasty balloons had a number of issues that hindered the procedure success and limited its application. Irregular dilation and low burst pressure of the balloons resulted in frequent rupture, while thick guide catheters could easily inflict vessel trauma (Chatterjee, 2013; Mauro et al., 2014). Over the following decades, these devices were improved by reducing catheter crossing profiles, increasing balloon inflation pressures and the development of guidewire technologies. These advances helped diminish the incidence of complications such as intimal dissection and coronary perforation.

Arterial recoil, restenosis and abrupt arterial closure continued to be common complications (Dash, 2013), evidencing the need to preserve the dilation results in the long term (Rockley et al., 2019). A solution, the coronary stent, was invented during the 1980s and cleared for vascular use by the U.S. Food and Drug Administration (FDA) in 1994 (Mauro et al., 2014). The stent is a scaffold designed to maintain patency on the widened area. The stent is mounted over an angioplasty balloon and delivered in the same way. When it reaches the affected section, the balloon is inflated, expanding the stent and is pressing it against the inner wall of the coronary artery. Once the balloon is deflated and removed, the stent maintains its position keeping the artery open. The first stents, what are now called bare metal stents (BMS), were made from stainless steel. Afterwards, alloys like platinum-chromium and cobalt-chromium were used to provide higher strength with thinner profiles. To avoid cell proliferation and promote healing, drug eluting stents (DES), metal stents coated with a drug-infused polymer, were developed. Currently, metal stents are the most widely used. However, once the blood vessel has been remodeled there is no need for the stent to remain inside, and its prolonged presence within the artery involves risks such as chronic inflammation, intra-stent restenosis and late thrombosis (Garg and Serruys, 2010; Zhang et al., 2011b). When taking this into account, a stent that disappears once the healing is complete seems preferable. Current bioabsorbable scaffolds (BRS) are made of polymer or a suitable metal like magnesium (Zhang et al., 2011b). Despite their potential to improve long-term outcomes, the performance BRS exhibit in the first years after implantation is not yet comparable to that of DES (Byrne et al., 2017). Drug-coated balloons that transfer medication to the arterial wall are also available, but they have not been widely adopted for coronary procedures due to the still superior results of DES (Byrne et al., 2017). So while stents were first used as a corrective measure after a failed angioplasty, their added benefits encouraged further improvements on these devices and they are now used in over 90% of all PCIs (King, 1996; Ludman, 2014).

The present chapter offers a brief review of the angioplasty procedure, focusing on the materials, mechanical properties and manufacturing process of the balloon catheter and related research on the subject.

5.2 The angioplasty procedure

Revascularization aims to improve the prognosis of patients presenting stable angina or acute coronary syndromes. The physician must analyze the patient's medical history, symptoms, coronary anatomy and co-morbidities to determine if PCI is the appropriate course of action.

Percutaneous transluminal coronary angioplasty (PTCA), commonly known as angioplasty or balloon angioplasty, is a commonly-performed minimally-invasive procedure to restore blood flow in clogged arteries. After administration of local anesthesia, the interventional cardiologist inserts a guiding catheter either into the radial or femoral artery, although the latter is often preferred (Chatterjee, 2013). This catheter serves not only for the delivery of all the equipment, but also to monitor intra-arterial pressure and inject radiographic contrast. The guiding catheter, usually with a diameter of around 2mm (6 in the French catheter scale), is advanced into the aortic arch until it reaches the coronary ostium (see Fig. 5.1a). From this point on, a guide-wire is inserted until it reaches the lesion, guiding the advance with X-ray imaging and contrast injections (Fig. 5.1b). Afterwards, the deflated balloon catheter is mounted on the guide-wire and directed to the lesion site (Fig. 5.1c). The balloon is then inflated compressing the plaque outwards against the arterial wall, causing deep fissures in the plaque that spread through the intima into the media (Fig. 5.1d) (Ludman, 2014). This step might be repeated at the discretion of the physician. Once the balloon is deflated, some arterial recoil occurs due to the elastic properties of the plaque (Fig. 5.1e). To maintain the artery open, a stent is often implanted, inserting and deploying the scaffold with a balloon catheter (Fig. 5.1f).

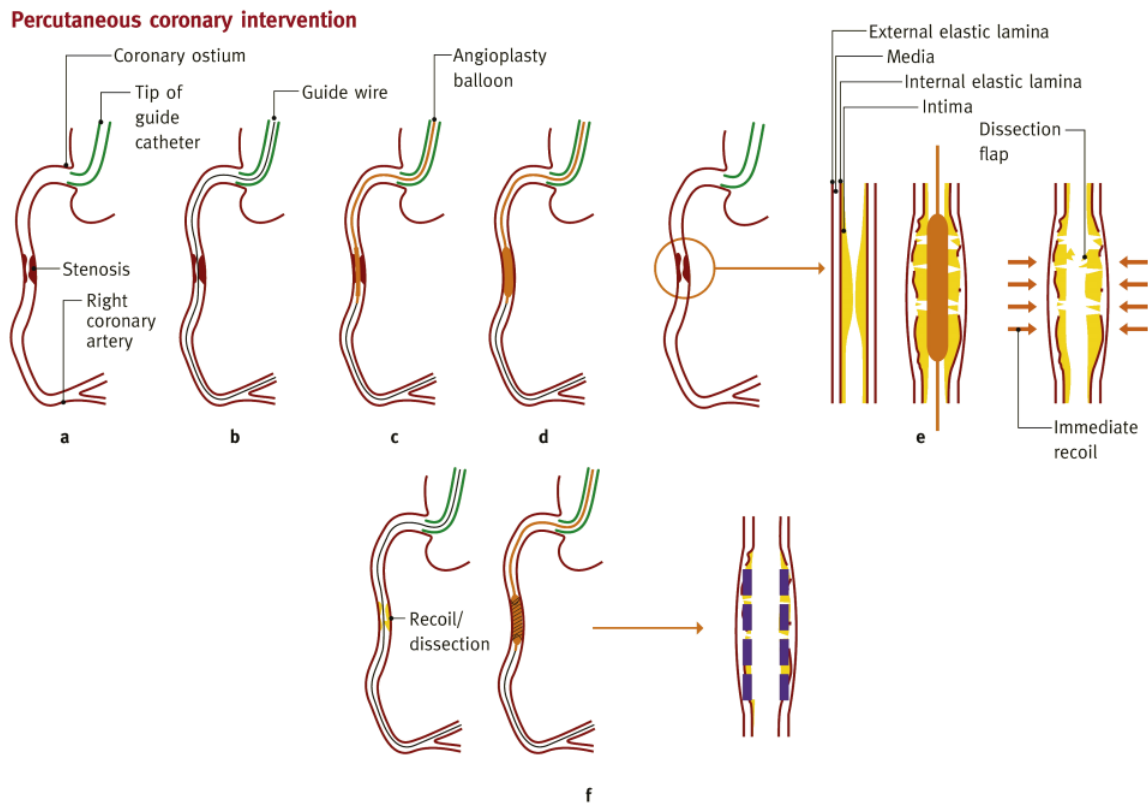


Figure 5.1: The angioplasty procedure. a) Insertion of a guide catheter from the femoral or radial artery up to the coronary artery ostium. b) Advance of a guide-wire to the lesion using X-ray and intermittent injection of radiographic contrast medium. c) A balloon catheter is slid over the guide-wire until it reaches the lesion site. d) Balloon inflation to compress plaque and restore blood flow. e) Instant elastic recoil. f) Stent placement to prevent further recoil and complications. *Adapted from Medicine, 42(9), Peter F. Ludman, Percutaneous coronary intervention, Pages 520-526, Copyright (2014), with permission from Elsevier.*

Nowadays, it is estimated that about 50% of the cases that would need bypass surgery are now being treated with angioplasty (Lambert et al., 2001), with this procedure being one of the most commonly performed in modern clinical practice (Tomberli et al., 2018). In contrast with bypass surgery, angioplasty results in shorter recovery times and lower treatment costs for patients (Rockley et al., 2019).

5.2.1 The balloon catheter

Balloon catheters have a crucial role in both the pre-dilation of the artery and the implantation of the stent. Underestimation of the balloon diameter can result in further damage of the arterial wall, while overestimation can cause underexpansion of the stent, which has been associated with in-stent restenosis and late-stent thrombosis (Fujii et al., 2005a). Therefore, an accurate control of the balloon diameter is needed to achieve adequate dilation and stent expansion, which will result in a higher success rate for PCI. To control the size of the balloon physicians refer to the compliance tables provide by balloon catheter manufacturers, which indicate the balloon diameters at given inflation pressures. The nominal pressure indicates the pressure at which the balloon achieves its designed diameter, and the rated burst pressure is the maximum statistically guaranteed pressure the balloon can withstand without failing. If the balloon is inflated above its rated burst pressure, the risk of rupture increases along with its possible derived complications such as local dissection and air embolization (Baim, 2005).

Balloon compliance is a measurement used by clinicians to indicate the ability of a balloon to

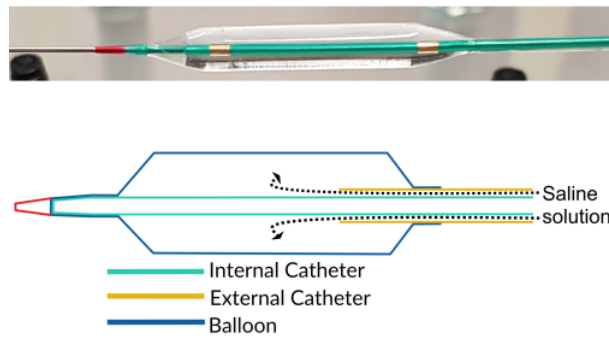


Figure 5.2: Top: Inflated PTCA balloon (Boston Scientific Maverick² Monorail model). Bottom: Model indicating the balloon film and internal and external catheters.

grow with pressure. It is defined as the diameter variation over the pressure variation between the nominal and rated burst pressures:

$$Compliance = (D_{burst} - D_{nominal}) / (P_{burst} - P_{nominal}) \frac{atm}{mm} \quad (5.1)$$

For example, if we take the manufacture's compliance curve for Boston Scientific's Maverick² PTCA balloon model with a labeled diameter of 3.5 mm and a length of 15 mm (Fig. 5.3), the nominal pressure is 6 atm, while the burst pressure and its corresponding burst pressure diameter are 12 atm and 3.81 mm, respectively. This gives a compliance of 0.052 atm/mm.

atm - kPa Pressure		3.5mm Balloon O.D.
5.0 - 507		3.45
6.0 - 608	NOMINAL	3.50
7.0 - 709		3.55
8.0 - 811		3.60
9.0 - 912		3.65
10.0 - 1013		3.71
11.0 - 1115		3.76
12.0 - 1216	RATED*	3.81
13.0 - 1317		--
14.0 - 1419		--

*Rated Burst Pressure and Stent Rated Burst Pressure. DO NOT EXCEED.

Figure 5.3: Picture of the compliance curve for the Boston Scientific's Maverick² PTCA. The nominal and rated burst pressures and diameters used to calculate the compliance of the balloon are given in this table.

Depending on the distensibility properties of the balloon, angioplasty catheters are divided into three categories (Karmelek, 2016):

Compliant balloons are used in applications that require high flexibility so that the balloon accommodates to the surrounding tissue and causes a full occlusion upon inflation. These devices are normally fabricated from polyurethane or silicone.

Semi-compliant or mid-pressure balloons are the standard; they achieve their nominal diameter at 6-10 bar (Byrne et al., 2017) and will continue to expand, until rupture, if

further pressure is applied. Often fabricated from Pebax (polyether block amide copolymers) or higher-durometer polyurethanes.

Non-compliant or high-pressure balloons are used for applications where high pressures up to 40 bar are required, such as for cases with highly calcified lesions or post-stent dilation. Their diameter increases slightly with pressure, about and their expansion is more uniform. They are typically fabricated from polyester, polyethylene terephthalate (PET) or nylon.

Standard PTCA balloons have cylindrical bodies with tapered ends (see Fig. 5.2 and 5.4). The balloon working length indicates the straight body section of the balloon. Typical PTCA balloon diameters range from 2 to 4 mm, with lengths going from 10 to 40 mm.

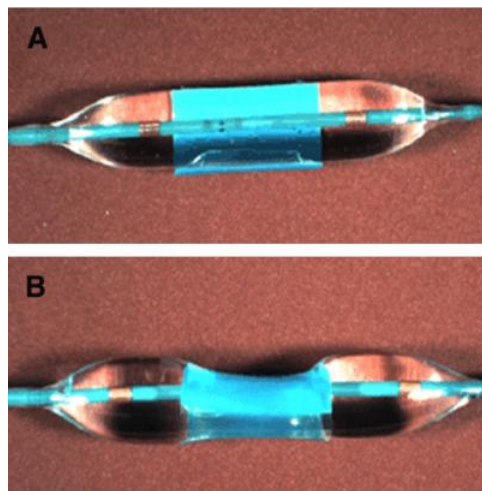


Figure 5.4: Bench test showing the different profiles between a noncompliant balloon (A) and a semi-compliant stent delivery balloon (B) during high-pressure (>14 atm) inflation. The semi-compliant balloon demonstrates a “dog bone” effect at the edge of the cylinder that can damage the vessel wall in vivo. *Reproduced from JACC: Cardiovascular Interventions, 1(1), Romagnoli et al., Drug-Eluting Stenting: The Case for Post-Dilation, Pages 520-526, Copyright (2008), with permission from Elsevier.*

The catheter shafts where balloons are mounted are fabricated from polymers like nylon, polyamide block copolymers, polyethylene, polyetherether ketone (PEEK) or thermoplastic polyesters. All balloon catheter materials are chosen for their high flexibility that allows them to access tortuous anatomies and high strength to sustain the inflation pressures while having the smallest possible thickness.

Manufacturing process

Three main manufacturing processes are required to fabricate balloon catheters: extrusion, blow molding and balloon-catheter assembly. Extrusion is used to produce plastic tubes or profiles by melting and pumping the selected polymer, forcing it through a tubing die that gives it the desired shape and subsequently cooling it to solidify the tube. Both the catheters and the preliminary shape for the balloon (the pre-form) are manufactured by extrusion. The pre-form of the balloon is then subjected to a specialized blow molding process that will transform it to its final shape (Fig. 5.5). During this process the pre-form is inserted into a glassform with the final diameter desired for the balloon. One end is welded shut and the other is connected to a compressed air supply. Heated jaws close around the part and warm it while pressure is maintained constant. Once a certain processing temperature is reached, high-pressure is applied and the tube is stretched axially to gain its final form. After cooling, the balloon is removed from the glassform and sterilized. (Sauerteig and Giese, 1999). Finally, the balloon and catheters

are assembled either with an adhesive or with a heat bonding process such as laser welding, and the balloon is folded to achieve a minimal crossing profile. Notice that both extrusion and blow-molding processes cause chain alignment in the polymer, inherently inducing anisotropy in the balloon (Eaton-Evans et al., 2006).

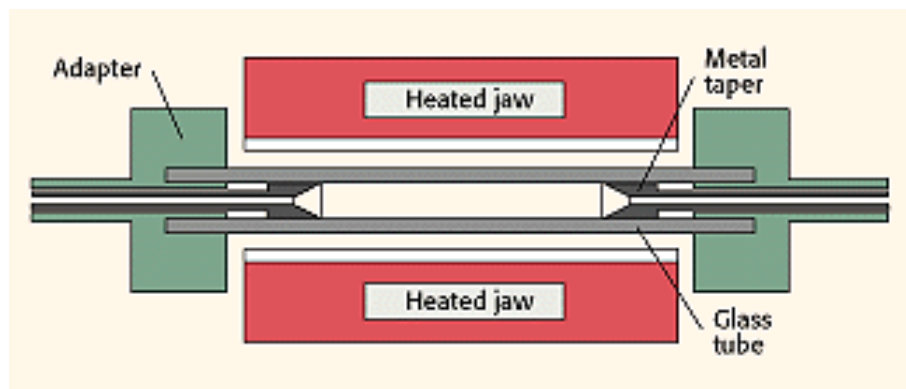


Figure 5.5: Top: Balloon blow molding process diagram.

5.2.2 Computational studies of balloon catheters

Experimental validation of balloon or stent deployment is not very usual (Azarnoush et al. (2018)) due to the technical difficulties it poses and the elevated cost of the devices. Therefore, finite element analysis (FEA), a well-established numerical technique, becomes an exceptional tool to virtually analyze the performance of PCI. FEA provides valuable information to help determine appropriate process parameters (i.e. balloon diameter, inflation pressure and length), predict the outcome of a procedure under specific constraints, and test devices in development stages (Holzapfel et al., 2002). Most FEA efforts in angioplasty are dedicated towards stent deployment, with models including balloon-artery (Holzapfel et al., 2002) stent-artery (Auricchio et al., 2001; Migliavacca et al., 2002, 2005; Brand et al., 2014), stent-balloon (Wang \tilde{A} et al., 2006; De Beule et al., 2008) or balloon-stent-artery (David Chua et al., 2004; Liang et al., 2005; Mortier et al., 2009; Capelli et al., 2009; Mortier et al., 2010; Gastaldi et al., 2010; Morlacchi et al., 2013; Schiavone and Zhao, 2015) interactions.

In general, finite element models are defined by a zero-stress geometry, a set of material properties, and boundary conditions.

Balloon geometry in FEA studies can be simplified as a thin-walled tube (Fig. 5.6a) (David Chua et al., 2004; Liang et al., 2005; Raamachandran and Jayavenkateshwaran, 2007), or use a full, tapered geometry (Kioussis et al., 2008a; Capelli et al., 2009; Mortier et al., 2010). While studies of plain balloon angioplasty can justify the use of a balloon geometry in its deployed state, modeling stent deployment is a different story. The study of De Beule et al. (2008) highlighted the importance of modeling stent deployment with folded balloons, finding that only this configuration produced results consistent with manufacturer-provided inflation curves. This was later corroborated by Martin and Boyle (2013) and Schiavone and Zhao (2015). Therefore, several studies consider the more realistic and complex geometry of the pre-deployment shape of the balloon when it is wrapped around the catheter (Fig. 5.6b), obtaining this folded profile either with a preliminary analysis with negative pressure (Gastaldi et al., 2010; Morlacchi et al., 2013) or by reconstructing it from micro-CT images (De Beule et al., 2008; Mortier et al., 2009; Martin and Boyle, 2013).

Modeling realistic balloon mechanical properties is a complex task. Not only is the balloon film anisotropic, but balloon deployment and inflation kinematics also come into play. First,

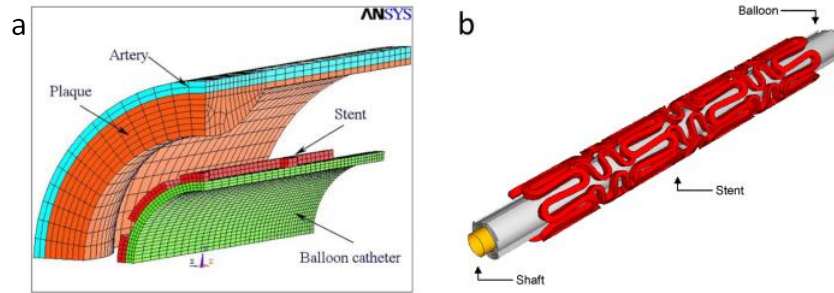


Figure 5.6: Different geometries used for FE analyses involving balloon catheters. a) FE model of an artery-stent-balloon assembly depicting a simplified balloon geometry. Reprinted from *David Chua et al. (2004)*, with permission from Elsevier. b) Geometrical model of a commercially available stent and part of the delivery system (inner shaft and non-tapered part of the folded balloon) Reprinted from *De Beule et al. (2008)*, with permission from Elsevier

deployment occurs at low pressures and as the pressure continues to rise, balloon diameter increases until it reaches a certain load (determined by its mechanical properties and geometry) where it starts exhibiting nonlinear stiffening (Kiouisis et al., 2007). While the circumferential geometry of the balloon changes during inflation, axial stretching remains minimal. The model described in Kiouisis et al. (2008a) describes the balloon with two material axes, on the circumferential and axial directions, each with its own set of mechanical properties adapted to the peculiar behavior of the balloon, resulting in a realistic inflation curve (see Fig. 5.7).

However, the vast majority of FE models tend to simplify the behavior and describe the balloon as isotropic with either linear-elastic (Holzapfel et al., 2002; Schiavone and Zhao, 2015) or hyper-elastic (David Chua et al., 2004; Liang et al., 2005; Eftaxiopoulos and Atkinson, 2005; Schiavone and Zhao, 2015; Li et al., 2017; Azarnoush et al., 2018) properties. To derive the balloon material properties some studies fit the selected material model to the compliance data provided by the manufacturer (De Beule et al., 2008; Mortier et al., 2009). Another solution is to use experimentally obtained diameter-pressure curves to adjust the material model.

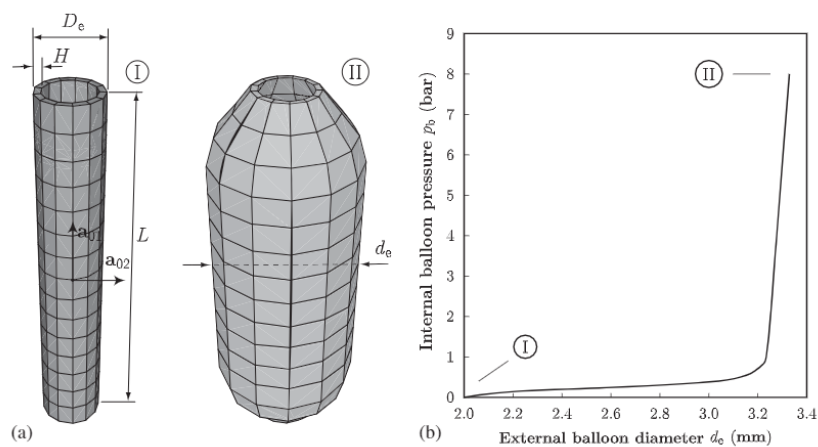


Figure 5.7: Finite element simulation of the dilation of a Groentzig-type balloon catheter: (a) geometry and computational mesh of the undeformed (I) and deformed (II) configurations of the balloon and (b) applied internal balloon pressure P_b versus external balloon diameter d_e . Initially, the balloon expands quickly and only a low internal pressure is needed for its deformation. As the pressure exceeds approximately 1 bar, the balloon stiffens and deforms only slightly. Reproduced from *Kiouisis et al. (2008a)* with permission from John Wiley and Sons.

Experimental work to study angioplasty

Although computational analyses provide an effective way to test balloon deployment, they are still approximations and need to be validated using experimental data (Liang et al., 2005). Characterization of angioplasty balloons is mostly oriented towards its performance characteristics, such as pressure-diameter curves and burst pressures. Inflation curves for balloons and stents are obtained either from manufacturer provided data (De Beule et al., 2008; Mortier et al., 2009) or experimentally by optically monitoring the device during inflation (Wang et al., 2006; Kioussis et al., 2008b). More recently, intravascular imaging has been used to monitor balloon deployment and inflation inside arterial phantoms (Azarnoush et al., 2018).

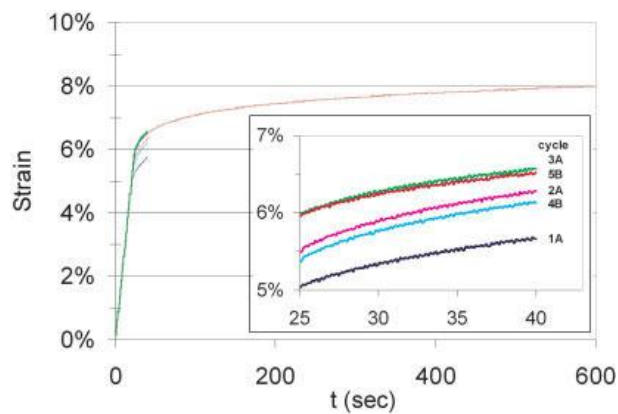
As mentioned in a previous section, the mechanical properties of these components are influenced not only by the material chosen for their fabrication, but also by the forming processes. Therefore, to obtain accurate material properties, characterization should be made using the formed materials (Daver et al., 2010). In the case of balloon catheters their small dimensions pose an additional challenge, limiting the amount of material available for testing and the possible testing methods. This, along to the high cost of the devices, could explain why such few efforts have been made to characterize the mechanical properties of its individual components, namely the catheters and the balloon film.

The internal and external catheters of the balloon are fabricated from different material, thus exhibiting distinct mechanical properties. Todo et al. (2016) described a theoretical model to describe the deformation of dual-layered catheters used for balloon angioplasty, validating it with tensile tests. Their experiments confirmed that, for the catheters used, the outer layer exhibited greater resistance to rupture while the inner layer had a much longer elongation of fracture.

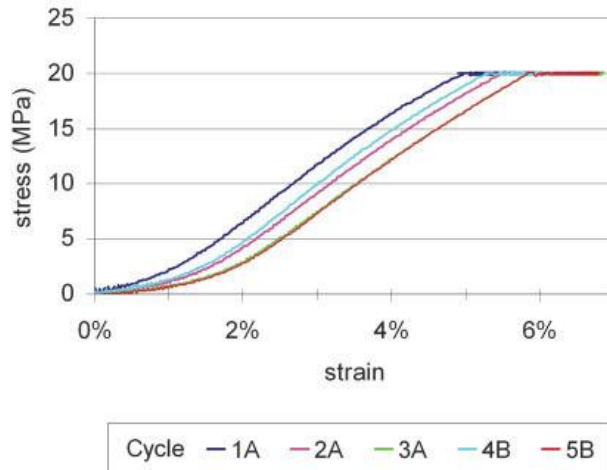
Balloon polymer films have been characterized using inflation tests along with pseudotensile creep tests to analyze the effect of reprocessing (reuse) in their mechanical properties (Fedel et al., 2006). For the creep tests, samples were loaded at a constant displacement rate until they reached their nominal force, calculated from the balloon's nominal pressure using Laplace's law, holding the load for 15 seconds before releasing the specimen. After repeating this twice, samples were left to recover for 1 hour before the test was repeated two more times. Their results (Fig. 5.8) showed that the balloon film presented non-linear viscoelastic behavior when maintained under tension. Also, residual strain was present between each of the elongations, which was partially reabsorbed after the resting period of 1 hour. This suggests the balloon material has a viscoplastic behavior.

5.3 My next steps and works performed

As previously mentioned in this chapter, angioplasty balloon inflation is often studied using computational analysis by using the mechanical properties derived from the inflation pressure-diameter curve provided by the manufacturer, which presents some limitations. Indeed, previous studies (More et al., 1996; Hehrlein et al., 2001) and the observations within our own group suggest that manufacturer compliance tables are not completely accurate. Moreover, most of these models only consider one inflation, when in reality, the interventional cardiologist often needs to inflate the balloon more than once during an angioplasty procedure. Therefore, before using an angioplasty balloon, it is essential to know its viscoelasto-plastic mechanical properties. Indeed, the balloon has a memory and its mechanical response will depend strongly on the stresses (i.e. inflations during clinical procedure) it has previously undergone.



(a)



(b)

Figure 5.8: Pseudotensile tests for a 3.0-mm balloon. Polymer samples were loaded at 3 mm/min up to nominal load (i.e. 20 MPa), and the load was then held constant for 15 s. Three consecutive loading cycles (1A–3A) were performed, followed by a resting period of 1 h. Specimens were then loaded twice more (cycles 4B–5B) with a loading time of 10 min for the final cycle (5B). (a) Each device tested showed polymers creep within the 15-s loading time. (b) Stress–strain curves evidenced a progressive deformation of balloon materials, partially reabsorbed within 1-h resting time. *Reproduced from Fedel et al. (2006) with permission from John Wiley and Sons.*

Few efforts have been done to experimentally obtain the viscoelasto-plastic mechanical properties of the balloon polymer film. Testing difficulties related to sample size and device high-cost may be behind the lack of more experimental studies for angioplasty balloons. From these studies, there is evidence of a viscoelasto-plastic behavior of the balloon film. However, having precise experimental data could be of great value to improve our understanding of the inflation dynamics of the balloon.

For all these reasons, I decided to investigate the viscoelasto-plastic properties of the angioplasty balloon. On the recommendation of Dr. Finet, we focused our experimental studies on the Boston Scientific Maverick² balloon (3.5mm diameter x 15 mm length). To achieve this, a series of characterization tests, presented in **Chapter 6**, were designed to characterize and highlight these mechanical properties:

First, pressure-diameter inflation curves were obtained in collaboration with Dr. Guillaume Cellier at the Hospital Louis-Pradel in Lyon, by performing consecutive inflation tests. Later, to improve these tests, an experimental bench and protocol were designed and applied to obtain higher definition in pressure and diameter measurements from inflation and short-time creep tests.

Then, uniaxial tensile tests and cyclic tensile tests were performed at Tecnológico de Monterrey in Mexico, in collaboration with Professor Alex Elías. A tensile test machine designed for biological samples was used to obtain accurate force measurements and high-resolution images during these tests.

Finally, in **Chapter 7**, the results of these tests were used for a modeling approach that aimed to isolate the viscous, elastic and plastic responses of the balloon polymer film. This characterization could be later used to create a model to accurately predict pressure-diameter curves for consecutive inflations of the balloon.

Chapter 6

Experimental characterization of the viscoelasto-plastic behavior of balloon catheters: Application to Boston Scientific's Maverick² model

6.1 Introduction

Balloon catheters have a crucial role in both the pre-dilation of the artery and the implantation of the stent. Underestimation of the balloon diameter can result in further damage of the arterial wall, while overestimation can cause underexpansion of the stent, which has been associated with in-stent restenosis and late-stent thrombosis (Fuji et al., 2005b). Therefore, an accurate control of the balloon diameter is needed to achieve adequate dilation and stent expansion, which will result in a higher success rate for percutaneous transluminal coronary angioplasty (PTCA).

The majority of balloon catheter manufacturers provide compliance tables that relate the balloon diameters at given inflation pressures. However, previous studies (More et al., 1996; Hehrlein et al., 2001) as well as our own group's clinical observations suggest that balloon compliance data (pressure vs diameter) for angioplasty catheters may not be accurately predicted by the manufacturers' published data, neither *in vivo* nor *in vitro*. *In vivo* balloon size is likely to be affected by factors such as lesion characteristics and elasticity of the vessel wall (More et al., 1996) as well as polymer material properties and compliance of the balloon in question (Hehrlein et al., 2001). Since the interventional cardiologist takes these compliance tables as a guide when using these devices, such inaccuracies could have important clinical implications for performing precise angioplasty procedures. For example, overexpansion of the arterial wall generates mechanical injury, which triggers pathological responses that may hinder PCI results (Kioussis et al., 2009).

In addition to compliance tables, manufacturers also indicate the working range. This inflation range is between (1) the nominal pressure required for the balloon to reach its labeled diameter, and (2) the rated burst pressure, at which 99.9 % of balloons can survive with 95 % confidence. Angioplasty protocols often include consecutive inflations and deflations within this defined working range. Previous studies (Fedel et al., 2006) have highlighted the viscoplastic mechanical behavior of the balloon film, which results in compliance variations between consecutive pressurizations. Understanding the mechanical phenomena involved in

balloon inflation can help develop tools and guidelines for more accurate and successful inflation protocols.

This chapter focuses on the mechanical characterization of a specific model of PTCA dilation catheter, namely the Maverick² (Boston Scientific, Santa Clara, CA, USA). A series of geometrical measurements and mechanical tests were performed on the PTCA balloon catheter components (polymeric film and catheters) to define its behavior and serve as a base to create an inflation model.

6.2 Materials and methods

The Maverick² PTCA dilation catheter chosen for this study has a 3.5 mm nominal diameter at 6 atm, with a working length of 15 mm. The compliant balloon is mounted on the tip of the catheter, which is divided in two: an internal catheter (green) where the gold markers are located and that slides over the guidewire, and an external catheter (transparent) used to inflate the balloon with saline solution (see Fig. 6.1).

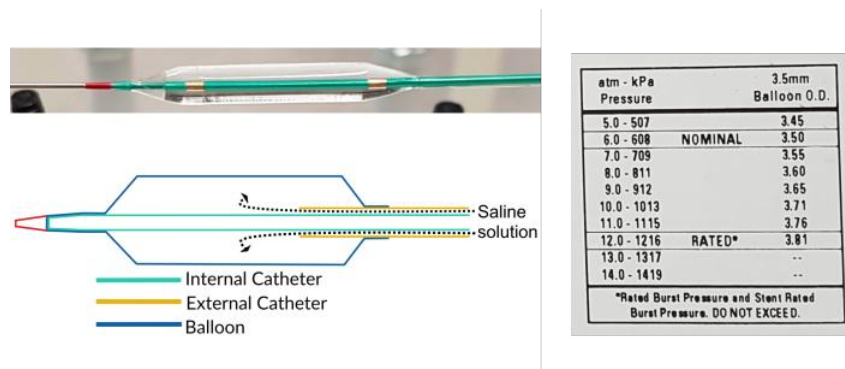


Figure 6.1: Left, top: Deployed Maverick² balloon. Left, bottom: Diagram of the balloon catheter. Right: Compliance chart provided by the manufacturer (Boston Scientific) indicating a nominal diameter of 3.5 mm at a nominal pressure of 6 atm, and a burst pressure of 12 atm.

6.2.1 Balloon catheter measurements

First, the key features of the balloon were measured using an stereomicroscope (SteREO Discovery.V8, Carl Zeiss). These measurements included the diameters and thicknesses of both catheters (Fig. 6.3), as well as distances between the main features of the balloon. At least five measurements were taken for each feature. All measurements are summarized in Figure 6.2.

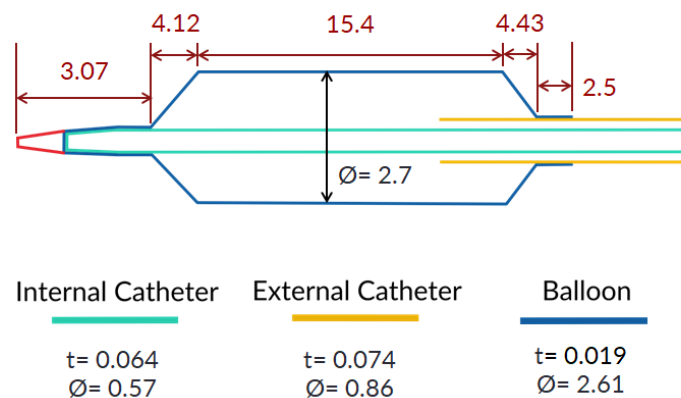


Figure 6.2: Diagram of the balloon catheter indicating the main features and dimensions. Thicknesses (t) and diameters (\varnothing) of the internal and external catheters, and the balloon are also given. All measurements are in mm.

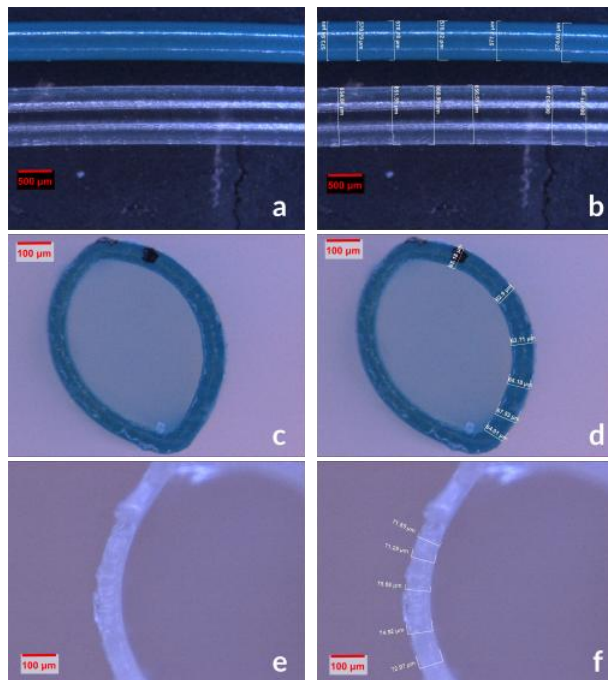


Figure 6.3: Images and measurements obtained from the catheters with the stereo microscope. a,b) Internal (green) and external (transparent) catheter diameters. c,d) Measurements of the internal catheter thickness. e,f) Measurements of the external catheter thickness.

To measure the balloon film thickness, samples of 2x2 mm were imaged with a digital holographic microscope (Lyncéetech, Switzerland) to obtain an accurate profile of the film edges (see Figure 6.4). From the resulting images, 25 measurements were taken with the software ImageJ (NIH, Bethesda, MD, USA), resulting in a thickness of 19 ± 0.67 microns (mean \pm SD). These experiments were performed in collaboration with Dr. Yves Usson from TIMC-IMAG Laboratory in Grenoble.

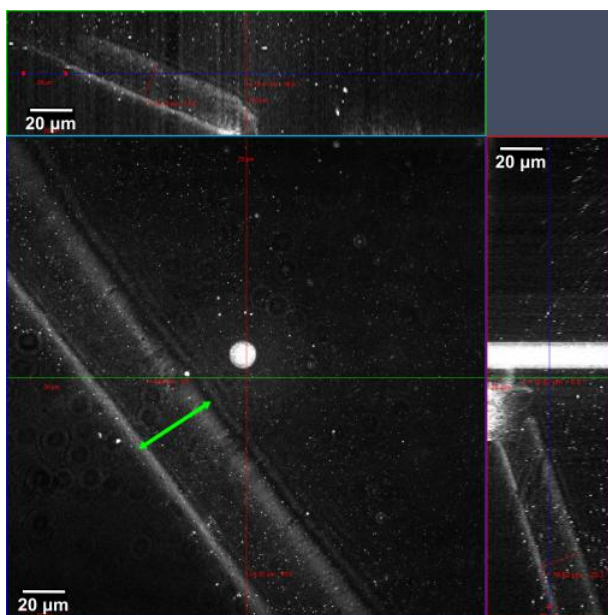


Figure 6.4: Images of the balloon film obtained with a holographic microscope, the green arrow indicates the thickness of the film. Thickness measurements were carried out using ImageJ software.

6.2.2 Balloon catheter inflation experiments

Static inflation tests

A first set of inflations were performed in collaboration with Guillaume Cellier, PhD, at the Louis Pradel Cardiology Hospital in Lyon, France. The objective was to obtain a general idea of the balloon pressure-diameter dynamics for consecutive inflations. The test was monitored by an electro-optical camera (Edmund, GB) attached to an E-Z00M6 binocular microscope (Edmund, GB). All images were treated through the uEye Cockpit software (IDS Imaging Development Systems GmbH, Obersulm, Germany) and the measurements were later performed using ImageJ.

For all of these test protocols, a picture was acquired at each pressure step. Diameter measurements were performed at three different sites (Fig. 6.5), a distal and proximal diameter corresponding to the internal end of each radiopaque marker, and one more measurement at the center of the balloon. The reported diameter at each step is the mean of these three values. Moreover, the distance between the two radiopaque markers (l_z) was also recorded during these pressure inflations (see Fig. 6.5).

First, the balloon was filled with water at 37°C and fixed on a horizontal plane next to a millimetric ruler to set the scale at the image processing stage. To pressurize the balloon and monitor the pressure, a PTCA manual inflator was used. The balloon was subjected to three inflations with increments of 2 atm, until 20 atm. Results of this test are shown in Figure 6.6

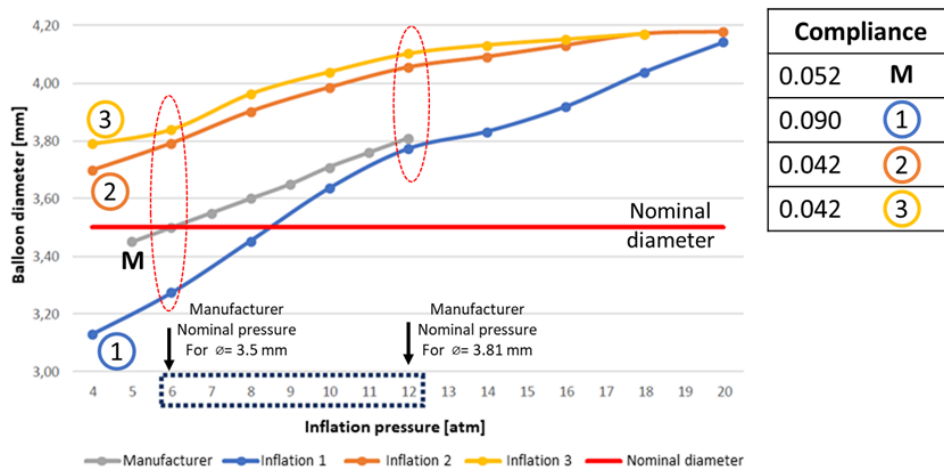
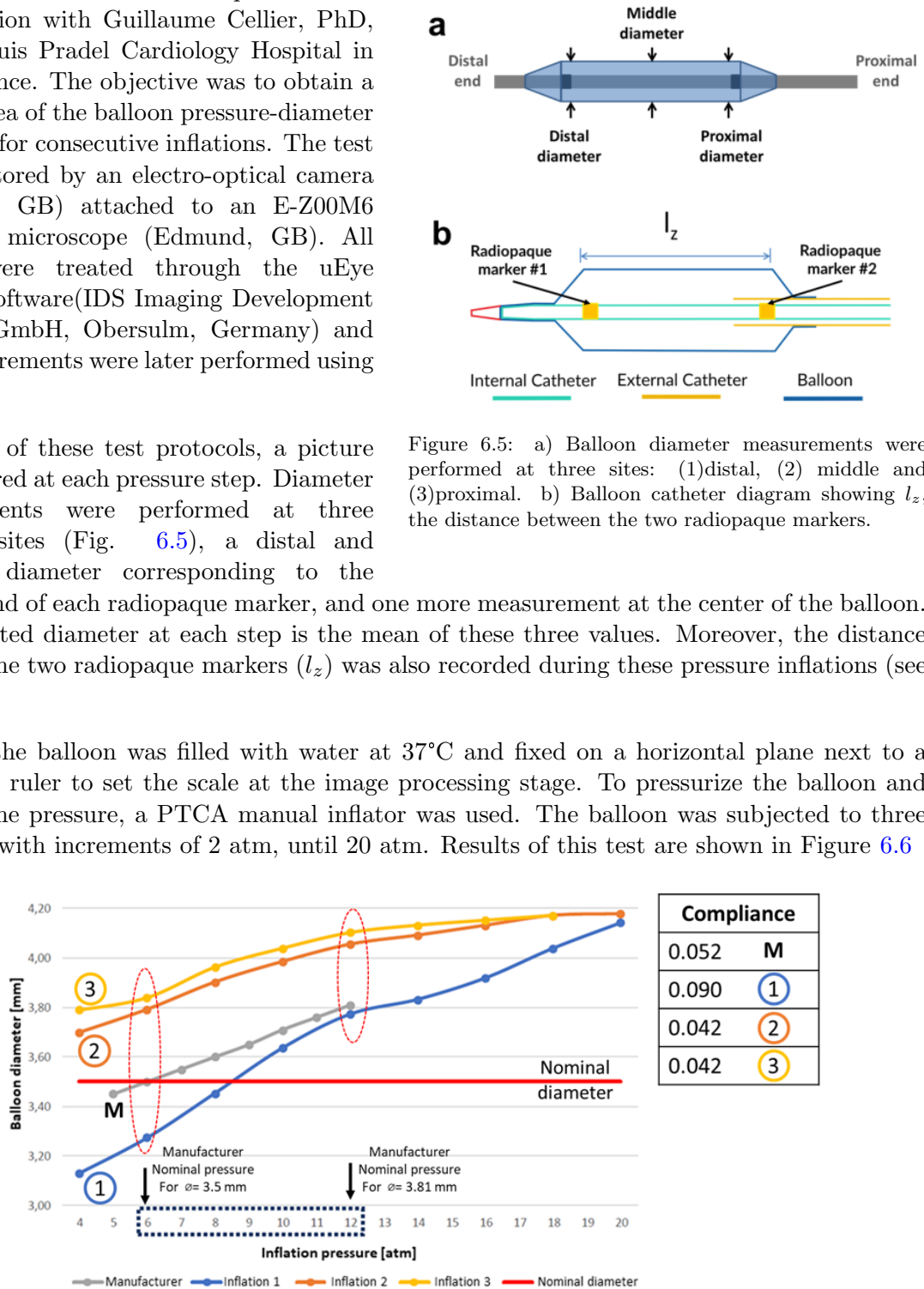


Figure 6.6: Inflation of a Boston Scientific Maverick² balloon catheter in air at ambient temperature. Three consecutive inflations to 20 atm were performed. The manufacturer curve (M) is also plotted. Compliance values for each curve are given in the table at the right. Adapted from Cellier (2017).

Another balloon was inflated under these conditions (Fig. 6.7), but this time the first inflation

was only until 12 atm (the rated burst pressure for this balloon), the next inflation was until 20 atm, and for the final inflation, pressure was increased until rupture (18 atm).

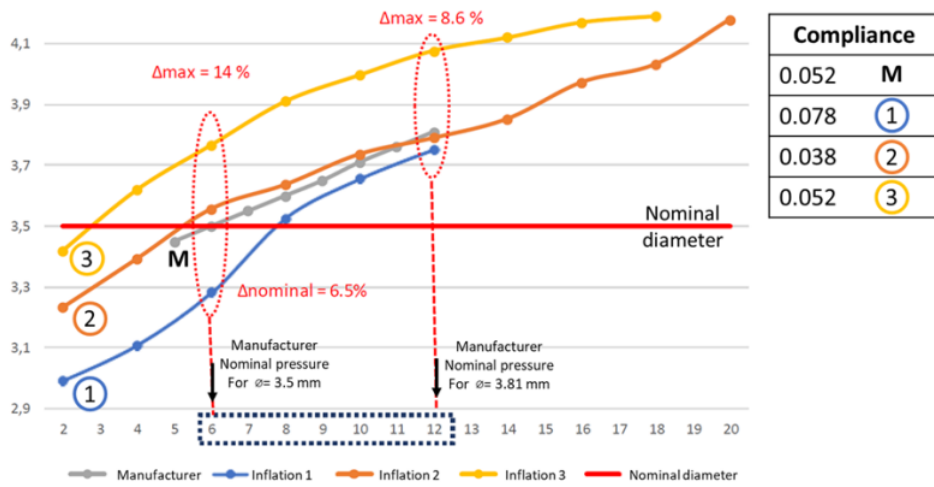


Figure 6.7: Inflation of a Boston Scientific Maverick² balloon catheter in air at ambient temperature. Three consecutive inflations, the first until 12 atm (the rated burst pressure for this balloon), the second until 20 atm and the third one until rupture (18 atm). The anufacturer compliance curve is also plotted (M). Compliance values for each curve are given in the table at the right. Adapted from Cellier (2017).

Another set of inflations was performed, this time with the balloon submerged in water at 37°C. The first inflation went up to 20 atm and the second up to 18 atm. The resulting curves (see Fig.6.8) had a similar behavior to those of the inflations at room temperature, showing a significant change between the first and second inflation profiles.

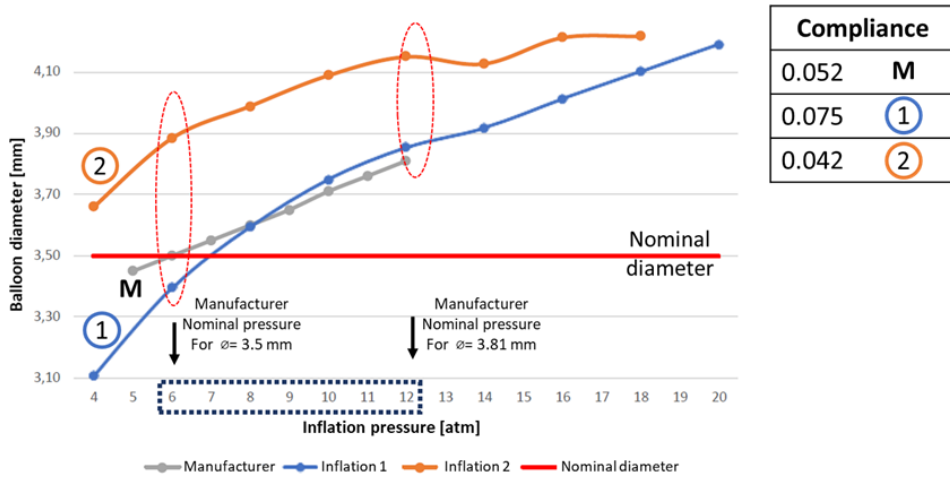


Figure 6.8: Inflation of a Boston Scientific Maverick² balloon catheter submerged in water at 37°C. Two consecutive inflations, the first two until 20 atm and the manufacturer compliance curve (M) are plotted. Compliance values for each curve are given in the table at the right. Adapted from Cellier (2017).

In a different test, the balloon was subjected to two inflations in air at ambient temperature (with the same 2 atm increments) up to 20 mmHg, each cycle separated by only a few minutes. The balloon was left to rest for 16 hours before repeating the same protocol. The results (Fig. 6.9) suggest an elasto-plastic behavior, since there was little to no recovery between the second inflation at T=0 and the first inflation at T=16h. A recovery would have indicated a stronger viscoelastic behavior.

Longitudinal compliance was also assessed by fixing the balloon at the proximal segment

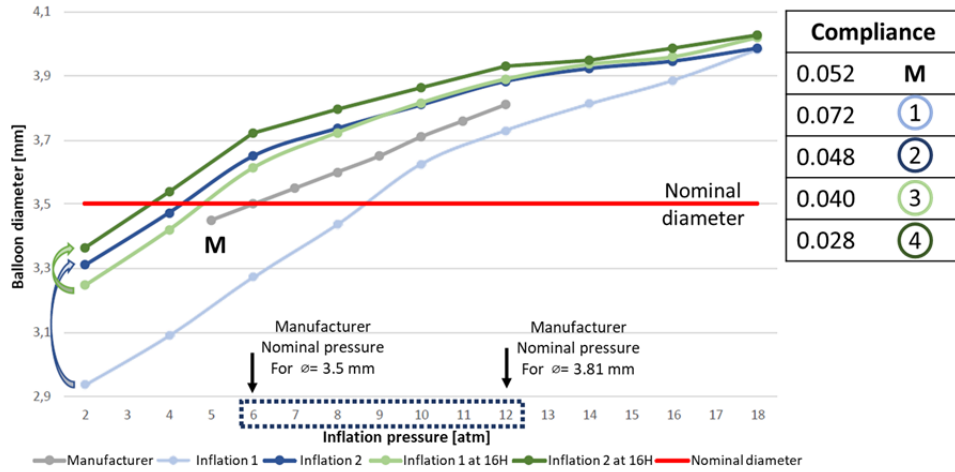


Figure 6.9: Inflation of a Boston Scientific Maverick² balloon catheter in air at ambient temperature. Two successive inflations were performed on the balloon at $T=0$. Then, after $T=16$ hours, the same two inflations were repeated. This experiment highlights the viscoelastic properties of the balloon polymer film. *Adapted from Cellier (2017)*.

and comparing the position of the radiomarkers (attached to the internal catheter). Although circumferential compliance is greater, as expected, there is also an observable longitudinal enlargement of the balloon at higher pressures (Fig. 6.10).

These results served as a basis to define further testing, including inflation tests with a higher pressure resolution, as well as tensile tests.

New dynamic inflation bench

An original experimental setup (Fig. 6.11) was implemented to apply and control the pressure and to measure the temporal variation of the balloon diameter. A PTCA manual inflator was used to apply pressure inside the balloon and to monitor the pressure with a better resolution, a pressure sensor (Gems Sensors, 0-40 bar range, resolution of 0.1 bar) was used. To measure the diameter of the balloon, image sequences were acquired with a Chameleon 1.3 MP camera (FLIR Integrated Imaging Solutions Inc., BC, Canada) attached to a Nikon SMZ 1000 stereo microscope (Nikon Instruments Inc., NY, USA), that resulted in an image resolution of 198 pixels per mm with a maximum frame rate of 18 fps. To enhance contrast between the balloon and its surroundings, the distilled water used to inflate the balloon was dyed blue and the pictures were taken against a red background. These photographs were analyzed with ImageJ and Matlab (MathWorks, Inc., MA, US) to obtain the diameter at each step (Fig. 6.12).

Inflation test

Consecutive inflation-deflation tests were performed on one balloon. Pictures were taken to obtain the balloon diameter at each pressure step. A total of 8 inflations were made, always starting from $P_0 = 0$, and up to a specific pressure P_1 by step of (ΔP) . Notice that our protocol increased P_1 with each inflation from 1 to 20 atm following the protocol defined in Table 6.1. For each inflation, once P_1 was reached the pressure was instantaneously released, returning to $P_0 = 0$; an picture was taken at this moment as well. Inflation pressure steps (ΔP) were also adjusted depending on the desired data points at each step (Table 6.1). An increment ΔP was applied every 2 seconds. The waiting time between each inflation was 15 seconds. Plots in

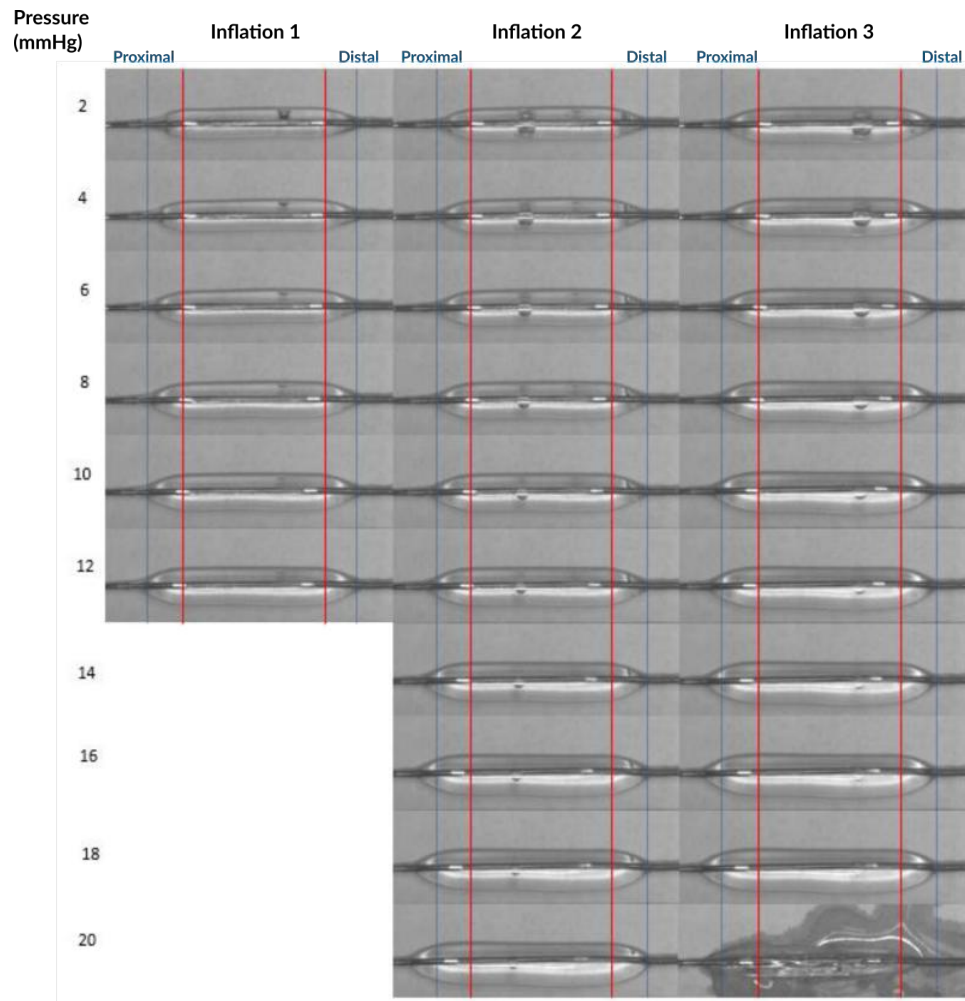


Figure 6.10: Three consecutive inflations of a Boston Scientific Maverick² balloon catheter in air at ambient temperature. The pictures show a small enlargement in the longitudinal dimensions of the balloon due to the increase in pressure. Adapted from Cellier (2017).

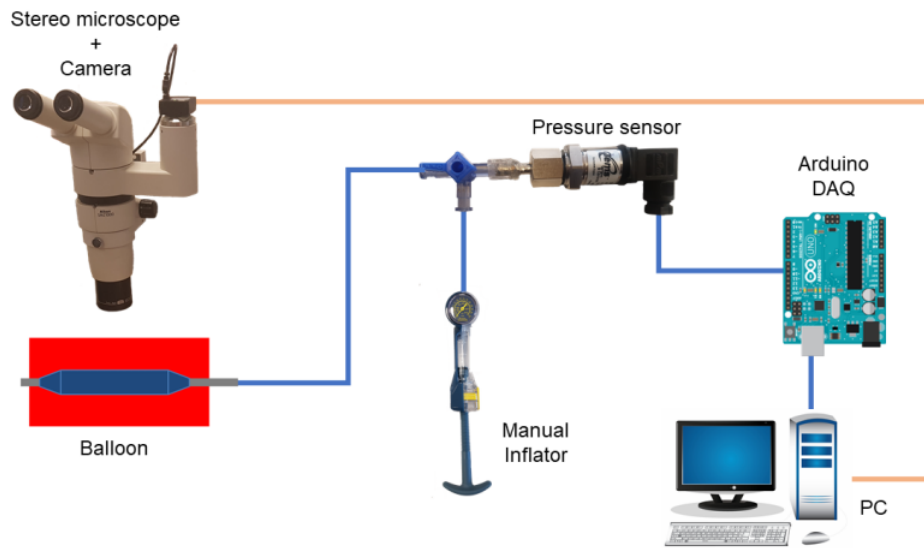


Figure 6.11: Experimental setup for dynamic inflation bench for the balloon. Pressure was applied with a manual angioplasty balloon inflator, and it was monitored using a pressure sensor (0.1 bar resolution) and a data acquisition card connected to a PC. Diameter was extracted (post-processing) from pictures taken using a camera attached to a stereo microscope.

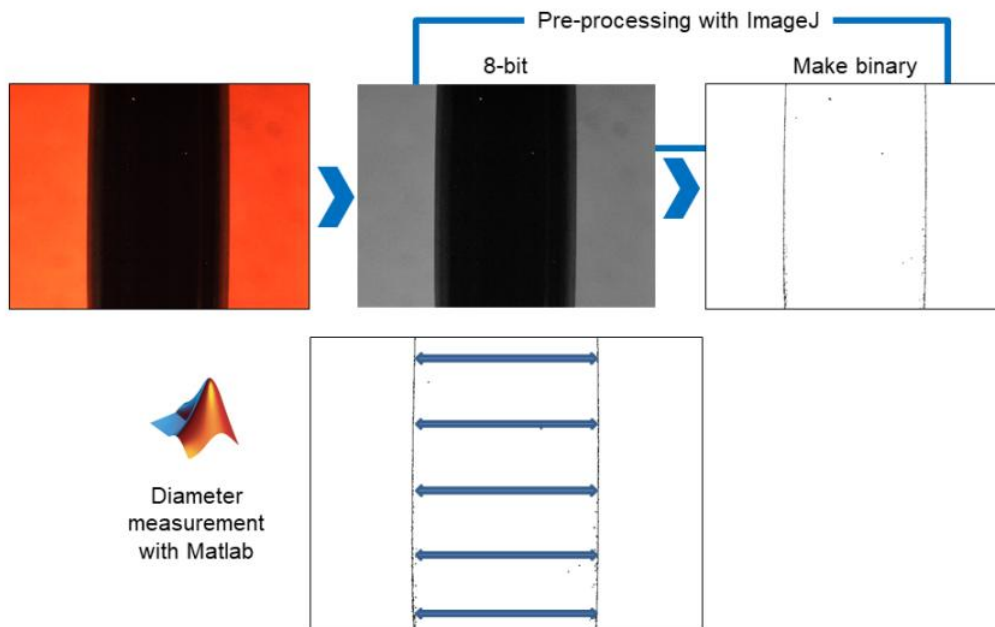


Figure 6.12: Image processing to obtain the balloon diameter. First, high-contrast images of the center of the balloon were acquired with a resolution of 198 pixels per mm. Using ImageJ, the images were pre-processed to find the edges of the balloon. Finally, using Matlab, the diameter at each line (corresponding to a longitudinal position) and an average diameter were calculated for each image.

Figures 6.13 to 6.14 present the results of these tests. We can again observe the plasticity effect, but this time with more precise pressure control and resolution. There is also a clear recovery during the 15 seconds between each inflation, as evidenced by the return points of each curve (Figure 6.14).

Table 6.1: Consecutive inflation protocol for a Maverick² balloon

Inflation	P_0 [bar]	P_1 [bar]	ΔP [bar]
# 1	0	1	
# 2	0	2	0.2
# 3	0	4	
# 4	0	6	0.5 (0-4) 0.2 (5-6)
# 5	0	8	0.5 (0-6) 0.2 (6-8)
# 6	0	12	
# 7	0	16	0.5
# 8	0	20	

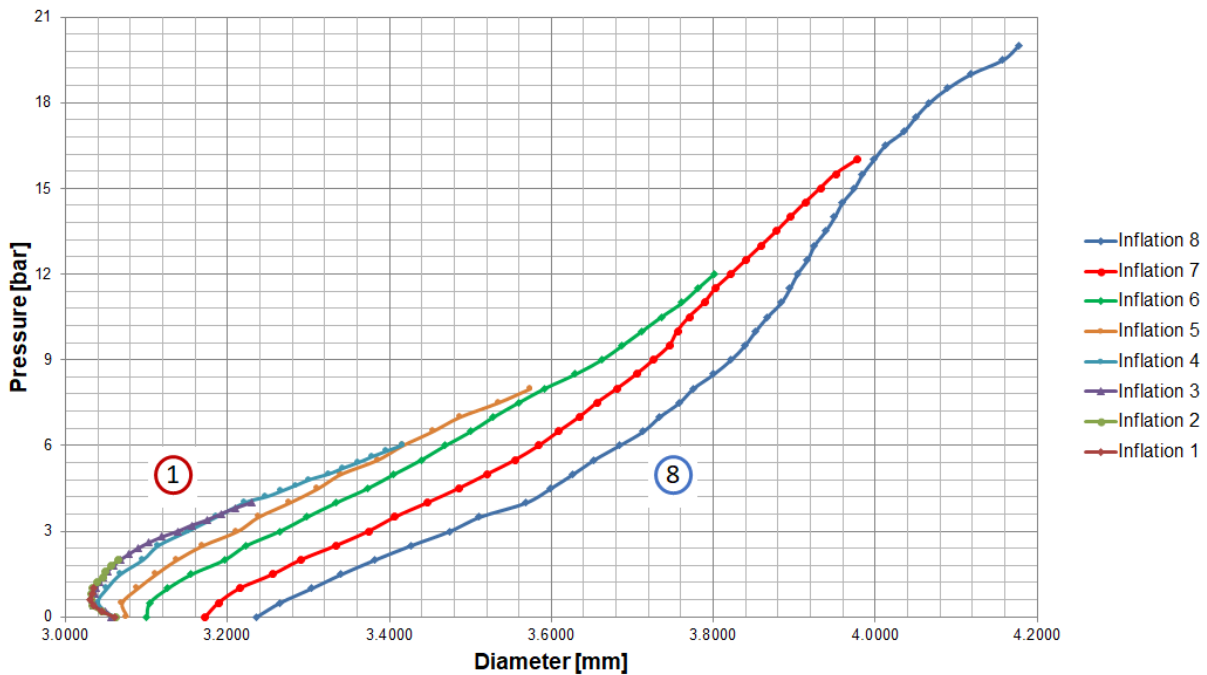


Figure 6.13: Diameter vs pressure results of the 8 consecutive inflations of the Maverick² balloon catheter.

Short-time inflation creep test

One balloon was subjected to a constant pressure of 6 bar for 20 seconds and then released. Images were taken at a rate of 100 ms to obtain the creep and recovery curves. The results of this test are shown in Figure 6.15.

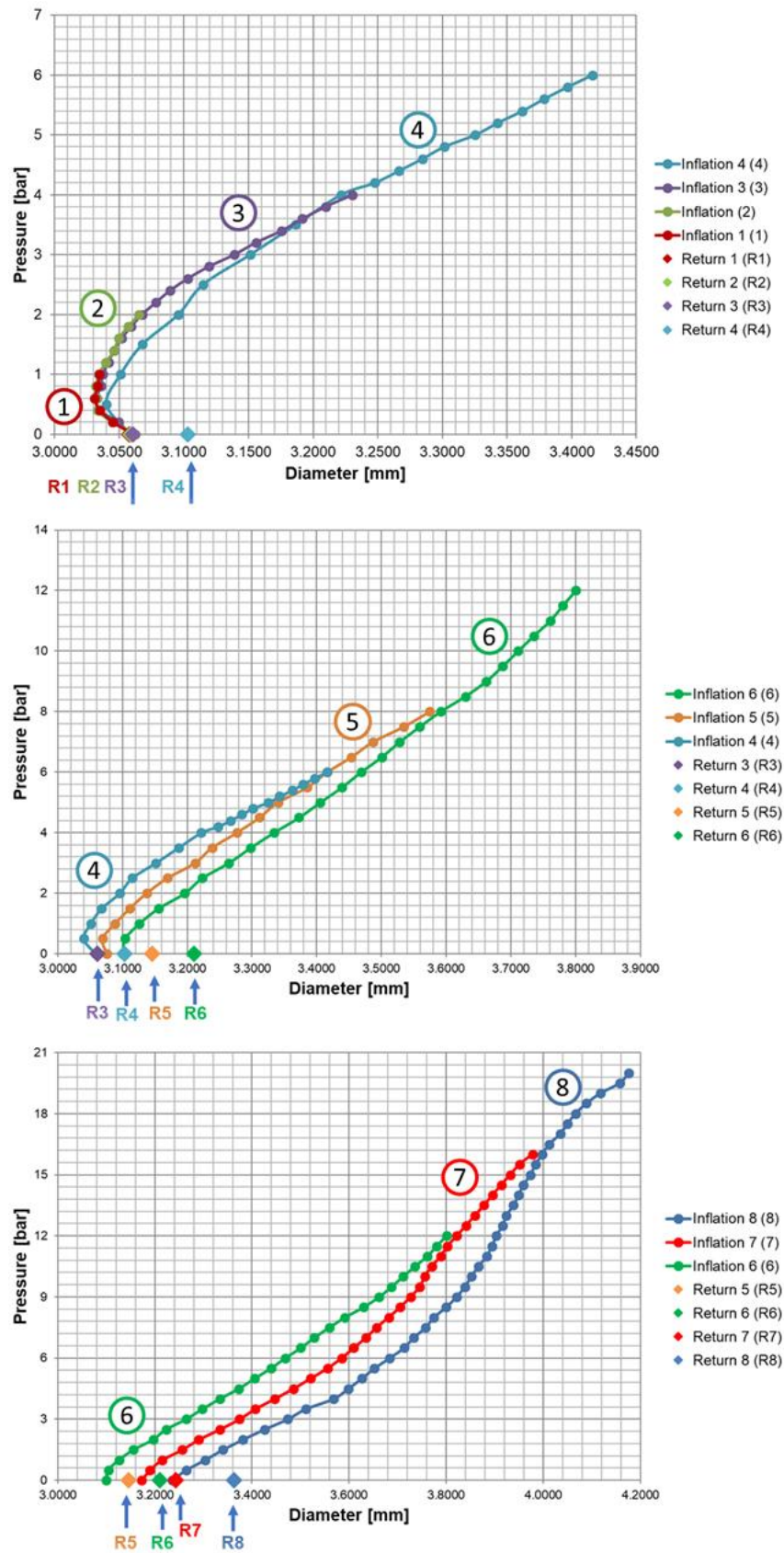


Figure 6.14: Diameter vs pressure results of inflations 1-4, 4-6 and 6-8 of the Maverick² balloon catheter. The instantaneous return points for each inflation are also included.

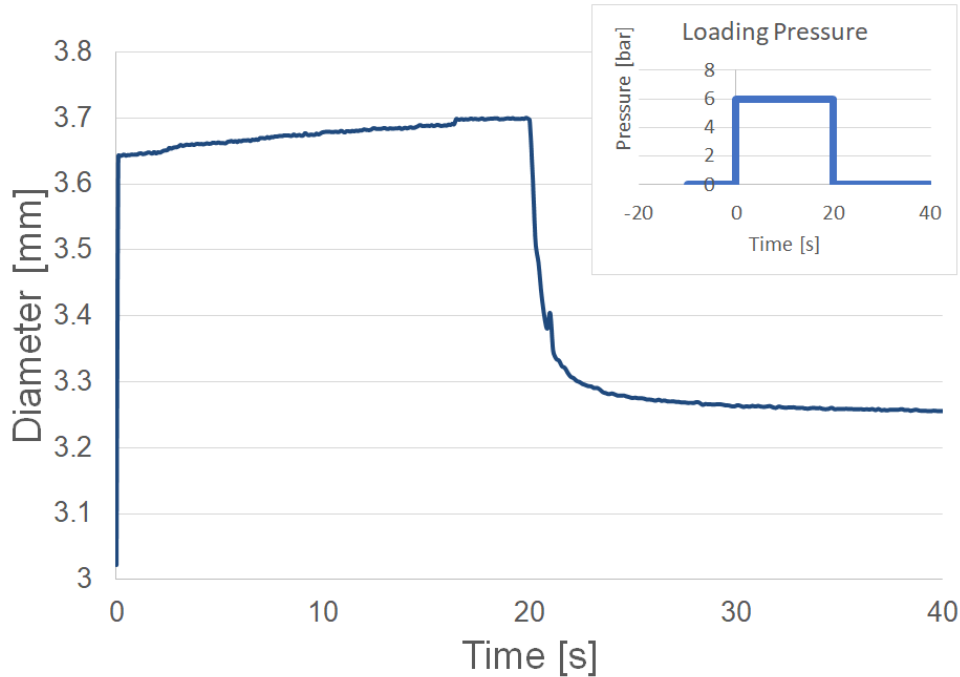


Figure 6.15: Diameter vs pressure results of short-time creep test of the Maverick² balloon catheter. A pressure of 6 bar (5.9 atm) was applied for 20 seconds and then released. Images were acquired at a rate of 100 ms for 40 s during the creep (20 s) and recovery stages (20 s).

6.2.3 Balloon polymer film tensile tests

Due to the alignment of the polymer chains during the fabrication process of the balloon film, an anisotropic behavior is expected. Therefore, the mechanical properties were measured in the circumferential and longitudinal direction of the balloon. Because of the reduced dimensions of the balloon film (3.5 mm diameter and 15 mm length), preparation of the specimens required a special protocol (Fig. 6.16). The balloon was deployed with a low pressure (0.1 bar) and cut into strips of 15x2 mm and 10x2 mm in the longitudinal and circumferential directions, respectively. Then, all samples were mounted following a protocol similar to the one of [Balakrishnan and Saha \(2011\)](#), to avoid ripping the film and to ensure a correct alignment. The strips were pasted between two rigid mica sheets of 15 x 5 x 1 mm. Special care was taken to avoid stretching the film during sample preparation.

A total of 5 specimens in each direction (circumferential and longitudinal) were tested in uniaxial tension using the Biotester 5000 (Cellscale, CA) test system with a load cell of 10 N (Fig. 6.17). Using the same configuration, another set of specimens was tested under cyclic load under controlled strain. All tests for the balloon film were performed at a displacement rate of 3 mm/min. Contactless displacement measurement was achieved by digital image correlation. Graphite powder markers were added at the mounted film sample and images were acquired (resolution) for post-processing using the Labjoy software (Cellscale, CA) (Fig. 6.18). Image tracking is based on a template matching algorithm that defines an area of pixels (template) on the source image ($T = n$) and determines the optimal location of the template on the target image ($T = n+1$) within a predefined search area. A source template of 31 x 31 pixels and a search region of 15 x 15 pixels were used. Force measurements and digital images were recorded at a rate of 1 Hz.

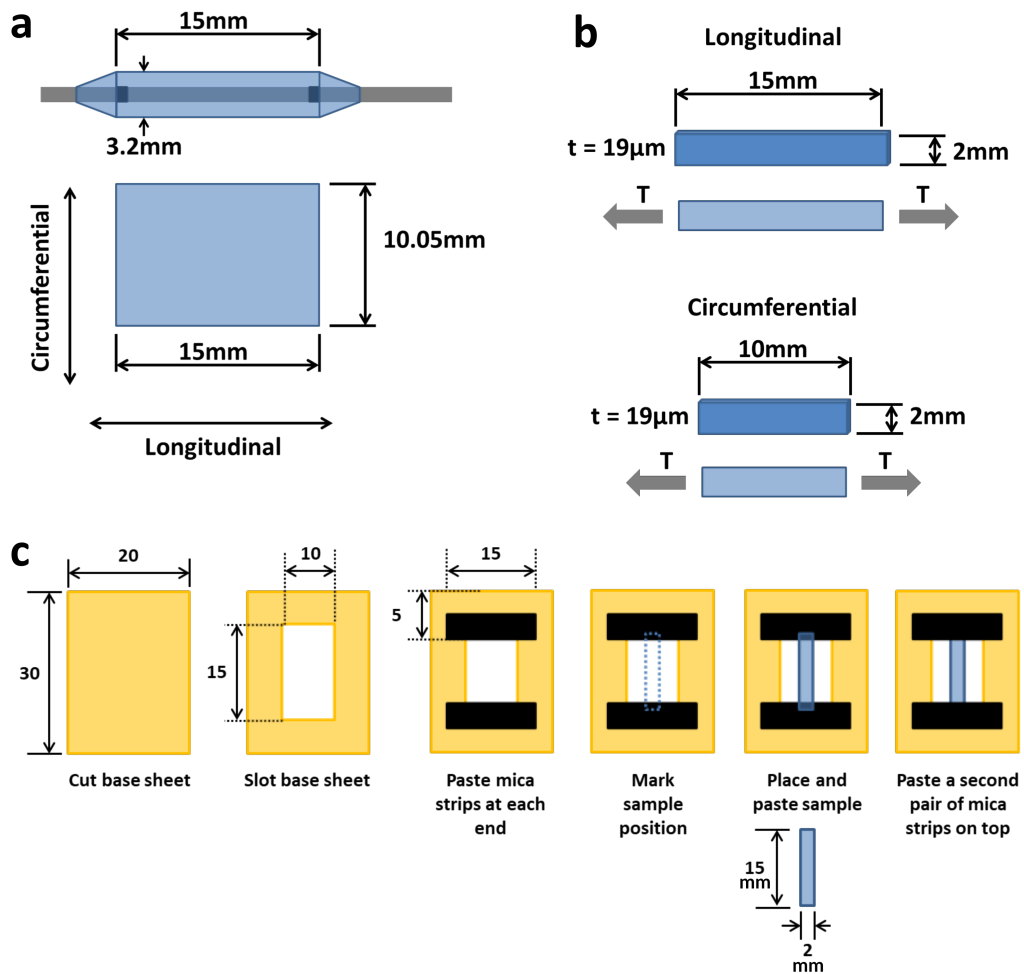


Figure 6.16: Sample preparation protocol. (a) Each balloon provided a film of approximately 10.05 x 15 mm, that was cut in the circumferential and longitudinal directions (b). (c) The sample was mounted between two acrylic strips pasted to a base sheet, using an epoxy resin. This ensured the correct alignment of the sample. Once the sample was placed on the testing machine, both sides of the base sheet were cut.

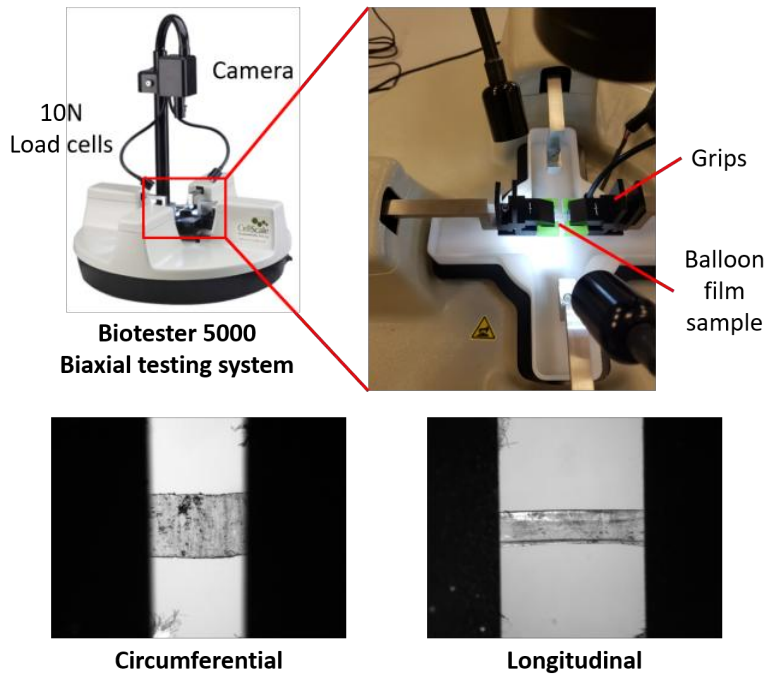


Figure 6.17: Top: Biotester 5000 biaxial testing system used for the uniaxial tensile tests of the balloon polymer film. The sample was mounted using mechanical grips. Bottom: Samples in the circumferential and longitudinal direction mounted on the machine. Graphite powder was added to surface of the sample to serve as markers to calculate the displacement with a digital image correlation post-process.

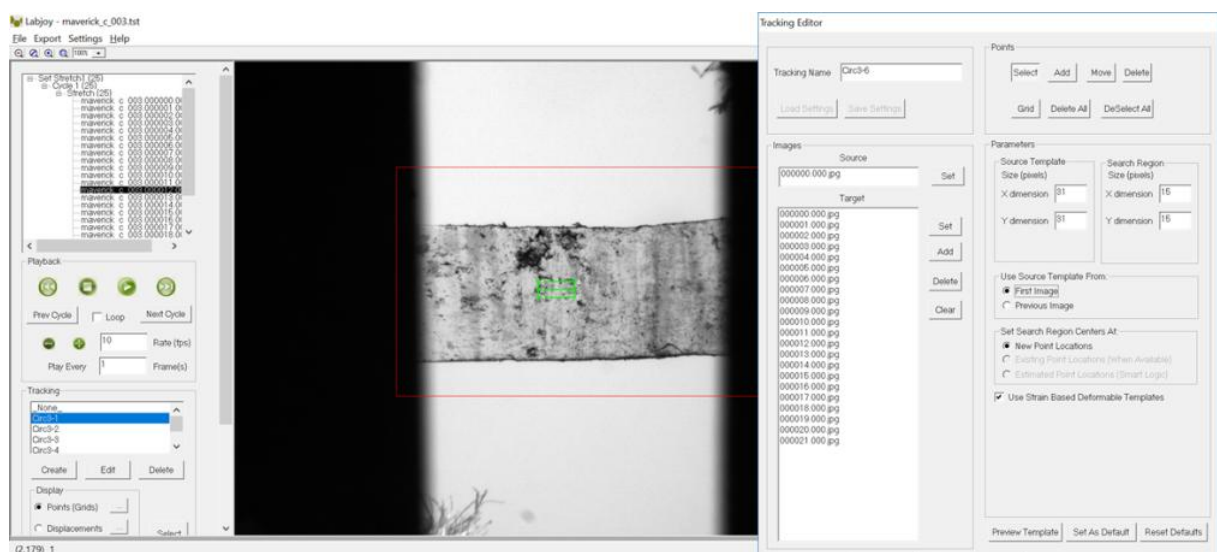


Figure 6.18: Integrated image analysis module of the Labjoy software used to quantify the motions of image features. The tracking editor window allows the modification of the digital image correlation process parameters.

Figure 6.19 presents the mean curves obtained from the tensile tests in the circumferential and longitudinal directions of the balloon film, when a constant displacement value of 3 mm/min. All the experimental curves for each direction are provided in Appendix D. The force acquisitions were used to calculate the engineering stress. The force was divided by the undeformed cross-section S_0 , which is equal to the thickness ($19 \mu\text{m}$) times the width (2 mm) of the samples. The cross-section S_0 was the same for both the circumferential and longitudinal samples.

In both tensile tests (under a constant displacement rate and under cyclic load) the circumferential direction showed that at low stretch ratios the longitudinal stress is slightly higher than the one in the circumferential direction, while between $\lambda = 1.1$ to 1.2, the stresses seem to be very similar. But once the stretch ratio is above 1.2, the circumferential stress increases at a much higher rate than the longitudinal one.

The Poisson ratio was calculated by tracking the displacement of a set of 2 markers in the direction of the applied force and 2 more markers in the direction perpendicular to the load. Five different sets of points were taken from the center of each sample. The Poisson ratio ν was calculated as $\nu = -\varepsilon_t/\varepsilon_l$, where ε_t is the strain in the normal direction to the applied force, and ε_l is the strain in the direction of the applied load. The poisson ratio of the film was 0.36 ± 0.06 (Fig. 6.21). The poisson ratio was calculated with samples tested on the circumferential direction.

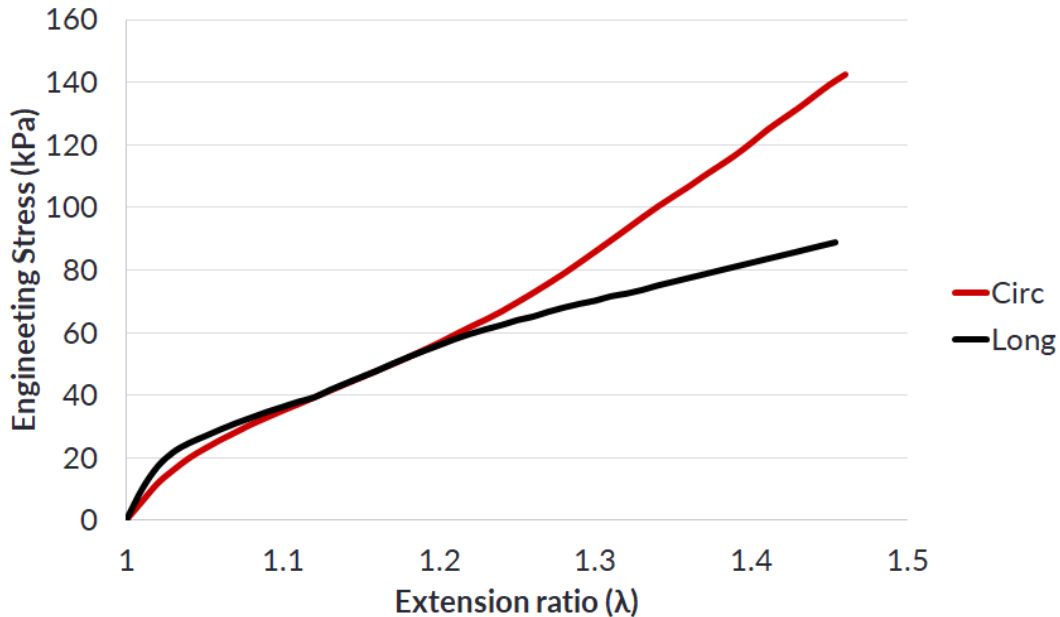


Figure 6.19: Resulting mean curves from balloon cyclic tensile tests in the circumferential (Circ) and longitudinal (Long) directions.

Figure 6.20 shows the experimental curves of the balloon under cyclic load, in both the circumferential and longitudinal directions. Five cycles were defined as follows: 80% of the average displacement at break of the uniaxial tensile samples was set as the maximum displacement (the displacement at the last cycle); this value was then divided by the number of cycles (5) so that each cycle had an equal displacement increment (see Fig. 6.20). The maximum extension values were $\lambda_{\theta}^{max} = l/l_0 = 1.48$ and $\lambda_Z^{max} = 1.34$ for the circumferential and longitudinal directions, respectively. The maximum circumferential extension of 1.48 indicates that the maximal diameter that could be reached with this balloon is close to 4.51 mm if we consider that 3.05 mm is the initial diameter of the balloon at zero pressure (Fig. 6.13 top). The results from these tests highlighted the plastic mechanical properties of the balloon film

(Fig. 6.20).

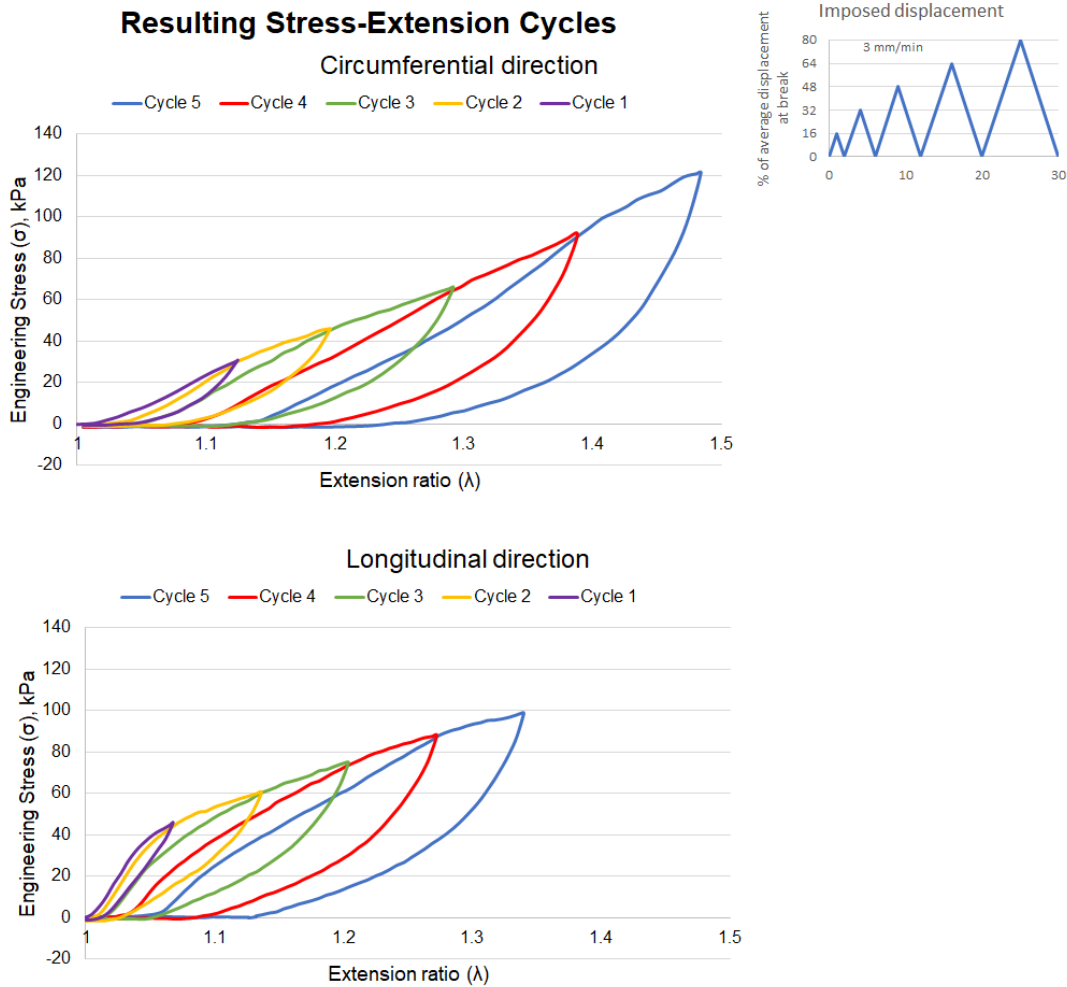


Figure 6.20: Resulting curves from balloon cyclic tensile tests in the circumferential and longitudinal directions.

6.2.4 Internal and external catheters tensile tests

The internal and external catheters were also tested under tensile tension. To avoid slipping, double-sided tape was adhered to the section where the grips would hold the intact catheter tubes. Samples were mounted on an Instron 3365 universal material testing machine (USA) with a 5kN load cell (Fig.6.22).

Five different specimens of each catheter were tested at a displacement rate of 15 mm/min. The resulting mean curves for each catheter are shown in Figure 6.23. All the experimental curves for each catheter specimen are provided in Appendix D. The engineering strain was calculating by dividing the force measurements by the initial cross-sectional area of the catheter tube. While the elongation at break of both catheters is very similar, the external catheter presents a tensile strenght 4 times higher than that of internal catheter.

6.2.5 Recording of balloon deployment and burst with high speed camera

The initial balloon deployment and its burst behaviors were recorded using a high-resolution NAC, Memrecam HX-6 camera, using a frame rate of 600 fps. The camera was adjusted so that the field of view enclosed the tapered ends of the balloon. The recording was triggered manually. The balloon was inflated using saline solution at ambient temperature, and pressure was applied

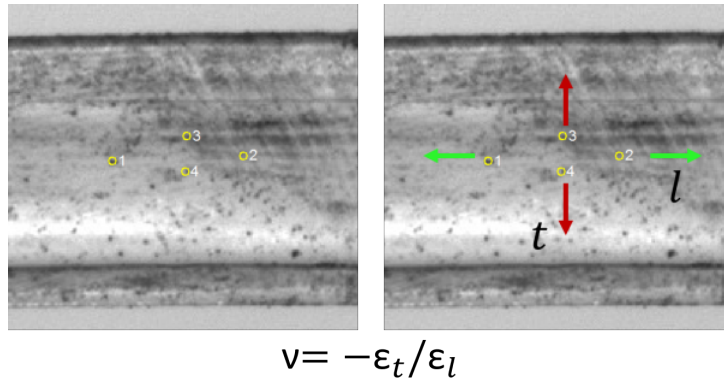


Figure 6.21: Top: Biotester 5000 biaxial testing system used for the uniaxial tensile tests of the balloon polymer film. The sample was mounted using mechanical grips. Bottom: Samples in the circumferential and longitudinal direction mounted on the machine. Graphite powder was added to surface of the sample to serve as markers to calculate the displacement with a digital image correlation post-process. ν = Poisson ratio; ε_l = strain parallel to the uniaxial tension; ε_t = strain perpendicular to the uniaxial tension.



Figure 6.22: Left: Internal catheter sample undergoing tensile tension test in the Instron 3365 universal material testing machine. Right: Section of the internal catheter with double sided tape to help grip the sample.

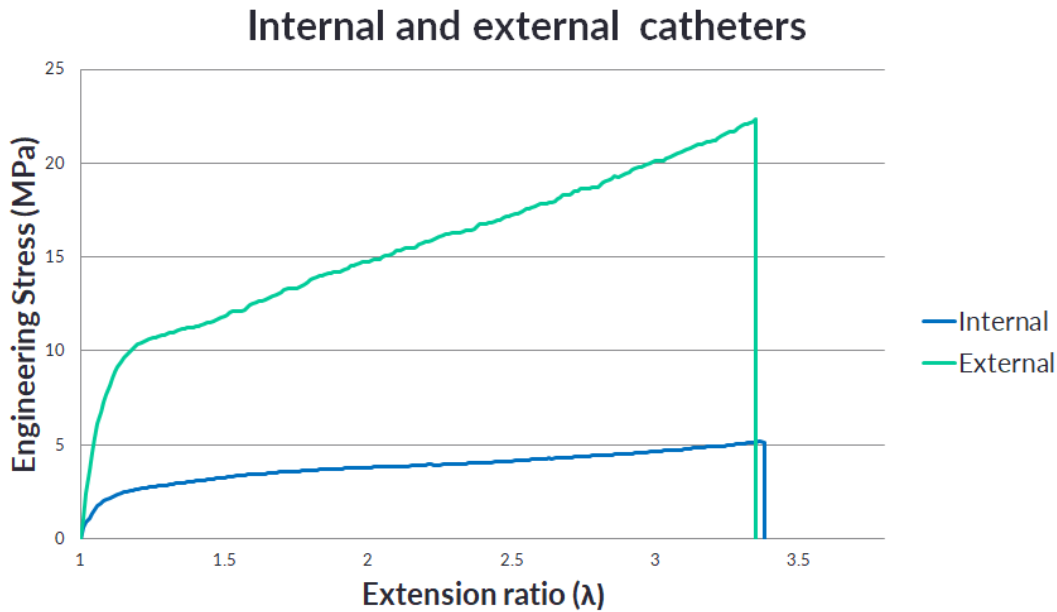


Figure 6.23: Mean curves from tensile tests of the internal and external catheters under tensile tension at a constant displacement rate of 15 mm/min.

with a manual angioplasty balloon inflator at a rate of approximately 4 atm per second (Fig. 6.24). Unfortunately, the frame rate was not enough to capture the initial deployment of the balloon, but the moment where the balloon ruptures was successfully recorded. A longitudinal tear could be observed after rupture.

6.3 Discussion

Balloon polymer film

The mechanical properties of the balloon are also influenced by the manufacturing process, as discussed in Chapter 6. The balloon is fabricated from an elastomeric material that exhibits viscoelastic and plastic properties that play an important role in balloon inflation. From the results of the inflation tests performed for this study, we could observe both of these behaviors.

By applying consecutive inflations at pressures above the nominal pressure (Figures 6.6 and 6.8), the compliance curves changed considerably, and differed from the compliance curve provided by the manufacturer, even during the first inflation. From Figure 6.9, presenting subsequent inflations after a sufficient recovery period of 16h, we can see that the curves after the recovery period do not resemble the first inflation curve, but the second, highlighting the plasticity effect of the material.

Inflations with smaller pressure steps and higher pressure resolution conveyed interesting results, since the inflation curves going from $P_0=0$ to $P_1=1,2,4$ and 6 bar had a common initial diameter and followed very close paths, with the last of these inflations ($P_1=6$) already deviating slightly at some points (Fig. 6.13). However, all subsequent inflations ($P_1=8,12,16,20$ bar) start at increasing diameters, which suggests the material was deformed beyond its elastic region (Fig 6.14). The recovery, evidenced by the slightly reduced diameter between inflation n and $n-1$, is a clear indication of the viscoelastic behavior of the polymer film.

Tensile tests in the two directions confirmed the anisotropic behavior of the balloon. The

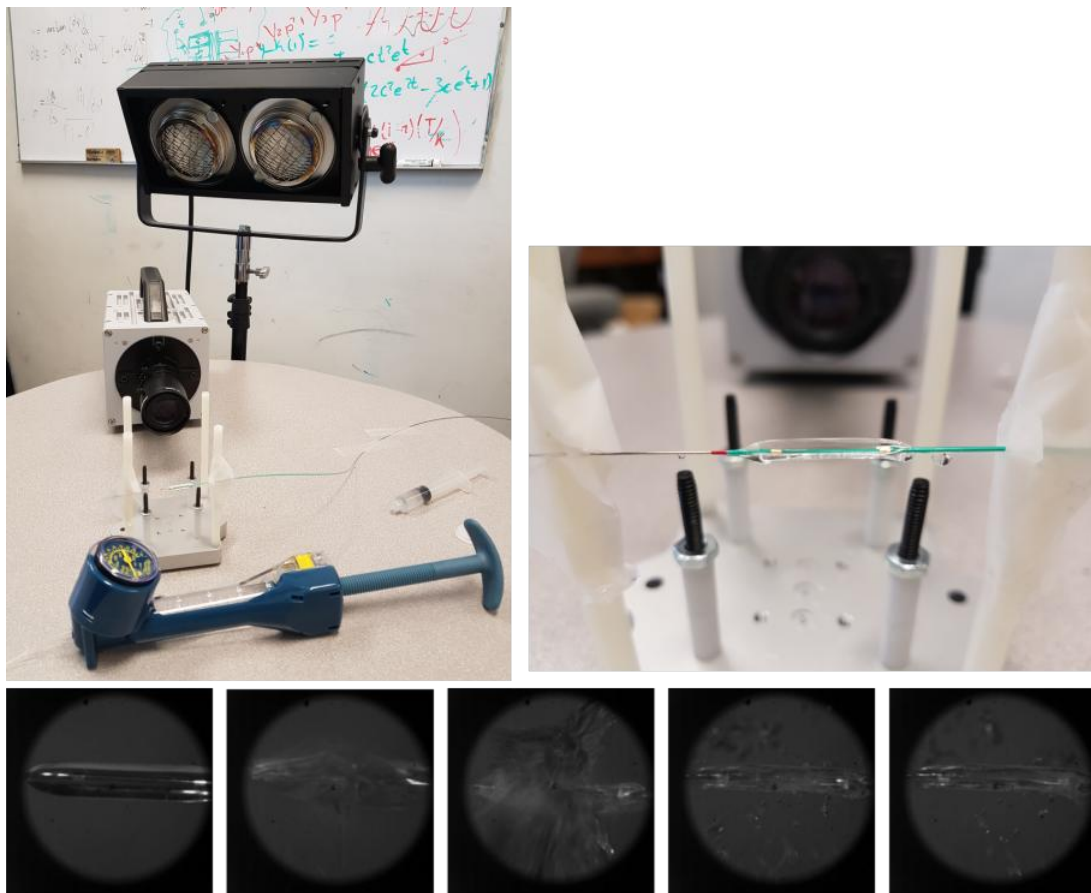


Figure 6.24: Top: Setup for the acquisition of high-speed video of the deployment and burst of the balloon catheter. Bottom: Images obtained from the bursting sequence.

circumferential direction had a stress at break of 149.35 ± 20.24 kPa, which was 1.6 times higher than the 89.07 ± 9.69 kPa for the longitudinal direction. The stretch ratio (λ) at break was 1.48 ± 0.02 and 1.44 ± 0.08 for the circumferential and longitudinal directions, respectively. The Pebax 7033 material datasheet (Arkema Inc, 2013) indicates that for a tensile load, the stress at break is 54 MPa, and the strain at break is close to 350%, obtained using the ASTM D638 standard test method for tensile properties of plastics. The material properties obtained with our tests are below the ones indicated in the material datasheet. This difference could be explained by the fact that the manufacturing process of the balloon catheter pre-form, the balloon blow molding process, its assembly and shrinking may have a significant effect in the mechanical properties of the polymer. Also, the sterilization procedures could introduce thermal and/or chemical stresses on the material (Fedel et al., 2006).

Longitudinal elongation of the balloon was present but minimal (Fig. 6.10), as expected, due to the balloon design constrictions. It is interesting to note that in the cases where balloons were ruptured during inflation, the failure mode was a longitudinal tear, consistent with the preferred mode of failure for balloon catheters.

Study limitations

Due to the high cost of the devices, a limited amount of balloons were available for testing. While several samples could be obtained from a single balloon for tensile testing, inflation tests were not repeated due to this limitation.

Tests were conducted at room temperature (25°C) and the balloon operates inside the human body at temperatures close to 37°C . The temperature difference usually affects the behavior of these polymers, but from the first inflations carried out (Figures 6.6 and 6.8) we observed only a small variation when tests were performed at these two temperatures.

For the tensile tests, only one displacement rate (3 mm/min) was used and it is well-known that strain-rate can significantly affect the stress-strain curves for viscoelastic polymers. However, the general plastic and viscoelastic behavior of the polymer, as well as the anisotropic properties of the film were observable at the selected strain rate.

Finally, the balloon diameter was unconstrained during the inflation tests, and its *in vivo* performance can be affected by lesion composition (lipid, calcifications, etc.) and the elasticity of the arterial wall (More et al., 1996). Nevertheless, the objective of our study is to have a better understanding of the material properties of the balloon and use it to generate a model to help predict its compliance. These free-inflation configuration allows for a more general behavior, which suits our goal.

6.4 Conclusions and perspectives

The tests performed during this study include not only inflation experiments that assess the compliance of the device, but also tensile tension tests to investigate the underlying mechanical phenomena that govern the balloon inflation. The plastic and viscoelastic behaviors of the balloon film were highlighted throughout the different test methods.

The next step in **Chapter 7** is to use the obtained data to create and validate a model that can mimic the viscoelasto-plastic behavior of the Boston Scientific Macerick² balloon. This model could be later used to predict the balloon diameter during consecutive inflations, and allow interventional cardiologists to have a better control during angioplasty.

Chapter 7

Modeling the viscoelasto-plastic response of balloon catheters for coronary angioplasty: Application to Boston Scientific's Maverick² model

7.1 Introduction

As mentioned in **Chapter 5**, previous studies regarding the mechanical characterization of the balloon catheter polymeric film are scarce. In **Chapter 6**, we investigated not only the inflation dynamics of an angioplasty balloon undergoing consecutive inflations, but we also characterized the polymeric film mechanical behavior with uniaxial cyclic tension tests. These experimental results provide a base for the definition of a mechanical model of the material behavior that accounts for the phenomena observed (namely, the viscoelasto-plastic behavior of the material) and the loading conditions used for the experiments.

For this purpose, this chapter presents a one-dimensional model - the generalized Bingham model - that was used to evaluate the contribution of the elastic and visco-plastic strains to the overall strain. The resulting nonlinear 1-D model aims to improve our understanding of the mechanical behavior of the balloon polymeric film and could set the basis for more accurate pressure-diameter curve predictions of consecutive inflations of angioplasty balloons. This study was performed in collaboration with Dr. Jean-Louis Martiel from TIMC-IMAG Laboratory in Grenoble.

7.2 Elementary viscoelastic-plastic one-dimensional model: generalized Bingham model.

The generalized Bingham model (GBM) model combining springs, dash-pots and friction elements is presented in figure 7.1. It consists of a pure elastic spring, the so-called elastic block, and a viscous-plastic block. This latter block is made of a spring, a dash-pot and a friction element in parallel (see figure 7.1).

Preparation of experimental data.

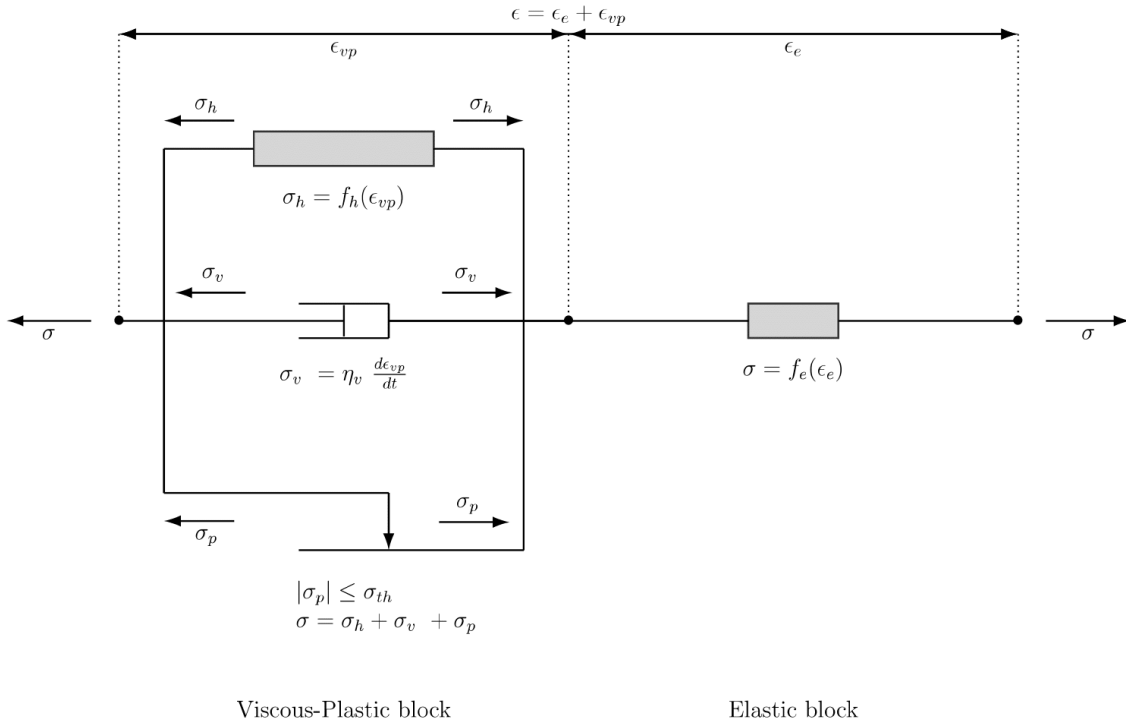


Figure 7.1: Sketch of the global model.

The experimental setup controlled the length, l of the sample; in turn, we measured the force, F , developed by the material in response to the extension l . Therefore, given the initial cross-sectional area of the material, A_0 , one has, directly the engineering (or first Piola-Kirchhoff) stress σ^{Eng} by dividing the force by A_0 . From the evolution of the sample length, we can compute the extension ratio $\lambda = \frac{l(t)}{l(0)}$ and the strain $\epsilon(t) = \lambda(t) - 1$. If we assume that the material is incompressible the area at time t is $A(t) = \frac{A_0}{\lambda(t)}$. Hence, we can extract the Cauchy stress σ^{Cauchy} from the experiment as

$$\sigma^{Cauchy}(t) = \frac{F(t)}{A(t)} = \lambda(t) \frac{F(t)}{A_0} = \lambda(t) \sigma^{Eng}(t). \quad (7.1)$$

The elastic block.

When strained by ϵ_e , the purely elastic spring (figure 7.1) develops a stress, denoted σ . Usually, the **elastic constitutive law**, i.e. the expression of stress as a function of strain, is given by a simple linear relation

$$\sigma = E_e \epsilon_e,$$

where E_e is a (pseudo) Young's modulus (with dimensions similar to those of stress, i.e. $Force/Area$). However, anticipating on the Results section, the stress-strain relationship is often non-linear

$$\sigma = f_e(\epsilon_e). \quad (7.2)$$

The function f_e is, in general, a complex expression of the stress. Nevertheless, based on the physics of strings, it is required that at zero strain, the spring develops no stress:

$$f_e(0) = 0, \quad (7.3)$$

The viscoelasto-plastic block.

The block consists of three elements in parallel. When strained by ϵ_{vp} , each element will develop a stress; however, since the three elements are in parallel, the total stress in the block, denoted σ , is the sum of the stresses developed in each branch

$$\sigma = \sigma_h + \sigma_v + \sigma_p, \quad (7.4)$$

where $\sigma_h, \sigma_v, \sigma_p$ are the stress developed in the elastic, viscous and plastic element of the block, respectively. Now, we turn our attention to the different relations between the strain ϵ_{vp} and σ .

First, σ_h , the stress in the spring, is linked to ϵ_{vp} via

$$\sigma_h = f_h(\epsilon_{vp}), \quad (7.5)$$

where f_h is a non-linear relation, similar to Eq. 7.2, with $f_h(0) = 0$. Second, the stress developed by the dash-pot is proportional to the rate of change of ϵ_{vp}

$$\sigma_v = \eta_v \frac{d\epsilon_{vp}}{dt}, \quad (7.6)$$

where η_v is the viscous damping coefficient (dimensions: $Force \times Time / Area$) which may depend on the viscous-plastic strain ϵ_{vp} . Third, the friction element, which is the source of irreversible deformations, is subjected to a stress, denoted σ_p , which reads

$$\begin{aligned} \sigma_p &= \sigma - \sigma_h - \sigma_v \\ &= \sigma - f_h(\epsilon_{vp}) - \eta_v \frac{d\epsilon_{vp}}{dt}, \end{aligned} \quad (7.7)$$

We distinguished three cases for the viscous-plastic regime, depending on the value of σ_p .

$$\begin{aligned}
 \frac{d\epsilon_{vp}}{dt} &= 0 && \text{if } |\sigma_p| = \left| \sigma - f_h(\epsilon_{vp}) - \eta_v \frac{d\epsilon_{vp}}{dt} \right| < \sigma_{th} \\
 \frac{d\epsilon_{vp}}{dt} &= \frac{1}{\eta_v} (\sigma - f_h(\epsilon_{vp}) - \sigma_{th}) > 0 && \text{if } \sigma_p = \sigma - f_h(\epsilon_{vp}) - \eta_v \frac{d\epsilon_{vp}}{dt} = \sigma_{th} \\
 \frac{d\epsilon_{vp}}{dt} &= \frac{1}{\eta_v} (\sigma - f_h(\epsilon_{vp}) + \sigma_{th}) < 0 && \text{if } \sigma_p = \sigma - f_h(\epsilon_{vp}) - \eta_v \frac{d\epsilon_{vp}}{dt} = -\sigma_{th}
 \end{aligned} \tag{7.8}$$

We can note that $|\sigma_p|$ is always bounded by σ_{th} .

Model combining all blocks.

We can combine the elastic and visco-plastic blocks, as in figure 7.1 and derive the whole set of equations. First, we give the total strain and its decomposition into an elastic and visco-plastic parts

$$\epsilon(t) = \epsilon_e + \epsilon_{vp} \tag{7.9}$$

Therefore, using the equations 7.2 and 7.9, one has:

$$\begin{aligned}
 \sigma &= f_e(\epsilon_e) \\
 &= f_e(\epsilon - \epsilon_{vp})
 \end{aligned} \tag{7.10}$$

Finally, since the **elastic** and **plastic blocks** are in series, the stress is the same for the two blocks, i.e. the stress σ in equation 7.2 and in equation 7.8 are the same. If we plug the stress (Eq. 7.10) in the expression for the rate of change of the viscous-plastic strain (see Eq. 7.8) we get the ordinary differential equation that summarizes the problem

$$\begin{aligned}
 \epsilon_e &= \epsilon(t) - \epsilon_{vp} \\
 \frac{d\epsilon_{vp}}{dt} &= \begin{cases} 0 & \text{if } |\sigma_p| < \sigma_{th} \\ \frac{1}{\eta_v} (f_e(\epsilon - \epsilon_{vp}) - f_h(\epsilon_{vp}) - \sigma_{th}) & \text{if } \sigma_p = \sigma_{th} \\ \frac{1}{\eta_v} (f_e(\epsilon - \epsilon_{vp}) - f_h(\epsilon_{vp}) + \sigma_{th}) & \text{if } \sigma_p = -\sigma_{th} \end{cases}
 \end{aligned} \tag{7.11}$$

Note the change of sign in the two last equations. One should specify the initial conditions, which read,

$$\begin{aligned}
 \epsilon(0) &= 0 \\
 \sigma(0) &= 0 \\
 \epsilon_{vp}(0) &= 0
 \end{aligned} \tag{7.12}$$

and solve the system 7.11.

Algorithm and solution.

Uniaxial experiments were used to measure the stress, denoted $\sigma^{exp}(t)$, as a function of the imposed strain, denoted $\epsilon^{exp}(t)$. At this stage, we can get a solution using the model equation 7.11 and the flow chart describing the algorithm (shown in figure 7.2). By comparing the computed stress $\sigma^{model}(t)$ to the experimental counterpart $\sigma^{exp}(t)$, we should likely be able to assign values to the model parameters. To do so, we minimized the difference between the experimental stress, σ^{exp} , and the computed stress, σ^{model}

$$J(\boldsymbol{\lambda}) = \sum_{t_n} \left| \frac{\sigma^{model}(t_n, \boldsymbol{\lambda})}{\sigma^{exp}(t_n)} - 1 \right|. \quad (7.13)$$

where the still unknown model parameters are represented by the vector $\boldsymbol{\lambda}$. For example, this vector collects the different scalar values necessary to define the polynomial expressions of the functions f_e , f_h and η_v as well as the threshold stress σ_{th} . The search for $\boldsymbol{\lambda}$ was performed by the Matlab function *lsqnonlin* which solves non-linear least square problems.

7.3 Results

First, we present the best fit parameters for the model. The best constitutive relation Eq. 7.2 is given by

$$f_e(\epsilon_e) = 261.046\epsilon_e + 1887.91\epsilon_e^2 + 6932.74\epsilon_e^3. \quad (7.14)$$

The constitutive relation Eq. 7.5 is well approximated by a polynomial function

$$f_h(\epsilon_{vp}) = 279.841\epsilon_{vp} + 9.57196\epsilon_{vp}^2 - 853.21\epsilon_{vp}^3, \quad (7.15)$$

where as the damping coefficient is

$$\eta_{vp}(\epsilon_e) = 67.7406\epsilon_{vp} + 53980.6\epsilon_{vp}^2 + 154.578\epsilon_{vp}^3 + 5061.67\epsilon_{vp}^4. \quad (7.16)$$

Finally, the threshold for plasticity is

$$\sigma_{th} = 4 \text{ kPa}. \quad (7.17)$$

This plasticity threshold corresponds to a strain deformation of $\epsilon_{th} = 0.014$, obtained by solving the equation $f_e(\epsilon) - \sigma_{th} = 0$, with f_e given by equation 7.14.

Two important remarks.

1. The functions Eqs. 7.14, 7.15 or 7.16 are valid for a strain in the interval $[0, 0.5]$ only. In consequence, one can use the polynomial approximation of f_e , f_h and η_{vp} in these limits, which corresponds to the experimental interval for ϵ^{exp} .

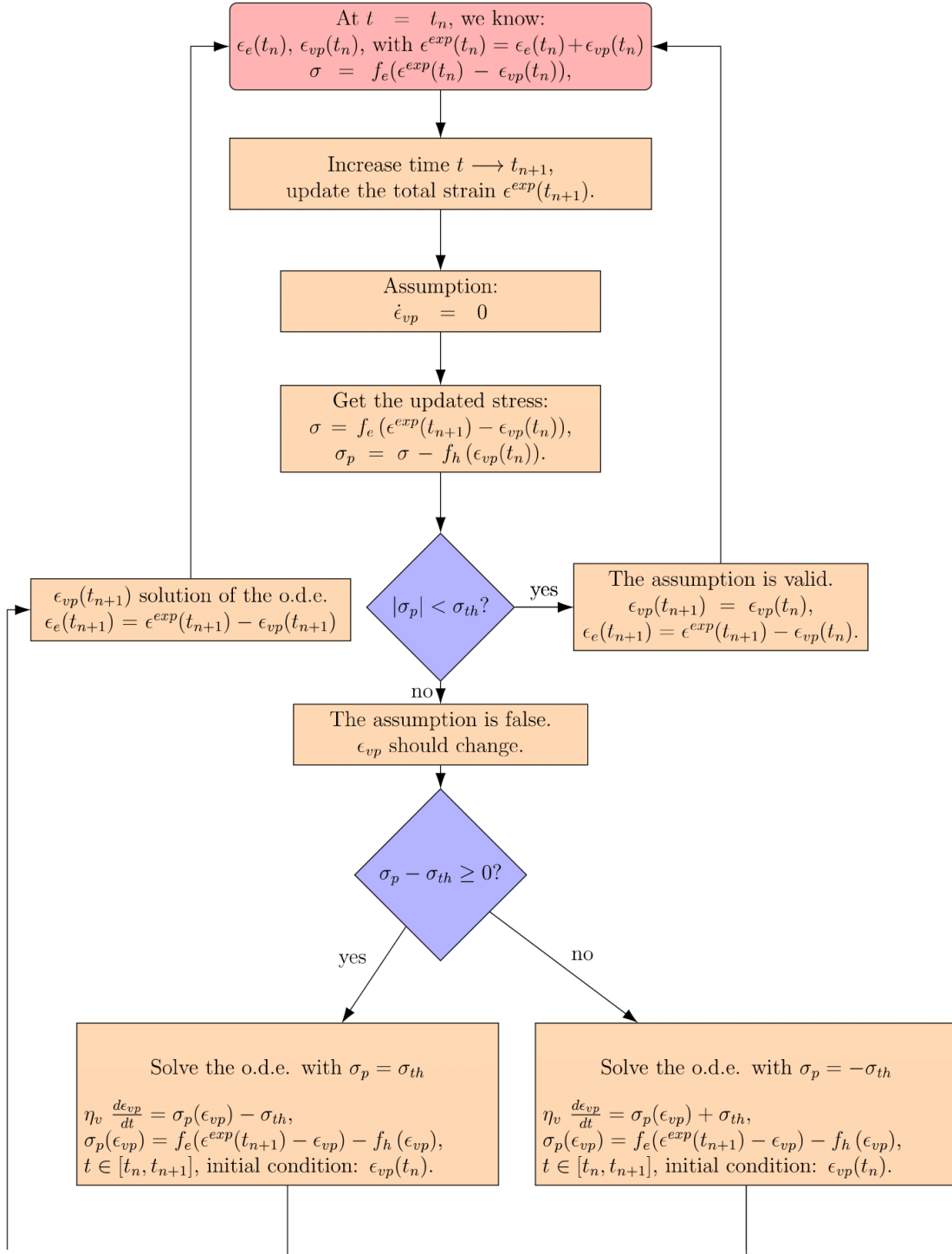


Figure 7.2: Flow chart describing the procedure to find a solution.

2. Ideally, the constitutive relations Eqs. 7.2, 7.5 or 7.6, which are modeled by f_e , f_h or η_{vp} , should reflect the physical properties of the springs and/or the dash-pot.

Model illustration

As shown in figure 7.3, the model considered accounts for the different phases (loading, plastic deformation and relaxation, as examined in the previous section) for the five consecutive cycles. When we look at the strain-stress representation (figure 7.4), all the experimental and model cycles are superposed, showing a good agreement between the model and the experiments.

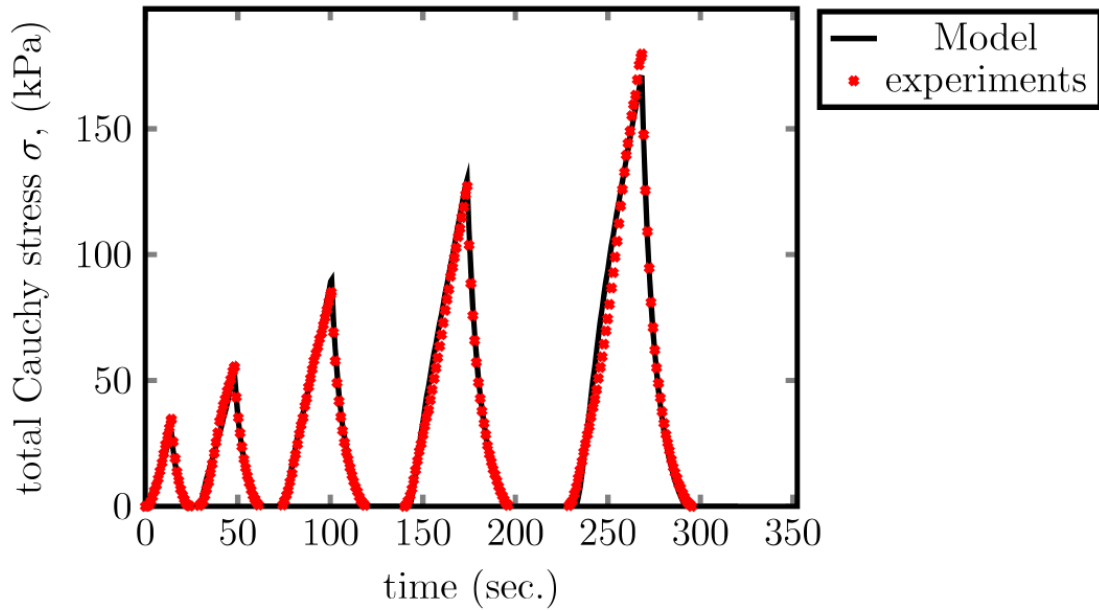


Figure 7.3: Time course of the stress. Experimental data are indicated with red dots; the model prediction is represented by the black solid line.

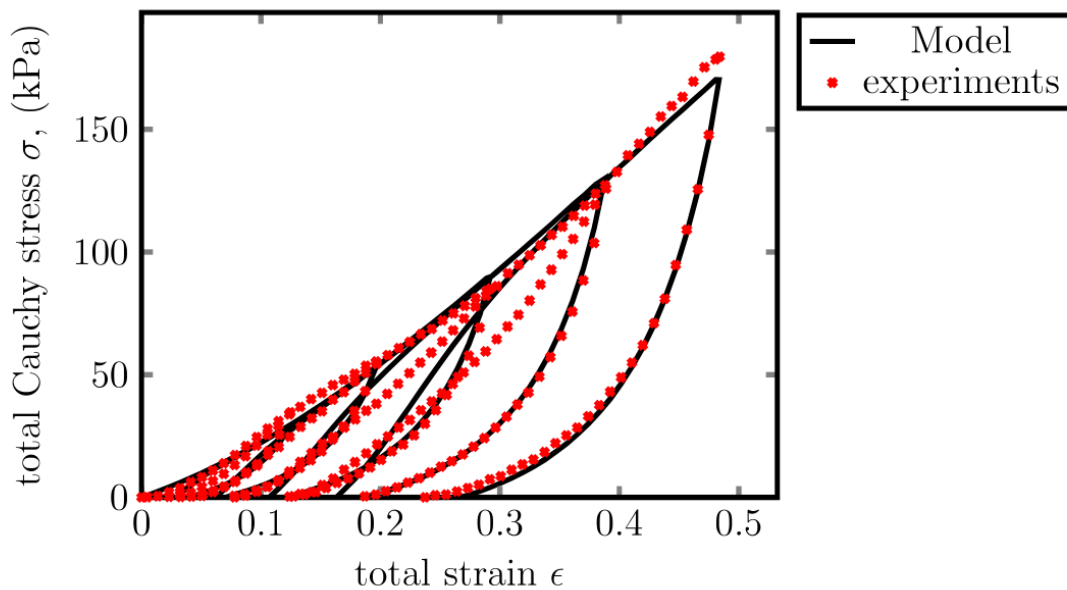


Figure 7.4: Fit of stress-strain in the $\epsilon - \sigma$ plane.

The model output gives some insight into the different deformations experienced by the material during one cycle. As shown in figure 7.5, the predicted elastic strain ϵ_e (red curve) adapts instantaneously to the imposed strain. On the other hand, the visco-elasto-plastic deformation ϵ_{vp} (blue curve) is triggered as soon as the stress is beyond the threshold σ_{th} . Basically, during the initial loading phase, ϵ_e increases, but ϵ_{vp} , although non-zero, remains at its minimum (see figure 7.5). However, as ϵ_e is beyond a threshold, ϵ_{vp} starts to increase, leading the transition of the deformation from elastic to plastic. In summary, we get that the **loading** and **plastic** phases are found by simply analyzing the data (see previous section). As the external stress starts its decreasing course, ϵ_e diminishes pulling ϵ_{vp} downwards (see equation 7.11 for a mathematical image of this phenomenon). When the deformation is below σ_{th} , ϵ_{vp} stalls and resumes its decrease as soon as the external loading resumes increasing.

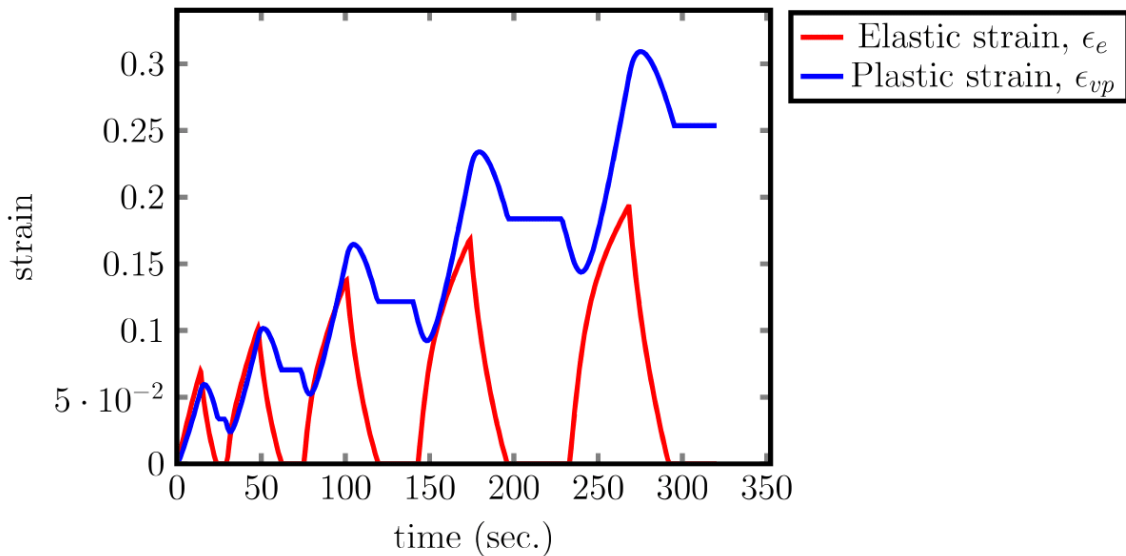


Figure 7.5: Model prediction for the elastic (red) and visco-plastic (blue) strains.

7.4 Conclusions and clinical implications

Uni-dimensional models are invaluable tools to dissect uniaxial traction experiments into elementary components, which, in our study, are a pure elastic spring in series with a visco-elasto-plastic block. The partition of the total experimental strain ϵ^{exp} into an elastic and visco-elasto-plastic strain is a direct prediction of our model.

Although another model could have been considered, this model is the simplest possible. In particular, we tried to fit the data using only linear elements (see equations 7.14 to 7.16), but none of these models were satisfactory. In consequence, we shifted to more complex expressions of the constitutive relations given by equations 7.2 to 7.6.

There exist some limitations of our work at the present state. One is that the numerical expression of the constitutive relations, given by the equations 7.14 to 7.16, does not exempt us from using an energy function that could incorporate the properties of the material (isotropy vs. anisotropy, non-linear hardening, ...). Another limitations is that these one-dimensional models are not sufficient to account for full 3D-models, which are required for a deeper understanding of the balloon inflation and that could allow the *diameter-pressure* characterization of the balloon. In this case, a more realistic model, including the balloon as a 3D-tapered cylinder should be considered.

Despite these limitations, the presented viscoelato-plastic nonlinear one-dimensional model

was in good agreement with the experimental results obtained from cyclic traction tests. Furthermore, the tensile tests results could be complemented by the inflation experiments to improve and validate a more complex model. Future improvements could include the use of a 3-D model that could also capture the inflation behavior of the balloon and provide more accurate predictions of the pressure-diameter curves of angioplasty balloons.

Conclusions and Perspectives

In this chapter, the main findings of this research work are summarized and general conclusions based on the studies presented in this dissertation are given. Furthermore, the contributions and limitations of this thesis are considered and suggestions for further research are delineated.

7.4.1 Part I. Imaging the atherosclerotic plaque in clinics

The first part of this dissertation was dedicated to the development of tools for plaque assessment using IVUS data analysis.

First, by reproducing the approach of [Zhang et al. \(2011b\)](#), we investigated the potential of b-mode images as an alternative to radio frequency data for the computation of strain maps of the arterial wall (**Chapter 2**). In a first part, IVUS images using real patient geometries were synthesized using a finite element (FE) model and an ultrasound simulation software. Then, these images were used to test a block matching (BM) algorithm that tracked the displacement based on the cross correlation coefficient criterion. The displacement maps estimated with the BM in the X (U_X) and Y (U_Y) directions were compared to those of the FE model. In a second step, the area strain (AS) index described in Zhang's approach ([Zhang et al., 2010](#)) was calculated with both the estimated BM displacement maps and the exact displacement maps coming from the FE simulations. Our results showed that when using the BM algorithm on b-mode images we obtain displacement maps that capture the general behavior of the arterial wall. However, there is a clear deficiency that comes from the low resolution that these gray-scale images provide, as evidenced by the AS maps. For the three cases used to test this algorithm, b-mode AS maps did not provide any clear indication of the plaque features. However, the AS maps calculated with the FE model displacement maps were able to identify areas where necrotic cores were present. From this study, I concluded that: (1) b-mode IVUS images do not have sufficient resolution to calculate accurate enough displacement maps to compute strain-elongograms, and (2) the AS of Zhang is a promising index for vulnerable plaque assessment that could be used with RF-based techniques.

My next step was the development of a new anisotropic elasticity-palpography technique (AE-PT) that could account for the anisotropic mechanical properties of the plaque (**Chapter 3**), which had been neglected by previous studies ([Céspedes et al., 2000](#); [Deleaval et al., 2013](#)). Based on continuum mechanics theory, an anisotropy index (AI) combining the three orthotropic Young's moduli was defined. The AE-PT was implemented in an algorithm and tested on synthesized RF IVUS data of five modeled plaque geometries, ten coronary lesions and one healthy vessel. Our results revealed that the novel AE-PT successfully quantified the apparent wall stiffness of the arterial wall, with all 18 estimated AI-palpograms had a reasonable agreement with the exact ones (with a mean relative error = 26.79 ± 48.84 %, [Table 3.4](#)). For geometries where one or two necrotic cores were present in the plaque, the estimated AI-palpogram amplitude was found close to the expected value of the fibrotic plaque, except at

the locations of the soft necrotic cores, where the AI value dropped significantly. Although the proposed AE-PT does not allow for a diagnosis of plaque vulnerability to rupture or the isolation of each of the Young's moduli of the plaque, it successfully highlights vulnerable plaques with one or more soft inclusions and could be used to assess the evolution of the mechanical properties of the plaque.

Once the AE-PT was validated with simulated RF IVUS data, the next step consisted in evaluating its performance using real IVUS sequences (**Chapter 4**). An *in vitro* validation protocol was designed using three anisotropic polyvinyl-alcohol (PVA) cryogel vascular phantoms, two of them with enhanced anisotropic properties. These phantoms were imaged with IVUS and the resulting RF sequences were used to calculate the AI-palpograms for each phantom. Moreover, the Young's moduli in radial (R), circumferential (θ) and longitudinal (Z) directions of each phantom were measured with uniaxial tensile tests and atomic force microscopy (AFM), showing good agreement between the results of the two mechanical testing techniques. Using the experimentally obtained Young's moduli and an incompressible homogeneous anisotropic medium model (Eq. 4.3), the Model AI was calculated. The initial RF IVUS AI-palpograms showed that the AE-PT is able to distinguish the change in mechanical properties present in the phantoms, resulting in higher AI values for the phantom with the highest anisotropy. The Model AI values overestimated by a factor up to 5 the RF IVUS AI values. However, these discrepancies could be explained by the assumptions used for the implemented model. This model assumes an incompressible homogeneous anisotropic medium, but this might not hold true for our anisotropic phantom experiment, therefore causing the observed AI value disagreement. Moreover, despite the differences between the two calculated AI values for each phantom, a similar tendency was found between them, with higher AI values corresponding for PH1 - the most anisotropic phantom - and the lowest AI values belonging to PH3 -with the least anisotropic mechanical properties. Altogether, these results indicate the potential of the AE-PT to follow the evolution of mechanical properties of atherosclerotic plaques, which could have an application in the assessment of the effect of drug-therapies in clinics.

Limitations and Perspectives

One limitation of our approach is that AE-PT model assumes incompressibility when this might not be the true. Furthermore, this is suspected to be the cause of the discrepancies between the Model AI and initial RF IVUS AI values. Therefore, a revision of Equation 4.3 might be necessary in order to account for a homogeneous anisotropic compressible medium. This improved model could provide an AI value that is comparable to the one of the obtained *in vitro* with our IVUS bench on our 3 phantoms by using our novel anisotropic-palpography imaging technique.

Another shortcoming of this study is that, while the AI is a combination of the three Young's moduli, it is not yet possible to isolate each of the individual moduli with our technique. Future efforts could be made to make the extraction of each of the Young's moduli possible.

Finally, the AE-PT presents an advantage over previous palpography techniques by accounting for the anisotropic mechanical properties of the plaque. Other plaque assessment techniques such as modulography could also benefit from a similar approach and improvement. Therefore, anisotropic modulography algorithms could be developed to provide more precise tools for plaque assessment.

7.4.2 Part II. Balloon angioplasty

In the second part of this thesis, the viscoelasto-plastic mechanical properties of the polymeric film of the Boston Scientific Maverick² angioplasty balloon were investigated (**Chapter 6**). Several testing methods were used to study the inflation behavior and the mechanical properties of the balloon. First, the balloon geometric features were identified using microscopy measurements. Then, an original experimental bench was built to improve the resolution of the pressure and diameter measurements during dynamic inflation tests. Consecutive inflation tests and short-creep tests were used to evaluate the change in diameter of the balloon under different pressure profiles. It was found that the experimental inflation curves differ from the compliance curve provide by the manufacturer, and that this curve changed considerably for consecutive inflations. Afterwards, a special protocol was designed to be able to test the small samples that could be obtained from the balloon film under uniaxial tension. The mechanical characterization of the thin balloon film with uniaxial tensile tests and uniaxial cyclic tensile tests were successfully characterized for both the longitudinal and circumferential directions. The viscoelasto-plastic behavior was clearly observed throughout the different inflation and mechanical characterization test results, agreeing with the similar available studies in the literature.

With the results obtained from the characterization tests, a viscoelato-plastic one-dimensional model was implemented. This model was able to isolate the elastic and visco-plastic strains present in the total experimental strain and gives further insight into the viscoelasto-plastic mechanical behavior of the balloon polymeric film.

Limitations and Perspectives

Regarding the experimental study, one of the limitations is that the balloon diameter was unconstrained during the inflation tests. The *in vivo* performance of the balloon can be affected by lesion composition and the elasticity of the arterial wall. However, for the purpose of this study, which was the characterization of the balloon inflation behavior, such an unconstricted configuration provides a more general behavior. Another possible limitation of the experimental characterization is the small amount of available balloons for the inflation tests. Even though some of these inflations were only performed on one balloon specimen, the general tendency among all tests was in agreement with the expected viscoelasto-plastic behavior of the balloon.

The viscoelato-plastic nonlinear one-dimensional model has a clear limitation in that it is not sufficient to account for the 3-D deformation models required to predict the inflation diameter of the balloon. Despite this limitation, it is able to differentiate between the elastic and visco-plastic strains among the overall strain experienced by the balloon and offers a good fit for the curves obtained from the uniaxial tensile tests and cyclic tensile tests.

Moreover, to our knowledge, this is one of the most comprehensive studies made for the characterization of the mechanical properties and inflation dynamics of an angioplasty balloon. We investigated not only the first inflation curve, but also consecutive inflations and the mechanical properties of the balloon film. This information could be used along with a more realistic 3-D model of the balloon to obtain an accurate prediction of the diameter-pressure behavior of the balloon under consecutive inflations. Such a model could aid interventional cardiologists to have a better control of the balloon diameter during balloon angioplasty procedures, potentially improving the outcome of these interventions.

Appendix A

Constitutive law in linear elasticity for incompressible orthotropic vascular tissues

The constitutive law is given using the cylindrical coordinate system (R, θ, Z) . In linear elasticity, the relationships between the material constants of a compressible orthotropic medium and the stress tensor $(\sigma_{ij}, \text{ with } i, j = R, \theta, Z)$ and strain tensor $(\varepsilon_{ij}, \text{ with } i, j = R, \theta, Z)$ components are given by [Berthelot \(1999\)](#):

$$\begin{pmatrix} \varepsilon_{RR} \\ \varepsilon_{\theta\theta} \\ \varepsilon_{ZZ} \\ 2\varepsilon_{\theta Z} \\ 2\varepsilon_{RZ} \\ 2\varepsilon_{R\theta} \end{pmatrix} = \begin{bmatrix} 1/E_R & -\nu_{\theta R}/E_\theta & -\nu_{ZR}/E_Z & 0 & 0 & 0 \\ -\nu_{R\theta}/E_R & 1/E_\theta & -\nu_{Z\theta}/E_Z & 0 & 0 & 0 \\ -\nu_{RZ}/E_R & -\nu_{\theta Z}/E_\theta & 1/E_Z & 0 & 0 & 0 \\ 0 & 0 & 0 & 1/G_{\theta Z} & 0 & 0 \\ 0 & 0 & 0 & 0 & 1/G_{RZ} & 0 \\ 0 & 0 & 0 & 0 & 0 & 1/G_{R\theta} \end{bmatrix} \begin{pmatrix} \sigma_{RR} \\ \sigma_{\theta\theta} \\ \sigma_{ZZ} \\ \sigma_{\theta Z} \\ \sigma_{RZ} \\ \sigma_{R\theta} \end{pmatrix} \quad (\text{A.1})$$

where $E_i (i = R, \theta, Z)$ are the three Young's moduli associated with the i directions, $G_{ij} = G_{ji} (i, j = R, \theta, Z \text{ with } i \neq j)$ are the three shear moduli associated with the ij planes, and $\nu_{ij} = \varepsilon_{jj}/\varepsilon_{ii} (i, j = R, \theta, Z \text{ with } i \neq j)$ are the six Poisson's ratios (i.e. the ratios of the strain in the j direction to the strain in the perpendicular i direction). Such orthotropic material also obeys to the reciprocity conditions: $\nu_{ij}/E_i = \nu_{ji}/E_j (i, j = R, \theta, Z \text{ with } i \neq j)$. Thanks to these relationships, the number of material constants drops to nine. Moreover, assuming that the vascular wall incompressibility imposes the following three relationships among the Poisson's ratios:

$$\nu_{R\theta} + \nu_{RZ} = 0 \quad (\text{A.2})$$

$$\nu_{\theta R} + \nu_{\theta Z} = 0 \quad (\text{A.3})$$

$$\nu_{ZR} + \nu_{Z\theta} = 0 \quad (\text{A.4})$$

So knowing the three Young's moduli E_R, E_θ and E_Z , we can extract the six Poisson's ratios.



Appendix B

The elastic anisotropy index AI

Assuming the vascular media as purely incompressible and under plane strain constraints, one can derive the following relationships (Berthelot, 1999):

$$\sigma_{RR}(R, \theta) - \sigma_{\theta\theta}(R, \theta) = C(R, \theta)\varepsilon_{RR}(R, \theta) \quad (\text{B.1})$$

with

$$C(R, \theta) = E_R(R, \theta)[1 - \nu_{RZ}(R, \theta)\nu_{ZR}(R, \theta)]^{-1} \quad (\text{B.2})$$

$$\nu_{RZ}(R, \theta) = \frac{1}{2} \left[1 - \frac{1}{k_1} + \frac{1}{k_2} \right] \quad (\text{B.3})$$

$$\nu_{ZR}(R, \theta) = \frac{1}{2} \left[1 - k_2 + \frac{k_2}{k_1} \right] \quad (\text{B.4})$$

$$k_1 = \frac{E_\theta(R, \theta)}{E_R(R, \theta)} \quad (\text{B.5})$$

and

$$k_2 = \frac{E_Z(R, \theta)}{E_R(R, \theta)} \quad (\text{B.6})$$

where $\sigma_{RR}(R, \theta)$, $\sigma_{\theta\theta}$ and $\varepsilon_{RR}(R, \theta)$ are the radial and circumferential stress and radial strain components, respectively.

In this linearized elasticity approach, we assumed that the incremental radial strain $\varepsilon(R, \theta)$ is proportional to the imposed change of pressure ΔP and inversely proportional to the anisotropic material constant $C(R, \theta)$:

$$\varepsilon(\theta) = \frac{\Delta P}{C(R, \theta)} g(R, \theta) \quad (\text{B.7})$$

where $g(R, \theta)$ is a correcting shape correcting shape function which accounts for the entire plaque morphology including regions of plaque heterogeneities. By substituting Eq. (B.7) into Eq. (B.1), Eq. (B.1) can be rewritten as follow:

$$\sigma_{RR}(R, \theta) - \sigma_{\theta\theta}(R, \theta) = \Delta P g(R, \theta) \quad (\text{B.8})$$

Taking advantage of this expression (Eq. (B.8)), the elastic anisotropy index AI (Eq. (3.1)) becomes

$$AI(\theta) = \frac{\Delta P \left| \int_{R_i(\theta)}^{R_p(\theta)} g(R, \theta) dR \right|}{\varepsilon(R, \theta)} \quad (\text{B.9})$$

Since we assumed that the unknown morphological function $g(R, \theta)$ does not depend of the mechanical properties and because this function escapes to direct measurements, we approximated it by a correcting homogeneous shape function $g^*(R, \theta)$ accounting only for the anatomical cross-sectional plaque geometry. This approximated correcting function was obtained by performing a FE simulation (with a loading blood pressure ΔP) in which the pathological vessel was assumed homogeneous and made of a quasi-incompressible isotropic material. This approximated shape function $g^*(R, \theta)$ was used to estimate the anisotropic palpography index:

$$AI(\theta) = \frac{\Delta P \left| \int_{R_i(\theta)}^{R_p(\theta)} g^*(R, \theta) dR \right|}{\varepsilon(r, \theta)} \quad (\text{B.10})$$

When considering a homogeneous pathologic lesion made of the same incompressible orthotropic medium (i.e. when $E_R(R, \theta) = E_R^0$, $E_\theta(R, \theta) = E_\theta^0$ and $E_Z(R, \theta) = E_Z^0$), whatever the plaque geometry and the palpography domain Ω_{palpo} considered (with $R_i(\theta) \leq R \leq R_p(\theta)$), Equations B.2 to B.6 become:

$$ModelAI(\theta) = E_R^0 \left[1 - \frac{1}{4} \left(1 - \frac{E_R^0}{E_\theta^0} + \frac{E_R^0}{E_Z^0} \right) \left(1 + \frac{E_Z^0}{E_R^0} - \frac{E_Z^0}{E_\theta^0} \right) \right]^{-1} \quad (\text{B.11})$$

Appendix C

Novel anisotropic elasticity-palpography technique applied to RF sequences of rabbit aortas

The anisotropic elasticity-palpography technique has been tested *in silico* with virtual RF data, and *in vitro* using RF sequences from polyvinyl alcohol cryogel vascular phantoms. Both of these tests rendered good results. To test the performance in an animal model, IVUS sequences of rabbit aortas were used. This appendix summarizes the findings of this *ex vivo* study.

C.1 Experimental *ex vivo* study of rabbit aortas

Rabbit population

Animal population consisted of two Watanabe rabbits. Rabbit aortas have similar dimensions to those of human coronaries (Abela et al., 2016). The following protocol was conducted. After general anesthesia, rabbits were euthanized, and the thoracic and abdominal aortas were immediately harvested in a 4°C Krebs-Henseleit (KH) solution. The length of the samples were measured before excision in order to later reproduce the longitudinal *in situ* stretch of the artery on the experimental bench. The surrounding tissue was removed after dissection and the arteries were submerged on the KH solution bath during all manipulations to avoid tissue deterioration.

IVUS acquisitions

The arterial sections were mounted on an experimental bench to acquire IVUS images with pressure recordings. The IVUS platform used to record the RF signal was the GALAXY™2 (Boston Scientific, Watertown, MA) equipped with a 30 MHz Atlantis™SR Pro 3.6 F catheter. Dynamic pressure profiles of small amplitudes were applied for the image acquisitions; the results presented here were extracted from sequences with cyclic sinusoidal dynamic pressure at 30 beats per minute (peristaltic pump model 1405 PBP, Harvard Apparatus, USA). The maximal and minimal mean cyclic pressure amplitudes were of 2.10 and 2.60 kPa, and a mean incremental pressure amplitude ΔP close to 0.025 kPa was used to extract a series of 300 sets of two consecutive RF-IVUS images (Im^i, Im^{i+1} with $i = 1$ to 300). This results in small displacements and allow the use of the small strain hypothesis. Even though these do not represent *in vivo* and pathological conditions, they allow the evaluation of the AI-palpography

algorithms' capabilities to extract the elasticity of the arterial tissues.

Mechanical testing and histology

After the IVUS acquisitions, sections of 10 and 16 microns (selected in the IVUS-imaged zone) were obtained with a microtome to be used in atomic force microscopy (AFM) and immunohistological stainings. Mechanical testing was performed on several sites over the arterial wall cross-sections with a servo-controlled AFM (Nanowizard II, JPK instruments, Berlin, Germany). Serial 16 μm -thick vessel sections were mounted on Poly-L-Lysine slides (Thermo-Scientific, France). The arterial wall, including the intima and media layers, were exposed for probing by AFM. Tissue samples were kept in KH buffer. All AFM measurements were made in liquid at room temperature, including cantilever calibration. For all specimens, mechanical testing was completed within 4 hours of harvesting the sample (a detailed description of the AFM protocol is given in [Tracqui et al. \(2011\)](#)). Biological characterization was achieved by means of two different histologic staining methods: Hematoxylin Eosin Saffron (HES) trichromatic staining and Oil Red O (ORO).

C.2 Rabbit aorta study results

Figure [C.1](#) presents the resulting mean AI-palpogram computed for the healthy thoracic rabbit aortic cross-section # S2. To test the reproducibility and the performance of the anisotropic elasticity-palpography technique we computed $n=296$ AI-palpograms from a sequence of 300 IVUS images. The computed averaged AI amplitude was 76.7 ± 78 kPa. This mean computed AI value was compared to $\text{AI} = 94.3$ kPa obtained by substituting the mean experimental values acquired ex vivo on healthy Watanabe aortic walls : $E_R = 38.2 \pm 1.7$ kPa ([Matsumoto et al., 2002](#)), $E_{\theta} = 93.7$ kPa ([Hasegawa and Watanabe, 1988](#)) and $E_Z = 53.4 \pm 60.1$ kPa from our AFM mechanical tests on the vessel wall into Eq. 3 from [Gómez et al. \(2019\)](#):

$$ModelAI(\theta) = E_R^0 \left[1 - \frac{1}{4} \left(1 - \frac{E_R^0}{E_\theta^0} + \frac{E_R^0}{E_Z^0} \right) \left(1 + \frac{E_Z^0}{E_R^0} - \frac{E_Z^0}{E_\theta^0} \right) \right]^{-1} \quad (\text{C.1})$$

which results from considering a homogeneous pathological lesion made of the same quasi-incompressible orthotropic medium (i.e. when $E_R(R, \theta) = E_R^0$, $E_\theta(R, \theta) = E_\theta^0$ and $E_Z(R, \theta) = E_Z^0$), whatever the plaque geometry and the palpography domain Ω_{palpo} considered (with $R_i(\theta) \leq R \leq R_o(\theta)$) ([Gómez et al., 2019](#)).

The mean computed AI value reasonably agrees with the AI value obtained using the experimental Young's moduli and Eq. [C.1](#).

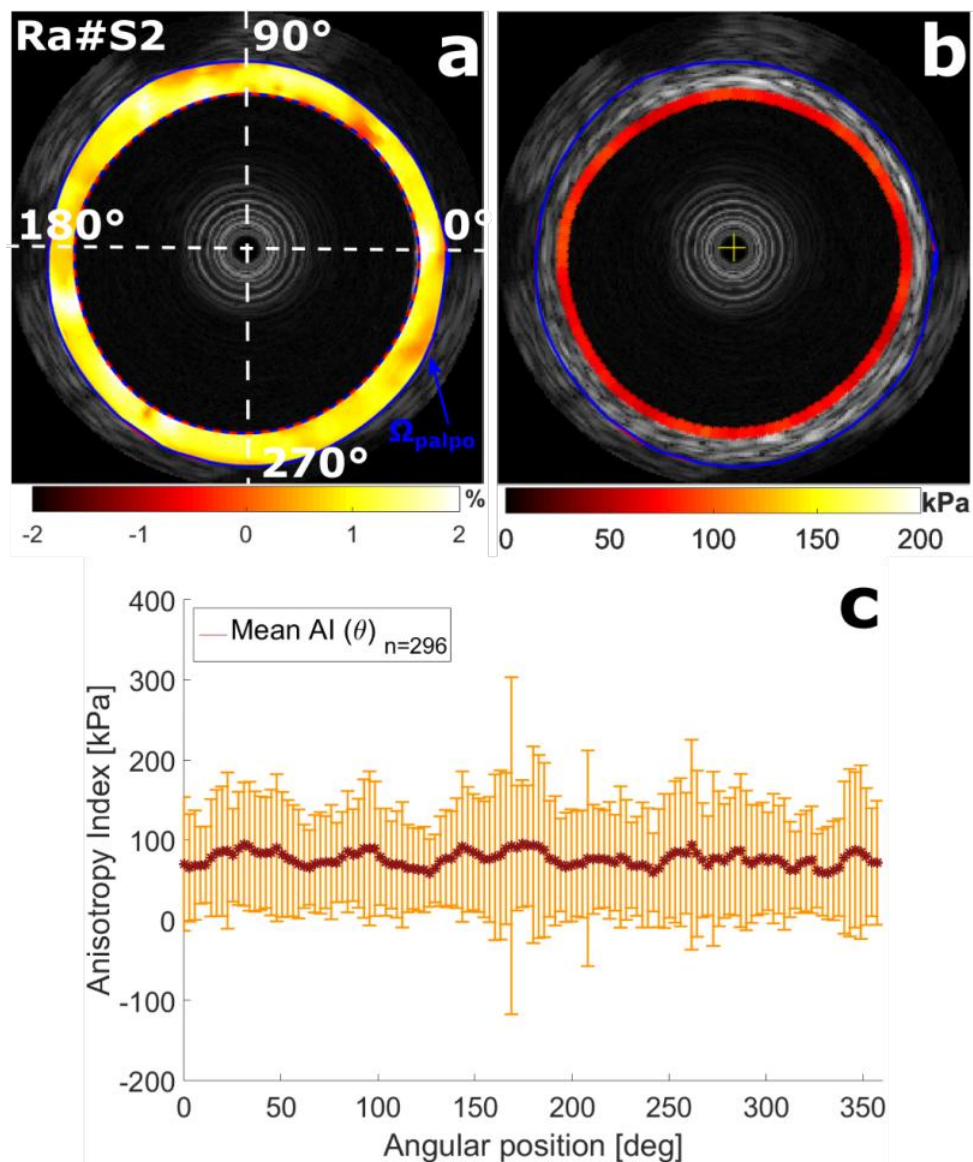


Figure C.1: Performance of the anisotropic elasticity-palpography technique algorithm to characterize *ex vivo* a healthy aortic wall of a Watanabe rabbit (Rabbit # S2) a) Vessel geometry (red contours), palpography domain (blue contour) and estimated LSME radial strain- elastogram. b) One IVUS image of the IVUS sequence with mean AI-palpogram. c) Mean estimated AI-palpogram with its standard deviation

Appendix D

Balloon mechanical test results

This appendix contains all the experimental curves corresponding to the balloon film and the catheter tensile tests, along with the main curves for each material and direction.

D.1 Balloon polymer film tensile tests

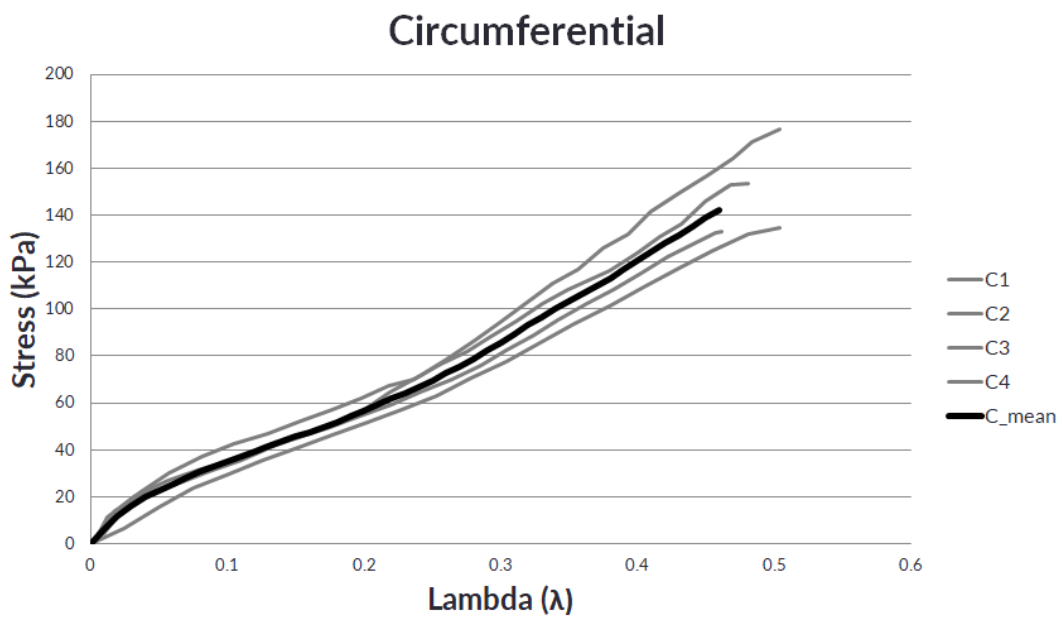


Figure D.1: Experimental curves from ballon uniaxial tensile tests in the circumferential direction.

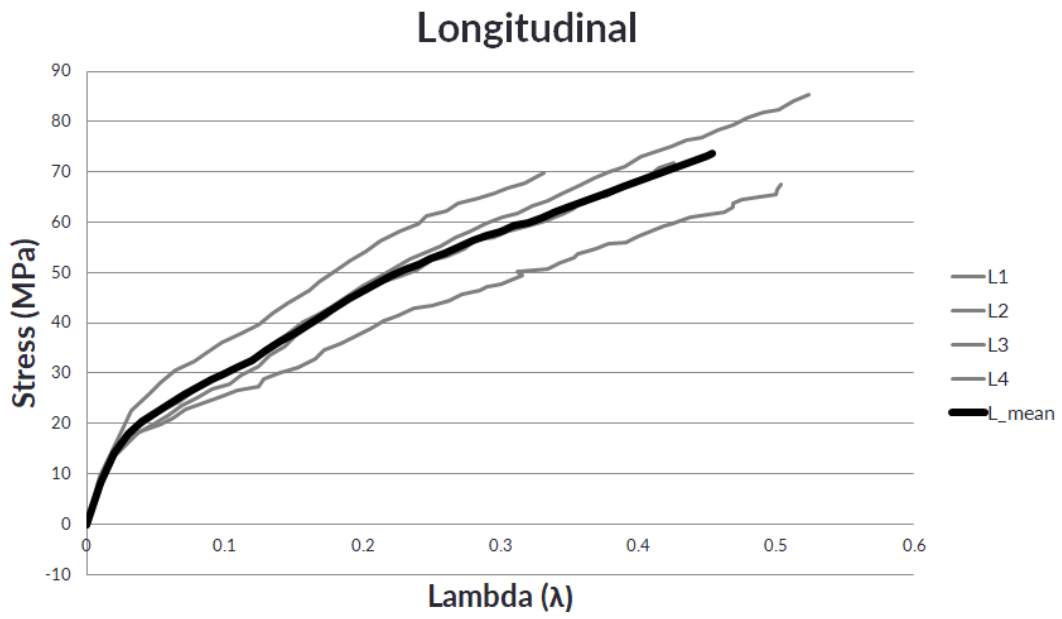


Figure D.2: Experimental curves from ballon uniaxial tensile tests in the longitudinal direction.

D.2 Catheter tensile tests

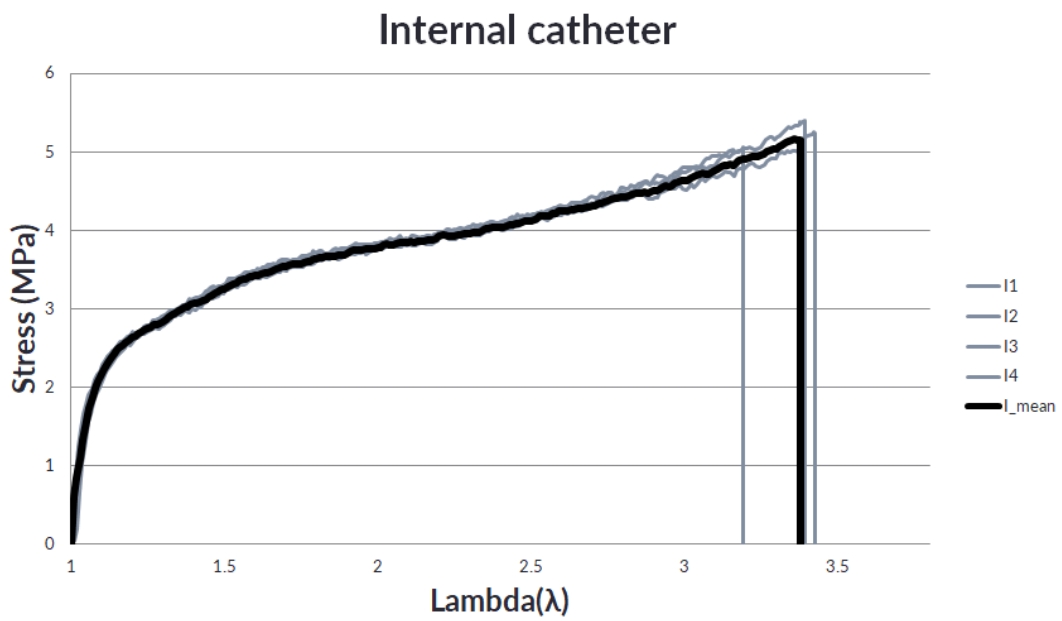


Figure D.3: Experimental curves from uniaxial tensile tests of the internal catheter.

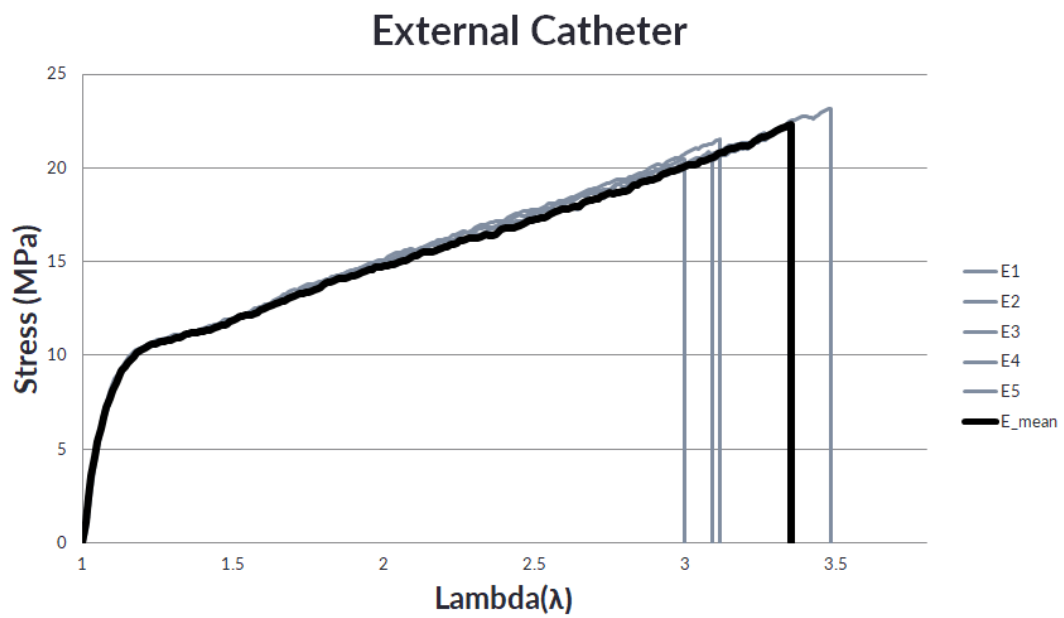


Figure D.4: Experimental curves from uniaxial tensile tests of the external catheter.

Appendix E

List of Publications and short CV

Journal article

2019

A **Gómez**, A Tacheau, G Finet, M Lagache, JL Martiel, S Le Floc'h, SK Yazdani, A Elias-Zuñiga, RI Pettigrew, G Cloutier, J Ohayon. *Intraluminal Ultrasonic Palpation Imaging Technique Revisited for Anisotropic Characterization of Healthy and Atherosclerotic Coronary Arteries: A Feasibility Study*. **Ultrasound in Medicine and Biology**, 45(1):35-49, 2019.

R Coppel, M Lagache, G Finet, G Rioufol, **A Gómez**, F Dérimay, M Malve, RI Pettigrew, J Ohayon. *Influence of collaterals on true FFR prediction for a left main stenosis with concomitant lesions: An in vitro study*. **Annals of Biomedical Engineering (ABME)**.

Book chapter

A **Gómez**, A Tacheau, S Le Floc'h, RI Pettigrew, G Cloutier, G Finet, and J Ohayon. *Intravascular Ultrasound Imaging of Human Coronary Atherosclerotic Plaque: Novel Morpho-Elastic Biomarkers of Instability*. Book chapter collaboration for **Biomechanics of Living Organs Series of Elsevier, Volume 3: Biomechanics of Coronary atherosclerotic Plaque: From Model to Patients**. Expected date of publication: July 2019.

E Peña, M Cilla, AT Latorre, MA Martínez, **A Gómez**, RI Pettigrew, G Finet, and J Ohayon. *Emergent biomechanical factors predicting vulnerable coronary atherosclerotic plaque rupture*. Book chapter collaboration for **Biomechanics of Living Organs Series of Elsevier, Volume 3: Biomechanics of Coronary atherosclerotic Plaque: From Model to Patients**. Expected date of publication: July 2019.

Oral communication in a conference

2018

A **Gómez**, A Tacheau, G Finet, SK Yazdani, M Lagache, RI Pettigrew, G Cloutier and J Ohayon. The Intravascular Ultrasound Anisotropic Elasticity-Palpography Technique: A

Reliable Tool for the Detection of Vulnerable Coronary Atherosclerotic Plaques. 8th World Congress of Biomechanics, 2018.

2017

A Gómez, A Tacheau, G Finet, R Coppel, M Lagache, JL Martiel, S Le Floc'h, RI Pettigrew, G Cloutier and J Ohayon. An intravascular ultrasound anisotropic elasticity-palpography technique for in vivo coronary atherosclerotic plaque detection and characterization. Computer Methods in Biomechanics and Biomedical Engineering, 42nd Société de Biomécanique Congress, 20:sup1, 97-98, 2017.

R Coppel, **A Gómez**, G Finet, M Mauro, RI Pettigrew, J Ohayon and M Lagache. Experimental Bench for Hemodynamic Study of Coronary Artery with Serial Stenoses: Fractional Flow Reserve Assessment. Computer Methods in Biomechanics and Biomedical Engineering, 42nd Société de Biomécanique Congress, 20:sup1, 45-46, 2017.

A Gómez, A Tacheau, G Finet, R Coppel, M Lagache, JL Martiel, S Le Floc'h, G Finet, RI Pettigrew, G Cloutier and J Ohayon. Intravascular ultrasound elasticity-palpography technique for mechanical characterization of coronary plaque anisotropy. VII International Conference on Computational Bioengineering, 2017.

ARMIDA GOMEZ

12 Rue Paul Janet, 38100, Grenoble
06 30 47 91 19

armida.gomez@univ-grenoble-alpes.fr

RESEARCH INTERESTS

Cardiovascular mechanics

Advanced materials modeling

Computational biomechanics

Design and manufacturing of medical devices

EDUCATION

Expected
June 2019

PhD in Biomechanics

Université Grenoble Alpes, France

Dissertation: "A novel anisotropic elasticity-palpography IVUS imaging tool and characterization of the viscoelasto-plastic properties of angioplasty balloons: Towards a better assessment and treatment of coronary artery diseases "
Jacques Ohayon, PhD

2015

M.S. in Manufacturing Systems

Tecnológico de Monterrey, Mexico

Dissertation: "Conceptual design of liquid injection molding machine for customizable implants"

Alex Elías, PhD

Research stay at the Universitat de Girona, Spain (2014)

Honors: *summa cum laude*

2013

B.S. in Mechatronics Engineering

Tecnológico de Monterrey, Mexico

Advanced Learning Program for High Achievement (ALPHA)

Semester abroad at the University of Illinois at Urbana-Champaign (2011)

Honors: *cum laude*

RESEARCH EXPERIENCE

2016-present

PhD Student, Université Grenoble Alpes, France

Laboratory TIMC-IMAG/ DyCTiM², UJF, CNRS UMR 5525, In³S

Intravascular ultrasound image analysis. Finite element simulations.

Mechanical characterization of angioplasty balloon catheters.

2015

Engineer Specialist, Tecnológico de Monterrey, Mexico

Nanotechnology for device design Research Group

Coordinate and participate in projects between industry and academia.

Planning and coordination of nanotechnology workshops for children.

2012

Design Engineering Intern, Sugoi Medical (startup), Mexico

Design for manufacturing of a bone marrow biopsy and aspiration needle.

Grant proposals preparation.

2010-2011

Research assistant, Tecnológico de Monterrey, Mexico

Medical devices Research Group

Mechanical characterization of NiTi alloy wire: material tests and

constitutive model. Proofreading of scientific documents in English.

SCHOLARSHIPS AND AWARDS

World Congress of Biomechanics travel grant from the Société de Biomécanique, 2018

Best poster presentation of ISCE doctoral school, 2017

CONACYT I2T2 Doctoral Scholarship, 2016

CONACYT National Scholarship, 2013-2015

Tecnológico de Monterrey Academic Talent Scholarship, 2008-2013

COMMITTEE AND ORGANIZATIONAL

Nano Monterrey 2015 International Forum

Local organizing committee: logistics

9th International Congress of Mechatronics Engineering "Automatización y Tecnología"

Coordinator of a research project award for undergraduate students

Advanced Learning Program for High Achievement (ALPHA) Student Council

Treasurer (2009-2010), Vicepresident (2010-2011)

SKILLS

Computer

Matlab

FEA: Comsol, ANSYS APDL, Abaqus

CAD: Solidworks, CREO, Inventor

Design: InDesign, Illustrator, Inkscape,
Flash, Photoshop

Equipment training

Confocal microscope

Atomic force microscopy

Preco MedPro laser system

Mechanical testing: Uniaxial, biaxial

Languages

Spanish - native

English - TOEFL IBT 114/120

French - B1

German - A2



Bibliography

- O. G. Abela, C. H. Ahsan, F. Alreefi, N. Salehi, I. Baig, A. Janoudi, and G. S. Abela. Plaque Rupture and Thrombosis: the Value of the Atherosclerotic Rabbit Model in Defining the Mechanism. *Curr. Atheroscler. Rep.*, 18(6):29, jun 2016. ISSN 1523-3804. doi: 10.1007/s11883-016-0587-0.
- M. Abran, G. Cloutier, M. H. R. Cardinal, B. Chayer, J. C. Tardif, and F. Lesage. Development of a photoacoustic, ultrasound and fluorescence imaging catheter for the study of atherosclerotic plaque. *IEEE Trans. Biomed. Circuits Syst.*, 8(5):696–703, 2014. ISSN 19324545. doi: 10.1109/TBCAS.2014.2360560.
- A. Ahmadi, J. Leipsic, R. Blankstein, C. Taylor, H. Hecht, G. W. Stone, and J. Narula. Do Plaques Rapidly Progress Prior to Myocardial Infarction?: The Interplay between Plaque Vulnerability and Progression, 2015. ISSN 15244571.
- A. Ahmadi, G. W. Stone, J. Leipsic, P. W. Serruys, L. Shaw, H. Hecht, G. Wong, B. L. Nørgaard, P. T. O’Gara, Y. Chandrashekar, and J. Narula. Association of coronary stenosis and plaque morphology with fractional flow reserve and outcomes. *JAMA Cardiol.*, 1(3):350–357, 2016. ISSN 23806591. doi: 10.1001/jamacardio.2016.0263.
- A. C. Akyildiz, L. Speelman, H. A. Nieuwstadt, H. van Brummelen, R. Virmani, A. van der Lugt, A. F. van der Steen, J. J. Wentzel, and F. J. Gijsen. The effects of plaque morphology and material properties on peak cap stress in human coronary arteries. *Comput. Methods Biomed. Biomed. Engin.*, 19(7):771–779, 2016. ISSN 14768259. doi: 10.1080/10255842.2015.1062091.
- A. A. Alsheikh-Ali, G. D. Kitsios, E. M. Balk, J. Lau, and S. Ip. The vulnerable atherosclerotic plaque: Scope of the literature. *Ann. Intern. Med.*, 153:387–395, 2010. ISSN 00034819. doi: 10.7326/0003-4819-153-6-201009210-00272.
- A. Arbab-Zadeh, M. Nakano, R. Virmani, and V. Fuster. Acute coronary events. *Circulation*, 125(9):1147–1156, 2012. ISSN 00097322. doi: 10.1161/CIRCULATIONAHA.111.047431.
- Arkema Inc. PEBA[®]X 7033 SA 01 MED Datasheet. Technical report, Arkema Incorporated, 2013. URL https://www.fosterpolymers.com/downloads/docs/pebax/tds/tds_{_}pebax_{_}7033_{_}sa01_{_}med.pdf.
- L. S. Athanasiou, P. Karvelis, S., A. I. Sakellarios, T. Exarchos, P., P. K. Siogkas, V. D. Tsakanikas, K. K. Naka, C. V. Bourantas, M. I. Papafaklis, G. Koutsouri, L. K. Michalis, O. Parodi, D. Fotiadis, and I. A hybrid plaque characterization method using intravascular ultrasound images. *Technol. Heal. Care*, 21(3):199–216, jan 2013. doi: 10.3233/THC-130717. URL <https://content.iospress.com/articles/technology-and-health-care/thc00717>.
- F. Auricchio, M. Di Loreto, and E. Sacco. Finite-element Analysis of a Stenotic Artery Revascularization Through a Stent Insertion. *Comput. Methods Biomed. Biomed. Engin.*,

BIBLIOGRAPHY

- 4(3):249–263, jan 2001. ISSN 1025-5842. doi: 10.1080/10255840108908007. URL <http://www.tandfonline.com/doi/abs/10.1080/10255840108908007>.
- H. Azarnoush, V. Pazos, S. Vergnole, B. Boulet, and G. Lamouche. Intravascular optical coherence tomography to validate finite-element simulation of angioplasty balloon inflation. *Phys. Med. Biol.*, 2018. doi: 10.1088/1361-6560/ab0d58. URL <https://doi.org/10.1088/1361-6560/ab0d58>.
- D. S. Baim. *Grossman’s Cardiac Catheterization, Angiography, and Intervention*. Wolters Kluwer Health, 2005. ISBN 0781755670.
- A. Balakrishnan and M. C. Saha. Effects of Ultrasound and Strain Rate on Tensile Mechanical Behavior of Thermoplastic Poly Urethane Thin Films. *J. Eng. Mater. Technol.*, 133(4), 2011. doi: 10.1115/1.4004695.
- R. A. Baldewsing, J. A. Schaar, F. Mastik, C. W. J. Oomens, and A. F. W. van der Steen. Assessment of vulnerable plaque composition by matching the deformation of a parametric plaque model to measured plaque deformation. *IEEE Trans. Med. Imaging*, 24(4):514–28, apr 2005.
- R. A. Baldewsing, F. Mastik, J. A. Schaar, P. W. Serruys, and A. F. van der Steen. Young’s modulus reconstruction of vulnerable atherosclerotic plaque components using deformable curves. *Ultrasound Med. Biol.*, 32(2):201–210, feb 2006a. doi: 10.1016/j.ultrasmedbio.2005.11.016.
- R. A. Baldewsing, J. A. Schaar, F. Mastik, and A. F. W. van der Steen. Local Elasticity Imaging of Vulnerable Atherosclerotic Coronary Plaques. *Adv. Cardiol.*, 44:35–61, 2006b. ISSN 0065-2326. doi: 10.1159/000096719.
- R. A. Baldewsing, M. G. Danilouchkine, F. Mastik, J. A. Schaar, P. W. Serruys, and A. F. W. van der Steen. An inverse method for imaging the local elasticity of atherosclerotic coronary plaques. *IEEE Trans. Inf. Technol. Biomed.*, 12(3):277–89, may 2008.
- E. J. Benjamin, M. J. Blaha, S. E. Chiuve, M. Cushman, S. R. Das, R. Deo, S. D. de Ferranti, J. Floyd, M. Fornage, C. Gillespie, C. R. Isasi, M. C. Jiménez, L. C. Jordan, S. E. Judd, D. Lackland, J. H. Lichtman, L. Lisabeth, S. Liu, C. T. Longenecker, R. H. Mackey, K. Matsushita, D. Mozaffarian, M. E. Mussolino, K. Nasir, R. W. Neumar, L. Palaniappan, D. K. Pandey, R. R. Thiagarajan, M. J. Reeves, M. Ritchey, C. J. Rodriguez, G. A. Roth, W. D. Rosamond, C. Sasson, A. Towfighi, C. W. Tsao, M. B. Turner, S. S. Virani, J. H. Voeks, J. Z. Willey, J. T. Wilkins, J. H. Wu, H. M. Alger, S. S. Wong, P. Muntner, and American Heart Association Statistics Committee and Stroke Statistics Subcommittee. Heart Disease and Stroke Statistics-2017 Update: A Report From the American Heart Association. *Circulation*, 135(10):e146–e603, 2017. ISSN 1524-4539. doi: 10.1161/CIR.0000000000000485.
- J. F. Bentzon, F. Otsuka, R. Virmani, and E. Falk. Mechanisms of plaque formation and rupture. *Circ. Res.*, 114(12), 2014. ISSN 15244571. doi: 10.1161/CIRCRESAHA.114.302721.
- J.-M. Berthelot. Elastic Behavior of an Orthotropic Composite. In *Compos. Mater. Mech. Behav. Struct. Anal.*, pages 186–194. 1999. doi: 10.1007/978-1-4612-0527-2_10.
- J. Bonet and R. D. Wood. *Nonlinear continuum mechanics for finite element analysis*. Cambridge University Press, 1997. ISBN 052157272X.
- C. V. Bourantas, F. A. Jaffer, F. J. Gijsen, G. Van Soest, S. P. Madden, B. K. Courtney, A. M. Fard, E. Tenekecioglu, Y. Zeng, A. F. Van Der Steen, S. Emelianov, J. Muller, P. H. Stone,

- L. Marcu, G. J. Tearney, and P. W. Serruys. Hybrid intravascular imaging: Recent advances, technical considerations, and current applications in the study of plaque pathophysiology. *Eur. Heart J.*, 38:400–412, 2017. ISSN 15229645. doi: 10.1093/eurheartj/ehw097.
- A. Bouvier, F. Deleaval, M. M. Doyley, S. K. Yazdani, G. Finet, S. Le Floch, G. Cloutier, R. I. Pettigrew, and J. Ohayon. A direct vulnerable atherosclerotic plaque elasticity reconstruction method based on an original material-finite element formulation: theoretical framework. *Phys. Med. Biol.*, 58(23):8457–8476, dec 2013. doi: 10.1088/0031-9155/58/23/8457.
- M. Brand, I. Avrahami, S. Einav, and M. Ryvkin. Numerical models of net-structure stents inserted into arteries. *Comput. Biol. Med.*, 2014. ISSN 18790534. doi: 10.1016/j.complbiomed.2014.06.015.
- E. Brunenberg, O. Pujol, B. ter Haar Romeny, and P. Radeva. Automatic IVUS Segmentation of Atherosclerotic Plaque with Stop & Go Snake. In *MICCAI 2006 Med. Image Comput. Comput. Interv. – MICCAI 2006*, pages 9–16. Springer, Berlin, Heidelberg, 2006. doi: 10.1007/11866763_2. URL http://link.springer.com/10.1007/11866763_{_}2.
- R. A. Byrne, G. W. Stone, J. Ormiston, and A. Kastrati. Coronary balloon angioplasty, stents, and scaffolds. *Lancet*, 390(10096):781–792, aug 2017. doi: 10.1016/S0140-6736(17)31927-X. URL <https://www.sciencedirect-com.gaelnomade-2.grenet.fr/science/article/pii/S014067361731927X>.
- C. Capelli, F. Gervaso, L. Petrini, G. Dubini, and F. Migliavacca. Assessment of tissue prolapse after balloon-expandable stenting: Influence of stent cell geometry. *Med. Eng. Phys.*, 31:441–447, 2009. doi: 10.1016/j.medengphy.2008.11.002. URL <https://pdf.sciencedirectassets.com/271469/1-s2.0-S1350453309X00044/1-s2.0-S135045330800204X/main.pdf?x-amz-security-token=FQoGZXIvYXZdZEEkaDJZVx{%}2F0lexJ{%}2F9HIuyK3A3PiJd1DUlYxtwaOzobOweNJ5Y2f2H20SWiZSinMEEbJH>
- J. D. Caplan, S. Waxman, R. W. Nesto, and J. E. Muller. Near-Infrared Spectroscopy for the Detection of Vulnerable Coronary Artery Plaques. *J. Am. Coll. Cardiol.*, 47(8):C92–6, 2006. ISSN 07351097. doi: 10.1016/j.jacc.2005.12.045.
- L. Cardoso and S. Weinbaum. Changing Views of the Biomechanics of Vulnerable Plaque Rupture: A Review. *Ann. Biomed. Eng.*, 42(2):415–431, 2014. doi: 10.1007/s10439-013-0855-x.
- J. L. Cavalcante and E. Larose. Intravascular MRI for Plaque Characterization: Are We Close to Reality? *Curr. Cardiol. Rep.*, 18(9):89, 2016. ISSN 1523-3782. doi: 10.1007/s11886-016-0766-1.
- G. Cellier. Etude expérimentale et comparative de la compliance des ballons d’angioplastie coronaire. Technical report, Hôpital Cardio-vasculaire Louis PRADEL, Lyon, France, 2017.
- E. I. Céspedes, C. L. De Korte, and A. F. Van Der Steen. Intraluminal ultrasonic palpation: assessment of local and cross-sectional tissue stiffness. *Ultrasound Med. Biol.*, 26(3):385–396, 2000. ISSN 03015629. doi: 10.1016/S0301-5629(99)00169-6.
- I. Céspedes, J. Ophir, H. Ponnekanti, and N. Maklad. Elastography: Elasticity imaging using ultrasound with application to muscle and breast in vivo. *Ultrason. Imaging*, 15:73–88, 1993.
- G. Chagnon, J. Ohayon, J.-L. Martiel, and D. Favier. Hyperelasticity Modeling for Incompressible Passive Biological Tissues. In *Biomech. Living Organs*, pages 3–30. Elsevier, 2017. ISBN 9780128040096. doi: 10.1016/B978-0-12-804009-6.00001-8.

BIBLIOGRAPHY

- S. Chatelin, M. Bernal, T. Deffieux, C. Papadacci, P. Flaud, A. Nahas, C. Boccara, J.-L. Gennisson, M. Tanter, and M. Pernot. Anisotropic polyvinyl alcohol hydrogel phantom for shear wave elastography in fibrous biological soft tissue: a multimodality characterization. *Phys. Med. Biol.*, 59(22):6923–6940, nov 2014. ISSN 0031-9155. doi: 10.1088/0031-9155/59/22/6923. URL <http://stacks.iop.org/0031-9155/59/i=22/a=6923?key=crossref.2a5682fe172f0a85f5fe71d63e648e81>.
- K. Chatterjee. *Cardiology : an illustrated textbook*. Jaypee Brothers Medical Publisher, 1st edition, 2013. ISBN 9789350252758.
- J. M. Cheng, H. M. Garcia-Garcia, S. P. M. De Boer, I. Kardys, J. H. Heo, K. M. Akkerhuis, R. M. Oemrawsingh, R. T. Van Domburg, J. Ligthart, K. T. Witberg, E. Regar, P. W. Serruys, R. J. Van Geuns, and E. Boersma. In vivo detection of high-risk coronary plaques by radiofrequency intravascular ultrasound and cardiovascular outcome: Results of the ATHEROREMO-IVUS study. *Eur. Heart J.*, 35:639–947, 2014. ISSN 15229645. doi: 10.1093/eurheartj/eh484.
- R. Chopard, L. Boussel, P. Motreff, G. Rioufol, A. Tabib, P. Douek, D. Meyronet, D. Revel, and G. Finet. How reliable are 40 MHz IVUS and 64-slice MDCT in characterizing coronary plaque composition? An ex vivo study with histopathological comparison. *Int. J. Cardiovasc. Imaging*, 26(4):373–383, 2010. ISSN 1569-5794. doi: 10.1007/s10554-009-9562-y.
- K. C. Chu and B. K. Rutt. Polyvinyl alcohol cryogel: An ideal phantom material for MR studies of arterial flow and elasticity. *Magn. Reson. Med.*, 37(2):314–319, feb 1997. ISSN 07403194. doi: 10.1002/mrm.1910370230. URL <http://doi.wiley.com/10.1002/mrm.1910370230>.
- M. Cilla, E. Peña, and M. A. Martínez. 3D computational parametric analysis of eccentric atheroma plaque: influence of axial and circumferential residual stresses. *Biomech. Model. Mechanobiol.*, 11(7):1001–1013, 2012. ISSN 1617-7959. doi: 10.1007/s10237-011-0369-0.
- A. Cournand, R. L. Riley, E. S. Breed, E. D. Baldwin, D. W. Richards, M. S. Lester, and A. M. Jones. Measurement of cardiac output in man using the technique of catheterization of the right auricle or ventricle. *J. Clin. Invest.*, 24:106–116, 1945. URL <https://dm5migu4zj3pb.cloudfront.net/manuscripts/101000/101570/JCI45101570.pdf>.
- D. Dash. Complications of coronary intervention: abrupt closure, dissection, perforation. *Heart Asia*, 5(1):61–5, 2013. doi: 10.1136/heartasia-2013-010304. URL <http://www.ncbi.nlm.nih.gov/pubmed/27326079>.
- F. Daver, P. Girard, F. Thibault, P. Girard, F. Thibault, C. De Grandpré, and R. Diraddo. Enhancement of angioplasty balloon performance through annealing. Technical report, 2010. URL <https://www.researchgate.net/publication/48445993>.
- S. David Chua, B. MacDonald, and M. Hashmi. Finite element simulation of slotted tube (stent) with the presence of plaque and artery by balloon expansion. *J. Mater. Process. Technol.*, 155-156:1772–1779, 2004. doi: 10.1016/j.jmatprotec.2004.04.396. URL <https://pdf.sciencedirectassets.com/271356/1-s2.0-S0924013600X02312/1-s2.0-S0924013604004984/main.pdf?x-amz-security-token=FQoGZXIvYXZzEEUaDAW6eTZIbkYu1MWLoCK3A97apdIutB0dYD7C{%}2Btgs4dnpwGA{%}2F200Lm93e8WI8CqRw5f>
- M. De Beule, P. Mortier, S. Ste´phane, G. Carlier, B. Verhegghe, R. Van Impe, and P. Verdonck. Realistic finite element-based stent design: The impact of balloon folding. *J. Biomech.*, 41:383–389, 2008. doi: 10.1016/j.jbiomech.2007.08.014. URL www.elsevier.com/locate/jbiomech.

- C. L. De Korte, S. G. Carlier, F. Mastik, M. M. Doyley, A. F. W. Van Der Steen, P. W. Serruys, and N. Bom. Morphological and mechanical information of coronary arteries obtained with intravascular elastography: Feasibility study in vivo. *Eur. Heart J.*, 23:405–413, 2002. ISSN 0195668X. doi: 10.1053/euhj.2001.2806.
- F. Deleaval. *Caractérisation des propriétés mécaniques de la plaque d'athérome à partir de données échographiques endovasculaires : la technique de palpographie revisitée*. PhD thesis, Université de Grenoble, 2013.
- F. Deleaval, A. Bouvier, G. Finet, G. Cloutier, S. K. Yazdani, S. Le Floc'h, P. Clarysse, R. I. Pettigrew, and J. Ohayon. The Intravascular Ultrasound Elasticity-Palpography Technique Revisited: A Reliable Tool for the In Vivo Detection of Vulnerable Coronary Atherosclerotic Plaques. *Ultrasound Med. Biol.*, 39(8):1469–1481, 2013. ISSN 03015629. doi: 10.1016/j.ultrasmedbio.2013.03.001.
- C. Di Mario, G. Gøрге, R. Peters, P. Kearney, F. Pinto, D. Hausmann, C. von Birgelen, A. Colombo, H. Mudra, J. Roelandt, and R. Erbel. Clinical application and image interpretation in intracoronary ultrasound. Study Group on Intracoronary Imaging of the Working Group of Coronary Circulation and of the Subgroup on Intravascular Ultrasound of the Working Group of Echocardiography of the Eu. *Eur. Heart J.*, 19(2):207–29, 1998. ISSN 0195-668X.
- C. T. Dotter, J. Rösch, and M. P. Judkins. Transluminal dilatation of atherosclerotic stenosis. *Surg. Gynecol. Obstet.*, 127(4):794–804, oct 1968. URL <http://www.ncbi.nlm.nih.gov/pubmed/5675197>.
- M. M. Doyley. Model-based elastography: a survey of approaches to the inverse elasticity problem. *Phys. Med. Biol.*, 57(3):R35–73, 2012. ISSN 1361-6560. doi: 10.1088/0031-9155/57/3/R35.
- M. M. Doyley, F. Mastik, C. L. de Korte, S. G. Carlier, E. I. Céspedes, P. W. Serruys, N. Bom, and A. F. van der Steen. Advancing intravascular ultrasonic palpation toward clinical applications. *Ultrasound Med. Biol.*, 27(11):1471–80, 2001. ISSN 0301-5629. doi: 10.1016/S0301-5629(01)00457-4.
- J. Eaton-Evans, J. Dulieu-Barton, E. Little, and I. Brown. A New Approach to Stress Analysis of Vascular Devices using High Resolution Thermoelastic Stress Analysis. *Appl. Mech. Mater.*, 5-6:63–70, 2006. doi: 10.4028/www.scientific.net/AMM.5-6.63. URL <https://www-scientific-net.gaelnomade-1.grenet.fr/AMM.5-6.63.pdf>.
- D. A. Eftaxiopoulos and C. Atkinson. A nonlinear, anisotropic and axisymmetric model for balloon angioplasty. *Proc. R. Soc. A Math. Phys. Eng. Sci.*, 461(2056):1097–1128, apr 2005. doi: 10.1098/rspa.2004.1419. URL <http://www.royalsocietypublishing.org/doi/10.1098/rspa.2004.1419>.
- Z. A. Fayad, V. Fuster, K. Nikolaou, and C. Becker. Computed Tomography and Magnetic Resonance Imaging for Noninvasive Coronary Angiography and Plaque Imaging. *Circulation*, 106(15):2026–2034, oct 2002. doi: 10.1161/01.CIR.0000034392.34211.FC.
- M. Fedel, F. Tessarolo, P. Ferrari, C. Lö, N. Ghassemieh, G. M. Guarrera, and G. Nollo. Functional Properties and Performance of New and Reprocessed Coronary Angioplasty Balloon Catheters. *J. Biomed. Mater. Res. - Part B Appl. Biomater.*, 78B(2):364–372, 2006. doi: 10.1002/jbm.b.30496. URL www.interscience.wiley.com.
- G. Fichtinger, A. Martel, and T. Peters. *Medical image computing and computer-assisted intervention– MICCAI 2011 : 14th International Conference, Toronto, Canada, September 18-22, 2011, proceedings. Part I*. Springer, 2011. ISBN 9783642236228.

- G. Finet, J. Ohayon, and G. Rioufol. Biomechanical interaction between cap thickness, lipid core composition and blood pressure in vulnerable coronary plaque: impact on stability or instability. *Coron. Artery Dis.*, 15(1):13–20, 2004. ISSN 0954-6928. doi: 10.1097/00019501-200402000-00003.
- J. L. Fleg, G. W. Stone, Z. A. Fayad, J. F. Granada, T. S. Hatsukami, F. D. Kolodgie, J. Ohayon, R. Pettigrew, M. S. Sabatine, G. J. Tearney, S. Waxman, M. J. Domanski, P. R. Srinivas, and J. Narula. Detection of high-risk atherosclerotic plaque: Report of the NHLBI Working Group on current status and future directions. *JACC Cardiovasc. Imaging*, 5(9):941–55, 2012. ISSN 1936878X. doi: 10.1016/j.jcmg.2012.07.007.
- J. Fromageau, E. Brusseau, D. Vray, G. Gimenez, and P. Delachartre. Characterization of PVA cryogel for intravascular ultrasound elasticity imaging. *IEEE Trans. Ultrason. Ferroelectr. Freq. Control*, 50(10):1318–1324, 2003. ISSN 0885-3010. doi: 10.1109/TUFFFC.2003.1244748.
- J. Fromageau, J.-L. Gennisson, C. Schmitt, R. Maurice, R. Mongrain, and G. Cloutier. Estimation of polyvinyl alcohol cryogel mechanical properties with four ultrasound elastography methods and comparison with gold standard testings. *IEEE Trans. Ultrason. Ferroelectr. Freq. Control*, 54(3):498–509, mar 2007a. ISSN 0885-3010. doi: 10.1109/TUFFFC.2007.273. URL <http://ieeexplore.ieee.org/document/4139330/>.
- J. Fromageau, J.-L. Gennisson, C. Schmitt, R. Maurice, R. Mongrain, and G. Cloutier. Estimation of polyvinyl alcohol cryogel mechanical properties with four ultrasound elastography methods and comparison with gold standard testings. *IEEE Trans. Ultrason. Ferroelectr. Freq. Control*, 54(3):498–509, mar 2007b. ISSN 0885-3010. doi: 10.1109/TUFFFC.2007.273. URL <http://ieeexplore.ieee.org/document/4139330/>.
- K. Fujii, S. G. Carlier, G. S. Mintz, Y.-m. Yang, I. Moussa, G. Weisz, G. Dangas, R. Mehran, A. J. Lansky, E. M. Kreps, M. Collins, G. W. Stone, J. W. Moses, and M. B. Leon. Stent underexpansion and residual reference segment stenosis are related to stent thrombosis after sirolimus-eluting stent implantation. *J. Am. Coll. Cardiol.*, 45(7):995–998, apr 2005a. doi: 10.1016/j.jacc.2004.12.066. URL <https://linkinghub.elsevier.com/retrieve/pii/S0735109705001233>.
- K. Fujii, S. G. Carlier, G. S. Mintz, Y.-m. Yang, I. Moussa, G. Weisz, G. Dangas, R. Mehran, A. J. Lansky, E. M. Kreps, M. Collins, G. W. Stone, J. W. Moses, and M. B. Leon. Stent underexpansion and residual reference segment stenosis are related to stent thrombosis after sirolimus-eluting stent implantation. *J. Am. Coll. Cardiol.*, 45(7):995–998, apr 2005b. doi: 10.1016/j.jacc.2004.12.066. URL <https://linkinghub.elsevier.com/retrieve/pii/S0735109705001233>.
- H. M. Garcìa-Garcìa, B. D. Gogas, P. W. Serruys, and N. Bruining. IVUS-based imaging modalities for tissue characterization: similarities and differences. *Int J Cardiovasc Imaging*, 27:215–224, 2011. doi: 10.1007/s10554-010-9789-7. URL https://www.ncbi.nlm.nih.gov/pmc/articles/PMC3078312/pdf/10554_{ }2010_{ }Article_{ }9789.pdf.
- S. Garg and P. W. Serruys. Coronary Stents. *J. Am. Coll. Cardiol.*, 56(10):S43–S78, aug 2010. doi: 10.1016/j.jacc.2010.06.008. URL <https://linkinghub.elsevier.com/retrieve/pii/S0735109710023739>.
- D. Gastaldi, S. Morlacchi, R. Nichetti, C. Capelli, G. Dubini, L. Petrini, and F. Migliavacca. Modelling of the provisional side-branch stenting approach for the treatment of atherosclerotic coronary bifurcations: Effects of stent positioning. *Biomech. Model. Mechanobiol.*, 2010. ISSN 16177959. doi: 10.1007/s10237-010-0196-8.

BIBLIOGRAPHY

- S. C. Gerretsen, M. E. Kooi, S. Schalla, T. Delhaas, G. Snoep, J. M. A. Van Engelshoven, and T. Leiner. Magnetic resonance imaging of the coronary arteries. *Cardiovasc. J. Afr.*, 18(4): 248–59, 2007.
- N. Gessert, M. Lutz, M. Heyder, S. Latus, D. M. Leistner, Y. S. Abdelwahed, and A. Schlaefer. Automatic Plaque Detection in IVOCT Pullbacks Using Convolutional Neural Networks. *IEEE Trans. Med. Imaging*, pages 1–1, 2018. ISSN 0278-0062. doi: 10.1109/TMI.2018.2865659.
- F. J. Gijzen and F. Migliavacca. Plaque mechanics. *J. Biomech.*, 47:763–764, 2014. doi: 10.1016/j.jbiomech.2014.01.031.
- F. J. H. Gijzen, J. J. Wentzel, A. Thury, F. Mastik, J. A. Schaar, J. C. H. Schuurbijs, C. J. Slager, W. J. van der Giessen, P. J. de Feyter, A. F. W. van der Steen, and P. W. Serruys. Strain distribution over plaques in human coronary arteries relates to shear stress. *Am. J. Physiol. Circ. Physiol.*, 295(4):H1608–H1614, 2008. ISSN 0363-6135. doi: 10.1152/ajpheart.01081.2007.
- P. E. Gill, W. Murray, and M. A. Saunders. SNOPT: An SQP Algorithm for Large-Scale Constrained Optimization. *SIAM Rev.*, 47(1):99–131, jan 2005. doi: 10.1137/S0036144504446096.
- S. Glagov, E. Weisenberg, C. K. Zarins, R. Stankunavicius, and G. J. Kolettis. Compensatory Enlargement of Human Atherosclerotic Coronary Arteries. *N. Engl. J. Med.*, 316(22): 1371–1375, may 1987. doi: 10.1056/NEJM198705283162204.
- GlobalData. ACUTE CORONARY SYNDROME - CURRENT AND FUTURE PLAYERS. Technical report, GlobalData, 2014.
- GlobalData. Asia-Pacific Interventional Cardiology Procedures Outlook to 2021. Technical Report April, GlobalData, 2016a.
- GlobalData. EU5 Interventional Cardiology Procedures Outlook to 2021. Technical Report April, GlobalData, 2016b.
- GlobalData. United States Interventional Cardiology Procedures Outlook to. Technical Report March, GlobalData, 2016c.
- GlobalData. EU5 Cardiovascular Surgery Outlook to 2021. Technical Report April, GlobalData, 2016d.
- GlobalData. United States Cardiovascular Surgery Outlook to 2021. Technical Report March, GlobalData, 2016e.
- S. Golemati, A. Gastounioti, and K. S. Nikita. Ultrasound-Image-Based Cardiovascular Tissue Motion Estimation. *IEEE Rev. Biomed. Eng.*, 9:208–218, 2016. doi: 10.1109/RBME.2016.2558147.
- A. Gómez, A. Tacheau, G. Finet, M. Lagache, J.-L. Martiel, S. Floc’h, S. Yazdani, A. Elias-Zuñiga, R. Pettigrew, G. Cloutier, and J. Ohayon. Intraluminal Ultrasonic Palpation Imaging Technique Revisited for Anisotropic Characterization of Healthy and Atherosclerotic Coronary Arteries: A Feasibility Study. *Ultrasound Med. Biol.*, 45(1), 2019. ISSN 1879291X. doi: 10.1016/j.ultrasmedbio.2018.08.020.
- R. C. Gonzalez and R. E. Woods. *Digital image processing*. Prentice Hall, New Jersey, 2nd edition, 2002. ISBN 0201180758.

- J. F. Granada, D. Wallace-Bradley, H. K. Win, C. L. Alviar, A. Builes, E. I. Lev, R. Barrios, D. G. Schulz, A. E. Raizner, and G. L. Kaluza. In Vivo Plaque Characterization Using Intravascular Ultrasound–Virtual Histology in a Porcine Model of Complex Coronary Lesions. *Arterioscler. Thromb. Vasc. Biol.*, 27(2):387–393, feb 2007. doi: 10.1161/01.ATV.0000253907.51681.0e. URL <https://www.ahajournals.org/doi/10.1161/01.ATV.0000253907.51681.0e>.
- M. A. Granero, M. A. Gutierrez, and E. T. Costa. Rebuilding IVUS images from raw data of the RF signal exported by IVUS equipment. *Emerg. Trends Image Process. Comput. Vis. Pattern Recognit.*, pages 87–97, jan 2015. doi: 10.1016/B978-0-12-802045-6.00006-5.
- X. Guo, J. Zhu, A. Maehara, D. Monoly, H. Samady, L. Wang, K. L. Billiar, J. Zheng, C. Yang, G. S. Mintz, D. P. Giddens, and D. Tang. Quantify patient-specific coronary material property and its impact on stress/strain calculations using in vivo IVUS data and 3D FSI models: a pilot study. *Biomech. Model. Mechanobiol.*, 16(15):333–344, 2017. ISSN 16177940. doi: 10.1007/s10237-016-0820-3.
- D. Hackett, G. Davies, and A. Maseri. Pre-existing coronary stenoses in patients with first myocardial infarction are not necessarily severe. *Eur. Heart J.*, 9(12):1317–1323, dec 1988. doi: 10.1093/oxfordjournals.eurheartj.a062449.
- G. K. Hansson. Inflammation, Atherosclerosis, and Coronary Artery Disease, apr 2005. ISSN 0028-4793. URL [www.nejm.orghttp://www.nejm.org/doi/abs/10.1056/NEJMra043430](http://www.nejm.org/doi/abs/10.1056/NEJMra043430).
- M. Hasegawa and Y. Watanabe. Rheological properties of the thoracic aorta in normal and WHHL rabbits. *Biorheology*, 25(1-2):147–56, 1988.
- C. Hehrlein, J. J. DeVries, T. A. Wood, S. D. Haller, A. Arab, A. C. Kloostra, M. A. Lauer, and T. A. Fischell. Overestimation of stent delivery balloon diameters by manufacturers’ compliance tables: A quantitative coronary analysis of Duet and NIR stent implantation. *Catheter. Cardiovasc. Interv.*, 53(4):474–478, aug 2001. doi: 10.1002/ccd.1205. URL <http://doi.wiley.com/10.1002/ccd.1205>.
- G. A. Holzapfel. *Nonlinear solid mechanics : a continuum approach for engineering*. Wiley, 2000. ISBN 9780471823193.
- G. A. Holzapfel, M. Stadler, and C. A. J. Schulze-Bauer. A Layer-Specific Three-Dimensional Model for the Simulation of Balloon Angioplasty using Magnetic Resonance Imaging and Mechanical Testing. *Ann. Biomed. Eng.*, 30(6):753–767, 2002. doi: 10.1114/1.1492812. URL <https://link-springer-com.gaelnomade-2.grenet.fr/content/pdf/10.1114/1.1492812.pdf>.
- G. A. Holzapfel, G. Sommer, C. T. Gasser, and P. Regitnig. Determination of layer-specific mechanical properties of human coronary arteries with nonatherosclerotic intimal thickening and related constitutive modeling. *Am. J. Physiol. Circ. Physiol.*, 289(5):H2048–H2058, 2005. ISSN 0363-6135. doi: 10.1152/ajpheart.00934.2004.
- X.-B. Hu, P.-F. Zhang, H.-J. Su, X. Yi, L. Chen, Y.-Y. Rong, K. Zhang, X. Li, L. Wang, C.-L. Sun, X.-J. Cai, L. Li, J.-T. Song, X.-M. Dai, X.-D. Sui, Y. Zhang, and M. Zhang. Intravascular Ultrasound Area Strain Imaging Used to Characterize Tissue Components and Assess Vulnerability of Atherosclerotic Plaques in a Rabbit Model. *Ultrasound Med. Biol.*, 37(10):1579–1587, 2011. ISSN 0301-5629. doi: <https://doi.org/10.1016/j.ultrasmedbio.2011.06.025>. URL <http://www.sciencedirect.com/science/article/pii/S0301562911012117>.
- J. Jensen and N. Svendsen. Calculation of pressure fields from arbitrarily shaped, apodized, and excited ultrasound transducers. *IEEE Trans. Ultrason. Ferroelectr. Freq. Control*, 39(2): 262–267, 1992. ISSN 0885-3010. doi: 10.1109/58.139123.

- H. Kanai, H. Hasegawa, M. Ichiki, F. Tezuka, and Y. Koiwa. Elasticity Imaging of Atheroma With Transcutaneous Ultrasound. *Circulation*, 107(24):3018–3021, jun 2003. doi: 10.1161/01.CIR.0000078633.31922.8A.
- K. Karmelek. Balloon catheters: What are some key design considerations? — Medical Design and Outsourcing, 2016. URL <https://www.medicaldesignandoutsourcing.com/balloon-catheters-key-design-considerations/>.
- A. Katouzian, E. D. Angelini, S. G. Carlier, J. S. Suri, N. Navab, and A. F. Laine. A State-of-the-Art Review on Segmentation Algorithms in Intravascular Ultrasound (IVUS) Images. *IEEE Trans. Inf. Technol. Biomed.*, 16(5):823–834, sep 2012. doi: 10.1109/TITB.2012.2189408. URL <http://ieeexplore.ieee.org/document/6159086/>.
- A. Kelly-Arnold, N. Maldonado, D. Laudier, E. Aikawa, L. Cardoso, and S. Weinbaum. Revised microcalcification hypothesis for fibrous cap rupture in human coronary arteries. *Proc. Natl. Acad. Sci.*, 110(26):10741–10746, 2013. ISSN 0027-8424. doi: 10.1073/pnas.1308814110.
- A. S. Khalil, B. E. Bouma, and M. R. Kaazempur Mofrad. A Combined FEM/Genetic Algorithm for Vascular Soft tissue Elasticity Estimation. *Cardiovasc. Eng.*, 6(3):93–102, nov 2006. doi: 10.1007/s10558-006-9013-5.
- K. Kim, W. Weitzel, J. Rubin, H. Xie, X. Chen, and M. O’Donnell. Vascular intramural strain imaging using arterial pressure equalization. *Ultrasound Med. Biol.*, 30(6):761–771, jun 2004. doi: 10.1016/j.ultrasmedbio.2004.04.003.
- S. B. King. Angioplasty From Bench to Bedside to Bench. *Circulation*, 93(9):1621–1629, may 1996. doi: 10.1161/01.CIR.93.9.1621. URL <https://www.ahajournals.org/doi/10.1161/01.CIR.93.9.1621>.
- D. E. Kioussis, T. Christian Gasser, and G. A. Holzapfel. A Numerical Model to Study the Interaction of Vascular Stents with Human Atherosclerotic Lesions. *Ann. Biomed. Eng.*, 35(11):1857–1869, 2007. doi: 10.1007/s10439-007-9357-z. URL <https://link-springer-com.gaelnomade-2.grenet.fr/content/pdf/10.1007/2Fs10439-007-9357-z.pdf>.
- D. E. Kioussis, T. C. Gasser, and G. A. Holzapfel. Smooth contact strategies with emphasis on the modeling of balloon angioplasty with stenting. *Int. J. Numer. Methods Eng.*, 75(7):826–855, aug 2008a. doi: 10.1002/nme.2277. URL <http://doi.wiley.com/10.1002/nme.2277>.
- D. E. Kioussis, A. R. Wulff, and G. A. Holzapfel. Experimental Studies and Numerical Analysis of the Inflation and Interaction of Vascular Balloon Catheter-Stent Systems. *Ann. Biomed. Eng.*, 37(2):315–330, 2008b. doi: 10.1007/s10439-008-9606-9. URL <http://download.springer.com.gaelnomade-1.grenet.fr/static/pdf/558/art/253A10.1007/252Fs10439-008-9606-9.pdf?originUrl=http/3A/2F/2Flink.springer.com/2Farticle/2F10.1007/2Fs10439-008-9606-9&token2=exp=1494336686~ac1=/2Fstatic/2Fpdf/2F558/2Fart/25253A10.10>.
- D. E. Kioussis, A. R. Wulff, and G. A. Holzapfel. Experimental Studies and Numerical Analysis of the Inflation and Interaction of Vascular Balloon Catheter-Stent Systems. *Ann. Biomed. Eng.*, 37(2):315–330, feb 2009. doi: 10.1007/s10439-008-9606-9. URL <http://link.springer.com/10.1007/s10439-008-9606-9>.
- A. M. Kok, L. Speelman, R. Virmani, A. F. Steen, F. J. Gijssen, and J. J. Wentzel. Peak cap stress calculations in coronary atherosclerotic plaques with an incomplete necrotic core geometry. *Biomed. Eng. Online*, 15:48, 2016. ISSN 1475925X. doi: 10.1186/s12938-016-0162-5.
- B. J. Lambert, F.-W. F.-W. Tang, W. J. W. J. Rogers, and Rapra Technology Limited. *Polymers in medical applications*. Rapra Technology, 2001. ISBN 9781859572597.

BIBLIOGRAPHY

- E. Larose, Y. Yeghiazarians, P. Libby, E. K. Yucel, M. Aikawa, D. F. Kacher, E. Aikawa, S. Kinlay, F. J. Schoen, A. P. Selwyn, and P. Ganz. Characterization of human atherosclerotic plaques by intravascular magnetic resonance imaging. *Circulation*, 112:2324–2331, 2005. ISSN 00097322. doi: 10.1161/CIRCULATIONAHA.105.538942.
- S. Le Floc’h, J. Ohayon, P. Tracqui, G. Finet, A. M. Gharib, R. L. Maurice, G. Cloutier, and R. I. Pettigrew. Vulnerable atherosclerotic plaque elasticity reconstruction based on a segmentation-driven optimization procedure using strain measurements: Theoretical framework. *IEEE Trans. Med. Imaging*, 28(7):1126–1137, 2009. ISSN 02780062. doi: 10.1109/TMI.2009.2012852.
- S. Le Floc’h, G. Cloutier, G. Finet, P. Tracqui, R. I. Pettigrew, and J. Ohayon. On the potential of a new IVUS elasticity modulus imaging approach for detecting vulnerable atherosclerotic coronary plaques: In vitro vessel phantom study. *Phys. Med. Biol.*, 55:5701–5721, 2010. ISSN 00319155. doi: 10.1088/0031-9155/55/19/006.
- S. Le Floc’h, G. Cloutier, Y. Saijo, G. Finet, S. K. Yazdani, F. Deleaval, G. Rioufol, R. I. Pettigrew, and J. Ohayon. A Four-Criterion Selection Procedure for Atherosclerotic Plaque Elasticity Reconstruction Based on in Vivo Coronary Intravascular Ultrasound Radial Strain Sequences. *Ultrasound Med. Biol.*, 38(12):2084–2097, 2012. ISSN 03015629. doi: 10.1016/j.ultrasmedbio.2012.07.021.
- R. Lee, A. Grodzinsky, E. Frank, R. Kamm, F. Schoen, R. T. Lee, A. J. Grodzinsky, E. H. Frank, R. D. Kamm, and F. J. Schoen. Structure-dependent dynamic mechanical behavior of fibrous caps from human Structure-Dependent Dynamic Mechanical Behavior of Fibrous Caps From Human Atherosclerotic Plaques. *Circulation*, 83:1764–1770, 1991. ISSN 0009-7322.
- R. T. Lee, H. M. Loree, G. C. Cheng, E. H. Lieberman, N. Jaramillo, and F. J. Schoen. Computational structural analysis based on intravascular ultrasound imaging before in vitro angioplasty: Prediction of plaque fracture locations. *J. Am. Coll. Cardiol.*, 21(3):777–782, mar 1993. ISSN 07351097. doi: 10.1016/0735-1097(93)90112-E.
- H. Li, T. Liu, M. Wang, D. Zhao, A. Qiao, X. Wang, J. Gu, Z. Li, and B. Zhu. Design optimization of stent and its dilatation balloon using kriging surrogate model. *Biomed. Eng. Online*, 16(13), 2017. doi: 10.1186/s12938-016-0307-6. URL <https://biomedical-engineering-online.biomedcentral.com/track/pdf/10.1186/s12938-016-0307-6>.
- Z. Li, L. Wang, X. Hu, P. Zhang, Y. Chen, X. Liu, M. Xu, Y. Zhang, and M. Zhang. Effect of rosuvastatin on atherosclerotic plaque stability: An intravascular ultrasound elastography study. *Atherosclerosis*, 248:27–35, 2016. doi: 10.1016/j.atherosclerosis.2016.02.028.
- D. K. Liang, D. Z. Yang, M. Qi, and W. Q. Wang. Finite element analysis of the implantation of a balloon-expandable stent in a stenosed artery B. *Int. J. Cardiol.*, 104:314–318, 2005. doi: 10.1016/j.ijcard.2004.12.033.
- P. Libby, P. M. Ridker, and A. Maseri. Inflammation and atherosclerosis. *Circulation*, 105(9): 1135–43, 2002. ISSN 1524-4539. doi: 10.1161/HC0902.104353.
- S. Lobregt and M. Viergever. A discrete dynamic contour model. *IEEE Trans. Med. Imaging*, 14(1):12–24, mar 1995. doi: 10.1109/42.370398.
- H. M. Loree, R. D. Kamm, R. G. Stringfellow, and R. T. Lee. Effects of fibrous cap thickness on peak circumferential stress in model atherosclerotic vessels. *Circ. Res.*, 71(4):850–8, oct 1992.

- H. M. Loree, B. J. Tobias, L. J. Gibson, R. D. Kamm, D. M. Small, and R. T. Lee. Mechanical properties of model atherosclerotic lesion lipid pools. *Arterioscler. Thromb. a J. Vasc. Biol.*, 14(2):230–4, 1994. ISSN 1049-8834. doi: 10.1161/01.ATV.14.2.230.
- P. F. Ludman. Percutaneous coronary intervention. *Medicine (Baltimore)*., 42(9):520–526, sep 2014. doi: 10.1016/J.MPMED.2014.06.005. URL <https://www-sciencedirect-com.gaelnomade-2.grenet.fr/science/article/pii/S1357303914001704>.
- J. Luo, K. Ying, and J. Bai. Elasticity reconstruction for ultrasound elastography using a radial compression: An inverse approach. *Ultrasonics*, 44:e195–e198, dec 2006. doi: 10.1016/j.ultras.2006.06.006.
- R. D. Madder, M. Husaini, A. T. Davis, S. Vanoosterhout, M. Khan, D. Wohns, R. F. Mcnamara, K. Wolschleger, J. Gripar, J. S. Collins, M. Jacoby, J. M. Decker, M. Hendricks, S. T. Sum, S. Madden, J. H. Ware, and J. E. Muller. Large lipid-rich coronary plaques detected by near-infrared spectroscopy at non-stented sites in the target artery identify patients likely to experience future major adverse cardiovascular events. *Eur. Heart J. Cardiovasc. Imaging*, 17:393–399, 2016. ISSN 20472412. doi: 10.1093/ehjci/jev340.
- Y. Majdouline, J. Ohayon, Z. Keshavarz-Motamed, M. H. Roy Cardinal, D. Garcia, L. Allard, S. Lerouge, F. Arsenault, G. Soulez, and G. Cloutier. Endovascular shear strain elastography for the detection and characterization of the severity of atherosclerotic plaques: In vitro validation and in vivo evaluation. *Ultrasound Med. Biol.*, 40(5):890–903, 2014. ISSN 1879291X. doi: 10.1016/j.ultrasmedbio.2013.12.008.
- D. Martin and F. Boyle. Finite element analysis of balloon-expandable coronary stent deployment: Influence of angioplasty balloon configuration. *Int. j. numer. method. biomed. eng.*, 29(11):1161–1175, nov 2013. doi: 10.1002/cnm.2557. URL <http://doi.wiley.com/10.1002/cnm.2557>.
- T. Matsumoto, H. Abe, T. Ohashi, Y. Kato, and M. Sato. Local elastic modulus of atherosclerotic lesions of rabbit thoracic aortas measured by pipette aspiration method. *Physiol. Meas.*, 23:635–648, 2002.
- R. Maurice and M. Bertrand. Lagrangian speckle model and tissue-motion estimation-theory [ultrasonography]. *IEEE Trans. Med. Imaging*, 18(7):593–603, 1999. ISSN 02780062. doi: 10.1109/42.790459.
- R. L. Maurice, J. Ohayon, G. Finet, and G. Cloutier. Adapting the Lagrangian speckle model estimator for endovascular elastography: Theory and validation with simulated radio-frequency data. *J. Acoust. Soc. Am.*, 116(2):1276–1286, 2004a. ISSN 0001-4966. doi: 10.1121/1.1771615.
- R. L. Maurice, J. Ohayon, Y. Frétny, M. Bertrand, G. Soulez, and G. Cloutier. Noninvasive Vascular Elastography: Theoretical Framework. *IEEE Trans. Med. Imaging*, 23(2):164–180, 2004b. ISSN 02780062. doi: 10.1109/TMI.2003.823066.
- R. L. Maurice, M. Daronat, J. Ohayon, É. Stoyanova, F. S. Foster, and G. Cloutier. Non-invasive high-frequency vascular ultrasound elastography. *Phys. Med. Biol.*, 50(7):1611–1628, 2005. ISSN 0031-9155. doi: 10.1088/0031-9155/50/7/020.
- R. L. Maurice, J. Fromageau, É. Brusseau, G. Finet, G. Rioufol, and G. Cloutier. On the Potential of the Lagrangian Estimator for Endovascular Ultrasound Elastography: In Vivo Human Coronary Artery Study. *Ultrasound Med. Biol.*, 33(8):1199–1205, 2007. ISSN 03015629. doi: 10.1016/j.ultrasmedbio.2007.01.018.

BIBLIOGRAPHY

- M. A. Mauro, K. P. J. Murphy, K. R. Thomson, A. C. Venbrux, and R. A. Morgan. *Image-guided interventions: Expert Radiology Series*. Elsevier, 2nd edition, 2014. ISBN 1455753971.
- F. Migliavacca, L. Petrini, M. Colombo, F. Auricchio, and R. Pietrabissa. Mechanical behavior of coronary stents investigated through the finite element method. *J. Biomech.*, 35:803–811, 2002.
- F. Migliavacca, L. Petrini, V. Montanari, I. Quagliana, F. Auricchio, and G. Dubini. A predictive study of the mechanical behaviour of coronary stents by computer modelling. *Med. Eng. Phys.*, 27:13–18, 2005. ISSN 13504533. doi: 10.1016/j.medengphy.2004.08.012. URL http://ac.els-cdn.com.gaelnomade-1.grenet.fr/S1350453304001444/1-s2.0-S1350453304001444-main.pdf?_tid=abb50c2a-07f5-11e7-9319-00000aab0f6b&acdnat=1489413918{}_ab16f61795205e47189936d6dd037963.
- L. E. Millon, H. Mohammadi, and W. K. Wan. Anisotropic polyvinyl alcohol hydrogel for cardiovascular applications. *J. Biomed. Mater. Res. Part B Appl. Biomater.*, 79B(2):305–311, nov 2006. ISSN 1552-4973. doi: 10.1002/jbm.b.30543. URL <http://doi.wiley.com/10.1002/jbm.b.30543>.
- L. E. Millon, C. J. Oates, and W. Wan. Compression properties of polyvinyl alcohol-bacterial cellulose nanocomposite. *J. Biomed. Mater. Res. - Part B Appl. Biomater.*, 90 B(2):922–929, 2009. ISSN 15524981. doi: 10.1002/jbm.b.31364.
- Mingxi Wan, Yangmei Li, Junbo Li, Yaoyao Cui, and Xiaodong Zhou. Strain imaging and elasticity reconstruction of arteries based on intravascular ultrasound video images. *IEEE Trans. Biomed. Eng.*, 48(1):116–120, 2001. doi: 10.1109/10.900271. URL <http://ieeexplore.ieee.org/document/900271/>.
- U. Morbiducci, A. M. Kok, B. R. Kwak, P. H. Stone, D. A. Steinman, and J. J. Wentzel. Atherosclerosis at arterial bifurcations: Evidence for the role of haemodynamics and geometry. *Thromb. Haemost.*, 115:484–492, 2016. ISSN 03406245. doi: 10.1160/TH15-07-0597.
- R. S. More, M. J. Brack, and A. H. Gershlick. Angioplasty balloon compliance: Can in vivo size be predicted from in vitro pressure profile measurements? *Clin. Cardiol.*, 19(5):393–397, may 1996. doi: 10.1002/clc.4960190512. URL <http://doi.wiley.com/10.1002/clc.4960190512>.
- S. Morlacchi, S. G. Colleoni, R. Cárdenes, C. Chiastra, J. L. Diez, I. Larrabide, and F. Migliavacca. Patient-specific simulations of stenting procedures in coronary bifurcations: Two clinical cases. *Med. Eng. Phys.*, 2013. ISSN 13504533. doi: 10.1016/j.medengphy.2013.01.007.
- P. Mortier, M. De Beule, D. Van Loo, B. Verheghe, and P. Verdonck. Finite element analysis of side branch access during bifurcation stenting. *Med. Eng. Phys.*, 31:434–440, 2009. doi: 10.1016/j.medengphy.2008.11.013. URL <https://pdf.sciencedirectassets.com/271469/1-s2.0-S1350453309X00044/1-s2.0-S1350453308002038/main.pdf?x-amz-security-token=FQoGZXIvYXZdEE0aDKwRJW5PnU8KoA28CyK3A5xtKF0p1wNM08ZOHAEO{}}252Bm9gvrTFNoKV2czP6ZzjCeIU710c>.
- P. Mortier, G. A. Holzapfel, M. De Beule, D. V. Loo, Y. Taeymans, P. Segers, P. Verdonck, and B. Verheghe. A Novel Simulation Strategy for Stent Insertion and Deployment in Curved Coronary Bifurcations: Comparison of Three Drug-Eluting Stents. *Ann. Biomed. Eng.*, 38(1):88–99, 2010. doi: 10.1007/s10439-009-9836-5. URL <https://link-springer-com.gaelnomade-2.grenet.fr/content/pdf/10.1007{s}2Fs10439-009-9836-5.pdf>.

BIBLIOGRAPHY

- S. Motoyama, H. Ito, M. Sarai, T. Kondo, H. Kawai, Y. Nagahara, H. Harigaya, S. Kan, H. Anno, H. Takahashi, H. Naruse, J. Ishii, H. Hecht, L. J. Shaw, Y. Ozaki, and J. Narula. Plaque Characterization by Coronary Computed Tomography Angiography and the Likelihood of Acute Coronary Events in Mid-Term Follow-Up. *J. Am. Coll. Cardiol.*, 66(4):337–346, jul 2015. doi: 10.1016/j.jacc.2015.05.069.
- M. Naghavi, P. Libby, E. Falk, S. W. Casscells, S. Litovsky, J. Rumberger, J. J. Badimon, C. Stefanadis, P. Moreno, G. Pasterkamp, Z. Fayad, P. H. Stone, S. Waxman, P. Raggi, M. Madjid, A. Zarrabi, A. Burke, C. Yuan, P. J. Fitzgerald, D. S. Siscovick, C. L. de Korte, M. Aikawa, K. E. Juhani Airaksinen, G. Assmann, C. R. Becker, J. H. Chesebro, A. Farb, Z. S. Galis, C. Jackson, I.-K. Jang, W. Koenig, R. A. Lodder, K. March, J. Demirovic, M. Navab, S. G. Priori, M. D. Reikhter, R. Bahr, S. M. Grundy, R. Mehran, A. Colombo, E. Boerwinkle, C. Ballantyne, W. Insull, R. S. Schwartz, R. Vogel, P. W. Serruys, G. K. Hansson, D. P. Faxon, S. Kaul, H. Drexler, P. Greenland, J. E. Muller, R. Virmani, P. M. Ridker, D. P. Zipes, P. K. Shah, and J. T. Willerson. From Vulnerable Plaque to Vulnerable Patient: A Call for New Definitions and Risk Assessment Strategies: Part I. *Circulation*, 108(14):1664–1672, 2003. doi: 10.1161/01.CIR.0000087480.94275.97.
- A. Nair, B. D. Kuban, E. M. Tuzcu, P. Schoenhagen, S. E. Nissen, and D. G. Vince. Coronary Plaque Classification With Intravascular Ultrasound Radiofrequency Data Analysis. *Circulation*, 106(17):2200–2206, oct 2002. doi: 10.1161/01.CIR.0000035654.18341.5E. URL <https://www.ahajournals.org/doi/10.1161/01.CIR.0000035654.18341.5E>.
- R. Nayak, S. Huntzicker, J. Ohayon, N. Carson, V. Dogra, G. Schifitto, and M. M. Doyley. Principal Strain Vascular Elastography: Simulation and Preliminary Clinical Evaluation. *Ultrasound Med. Biol.*, 43(3):682–699, 2017. ISSN 1879291X. doi: 10.1016/j.ultrasmedbio.2016.11.010.
- NHLBI. Atherosclerosis — National Heart, Lung, and Blood Institute (NHLBI), 2018. URL <https://www.nhlbi.nih.gov/health-topics/atherosclerosis>.
- S. J. Nicholls, R. Puri, T. Anderson, C. M. Ballantyne, L. Cho, J. J. P. Kastelein, W. Koenig, R. Somaratne, H. Kassahun, J. Yang, S. M. Wasserman, R. Scott, I. Ungi, J. Podolec, A. O. Ophuis, J. H. Cornel, M. Borgman, D. M. Brennan, and S. E. Nissen. Effect of Evolocumab on Progression of Coronary Disease in Statin-Treated Patients. *JAMA*, 316(22):2373, dec 2016. ISSN 0098-7484. doi: 10.1001/jama.2016.16951. URL <http://jama.jamanetwork.com/article.aspx?doi=10.1001/jama.2016.16951>.
- K. Nikolaou, H. Alkadhi, F. Bamberg, S. Leschka, and B. J. Wintersperger. MRI and CT in the diagnosis of coronary artery disease: indications and applications. *Insights Imaging*, 2(1): 9–24, feb 2011. doi: 10.1007/s13244-010-0049-0.
- T. Nozue, S. Yamamoto, S. Tohyama, S. Umezawa, T. Kunishima, A. Sato, S. Miyake, Y. Takeyama, Y. Morino, T. Yamauchi, T. Muramatsu, K. Hibi, T. Sozu, M. Terashima, and I. Michishita. Statin treatment for coronary artery plaque composition based on intravascular ultrasound radiofrequency data analysis. *Am. Heart J.*, 163(2):191–9.e1, 2012. ISSN 1097-6744. doi: 10.1016/j.ahj.2011.11.004.
- J. Ohayon, P. Teppaz, G. Finet, and G. Rioufol. In-vivo prediction of human coronary plaque rupture location using intravascular ultrasound and the finite element method. *Coron. Artery Dis.*, 12(8), 2001. ISSN 0954-6928.
- J. Ohayon, G. Finet, F. Treyve, G. Rioufol, and O. Dubreuil. A three-dimensional finite element analysis of stress distribution in a coronary atherosclerotic plaque: In-vivo prediction of plaque rupture location. *Res. Signpost*, 37661, 2005.

- J. Ohayon, O. Dubreuil, P. Tracqui, S. Le Floc'h, G. Rioufol, L. Chalabreysse, F. Thivolet, R. I. Pettigrew, and G. Finet. Influence of residual stress/strain on the biomechanical stability of vulnerable coronary plaques: potential impact for evaluating the risk of plaque rupture. *Am J Physiol Hear. Circ Physiol*, 293:1987–1996, 2007. doi: 10.1152/ajpheart.00018.2007.In.
- J. Ohayon, G. Finet, A. M. Gharib, D. A. Herzka, P. Tracqui, J. Heroux, G. Rioufol, M. S. Kotys, A. Elagha, and R. I. Pettigrew. Necrotic core thickness and positive arterial remodeling index: emergent biomechanical factors for evaluating the risk of plaque rupture. *AJP Hear. Circ. Physiol.*, 2008. ISSN 0363-6135. doi: 10.1152/ajpheart.00005.2008.
- J. Ohayon, A. M. Gharib, A. Garcia, J. Heroux, S. K. Yazdani, M. Malve, P. Tracqui, M.-A. Martinez, M. Doblare, G. Finet, and R. I. Pettigrew. Is arterial wall-strain stiffening an additional process responsible for atherosclerosis in coronary bifurcations?: an in vivo study based on dynamic CT and MRI. *AJP Hear. Circ. Physiol.*, 301:H1097–H1106, 2011. ISSN 0363-6135. doi: 10.1152/ajpheart.01120.2010.
- J. Ohayon, G. Finet, S. Le Floc'h, G. Cloutier, A. M. Gharib, J. Heroux, and R. I. Pettigrew. Biomechanics of atherosclerotic coronary plaque: Site, stability and in vivo elasticity modeling. In *Ann. Biomed. Eng.*, pages 269–279, 2014. ISBN 1043901308881. doi: 10.1007/s10439-013-0888-1.
- J. Ophir, I. Céspedes, H. Ponnekanti, Y. Yazdi, and X. Li. Elastography: A quantitative method for imaging the elasticity of biological tissues. *Ultrason. Imaging*, 13:111–134, 1991. ISSN 01617346. doi: 10.1177/016173469101300201.
- K. J. Overbaugh. Acute Coronary Syndrome. *Am. J. Nurs.*, 109(5):42–52, 2009.
- P. M. P. M. Pardalos, T. F. T. F. Coleman, and P. Xanthopoulos. *Optimization and data analysis in biomedical informatics*. Springer, 2012. ISBN 9781461441335.
- S. Paxton, M. Peckham, A. Knibbs, S. Paxton, A. Knibbs, and M. Peckham. The Leeds Histology Guide, 2003. URL <http://histology.leeds.ac.uk/circulatory/arteries.php>.
- J. Poree, B. Chayer, G. Soulez, J. Ohayon, and G. Cloutier. Noninvasive Vascular Modulography Method for Imaging the Local Elasticity of Atherosclerotic Plaques: Simulation and In Vitro Vessel Phantom Study. *IEEE Trans. Ultrason. Ferroelectr. Freq. Control*, 64(12):1805–1817, 2017. ISSN 0885-3010. doi: 10.1109/TUFFC.2017.2757763.
- J. Raamachandran and K. Jayavenkateshwaran. Modeling of stents exhibiting negative Poisson's ratio effect. *Comput. Methods Biomech. Biomed. Engin.*, 10(4):245–255, aug 2007. ISSN 1025-5842. doi: 10.1080/10255840701198004. URL <http://www.tandfonline.com/doi/abs/10.1080/10255840701198004>.
- M. S. Richards and M. M. Dooley. Investigating the impact of spatial priors on the performance of model-based IVUS elastography. *Phys. Med. Biol.*, 56(22):7223–7246, 2011. ISSN 0031-9155. doi: 10.1088/0031-9155/56/22/014.
- M. S. Richards, R. Perucchio, and M. M. Dooley. Visualizing the Stress Distribution Within Vascular Tissues Using Intravascular Ultrasound Elastography: A Preliminary Investigation. *Ultrasound Med. Biol.*, 41:1616–1631, 2015. doi: 10.1016/j.ultrasmedbio.2015.01.022.
- J. Rigla. Atherosclerotic Plaque Progression and OCT/IVUS Assessment. *Comput. Vis. Intravasc. Imaging Comput. Stenting*, pages 33–51, jan 2017. doi: 10.1016/B978-0-12-811018-8.00002-3.

- G. Rioufol, G. Finet, I. Ginon, X. André-Fouët, R. Rossi, E. Vialle, E. Desjoyaux, G. Convert, J. F. Huret, and A. Tabib. Multiple atherosclerotic plaque rupture in acute coronary syndrome: A three-vessel intravascular ultrasound study. *Circulation*, 106:804–808, 2002. ISSN 00097322. doi: 10.1161/01.CIR.0000025609.13806.31.
- M. Rockley, P. Jetty, G. Wells, K. Rockley, and D. Fergusson. Prolonged versus brief balloon inflation during arterial angioplasty for de novo atherosclerotic disease: protocol for a systematic review. *Syst. Rev.*, 8(1):45, dec 2019. ISSN 2046-4053. doi: 10.1186/s13643-019-0955-2.
- M. Rosales and P. Radeva. A Basic Model for IVUS Image Simulation. In *Handb. Biomed. Image Anal.*, pages 1–55. Springer US, Boston, MA, 2005. doi: 10.1007/0-306-48551-6_1.
- R. Ross. Atherosclerosis — An Inflammatory Disease. *N. Engl. J. Med.*, 340(2):115–126, jan 1999. doi: 10.1056/NEJM199901143400207.
- M.-H. Roy Cardinal, J. Meunier, G. Soulez, R. L. Maurice, É. Therasse, G. Cloutier, G. Soulez, and G. Cloutier. Intravascular Ultrasound Image Segmentation: A Three-Dimensional Fast-Marching Method Based on Gray Level Distributions. *IEEE Trans. Med. Imaging*, 25(5), 2006. doi: 10.1109/TMI.2006.872142. URL <https://lbum-crchum.com/publications-fichiers/w69-ieee-tmi-2006-Roy-Cardinal.pdf>.
- L. Ryan and F. Foster. Ultrasonic Measurement of Differential Displacement and Strain in a Vascular Model. *Ultrason. Imaging*, 19(1):19–38, jan 1997. doi: 10.1177/016173469701900102. URL <http://journals.sagepub.com/doi/10.1177/016173469701900102>.
- F. J. Rybicki. Protocol Fundamentals For Coronary Computed Tomography Angiography. *US Cardiol. Rev.*, 2(1):119–121, 2005.
- Y. Saijo, A. Tanaka, T. Iwamoto, E. Dos, S. Filho, M. Yoshizawa, A. Hirosaka, M. Kijima, Y. Akino, Y. Hanadate, and T. Yambe. Intravascular two-dimensional tissue strain imaging. *Ultrasonics*, 44:e147–e151, 2006. doi: 10.1016/j.ultras.2006.06.049.
- E. Santos Filho, Y. Saijo, A. Tanaka, and M. Yoshizawa. Detection and Quantification of Calcifications in Intravascular Ultrasound Images by Automatic Thresholding. *Ultrasound Med. Biol.*, 34(1):160–165, jan 2008. doi: 10.1016/J.ULTRASMEDBIO.2007.06.025. URL <https://www.sciencedirect-com.gaelnomade-2.grenet.fr/science/article/pii/S0301562907003365>.
- S. Sathyanarayana, S. Carlier, W. Li, and L. Thomas. Characterisation of atherosclerotic plaque by spectral similarity of radiofrequency intravascular ultrasound signals. *EuroIntervention*, 5(1):133–9, may 2009. URL <http://www.ncbi.nlm.nih.gov/pubmed/19577995>.
- K. Sauerteig and M. Giese. The Effect of Extrusion and Blow Molding Parameters on Angioplasty Balloon Production. *J. Appl. Med. Polym.*, 3:11–14, 1999.
- J. Schaar, J. E. Muller, E. Falk, R. Virmani, V. Fuster, P. W. Serruys, A. Colombo, C. Stefanadis, S. Ward Casscells, P. R. Moreno, A. Maseri, and A. F. van der Steen. Terminology for high-risk and vulnerable coronary artery plaques. *Eur. Heart J.*, 25(12):1077–1082, jun 2004. doi: 10.1016/j.ehj.2004.01.002.
- J. A. Schaar, C. L. De Korte, F. Mastik, L. C. A. Van Damme, R. Krams, P. W. Serruys, and A. F. W. Van Der Steen. Three-dimensional palpography of human coronary arteries: Ex vivo validation and in-patient evaluation. *Herz*, 30:125–33, 2005. ISSN 03409937. doi: 10.1007/s00059-005-2642-4.

- J. A. Schaar, F. Mastik, E. Regar, C. A. den Uil, F. J. Gijssen, J. J. Wentzel, P. W. Serruys, and A. F. W. van der Stehen. Current diagnostic modalities for vulnerable plaque detection. *Curr. Pharm. Des.*, 13(10):995–1001, 2007. ISSN 1873-4286.
- A. Schiavone and L. G. Zhao. A study of balloon type, system constraint and artery constitutive model used in finite element simulation of stent deployment. *Mech. Adv. Mater. Mod. Process.*, 1(1):1, dec 2015. ISSN 2198-7874. doi: 10.1186/s40759-014-0002-x. URL <http://www.mammp-journal.com/content/1/1/1>.
- D. Sheet, A. Karamalis, A. Eslami, P. Noël, J. Chatterjee, A. K. Ray, A. F. Laine, S. G. Carlier, N. Navab, and A. Katouzian. Joint learning of ultrasonic backscattering statistical physics and signal confidence primal for characterizing atherosclerotic plaques using intravascular ultrasound. *Med. Image Anal.*, 18(1):103–17, jan 2014. doi: 10.1016/j.media.2013.10.002.
- H. Sinclair, C. Bourantas, A. Bagnall, G. S. Mintz, and V. Kunadian. OCT for the identification of vulnerable plaque in acute coronary syndrome. *JACC Cardiovasc. Imaging*, 8(2):198–209, 2015. ISSN 18767591. doi: 10.1016/j.jcmg.2014.12.005.
- S. Soleimanifard, K. Z. Abd-Elmoniem, H. K. Agarwal, M. S. Tomas, T. Sasano, E. Vonken, A. Youssef, M. R. Abraham, T. P. Abraham, and J. L. Prince. Identification of myocardial infarction using three-dimensional strain tensor fractional anisotropy. In *2010 IEEE Int. Symp. Biomed. Imaging From Nano to Macro*, pages 468–471. IEEE, 2010. ISBN 978-1-4244-4125-9. doi: 10.1109/ISBI.2010.5490309.
- L. Soualmi, M. Bertrand, R. Mongrain, and J.-C. Tardif. Forward and Inverse Problems in Endovascular Elastography. In *Acoust. Imaging*, pages 203–209. Springer, Boston, MA, New York, NY, 1997. doi: 10.1007/978-1-4419-8588-0_33.
- H. C. Stary, A. B. Chandler, S. Glagov, J. R. Guyton, W. Insull, M. E. Rosenfeld, S. A. Schaffer, C. J. Schwartz, W. D. Wagner, and R. W. Wissler. A definition of initial, fatty streak, and intermediate lesions of atherosclerosis. A report from the Committee on Vascular Lesions of the Council on Arteriosclerosis, American Heart Association. *Circulation*, 89(5):2462–2478, may 1994. doi: 10.1161/01.CIR.89.5.2462.
- H. C. Stary, A. B. Chandler, R. E. Dinsmore, V. Fuster, S. Glagov, W. Insull, M. E. Rosenfeld, C. J. Schwartz, W. D. Wagner, and R. W. Wissler. A Definition of Advanced Types of Atherosclerotic Lesions and a Histological Classification of Atherosclerosis. *Arterioscler. Thromb. Vasc. Biol.*, 15(9):1512–1531, sep 1995. doi: 10.1161/01.ATV.15.9.1512.
- C. Stefanadis, C. Antoniou, D. Tsiachris, and P. Pietri. Coronary Atherosclerotic Vulnerable Plaque: Current Perspectives. *J. Am. Heart Assoc.*, 6(3), mar 2017. ISSN 2047-9980. doi: 10.1161/JAHA.117.005543.
- C. Sumi and K. Nakayama. A robust numerical solution to reconstruct a globally relative shear modulus distribution from strain measurements. *IEEE Trans. Med. Imaging*, 17(3):419–428, jun 1998. doi: 10.1109/42.712131.
- A. Tacheau, S. Le Floch, G. Finet, M. M. Doyley, R. I. Pettigrew, G. Cloutier, and J. Ohayon. The Imaging Modulography Technique Revisited for High-Definition Intravascular Ultrasound: Theoretical Framework. *Ultrasound Med. Biol.*, 42(3):727–741, 2016. ISSN 1879291X. doi: 10.1016/j.ultrasmedbio.2015.11.015.
- A. Taki, A. Kermani, S. Ranjbarnavazi, and A. Pourmodheji. Overview of Different Medical Imaging Techniques for the Identification of Coronary Atherosclerotic Plaques. *Comput. Vis. Intravasc. Imaging Comput. Stenting*, pages 79–106, jan 2017. doi: 10.1016/B978-0-12-811018-8.00004-7.

BIBLIOGRAPHY

- H. Talhami, L. Wilson, and M. Neale. Spectral tissue strain: A new technique for imaging tissue strain using intravascular ultrasound. *Ultrasound Med. Biol.*, 20(8):759–772, jan 1994. doi: 10.1016/0301-5629(94)90033-7. URL <https://www.sciencedirect-com.gaelnomade-2.grenet.fr/science/article/pii/0301562994900337>.
- D. Tang, Z. Teng, G. Canton, T. S. Hatsukami, L. Dong, X. Huang, and C. Yuan. Local critical stress correlates better than global maximum stress with plaque morphological features linked to atherosclerotic plaque vulnerability: An in vivo multi-patient study. *Biomed. Eng. Online*, 8:15, 2009. ISSN 1475925X. doi: 10.1186/1475-925X-8-15.
- T. Thim, M. K. Hagensen, D. Wallace-Bradley, J. F. Granada, G. L. Kaluza, L. Drouet, W. P. Paaske, H. E. Bøtker, and E. Falk. Unreliable Assessment of Necrotic Core by Virtual Histology Intravascular Ultrasound in Porcine Coronary Artery Disease. *Circ. Cardiovasc. Imaging*, 3(4):384–391, jul 2010. doi: 10.1161/CIRCIMAGING.109.919357.
- V. Thondapu, C. V. Bourantas, N. Foin, I.-K. K. Jang, P. W. Serruys, and P. Barlis. Biomechanical stress in coronary atherosclerosis: emerging insights from computational modelling. *Eur. Heart J.*, 38(2):81–92, feb 2016. ISSN 0195-668X. doi: 10.1093/eurheartj/ehv689.
- S. Timoshenko and J. N. J. N. Goodier. *Theory of elasticity*. McGraw-Hill, New York, 3. ed. edition, 1970. ISBN 9780070647206.
- M. Todo, K. Yoshiya, and T. Matsumoto. A theoretical model to predict tensile deformation behavior of balloon catheter. *J. Mech. Behav. Biomed. Mater.*, 62: 236–239, 2016. doi: 10.1016/j.jmbbm.2016.04.044. URL www.elsevier.com/locate/jmbbmAvailableonlineatwww.sciencedirect.com.
- B. Tomberli, A. Mattesini, G. I. Baldereschi, and C. Di Mario. A Brief History of Coronary Artery Stents. *Rev. Española Cardiol. (English Ed.)*, 71(5):312–319, may 2018. doi: 10.1016/j.rec.2017.11.022. URL <https://linkinghub.elsevier.com/retrieve/pii/S1885585717305881>.
- D. Tousoulis, M. Drakopoulou, K. Toutouzas, and D. Tousoulis. Acute Coronary Syndromes. *Coron. Artery Dis.*, pages 201–233, jan 2018. doi: 10.1016/B978-0-12-811908-2.00012-X.
- P. Tracqui, A. Broisat, J. Toczek, N. Mesnier, J. Ohayon, and L. Riou. Mapping elasticity moduli of atherosclerotic plaque in situ via atomic force microscopy. *J. Struct. Biol.*, 174(1): 115–123, apr 2011. doi: 10.1016/j.jsb.2011.01.010.
- E. E. van der Wall, H. W. Vliegen, A. de Roos, and A. V. Brusckhe. Magnetic Resonance Imaging in Coronary Artery Disease. *Circulation*, 92(9):2723–2739, nov 1995. doi: 10.1161/01.CIR.92.9.2723.
- R. Virmani. Are Our Tools for the Identification of TCFA Ready and Do We Know Them? *JACC Cardiovasc. Imaging*, 4(6):656–658, 2011. doi: 10.1016/j.jcmg.2011.01.019.
- R. Virmani, F. D. Kolodgie, A. P. Burke, A. Farb, and S. M. Schwartz. Lessons from sudden coronary death: a comprehensive morphological classification scheme for atherosclerotic lesions. *Arterioscler. Thromb. Vasc. Biol.*, 20(5):1262–75, may 2000.
- R. Virmani, A. P. Burke, A. Farb, and F. D. Kolodgie. Pathology of the Vulnerable Plaque. *J. Am. Coll. Cardiol.*, 47(8):C13–C18, apr 2006. ISSN 07351097. doi: 10.1016/j.jacc.2005.10.065.
- B. F. Waller, C. M. Orr, J. D. Slack, C. A. Pinkerton, J. Van Tassel, and T. Peters. Anatomy, histology, and pathology of coronary arteries: A review relevant to new interventional and imaging techniques-Part I. *Clin. Cardiol.*, 15(6):451–457, jun 1992. ISSN 01609289. doi: 10.1002/clc.4960150613.

BIBLIOGRAPHY

- W.-Q. Wang, D.-K. Liang, D.-Z. Yang, and M. Qi. Analysis of the transient expansion behavior and design optimization of coronary stents by finite element method. *J. Biomech.*, 39:21–32, 2006. doi: 10.1016/j.jbiomech.2004.11.003. URL www.elsevier.com/locate/jbiomech.
- N. Widynski, J. Porée, M. H. Roy Cardinal, J. Ohayon, G. Cloutier, and D. Garcia. A sequential Bayesian based method for tracking and strain palpography estimation of arteries in intravascular ultrasound images. In *IEEE Int. Ultrason. Symp. IUS*, pages 515–518, 2014. ISBN 9781479970490. doi: 10.1109/ULTSYM.2014.0127.
- World Health Organisation. Cardiovascular diseases (CVDs), 2017. URL [http://www.who.int/news-room/fact-sheets/detail/cardiovascular-diseases-\(cvds\)](http://www.who.int/news-room/fact-sheets/detail/cardiovascular-diseases-(cvds)).
- K. Yahagi, F. D. Kolodgie, F. Otsuka, A. V. Finn, H. R. Davis, M. Joner, and R. Virmani. Pathophysiology of native coronary, vein graft and in-stent atherosclerosis. *Nat. Rev. Cardiol.*, 13(2):79–98, feb 2016. doi: 10.1038/nrcardio.2015.164.
- S. Yazdani. Chapter 28. In J. Ohayon, G. Finet, and R. Pettigrew, editors, *Biomech. Coron. Atheroscler. Plaque From Model to Patient*, chapter 28. Elsevier, 1st edition, 2019.
- P.-F. Zhang, H.-J. Su, M. Zhang, J.-F. Li, C.-X. Liu, S.-F. Ding, Y. Miao, L. Chen, X.-N. Li, X. Yi, and Y. Zhang. Atherosclerotic plaque components characterization and macrophage infiltration identification by intravascular ultrasound elastography based on b-mode analysis: validation in vivo. *Int. J. Cardiovasc. Imaging*, 27(1):39–49, jan 2011a. doi: 10.1007/s10554-010-9659-3. URL <http://link.springer.com/10.1007/s10554-010-9659-3>.
- Q. Zhang, Y. Wang, W. Wang, J. Ma, J. Qian, and J. Ge. Automatic Segmentation of Calcifications in Intravascular Ultrasound Images Using Snakes and the Contourlet Transform. *Ultrasound Med. Biol.*, 36(1):111–129, jan 2010. doi: 10.1016/J.ULTRASMEDBIO.2009.06.1097. URL <https://www.sciencedirect-com.gaelnomade-2.grenet.fr/science/article/pii/S0301562909013830>.
- X. Zhang, C. McKay, and M. Sonka. Tissue characterization in intravascular ultrasound images. *IEEE Trans. Med. Imaging*, 17(6):889–899, 1998. doi: 10.1109/42.746622. URL <http://ieeexplore.ieee.org/document/746622/>.
- Y. Zhang, M. Forsyth, B. Hinton, G. G. Wallace, and G. Wallace. Control of biodegradation of a Mg alloy in simulated body fluid CONTROL OF BIODEGRADATION OF A MG ALLOY IN SIMULATED BODY FLUID. *18th Int. Corros. Congr. 2011*, pages 1813–1820, 2011b. URL <http://ro.uow.edu.au/aiimpapers/349>.

List of Figures

1.1 In the EU5, US and Asia-Pacific regions the number of Interventional Cardiology Procedures performed grew from 2,967,778, 3,181,248, and 3,748,122 respectively in 2007 to 3,390,703, 3,181,117, and 5,748,150 each in 2014. The number of Interventional Cardiology Procedures performed is forecasted to reach 3,904,138, 3,153,411, and 9,879,191 for each of the aforementioned regions in 2021. Source: (GlobalData, 2016a,b,c) 20

1.2 Schematic of the three layers of the coronary artery wall. 21

1.3 Human coronary lesion morphologies categorized as nonatherosclerotic intimal lesions, progressive atherosclerotic lesions, lesions with acute thrombi, and complications of haemorrhage and/or thrombus with healing and stabilization. Reprinted from Nature Reviews Cardiology, 13(2), K. Yagahi et al., Pathophysiology of native coronary, vein graft and in-stent atherosclerosis, 79-98, Copyright (2016), with permission from Elsevier. 23

1.4 Schematic description of the positive coronary remodeling described by Glagov et al. (1987). Reproduced from Glagov et al. (1987). 24

1.5 Possible insertion sites for IVUS catheter: the femoral and radial arteries. 26

1.6 Intravascular ultrasound (IVUS) imaging modes. The positive envelope of each of the 1-D A-lines (RF lines) is obtained, stacked in the angular direction and presented in a 2-D gray-scale image to create polar B-mode IVUS images. For a more familiar representation, the polar B-mode IVUS is geometrically transformed to cartesian B-mode IVUS images that depict a cross-section of the artery. 26

1.7 Block diagram of reconstruction process of IVUS image from RF raw data. Reprinted from Emerging Trends in Image Processing, Computer Vision and Pattern Recognition, Vol /edition number, Granero et al., Chapter 6 - Rebuilding IVUS images from raw data of the RF signal exported by IVUS equipment, Pages 87-97, Copyright (2015), with permission from Elsevier. 27

1.8 Performance of the improved elasticity-palpography technique. (a) Contours (in red) of an idealized eccentric and circular plaque model (called plaque 1) in which the lesion is homogeneous. The palpography domain, Ω_{palpo} , is also given (blue contours). (b) Radial strain elastogram computed in the palpography domain. (c) Computed original (Céspedes et al. 2000) stress-strain modulus (S-SM) palpogram. (d) Comparisons between original S-SM, improved (Revisited) S-SM and averaged Young’s modulus (AYM) palpograms. From Deleaval et al. (2013) 32

<p>1.9 Performance of the improved elasticity-palpography technique in detecting a vulnerable plaque with two necrotic cores. (a) Intravascular ultrasound image of plaque 2 with plaque constituents (red contours). The boundaries of the palpography domain, Ω_{palpo}, are also given (blue contours). (b) Radial strain elastogram in the palpography domain. (c) Computed improved (Revisited) stress-strain modulus (S-SM) palpogram. (d) Comparisons between original S-SM (Céspedes et al. 2000), improved (Revisited) S-SM and averaged Young’s modulus (AYM) palpograms. nc= necrotic core, fi= fibrous region. From Deleaval et al. (2013)</p>	33
<p>1.10 Illustration of the successive calculation steps performed in our plaque elasticity reconstruction algorithm iMOD based on a segmentation-driven optimization procedure using LSME strain measurements. LSME= Lagrangian speckle model estimator; MST=Modified Sumi’s transform; DWS= Dynamic watershed segmentation; RMS= Root mean square; PFEM= Parametric finite element model (see section 4.1 for more details). Adapted from Le Floc’h. et al., 2010. On the potential of a new IVUS elasticity modulus imaging approach for detecting vulnerable atherosclerotic coronary plaques: in vitro vessel phantom study. Phys. Med. Biol. 55, 5701-5721. Copyright. Institute of Physics and Engineering in Medicine. Reproduced by permission of IOP Publishing. All rights reserved. . . .</p>	35
<p>1.11 Performance of the elasticity reconstruction algorithm iMOD to characterize locally the mechanical properties of the homogeneous vessel phantom wall using experimental RF-IVUS images acquired with a Volcano Therapeutics REMORA IVUS system. a) IVUS image (the red contours delimit the boundaries of the vessel wall); b) cross-section image of the homogeneous cryogel vessel phantom; c) measured LSME radial strain field obtained by using the Lagrangian speckle model estimator (LSME). This strain field results from two consecutive IVUS images recorded at a pressure of 0.25 kPa and 0.5 kPa, respectively; d) spatial pseudo-gradient elasticity field dW (Eq.1.19) resulting from the modified Sumi’s transform (MST) procedure. Contours of the elastic heterogeneity domains were obtained thanks to the dynamic watershed segmentation (DWS) method; e) final Young’s modulus map (or modulogram); f) resulting computed radial strain map obtained when performing a finite element simulation with the final modulogram presented in (e). Qualitatively, there is a noticeable good agreement between the PFEM-computed (f) and IVUS-measured (c) radial strain distributions. Adapted from Le Floc’h. et al., 2010. On the potential of a new IVUS elasticity modulus imaging approach for detecting vulnerable atherosclerotic coronary plaques: in vitro vessel phantom study. Phys. Med. Biol. 55, 5701-5721. Copyright. Institute of Physics and Engineering in Medicine. Reproduced by permission of IOP Publishing. All rights reserved.</p>	37

<p>1.12 Performance of the elasticity reconstruction algorithm iMOD to characterize locally the mechanical properties of the heterogeneous vessel phantom wall with two soft inclusions using experimental RF-IVUS images acquired with a Volcano Therapeutics REMORA IVUS system. a) IVUS image; b) cross-section image of the heterogeneous cryogel vessel phantom; c) measured LSME radial strain field resulting from two consecutive IVUS images recorded pressures of 4 kPa and 4.5 kPa, respectively; d) spatial pseudo-gradient elasticity field with the potential contours of the elastic heterogeneity domains with contours of the elastic heterogeneity domains; e) final Young’s modulus map (or modulogram); f) resulting computed radial strain map obtained when performing a finite element simulation with the final modulogram presented in (e). Qualitatively, there is a noticeable good agreement between the PFEM-computed (f) and IVUS-measured (c) radial strain distributions. Adapted from Le Floc’h. et al., 2010. On the potential of a new IVUS elasticity modulus imaging approach for detecting vulnerable atherosclerotic coronary plaques: in vitro vessel phantom study. <i>Phys. Med. Biol.</i> 55, 5701-5721. Copyright. Institute of Physics and Engineering in Medicine. Reproduced by permission of IOP Publishing. All rights reserved. . . .</p>	38
<p>1.13 Performance of our elasticity reconstruction algorithm iMOD to characterize ex vivo the mechanical properties of a healthy aortic wall of a Watanabe rabbit (Rabbit # S2) using experimental RF-IVUS images acquired with a Boston Scientific GALAXY2 IVUS system. a) IVUS image (the red contours delimit the boundaries of the vessel wall); b) trichrome, haematoxylin, erythrosine, safran (HES) staining of the healthy aortic wall where nucleus, cytoplasm and fibrosis are in blue, pink and yellow, respectively (no atherosclerotic lesion was observed); c) measured LSME radial strain field resulting from two consecutive IVUS images recorded at pressures of 2.3 kPa and 2.23 kPa, respectively; d) spatial pseudo-gradient elasticity field dW (Eq.1.20) resulting from the modified Sumi’s transform (MST) procedure. Contours of the elastic heterogeneity domains were obtained thanks to the dynamic watershed segmentation (DWS) method; e) final Young’s modulus map (or modulogram); f) resulting computed radial strain map obtained when performing a finite element simulation with the final modulogram presented in (e). Adapted from Deleaval (2013).</p>	39
<p>1.14 Performance of our elasticity reconstruction algorithm iMOD to characterize in vivo the mechanical properties of a human atherosclerotic plaque (patient # 9) using experimental RF-IVUS images acquired with a Boston Scientific GALAXY2 IVUS system. a) IVUS image (the red contours delimit the boundaries of the vessel wall); b) spatial distribution of the RF-correlation coefficient; c) measured LSME radial strain field obtained by using the Lagrangian speckle model estimator (LSME); d) spatial pseudo-gradient elasticity field dW (Eq.1.20) resulting from the modified Sumi’s transform (MST) procedure. Contours of the elastic heterogeneity domains were obtained thanks to the dynamic watershed segmentation (DWS) method; e) final Young’s modulus map (or modulogram); f) resulting computed radial strain map obtained when performing a finite element simulation with the final modulogram presented in (e). Qualitatively, there is a noticeable good agreement between the PFEM-computed (f) and IVUS-measured (c) radial strain distributions. Adapted from Le Floc’h et al., 2012. A four-criterion selection procedure for atherosclerotic plaque elasticity reconstruction based on in vivo coronary intravascular ultrasound radial strain sequences. <i>Ultrasound in Med. & Biol.</i> 38(12), 2084-2097.</p>	40

1.15	Performance of our elasticity reconstruction algorithm iMOD to characterize in vivo the mechanical properties of a human atherosclerotic plaque (patient # 11) using experimental RF-IVUS images acquired with a Boston Scientific GALAXY2 IVUS system. a) IVUS image; b) spatial distribution of the RF-correlation coefficient; c) measured LSME radial strain field; d) spatial pseudo-gradient elasticity MST field with elastic heterogeneity domains; e) final Young's modulus map (or modulogram); f) computed radial strain map. Adapted from Le Floc'h et al., 2012. A four-criterion selection procedure for atherosclerotic plaque elasticity reconstruction based on in vivo coronary intravascular ultrasound radial strain sequences. <i>Ultrasound in Med. & Biol.</i> 38(12), 2084-2097.	41
2.1	(A) Intravascular ultrasound (IVUS) b-mode image of a concentric atherosclerotic plaque, (B) luminal and media-adventitia borders delineated semi-automatically, (C) triangular meshes constructed by Delaunay triangulation, (D) IVUS elastogram for area strain, (E) corresponding histologic slice with Oil-red O staining (4X) showing lipid deposits and (F) corresponding histologic slice with pico-sirius staining by polarized light (4X) showing collagen. ROIs were outlined on histologic slices (E) and (F). Reproduced from Hu et al. (2011).	45
2.2	Diagram of block-matching algorithm. The red square in image at time T (b) is the yellow tagged point in the original IVUS image (a), and this square will move to the location marked as the black square at time ($T = \Delta T$) (c). The predefined block size is M x M pixels, and the search window is N x N pixels. Reproduced from Zhang et al. (2011a).	46
2.3	Contours of atherosclerotic plaques and constituents obtained from patients' IVUS images. L= lumen, fi= fibrosis, nc= necrotic core.	48
2.4	Diagram of the block-matching (BM) process for two successive IVUS b-mode images. CC: correlation coefficient; AS index: Area strain index (Eq. 2.1).	50
2.5	Performance of the b-mode based algorithm of Zhang in a plaque with a necrotic core (Plaque# 12). First, a Finite Element Analysis (FEA) is performed using the contours of the arterial geometry and the exact displacement maps U_x and U_y are computed. Then, using the Field II ultrasound simulation software, b-mode images of the plaque are synthesized. These images are used with the Block Matching (BM) algorithm to obtain the estimated displacement maps U_x and U_y . The points with a correlation higher than 0.9 are used to create a triangular element mesh that we call Zhang's mesh. Using Zhang's mesh and the U_x and U_y maps estimated with the BM algorithm, the Area Strain (AS) index is calculated for each element in the mesh. Finally, this estimated BM AS map is compared to the exact AS FEA map obtained using the FE Mesh and the exact FE U_x and U_y maps.	51

2.6	Performance of the b-mode based algorithm of Zhang in a plaque with a necrotic core (Plaque# 13). First, a Finite Element Analysis (FEA) is performed using the contours of the arterial geometry and the exact displacement maps U_x and U_y are computed. Then, using the Field II ultrasound simulation software, b-mode images of the plaque are synthesized. These images are used with the Block Matching (BM) algorithm to obtain the estimated displacement maps U_x and U_y . The points with a correlation higher than 0.9 are used to create a triangular element mesh that we call Zhang’s mesh. Using Zhang’s mesh and the U_x and U_y maps estimated with the BM algorithm, the Area Strain (AS) index is calculated for each element in the mesh. Finally, this estimated BM AS map is compared to the exact AS FEA map obtained using the FE Mesh and the exact FE U_x and U_y maps.	52
2.7	Performance of the b-mode based algorithm of Zhang in a plaque with two necrotic cores (Plaque# 16). First, a Finite Element Analysis (FEA) is performed using the contours of the arterial geometry and the exact displacement maps U_x and U_y are computed. Then, using the Field II ultrasound simulation software, b-mode images of the plaque are synthesized. These images are used with the Block Matching (BM) algorithm to obtain the estimated displacement maps U_x and U_y . The points with a correlation higher than 0.9 are used to create a triangular element mesh that we call Zhang’s mesh. Using Zhang’s mesh and the U_x and U_y maps estimated with the BM algorithm, the Area Strain (AS) index is calculated for each element in the mesh. Finally, this estimated BM AS map is compared to the exact AS FEA map obtained using the FE Mesh and the exact FE U_x and U_y maps.	53
3.1	Contours of idealized concentric and eccentric plaques used to validate the theoretical background. L= lumen, fi= fibrosis.	58
3.2	Contours of atherosclerotic plaques and constituents obtained from patients’ IVUS images. L= lumen, fi= fibrosis, nc= necrotic core, df= dense fibrosis, h= healthy arterial tissue.	59
3.3	Real contour (plaque 2) of an atherosclerotic plaque with a necrotic core obtained from a patient’s IVUS image. From this plaque, three modeled contours were built (plaques 2A-C) where the cap thickness (Cap_{thick}) increases from 93 μm to 600 μm . L= lumen, fi= fibrosis, nc= necrotic core.	60
3.4	Boundary conditions applied for the FE simulations. a) Pressure was applied to the lumen boundary and the external boundary was left free. b) The edges corresponding to the four cardinal points were constrained in the circumferential direction and sliding conditions were imposed on the two cross-sections of the vessel segment.	60

LIST OF FIGURES

3.5	Diagram for the process to obtain the spatial displacement and strain field distributions. First, the contours of the plaque constituents were extracted from IVUS images and used to create a 3-D model. A pressure gradient equivalent to the one between two IVUS frames was applied inside the lumen and the resulting radial strain distribution within the plaque was extracted ($\varepsilon_{RR}^*(R, \theta)$). This exact radial strain distribution was used as an input for the ultrasound simulation software Field II to obtain simulated RF IVUS frames. Later, the Modified lagrangian speckle estimator (MLSME) technique was used to estimate the radial strain distribution $\varepsilon_{RR}(R, \theta)$, as it would do when applied directly to patient’s RF data.	63
3.6	Performance of the anisotropic elasticity-palpography technique on idealized homogeneous concentric and eccentric plaque models (plaques 0 and 1, respectively). a,d) Plaque geometries (red contours), palpography domains (blue contours) and estimated radial strain maps b,d) IVUS images with AI-palpograms. c,f) Comparisons between exact and estimated $AI(\theta)$ palpograms. fi = fibrotic plaque region.	65
3.7	Performance of the anisotropic elasticity-palpography technique to detect vulnerable plaques with one necrotic core (plaques 12, 14 and 15). a, b, c) Plaque geometries (red contours), palpography domains (blue contours) and estimated radial strain maps. b, e, h) IVUS images with AI-palpograms. c, f, i) Comparisons between exact and estimated $AI(\theta)$ palpograms. Areas shaded in yellow indicate the location of the necrotic core.	67
3.8	Performance of the anisotropic elasticity-palpography technique to detect vulnerable plaques with two necrotic cores (plaques 16 and 17). a, d) Plaque geometries (red contours), palpography domains (blue contours) and estimated radial strain maps. b, e) IVUS images with AI-palpograms. c, f) Comparisons between exact and estimated $AI(\theta)$ palpograms. Areas shaded in yellow indicate the locations of the two necrotic cores.	67
3.9	Performance of the anisotropic elasticity-palpography technique to detect a stable plaque with one dense fibrosis inclusion (plaque 19). a) Plaque geometry (red contour), palpography domain (blue contour) and estimated radial strain map. b) IVUS images with AI-palpogram. c) Comparison between exact and estimated $AI(\theta)$ palpograms. The area shaded in yellow indicates the location of the dense fibrosis inclusion. df = dense fibrosis.	68
3.10	Performance of the anisotropic elasticity-palpography technique to detect a stable homogeneous fibrotic plaque (plaque 11) and a healthy coronary cross-section (healthy 1). a,d) Plaque/artery geometry (red contours), palpography domain (blue contours) and estimated radial strain map. b,e) IVUS image with the AI-palpogram. c,f) Comparison between the exact and the estimated $AI(\theta)$ palpograms.	68
3.11	Effect of Cap_{thick} on the resulting anisotropic elasticity palpogram. Simulations were performed with plaque 2. a, c, e, g) Plaque geometries (red contours), palpography domains (blue contours) and estimated radial strain maps. b, d, f, h) Comparisons between exact and estimated $AI(\theta)$ palpograms. i) Comparison between all estimated AI-palpograms. Areas shaded in yellow indicate the location of the necrotic core. fi = fibrotic plaque region. nc = necrotic core. . . .	69

<p>3.12 Effect of the palpography domain size on the resulting anisotropic elasticity palpogram. Simulations were performed with plaque 0 considering three palpography domain thicknesses. a, d, g) Plaque geometries (red contours), palpography domains (blue contours) and estimated radial strain maps. b, e, h) IVUS images with AI-palpograms. c, f, i) Comparisons between exact and estimated $AI(\theta)$ palpograms.</p>	71
<p>3.13 Effect of the palpography domain size on the resulting anisotropic elasticity palpogram. Simulations were performed with plaque 2 considering three palpography domain thicknesses. a, d, g) Plaque geometries (red contours), palpography domains (blue contours) and estimated radial strain maps. b, e, h) IVUS images with AI-palpograms. c, f, i) Comparisons between exact and estimated $AI(\theta)$ palpograms. The area shaded in yellow indicates the location of the necrotic core.</p>	72
<p>3.14 Effect of the palpography domain size on the resulting anisotropic elasticity palpogram. Simulations were performed with plaque 12 considering three palpography domain thicknesses. a, d, g) Plaque geometries (red contours), palpography domains (blue contours) and estimated radial strain maps. b, e, h) IVUS images with AI-palpograms. c, f, i) Comparisons between exact and estimated $AI(\theta)$ palpograms. The area shaded in yellow indicates the location of the necrotic core.</p>	73
<p>3.15 Effect of the palpography domain size on the resulting anisotropic elasticity palpogram. Simulations were performed with plaque 13 considering three palpography domain thicknesses. a, d, g) Plaque geometries (red contours), palpography domains (blue contours) and estimated radial strain maps. b, e, h) IVUS images with AI-palpograms. c, f, i) Comparisons between exact and estimated $AI(\theta)$ palpograms. Areas shaded in yellow indicate the location of the necrotic core.</p>	74
<p>3.16 Effect of the palpography domain size on the resulting anisotropic elasticity palpogram. Simulations were performed with plaque 14 considering three palpography domain thicknesses. a, d, g) Plaque geometries (red contours), palpography domains (blue contours) and estimated radial strain maps. b, e, h) IVUS images with AI-palpograms. c, f, i) Comparisons between exact and estimated $AI(\theta)$ palpograms. Areas shaded in yellow indicate the location of the necrotic core.</p>	75
<p>3.17 Effect of the palpography domain size on the resulting anisotropic elasticity palpogram. Simulations were performed with plaque 17 considering three palpography domain thicknesses. a, d, g) Plaque geometries (red contours), palpography domains (blue contours) and estimated radial strain maps. b, e, h) IVUS images with AI-palpograms. c, f, i) Comparisons between exact and estimated $AI(\theta)$ palpograms. Areas shaded in yellow indicate the locations of the necrotic cores.</p>	76

LIST OF FIGURES

<p>3.18 Sensitivity analysis revealing the influence of measurement window (MW) size on the computed AI index-palpogram for idealized homogeneous plaques 0 and 1. Four MW sizes were considered for these simulations: 75 x 15 pixels, 101 x 21 pixels, 121 x 31 pixels and 151 x 31 pixels. a, c) Plaque geometries (red contours), palpography domains (blue contours) and estimated radial strain maps obtained with the 101 x 21-pixel MW size. b, d) Comparisons between exact and estimated $AI(\theta)$ palpograms.</p>	78
<p>3.19 Sensitivity analysis revealing the influence of measurement window (MW) size on the computed AI index-palpogram for plaques with soft inclusions (2 and 13). Four MW sizes were considered for these simulations: 75 x 15 pixels, 101 x 21 pixels, 121 x 31 pixels and 151 x 31 pixels. a, c) Plaque geometries (red contours), palpography domains (blue contours) and estimated radial strain maps obtained with the 101 x 21-pixel MW size. b, d) Comparisons between exact and estimated $AI(\theta)$ palpograms. Areas shaded in yellow indicate the locations of the necrotic cores. nc= necrotic core.</p>	78
<p>3.20 Sensitivity analysis revealing the influence of measurement window (MW) size on the computed AI index-palpogram for idealized homogeneous plaques 0 and 1. Four MW sizes were considered for these simulations: 75 x 15 pixels, 101 x 21 pixels, 121 x 31 pixels and 151 x 31 pixels. a, c) Plaque geometries (red contours), palpography domains (blue contours) and estimated radial strain maps obtained with the 101 x 21-pixel MW size. b, d) Comparisons between exact and estimated $AI(\theta)$ palpograms. Areas shaded in yellow indicate the locations of the dense fibrosis inclusions. df= dense fibrosis.</p>	79
<p>3.21 A 3-dimensional plot showing the significant influence of two Young's modulus ratios $k_1 = E_\theta/E_R$ and $k_2 = E_Z/E_R$ on the amplitude of the normalized elastic anisotropy index AI/E_R for values of k_1 and k_2 between 0.5 and 2. The white circle represents the value of the normalized AI for an isotropic atherosclerotic lesion when $E_R = E_\theta = E_Z$ (i.e $k_1 = k_2 = 1$).</p>	80
<p>4.1 Temperature profile for one freeze-thaw cycle for PVA phantom fabrication. A total of 8 cycles were applied to each phantom.</p>	85
<p>4.2 a) Cross-sections of the three PVA anisotropic phantoms. b) Schematic drawing of the experimental setup used for IVUS acquisitions. The PVA phantom was placed on a water tank and pressurized using a water column and an automatic syringe pump during the ultrasound acquisitions.</p>	86
<p>4.3 a) Phantom diagram showing the coordinate system (R, θ, Z). b) Diagram of a sample cut for the tensile tests.</p>	87
<p>4.4 Phantom sample mounted on the Biotester 5000 test system (Cellscale, CA) for uniaxial tensile testing using the biorakes system. The green rectangles indicates the tracking box used to calculate the strain using the block matching algorithm.</p>	88
<p>4.5 Engineering stress vs strain curves obtained from all the uniaxial tests of (a) PH1, (b) PH2 and (c) PH3 for the longitudinal (blue) and circumferential (black) directions. The mean curves for each direction (circumferential and longitudinal) are shown in a darker color.</p>	91

LIST OF FIGURES

4.6	Pictures of the opening angle tests. Cross-sections with a thickness of 2mm were cut from all three phantoms (PH1, PH2 and PH3). A cut in the radial direction was made to each of them and images were recorded before, right after and two hours after the radial cut. No change was observed.	92
4.7	Scanning electron microscopy (SEM) results. a) Phantom diagram showing the coordinate system used. b and c) Diagrams for cuts used to obtain samples for SEM that show the internal and external borders (plane θ - Z) and the cross-section (plane R - θ) surfaces imaged with SEM. d-f) SEM images obtained from the d) internal, e) external and f) cross-sectional surfaces for each of the phantoms (PH1, PH2 and PH3) with a magnification of 500x. The planes for each surface are also given.	94
4.8	Performance of the anisotropic elasticity palpogram using <i>in vitro</i> IVUS sequences of polyvinyl-alcohol cryogel vascular phantoms. a, d, g) Phantom geometries (red contours), palpography domains (blue contours) and estimated radial strain maps. b, e, h) IVUS images with AI-palpograms. c, f, i) Estimated $AI(\theta)$ palpograms with mean \pm standard variation values.	95
4.9	Mean anisotropic index (AI) value for each pressure step for phantoms PH1, PH2 and PH3. The bars indicate the standard deviation of AI at each pressure step. The first point, highlighted with a red dot, corresponds to the initial radio-frequency (RF) intravascular ultrasound (IVUS) AI.	97
5.1	The angioplasty procedure. a) Insertion of a guide catheter from the femoral or radial artery up to the coronary artery ostium. b) Advance of a guide-wire to the lesion using X-ray and intermittent injection of radiographic contrast medium. c) A balloon catheter is slid over the guide-wire until it reaches the lesion site. d) Balloon inflation to compress plaque and restore blood flow. e) Instant elastic recoil. f) Stent placement to prevent further recoil and complications. <i>Adapted from Medicine, 42(9), Peter F. Ludman, Percutaneous coronary intervention, Pages 520-526, Copyright (2014), with permission from Elsevier.</i>	105
5.2	Top: Inflated PTCA balloon (Boston Scientific Maverick ² Monorail model). Bottom: Model indicating the balloon film and internal and external catheters.	106
5.3	Picture of the compliance curve for the Boston Scientific's Maverick ² PTCA. The nominal and rated burst pressures and diameters used to calculate the compliance of the balloon are given in this table.	106
5.4	Bench test showing the different profiles between a noncompliant balloon (A) and a semi-compliant stent delivery balloon (B) during high-pressure (>14 atm) inflation. The semi-compliant balloon demonstrates a "dog bone" effect at the edge of the cylinder that can damage the vessel wall in vivo. <i>Reproduced from JACC: Cardiovascular Interventions, 1(1), Romagnoli et al., Drug-Eluting Stenting: The Case for Post-Dilation, Pages 520-526, Copyright (2008), with permission from Elsevier.</i>	107
5.5	Top: Balloon blow molding process diagram.	108

LIST OF FIGURES

5.6	Different geometries used for FE analyses involving balloon catheters. a) FE model of an artery-stent-balloon assembly depicting a simplified balloon geometry. <i>Reprinted from David Chua et al. (2004), with permission from Elsevier.</i> b) Geometrical model of a commercially available stent and part of the delivery system (inner shaft and non-tapered part of the folded balloon) <i>Reprinted from De Beule et al. (2008), with permission from Elsevier</i>	109
5.7	Finite element simulation of the dilation of a Groentzig-type balloon catheter: (a) geometry and computational mesh of the undeformed (I) and deformed (II) configurations of the balloon and (b) applied internal balloon pressure P_b versus external balloon diameter d_e . Initially, the balloon expands quickly and only a low internal pressure is needed for its deformation. As the pressure exceeds approximately 1 bar, the balloon stiffens and deforms only slightly. <i>Reproduced from Kiouisis et al. (2008a) with permission from John Wiley and Sons.</i>	109
5.8	Pseudotensile tests for a 3.0-mm balloon. Polymer samples were loaded at 3 mm/min up to nominal load (i.e. 20 MPa), and the load was then held constant for 15 s. Three consecutive loading cycles (1A–3A) were performed, followed by a resting period of 1 h. Specimens were then loaded twice more (cycles 4B–5B) with a loading time of 10 min for the final cycle (5B). (a) Each device tested showed polymers creep within the 15-s loading time. (b) Stress–strain curves evidenced a progressive deformation of balloon materials, partially reabsorbed within 1-h resting time. <i>Reproduced from Fedel et al. (2006) with permission from John Wiley and Sons.</i>	111
6.1	Left, top: Deployed Maverick ² balloon. Left, bottom: Diagram of the balloon catheter. Right: Compliance chart provide by the manufacturer (Boston Scientific) indicating a nominal diameter of 3.5 mm at a nominal pressure of 6 atm, and a burst pressure of 12 atm.	114
6.2	Diagram of the balloon catheter indicating the main features and dimensions. Thicknesses (t) and diameters (\varnothing) of the internal and external catheters, and the balloon are also given. All measurements are in mm.	114
6.3	Images and measurements obtained from the catheters with the stereo microscope. a,b) Internal (green) and external (transparent) catheter diameters. c,d) Measurements of the internal catheter thickness. e,f) Measurements of the external catheter thickness.	115
6.4	Images of the balloon film obtained with a holographic microscope, the green arrow indicates the thickness of the film. Thickness measurements were carried out using ImageJ software.	115
6.5	a) Balloon diameter measurements were performed at three sites: (1)distal, (2) middle and (3)proximal. b) Balloon catheter diagram showing l_z , the distance between the two radiopaque markers.	116
6.6	Inflation of a Boston Scientific Maverick ² balloon catheter in air at ambient temperature. Three consecutive inflations to 20 atm were performed. The manufacturer curve (M) is also plotted. Compliance values for each curve are given in the table at the right. <i>Adapted from Cellier (2017).</i>	116

LIST OF FIGURES

6.7 Inflation of a Boston Scientific Maverick² balloon catheter in air at ambient temperature. Three consecutive inflations, the first until 12 atm (the rated burst pressure for this balloon), the second until 20 atm and the third one until rupture (18 atm). The anufacturer compliance curve is also plotted (M). Compliance values for each curve are given in the table at the right. *Adapted from Cellier (2017)*. 117

6.8 Inflation of a Boston Scientific Maverick² balloon catheter submerged in water at 37°C. Two consecutive inflations, the first two until 20 atm and the manufacturer compliance curve (M) are plotted. Compliance values for each curve are given in the table at the right. *Adapted from Cellier (2017)*. 117

6.9 Inflation of a Boston Scientific Maverick² balloon catheter in air at ambient temperature. Two successive inflations were performed on the balloon at T=0. Then, after T=16 hours, the same two inflations were repeated. This experiment highlights the viscoelastic properties of the balloon polymer film. *Adapted from Cellier (2017)*. 118

6.10 Three consecutive inflations of a Boston Scientific Maverick² balloon catheter in air at ambient temperature. The pictures show a small enlargement in the longitudinal dimensions of the balloon due to the increase in pressure. *Adapted from Cellier (2017)*. 119

6.11 Experimental setup for dynamic inflation bench for the balloon. Pressure was applied with a manual angioplasty balloon inflator, and it was monitored using a pressure sensor (0.1 bar resolution and a data acquisition card connected to a PC. Diameter was extracted (post-processing) from pictures taken using a camera attached to a stereo microscope. 120

6.12 Image processing to obtain the balloon diameter. First, high-contrast images of the center pf the balloon were acquired with a resolution of 198 pixels per mm. Using ImageJ, the images were pre-processed to find the edges of the balloon. Finally, using Matlab, the diameter at each line (corresponding to a longitudinal position) and an average diameter were calculated for each image. 120

6.13 Diameter vs pressure results of the 8 consecutive inflations of the Maverick² balloon catheter. 121

6.14 Diameter vs pressure results of inflations 1-4, 4-6 and 6-8 of the Maverick² balloon catheter. The instantaneous return points for each inflation are also included. . . 122

6.15 Diameter vs pressure results of short-time creep test of the Maverick² balloon catheter. A pressure of 6 bar (5.9 atm) was applied for 20 seconds and then released. Images were acquired at a rate of 100 ms for 40 s during the creep (20 s) and recovery stages (20 s). 123

6.16 Sample preparation protocol. (a)Each balloon provided a film of approximately 10.05 x 15 mm, that was cut in the circumferential and longitudinal directions (b). (c)The sample was mounted between two acrylic strips pasted to a base sheet, using an epoxy resin. This ensured the correct alignment of the sample. Once the sample was placed on the testing machine, both sides of the base sheet were cut. 124

LIST OF FIGURES

6.17	Top: Biotester 5000 biaxial testing system used for the uniaxial tensile tests of the balloon polymer film. The sample was mounted using mechanical grips. Bottom: Samples in the circumferential and longitudinal direction mounted on the machine. Graphite powder was added to surface of the sample to serve as markers to calculate the displacement with a digital image correlation post-process.	125
6.18	Integrated image analysis module of the Labjoy software used to quantify the motions of image features. The tracking editor window allows the modification of the digital image correlation process parameters.	125
6.19	Resulting mean curves from balloon cyclic tensile tests in the circumferential (Circ) and longitudinal (Long) directions.	126
6.20	Resulting curves from balloon cyclic tensile tests in the circumferential and longitudinal directions.	127
6.21	Top: Biotester 5000 biaxial testing system used for the uniaxial tensile tests of the balloon polymer film. The sample was mounted using mechanical grips. Bottom: Samples in the circumferential and longitudinal direction mounted on the machine. Graphite powder was added to surface of the sample to serve as markers to calculate the displacement with a digital image correlation post-process. ν = Poisson ratio; ϵ_l = strain parallel to the uniaxial tension; ϵ_t = strain perpendicular to the uniaxial tension.	127
6.22	Left: Internal catheter sample undergoing tensile tension test in the Instron 3365 universal material testing machine. Right: Section of the internal catheter with double sided tape to help grip the sample.	128
6.23	Mean curves from tensile tests of the internal and external catheters under tensile tension at a constant displacement rate of 15 mm/min.	129
6.24	Top: Setup for the acquisition of high-speed video of the deployment and burst of the balloon catheter. Bottom: Images obtained from the bursting sequence.	129
7.1	Sketch of the global model.	134
7.2	Flow chart describing the procedure to find a solution.	138
7.3	Time course of the stress. Experimental data are indicated with red dots; the model prediction is represented by the black solid line.	139
7.4	Fit of stress-strain in the $\epsilon - \sigma$ plane.	139
7.5	Model prediction for the elastic (red) and visco-plastic (blue) strains.	140
C.1	Performance of the anisotropic elasticity-palpography technique algorithm to characterize <i>ex vivo</i> a healthy aortic wall of a Watanabe rabbit (Rabbit # S2) a) Vessel geometry (red contours), palpography domain (blue contour) and estimated LSME radial strain-elastogram. b) One IVUS image of the IVUS sequence with mean AI-palpogram. c) Mean estimated AI-palpogram with its standard deviation	153

LIST OF FIGURES

D.1	Experimental curves from ballon uniaxial tensile tests in the circumferential direction.	155
D.2	Experimental curves from ballon uniaxial tensile tests in the longitudinal direction.	156
D.3	Experimental curves from uniaxial tensile tests of the internal catheter.	156
D.4	Experimental curves from uniaxial tensile tests of the external catheter.	157

LIST OF FIGURES

List of Tables

- 1.1 An updated version of the modified AHA classification published in Virmani et al. (2000), which was based on the original AHA classification published in the mid 1990s (Stary et al., 1994, 1995). Reprinted from Nature Reviews Cardiology, 13(2), K. Yagahi et al., Pathophysiology of native coronary, vein graft and in-stent atherosclerosis, 79-98, Copyright (2016), with permission from Elsevier. 22

- 2.1 Zhang’s IVUS elastography methodology 47

- 3.1 Characteristics of the IVUS-detected and modelled atherosclerotic plaques and healthy artery used to test the performance of the proposed anisotropic elasticity-palpography technique. Cap_{thick} was randomly assigned (value in parentheses) when found to be under the limit of the B-mode spatial resolution obtained with the 40-MHz IVUS catheter (i.e., $< 90\mu\text{m}$). 58
- 3.2 Pressure applied inside the lumen for the FE simulations. Pressure values equivalent to the pressure change between two IVUS frames and are adjusted to achieve a radial strain close to 2% 61
- 3.3 Orthotropic and isotropic mechanical properties and anisotropy index values assigned for the healthy wall, fibrous plaque, dense fibrosis and soft necrotic core inclusions. 61
- 3.4 Accuracy of the proposed anisotropic elasticity-palpography technique and effect of estimated radial strain-elastogram (computed with a measurement window size of (101 pixels x 21 pixels)) on the estimated AI-palpograms (see Eqs. 3.6 and 3.7 for definitions of the mean relative errors MR_{error}^{AI} , $MR_{error}^{AI^*}$ and MR_{error}^{AI/AI^*}). Palpography thickness is 1mm unless otherwise indicated in parentheses beside the plaque number. SD= standard deviation. 66
- 3.5 Anisotropic Index values for different cap thicknesses (Cap_{thick}). Values for the exact ($AI^{exact}(\theta)$) and estimated indexes with the exact ($AI^{exact}(\theta)$) and estimated strain-palpograms($AI^*(\theta)$). 69
- 3.6 Effect of palpography domain thickness ($\Omega_{palpo} = 0.75 \text{ mm}, 1 \text{ mm}$ and 1.25 mm) on the accuracy of the anisotropic elasticity-palpography technique. All palpograms were computed with a measurement window size of 101 pixels x 21 pixels. 70
- 3.7 Effect of measuring window (MW) size on the accuracy of the anisotropic elasticity-palpography technique. All palpograms were computed with a palpography domain size $\Omega_{palpo}= 1\text{mm}$ 77

LIST OF TABLES

4.1	Coefficients for the exponential curve fit of the uniaxial tension tests in the circumferential (C)(E_θ) and longitudinal (L)(E_Z) directions. The product ab corresponds to the initial Young's modulus.	90
4.2	Atomic force microscopy (AFM) and tensile tests (TT) results of the anisotropic phantoms PH1, PH2 and PH3. The AFM values of PH1 in the circumferential (θ) and longitudinal (Z) directions shown in parenthesis were obtained to compare them to TT results in the same direction and show a good agreement between them.	92
4.3	Anisotropic Index (AI) calculation using a model with incompressibility assumption (Eq. 4.3) (Model AI). Model AI is computed with the minimum (Min), average (Mean) and maximum (Max) experimentally obtained values for each of the Young's moduli (E_R , E_θ and E_Z) for phantoms PH1, PH2 and PH3. The initial RF IVUS AI is obtained applying the anisotropic elasticity-palpography technique to the first frame of each phantom sequence.	93
4.4	Tendency indices of the mean Model AI values obtained with the model assuming incompressibility (Eq. 4.3) and mean Initial RF IVUS AI values computed with the anisotropic elasticity-palpography technique (AE-PT). The asterisk symbol indicates that the calculation of the tendency index is referred to PH3.	96
6.1	Consecutive inflation protocol for a Maverick ² balloon	121